Development of a Cantilever based Device for the Investigation of Malaria Vaccine Cross-Reactivity

Thesis submitted to the

University of Dublin

for the degree of

Doctor in Philosophy

Michael Walther

10264501

Supervisor:

Professor Martin Hegner

The School of Physics

and

Centre for Research on Adaptive

Nanostructures and Nanodevices,

Trinity College Dublin

January 2015

Declaration

I declare that this thesis has not been submitted as an exercise for a degree at this or any other university and it is entirely my own work.

I agree to deposit this thesis in the University's open access institutional repository or allow the Library to do so on my behalf, subject to Irish Copyright Legislation and Trinity College Library conditions of use and acknowledgement.

Michael Walther

26 January 2015

Summary

The invention of the atomic force microscope and subsequent implementation of cantilevers as transducers for sensing applications laid the foundation for the current use of cantilevers as biosensors. This application involves functionalisation of the surface with a bio-recognition layer, immersion of the sensors in a physiological environment and operation in either the static or the dynamic mode to transduce the biological interaction into a measurable signal. When operated in dynamic mode, the cantilever is actuated at its resonance frequency. Mass uptake on the sensor results in a resonance frequency shift, thereby transforming the cantilever into a sensitive microbalance. When operated in static mode, the cantilever deflects due to a differential surface stress between the top and bottom sensor surfaces based on molecular interactions between the sensor surfaces and the analyte under study. The differential stress builds up due to variable functionalised surfaces of the cantilever.

Despite the high sensitivity of the cantilever based biosensor, there is only a limited number of incidences in the literature where cantilevers have been successfully employed using the two operating modes in parallel in a liquid environment. In this thesis, the design, development, advancement and automation of a measurement platform utilising cantilevers operated in static and dynamic mode in a physiological environment is presented. LabVIEW was used to develop the instrument control, data analysis and user interfaces. The device has been designed to fulfil the requirement of a label-free assay to investigate the cross reactivity of malaria vaccine candidates to different antibodies.

The development of the measurement chamber capable of actuating the cantilevers up to their 17^{th} flexural resonance mode enabling measurements of hundreds of picograms in liquid and with a resolution of the static mode in the order of 2-3 nm is described. The read-out of the nanomechanical response of the cantilever is achieved by the optical beam deflection method. A position sensitive detector is used to determine frequencies and deflection of the cantilever based upon the movement of a reflected laser on the detector area.

Cantilever arrays containing 8 cantilevers with a length of 500 μm, a width of 100 μm, a thickness of 1 μm, and a centre to centre spacing of 250 μm are used. A laser mounted on a 3D automated micro-translation stage system provides sequential read-out of the

cantilevers. The micro-translation stage system facilitates a fully automated laser focussing process utilising an adapted version of the well-known travelling knife-edge method to determine a laser beam diameter. An optimally focussed laser spot is important in dynamic mode readout where micron-precise positioning is required to benefit from the excellent sensitivity of the optical beam deflection method.

The measurement platform incorporates an automated sample handling system enabling the local injection of sub microliter volumes of sample with excellent repeatability. Reducing the sample volume required, enables the ability to generate more data from the same total sample volume and hence the conservation of precious biological samples. The complete automation of the device allows the greatest reproducibility possible from experiment to experiment and reduces error due to user interaction.

After the development of a standard operating procedure for a cantilever based label-free assay, the cross reactivity of a malaria vaccine candidate, a synthetic peptide named UK-39, to different IgG antibodies was investigated. The antibodies under study are the EP3 and EP9 antibodies elicited by UK-39 and SP3 antibodies elicited by *P. falciparum* sporozoites. The cantilever arrays were able to distinguish in a qualitative manner the reactivity of the UK-39 between the three antibodies. Initial measurements demonstrated the successful interaction of the UK-39 to the immobilised antibodies on the cantilevers with total maximal mass uptakes on the cantilever surface of 380 $\pm$ 30 pg for the SP3 functionalised sensors, 80 $\pm$ 40 pg for the EP3 functionalised sensors and 160 $\pm$ 25 pg for the EP9 functionalised sensors. These findings were confirmed by the static mode measurements resulting in average deflections of the cantilevers of 26 $\pm$ 8 nm (SP3), 0 $\pm$ 2 nm (EP3) and 6 $\pm$ 2 nm (EP9). This is an indication, that the UK-39 shows strongest reactivity to SP3 antibodies, a moderate reactivity towards the EP9 antibodies and a low reactivity to the EP3 antibodies, although the EP3 and EP9 antibodies are elicited by the UK-39 peptide. These measurements represent a step towards label-free assays that have the capability to investigate the cross-reactivity of different vaccine candidates in a qualitative and quantitative manner.

Acknowledgements

This dissertation would not have been possible without the help and support of many people. It is my pleasure to express my gratitude to all the people from different scientific, cultural and personal backgrounds, who supported me during my PhD work.

I would like to express my gratitude to my supervisor, Prof Martin Hegner, for giving me the opportunity to conduct my PhD research in his group, and for giving me the chance to explore the world outside the scientific world by letting me go to the Innovation Academy, the Summer Schools abroad and all the other conferences. His support over the four years, expertise, understanding, advice and patience, added considerably to my PhD work. And a special thank you for the early morning squash games, which were always intended to be an easy game in the morning and ended up in a competitive game over 5 sets. Finally, I want to thank him again for the trust he gave me in fulfilling an interesting and interdisciplinary thesis.

Thanks to the current members of the Nanobiotech group in CRANN for all of their help and general support over the last years: Florian Wruck, Francesco Padovani, James Duffy and Dr Vivek Jadhav. And as well all the previous group members: Irina Ritsch, Sarah-Louise Ball, Sinéad Cullen, Dr Paul Fleming, Dr Jason Jensen, Dr Rohit Mishra, Dr Gyöngyi Lukács, Dr Niall G. Maloney, Dr Dorothea Brüggeman, Dr Ronan Daly, Dr Hélène Gaussier, Dr Dunja Skoko and Dr Ravi Joshi.

I would like to thank Dr Paul Fleming for his practical help, the many inspiring LabVIEW coding sessions and discussions about an algorithm problem and the inputs for the development of the latest generation of the measurement chamber. Paul has been a constant help, thanks to his critical thinking, motivating discussions and helping to promote the bicycle spirit among the group members.

Thanks also to Dr Claudia Daubenberger from the Swiss Tropical and Public Health Institute for her advice regarding malaria vaccine candidates and requirements for the newly developed assay. It would not have been possible to achieve the objective of this doctoral thesis without her knowledge of the vaccination research, providing the malaria vaccine candidate samples and antibody samples.

A huge thanks to Pat Murphy and Dave Grouse in the mechanical workshop in the School of Physics for the fruitful discussions and the manufacturing of the chambers complying with my accurate requirements even though my requests were challenging. Thank you!

Dr Vivek Jadhav and Florian Wruck for their help, humour, friendship and supply of tea, chocolate and Indian lunches!

A special thanks to my previous lab mates Dr Gyöngyi Lukács and Dr Niall G. Maloney for making it easy on a tough day and for their kind support and assistance whenever needed. And for sharing all the pizza slices while working late in the lab (the pizzas were eaten in the office not in the lab…).

And a big thanks to all my friends back in Switzerland, especially Benjamin Bircher, for his input regarding the device development, especially the optical read-out. I would like to thank Raphael Urbani for the fruitful scientific discussions on the ski slopes and for his friendship.

A special thanks goes to Dr Joanne Crean for her help with the dynamic light scattering measurements and for the tea breaks and discussions about life outside academia.

I would also to extend my thanks to my fellow Innovation Academy students, and especially the staff, Louise Andrews, Ruth Kearney and Catherine O'Brien for giving me the opportunity to broaden my horizon. It was a great experience being part of the Innovation Academy, having the opportunity to partake in the International Summer School in the Netherlands and all the other special events added additional values to my time as a postgraduate student.

In addition I acknowledge the financial support from Science Foundation Ireland, grant 09/IN.1/B2623-Hegner and the travel grant from the Innovation Academy, Trinity College Dublin.

Last but not least a big thank you to my parents, Hansjörg and Brigitte, my sister Carole, my brother-in-law Roman and my nephews Arno and Matteo for their constant love, support, encouragement and entertaining skype calls. Thank you!

Contents

Acronyms

AC: Alternating current

AFM: Atomic Force Microscope

AMA: Apical membrane antigen

AR: Anti-reflective

CAD: Computer-aided design

CNC: Computer numerical control

CPU: Central processing unit

CSP: Circumsporozoite protein

DAQ: Data acquisition board

DC: Direct current

DDT: Dichlorodiphenyltrichloroethane

DLS: Dynamic light scattering

DNA: Deoxyribonucleic acid

DOF: Depth of focus

ELISA: Enzyme-linked immunosorbent assay

FGEN board: frequency generator board

FPGA: Field programmable gate arrays

GUI: Graphical user interface

HEPES: 2-[4-(2-hydroxyethyl)piperazin-1-yl]ethanesulfonic acid

I/O: Input/output

IC: Integrated circuit

IgG: Immunoglobulin G

IRIV: Immuno-potentiating influenza virosomes

IUPAC: International Union of Pure and Applied Chemistry

LabVIEW: Laboratory Virtual Instrument Engineering Workbench

ND: Neutral density

NHS: N-hydroxysuccinimide

NTC: Negative temperature coefficient

OpAmp: Operational amplifier

PBS: Phosphate buffered saline

PCR: Polymerase chain reaction

PE: Phosphatidylethanolamine

PEEK: Poly-ether-ether-ketone

PEG: Poly(ethylene glycol)

PLL: Poly(L-lysine)

PLL-*g*-PEG: Poly(L-lysine)-graft-poly(ethylene glycol)

PSD: Position sensitive detector

QCM: Quartz crystal microbalance

Q-factor: Quality factor

RTOS: Real-time operating system

SAM: Self-assembled monolayers

SEM: Scanning electron microscope

SHO: Simple harmonic oscillator

SPR: Surface plasmon resonance

VCSEL: Vertical-cavity surface-emitting laser

VI: Virtual instrument

WHO: World Health Organization

Chapter 1

Introduction

1.1 Malaria

1.1.1 General

Malaria is a life-threatening infectious disease caused by unicellular protozoan parasites mostly of the genus *Plasmodium falciparum*, which is the deadliest to humans. The mosquito transmitted disease is a world leading cause of death and illness, where people living in developing countries in tropical and subtropical regions are the most vulnerable [1]. It is one of the most pressing public health problems at present. The World Health Organization estimates that there were 216 million cases of malaria worldwide in 2010 [2], where 81% of the victims were from the sub-Saharan Africa region. Furthermore, an estimated 655,000 persons died of malaria in 2010, where 86% of these were children under 5 years of age. Globally, there were 3.3 billion people at risk of malaria in 2010 as depicted in Figure 1. Severe cases of malaria lead quickly to death while milder forms damage kidneys, the liver and the nervous system. Hence, a strategy for the interruption of malaria transmission and ultimately elimination of the disease is much-needed to prevent these deaths [3, 4].

Figure 1: Areas at risk of malaria transmission, 2010. One-fifth of the world's population live in areas with a high risk of transmission. Adapted from WHO World Malaria Report (2011) [2].

1.1.2 Life Cycle of Plasmodium

The malaria parasite develops both in humans and in the female Anopheles mosquitoes leading to a complicated life cycle that is shown in Figure 2. The transmission of the parasite occurs by a bite of a mosquito, acting as a transmission vector, infected with plasmodia (protozoan malaria parasites).

Sporozoites, the infective form of the plasmodium, are injected through the saliva of the mosquito into the human blood stream. The sporozoites reproduce in the liver and are released as merozoites into the blood stream, where they invade red blood cells for further growth and multiplication until the red blood cell bursts and releases the merozoites [5, 6]. This stage of the life cycle is responsible for the major symptoms of malaria.

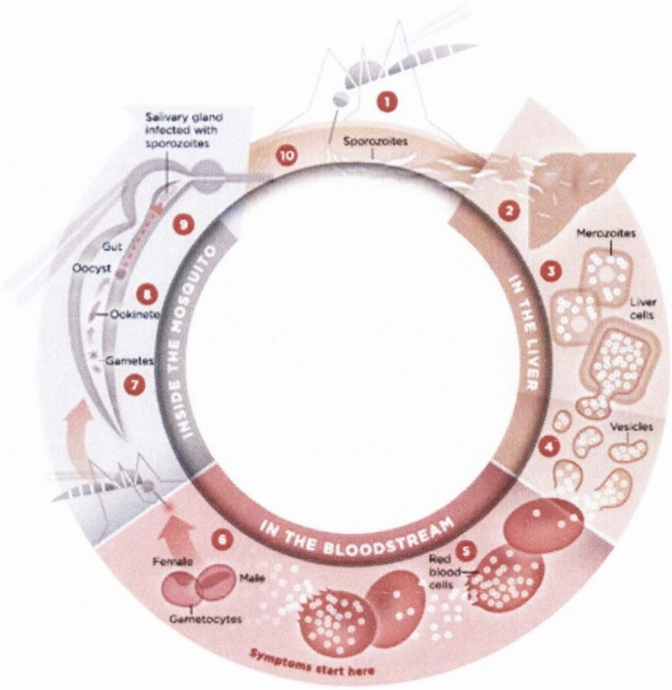

Figure 2: Life cycle of the malaria parasite (modified from [7]). 1) Sporozoites, the infectious form of the plasmodium, are injected into a human host through the saliva of an Anopheles mosquito. 2) These sporozoites enter the liver cells within minutes, 3) take on a new form, and multiply. 4) When the liver cells rupture, blood stage parasites (merozoites) are released. 5) Each merozoite invades a red blood cell, and multiplies into more merozoites until the red blood cell ruptures to release the merozoites. 6) Some merozoites change into the form called gametocytes, which do not cause disease but remain in the blood until they are cleared by drugs or the immune system, or 7) are taken up by the bite of a mosquito. 8) In the mosquito's stomach a 'male' gametocyte fertilizes a 'female' to form an oocyst, which matures into thousands of sporozoites. 9) The sporozoites swim to the mosquito's salivary glands. 10) The sporozoites will be injected into another human at the next bite of the Anopheles mosquito.

1.1.3 Strategies for Control and Elimination of Malaria

The life cycle of the plasmodium is complex and the plasmodium itself is adaptable as evidence by its survival over the centuries. Therefore, different strategies are required to try and control and reduce the risk of transmission in order to finally eradicate the disease. The strategy involves several approaches, vector control, use of antimalarial drugs and the development of a vaccine [1, 4].

1.1.4 Vector Control

By controlling the malaria vector (the Anopheles mosquito) the transmission of the parasite can be reduced and ultimately leading to an interruption of the life cycle of malaria. The most common technique is the use of indoor residual spraying (IRS) [8], however even after decades of using dichlorodiphenyltrichloroethane (DDT) for IRS, there is no equally effective and efficient alternative to circumvent the known adverse human and environmental effects linked to the use of DDT [9, 10]. Additionally, the vector can be prevented from getting infected, e.g from taking up gametocytes by biting an infected human. Long-lasting insecticidal nets can be used to interrupt the transmission from people to mosquito and vice versa [1].

1.1.5 Antimalarial drugs

Since 2006, artemisinin-based combination therapies (drugs, e.g. mefloquine, lumefantrine, etc. used in combination with the artemisinin derivative) are the treatment of choice for malaria. The combination therapy reduces the risk of parasites developing resistance against single-drug artemisinin preparations [11] as the inappropriate use of antimalarial drugs in the last century led to a widespread resistance in the malaria parasite [12]. Unfortunately, latest findings show that artemisinin resistance in *Plasmodium falciparum* has arisen and jeopardises the long-term plan of control, elimination and eradication of malaria [13]. Therefore, the spread of drug-resistant strains of malaria parasites is key and has to be dealt with properly.

1.1.6 Vaccination

The aim of vaccination is the generation of long-lasting and protective immunity. A single infection is often sufficient to generate protective immunity to a pathogen. Edward Jenner is well known around the world for his contribution to immunisation and the eradication of smallpox [14]. Vaccination is one of the most effective and cost-effective health interventions available [15]. It allows provoking an adaptive immune response in non-immune individuals by challenging their immune system with the pathogens without the harmful effects of the disease. Memory cells (specific B lymphocyte cells) will remember the pathogen that caused the disease and will respond quickly and efficiently the next time it is exposed to the same pathogen [16, 17].

A successful vaccine must possess several features in addition to its ability to induce a protective immune response. Firstly, it must be safe, even a low level of toxicity is intolerable. Secondly, the vaccine must be able to produce protective immunity in a very high proportion of the people to whom it is administered to and it must generate a long-lived immunological memory. And finally, vaccines should be very cheap if they are to be given to large populations [17].

Four types of vaccines are currently available:

- Live virus vaccines use the weakened form of the virus
- Inactivated vaccines are made from a protein or other small pieces taken from a virus or bacteria
- Toxoid vaccines contain a toxin or chemical made by the bacteria or virus to produce immunity to the harmful effects of the infection, instead of to the infection itself
- Biosynthetic vaccines contain manmade substances that are very similar to pieces of the natural pathogen

The drawback of biosynthetic vaccines is that the immune system is not activate in the same was as by a natural infection. The vaccines require additional components to mimic how infections normally activate immunity. These components are called adjuvants, which are defined as substances that enhance the immunogenicity of antigens.

It is believed that vaccinating against malaria is the best way to eradicate Malaria or at least to reduce disease and interrupt transmission. However, until today an effective vaccine has been neither introduced into clinical practice nor put on the market [18] and remains one of the most important scientific and public health challenges [19].

The development of a malaria vaccine is hampered by the fact that the malaria parasite proceeds through a succession of stages in human and mosquito hosts as shown in Figure 2, with stage specific expression of proteins. In malaria vaccine development, the pre-erythrocytic stage, the sporozoite, is targeted with the potential to prevent or reduce blood stage infection. The circumsporozoite protein (CSP), the major surface protein of the sporozoite, has been the target of several studies to develop a pre-erythrocyte vaccine that aimed at prevention of hepatocyte invasion by sporozoites [20].

Until today, there is no licensed vaccine available on the market, mainly because the research faces many challenges, including:

- The lack of highly qualified assays and models for assessing vaccine candidates
- Time-consuming and mostly label-based assays
- Requirement of large volumes of serum samples

1.2 Biosensor

A biosensor is according to IUPAC recommendations 1999 *an independently integrated receptor transducer device, which is capable of providing selective quantitative or semi-quantitative analytical information using a biological recognition element* [21]. The biological recognition element is a sensing layer containing bio-recognition elements (e.g. proteins, DNA, cells, etc.) defining the specificity of the biosensor [22]. The transducer alters (i.e. transduces) the signal caused by the interaction of the bio-recognition element with the analyte under study into an easily measurable and quantifiable signal (e.g. electric or optical signal) [23] as illustrated by Figure 3. Biosensors have been used widely for several applications, particularly to determine association and dissociation kinetics [24], protein-protein interaction [25] or nucleic acid hybridization [26].

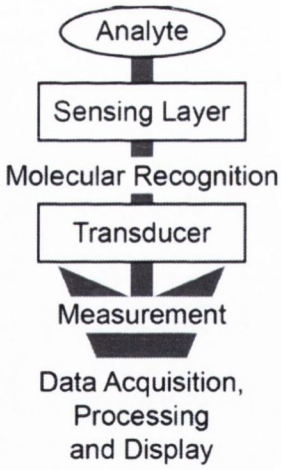

Figure 3: Conceptual diagram of the biosensor principle. The sensing layer recognises the analyte and the transducer converts this recognition process into a measurable signal.

1.2.1 Conventional Biosensor

Conventional assays for detection and identification of biological molecules can be classified into two main methods: labelled and label-free techniques. The evident

advantage of the label-free method over the labelled method is the eliminating of the need for fluorescent, chemical, or radiolabelled tags. Furthermore, label-free techniques are relatively easy to use and offer real-time data acquisition and analysis; hence, various bio-molecular interactions can be observed [27, 28].

The methods currently used to monitor the immune response to malaria vaccine candidates is the polymerase chain reaction (PCR), quartz crystal microbalance (QCM), surface plasmon resonance (SPR) and enzyme-linked immunosorbent assay (ELISA). PCR is used to analyse for the presence of parasite DNA in the blood sample, QCM is applied as a protein sensor (e.g. kinetics of antibody binding process) and ELISAs are plate-based assays designed to detect and quantify substances such as peptides, proteins and antibodies. Since ELISAs in general are highly adaptable to mass screening and automation, the ELISA test is used as a standard screening method for blood. However, this method can provide erroneous results under certain circumstances, especially the non-specific immobilization of the antigen in the microtiter plate. Furthermore, the limitation to the recognition of only one antibody per measurement slows down the malaria vaccine development.

The measurement of antibody responses in humans against recombinant parasite antigens by ELISA and SPR has been widely applied in population studies but it is still unclear how antibody levels relate to inhibitory function [29]. Furthermore, such assays typically do not measure antibody affinity and fine specificity, which may be critical for inhibitory activity. Hence, the time-consuming nature of the assays and small volumes of serum available from donors severely hamper the measurement of inhibitory antibodies raised *in vivo*.

1.2.2 Enzyme-linked Immunosorbent Assay

Enzyme-linked immunosorbent assays (ELISA) are the basis of most contemporary medical diagnostic tests in humans and animals [30]. Current applications include the diagnosis of HIV infection [31], detection of food contamination by cyanogenic glycoside [32], and detection of antibodies induced by experimental malaria vaccines [33]. ELISA utilises antibodies as a recognition element to detect the presence of the analyte, usually an antigen. The recognition antibody can be linked to an enzyme (e.g. labelled) and a substance containing the enzyme's substrate is added. The subsequent enzymatic reaction results in a detectable signal, usually a colour change read-out by a plate reader. ELISA can be divided into three main methods [34, 35]:

1. Direct ELISA
2. Indirect ELISA
3. Sandwich ELISA

For the direct ELISA methods antigens are attached to the solid phase through charge interactions. Enzyme-labelled antibodies are added to detect the adhered antigens after a washing step followed by adding of a substrate system. The subsequent colour change is the detectable signal by the plate reader. The indirect ELISA method involves the same steps as the direct method, except the detecting antibodies are not labelled with an enzyme. Instead, secondary antibodies from a different species linked to an enzyme are added to detect any bound antibodies followed by a colour change. The sandwich ELISA method exploits antibodies adhered to the solid phase to capture antigens. Enzyme-labelled antibodies then detect the bound antigen. The antigen must have at least two different antigenic sites, one for the immobilised antibody and one for the detection antibody.

1.2.3 Surface Plasmon Resonance

Surface plasmon resonance (SPR) sensing is a versatile label-free technique to investigate binding events of biomolecules. The SPR sensor comprise a glass substrate, a reflective surface (gold or other metal that enable plasmon generation) and overlaid with a functional coating. Light passing through the glass substrate as plasmon wave along the sample metal interface and is again reflected off the reflective surface to a photo detector. Surface plasmon waves at the sample and gold surface interface are created at certain angles of the incident light by coupling a portion of the light energy through the gold coating. The angle of incident light necessitated to perpetuate the surface plasmon wave is highly susceptible to refractive index changes [36] at the sensor surface due to mass change. The change of index of refraction at the interface is leading to a change in angle of the exiting ray back on the PSD. These changes of refractive index are used to investigate the association and dissociation of the biomolecules.

Current applications of the SPR technique include monitoring label-free bio-molecular binding events in liquid such as protein-ligand [37], protein-protein [38] or nucleotide hybridization [39] interactions. The SPR technique is not suitable for detection of bulk molecules due to the short penetration distance of ca. 200 nm [40] of the surface plasmons into the external medium. Furthermore, it can be that the molecular weight of the analyte is

too low to induce a change of index of refraction. Additionally, non-specific binding events interfere with the specific binding signals intended to be detected.

1.2.4 Quartz Crystal Microbalance

A quartz crystal microbalance (QCM) is a label-free sensing method that quantifies the addition or removal of mass to the sensor area by measuring a frequency change of a quartz crystal resonator. The QCM as a mass balance was introduced after Sauerbrey [41] demonstrated the theory and experiments relating the mass adsorbed on the sensor surface to a measurable frequency change of the oscillating quartz crystal. After the employment of the quartz crystal sensor in liquid environments [42, 43] the application range include chemical and biological research to investigate adsorption processes at solid-liquid interfaces. QCM has already achieved commercial success with over twenty different devices in 2010 [44]. Current applications for the QCM include the *in situ* study of enzymatic activities [45], monitoring the adsorption of proteins on surfaces [46-49] and the use as a protein sensor [50-52].

The QCM sensor consists of a circular piece of quartz that is sandwiched between two electrodes. By applying an AC voltage close to the resonance frequency of the crystal, the sensor is excited at its resonance frequency. The resonance frequency of the crystals is in the MHz regime and the sensitivity (e.g. measureable frequency change Δf) of the QCM depends on the thickness of the sensor as shown by Equation (1) [41].

$$\Delta \mathrm{m} = \frac{C}{n}\Delta f \tag{1}$$

with n being the harmonic number and C a constant characteristic of the crystal:

$$\mathrm{C} = \frac{t_q \rho_q}{f_0} \tag{2}$$

where t_q is the thickness of the quartz sensor, and ρ_q the density of quartz.

The absorbed mass Δm must be small relative to the mass of the quartz crystal to fulfil the linear relationship between the adsorbed or desorbed, mass and frequency change, respectively. Furthermore, the mass has to be rigidly adsorbed and evenly distributed over the area of the crystal .

1.2.5 Nanomechanical Biosensors

Cantilever based biosensors are being widely applied in the field of molecular interactions due to their universalism and easy functionalisation procedure with a broad range of biological molecules [53]. The cantilever based biosensors are designed to measure nanomechanical responses through a static deflection or resonance frequency shift in both ambient [54] and physiological environments [55-57]. The possibility to operate the cantilever sensor in liquid allows detection of the analyte under study in its physiological environment, providing useful insights into biological processes.

The potential of the cantilever biosensor relies on the high sensitivity combined with the label-free detection that avoids time-consuming amplification or labelling. The labelling might interfere within the molecular interaction and the amplification might be incomplete, hence distorting the measured signal. Additionally, the small dimension of the sensors results in a drastic reduction in the amount of sample required for the analysis and the scalability of the number of cantilevers in an array offer an advantage over the conventional biosensors as described in section 1.2.1.

The first applications of cantilevers as sensors were in the field of humidity sensing [58] and chemical sensing using the cantilever as a calorimeter [59]. The sensitivity of the cantilever sensor in the picogram regime for the dynamic mode was demonstrated by detection of mercury adsorbed on the cantilever from mercury vapour in air [60]. The build-up of differential surface stress due to the formation of self-assembled monolayers on the sensor surface was measured by Berger et al. [61]. Later it was shown that the grain size of the gold layer on the cantilever influences the surface stress and the origin of the transition phases during self-assembled monolayer formation [62].

All the initial sensing experiments were conducted using one single cantilever; to improve the reliability of the sensing technique a sensing and reference pair of cantilevers were implemented to suppress signals caused by external factors (e.g. nonspecific adsorption, ionic strength and temperature changes) [63]. After the implementation of a reference cantilever, the application area increased significantly. It was shown that a single base mismatch in a 12-mer oligonucleotides (hybridization of single-stranded DNAs) can be measured using cantilever arrays operated in static mode [64], followed by the utilisation of the arrays for DNA-binding and genomics experiments [54, 56, 65-69].

Cantilevers as label-free antibody-antigen binding assays have been used for the detection of prostate specific antigen [70, 71] and in combination with antibody fragments as receptor molecules [72] beside other applications as an immuno-based biosensor [73, 74]. Further applications of the cantilevers as biosensors include the sensing of protein aggregation [75], investigation of DNA-binding proteins with double-stranded DNA oligonucleotides [66], the detection of inflammatory biomarkers [76] and for the investigation of membrane protein-ligand interactions [77].

1.3 Cantilever Sensors

The invention of the Atomic Force Microscope in 1986 [78] combined with the amendment of micro-fabrication techniques has led to employment of cantilevers outside of the traditional applications (e.g. scanning probe microscopy) [79]. It was discovered in 1994 that silicon sensors are suitable as mechanical transducers for sensing applications. The first applications included humidity sensing [58] and chemical sensing using the cantilever as a calorimeter [59], followed by a broad range of applications such as gas [80], chemical [81], biological [64, 82, 83], explosives detection [84, 85] and mass sensing [55], amongst others.

The cantilevers employed as sensors are typically silicon based, however there have been polymer-based sensors utilised with the advantages of simple processing and high sensitivity due to the low Young's modulus of the polymer [86-88]. The dimensions of cantilevers used as nanomechanical sensors varies from sub-micron to millimetre sized structures depending on the specific applications, ideally arranged in an array format allowing for evaluation of different signals simultaneously and for *in-situ* references. The reference sensors allow de-coupling of environmental effects (e.g. thermal drift) or spurious events from relevant events on the cantilevers. This increases the reliability and throughput of nanomechanical sensors significantly.

The typically used cantilever array (IBM Zurich, Research Laboratory, Rüschlikon, Switzerland) in the work presented here is shown in Figure 4. It is made of silicon and consists of 8 cantilevers each with a length of 500 µm, a width of 100 µm and a thickness of 1 µm. The cantilevers are separated by a pitch of 250 µm. Additional advantage of the arrayed format is that the variation of the resonance across the 8 cantilevers varies by only 0.5% [89].

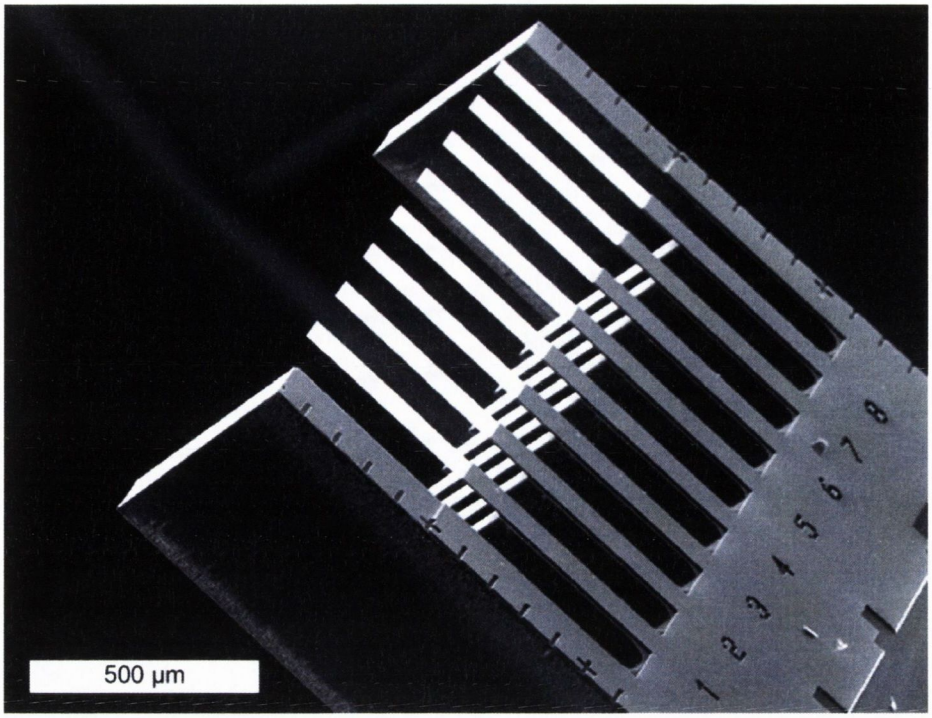

Figure 4: A scanning electron microscope image of a cantilever array (IBM Zurich, Research Laboratory, Rüschlikon, Switzerland). The array consists of 8 cantilevers with a length, width and thickness of 500 µm, 100 µm and 1 µm, respectively, separated by a pitch of 250 µm. The array allows the use of *in-situ* references during experiments. Different thicknesses are available and sizes range from 0.5 µm to 7 µm, providing different vibrational response and different sensitivity for surface stress measurements. The combination of label-free detection, *in-situ* reference, micro-array format and real-time measuring makes cantilever based sensors an interesting tool for new research areas [90]. Cantilever based sensors act as transducers in two modes, static and dynamic mode. In static mode they detect surface stress arising from adsorption of the analyte under study on the surface (described in detail in section 1.3.1.1) and in dynamic mode they detect mass changes by acting as a fine micro-balance (described in detail in section 1.3.1.2). The majority of the devices in the literature employ only one of the operational modes. To record the nanomechanical response of the cantilevers to the analyte, optical beam deflection [91] is used to read-out the deflection and the resonance frequency of the cantilevers which is outlined in more detail in section 1.3.2.

1.3.1 Principles of Operation

1.3.1.1 Surface Stress Detection: Static Mode

Operating the cantilevers in static mode, the bending of the cantilever is measured with respect to time. To detect the smallest forces possible using static mode, cantilevers with very low elastic spring constant are used. One of the cantilever surfaces is generally coated

with a functional layer (e.g. receptors) to enable specific reactions with the analyte under study. Ideally, the other surface is passivated to hinder analyte (e.g. protein) adsorption [92]. The bending arises due to a surface stress change induced by any molecular reaction which takes place on the functional layer.

Changes in the surface hydrophobicity or conformational changes of the adsorbed molecules, electrostatic, hydration, steric and van der Waals forces are responsible for the change in surface stress [89, 93, 94].

The work from G.G Stoney published in 1909 is the easiest and most extended model to study the surface stress produced on cantilevers [95]. The model relates the total surface stress difference between the top and bottom side, $\Delta\sigma$, with the radius R of the curvature of the cantilever:

$$\frac{1}{R} = \frac{6\Delta\sigma}{Et^2} \tag{3}$$

Where t is the thickness of the cantilever and E is the Young's modulus. To apply the Stoney equation the following assumptions have to be true [96]:

- The cantilever is thick compared to the thickness of the film, but still thin enough that it bends due to the stress in the film.
- The film is in a state of plane stress, meaning that in the plane of the film the stress is independent of direction.
- The rotation of the cantilever (i.e. bending angle) of the cantilever is infinitesimal

If the surface stress σ_1 is not compensated by the surface stress σ_2 on the other side of the cantilever it yields in a differential stress, $\Delta\sigma$, between the surface stresses of the top and bottom surface. This results in a bending moment M described by equation (4):

$$M = \frac{\Delta\sigma wt}{2} \tag{4}$$

Where $\Delta\sigma$ is the surface stresses difference, w the width of the cantilever and t the thickness of the cantilever. The bending moment M applied on the cantilever results in a deflection δ_M and bending angle Θ_M at the free end as shown in Figure 5.

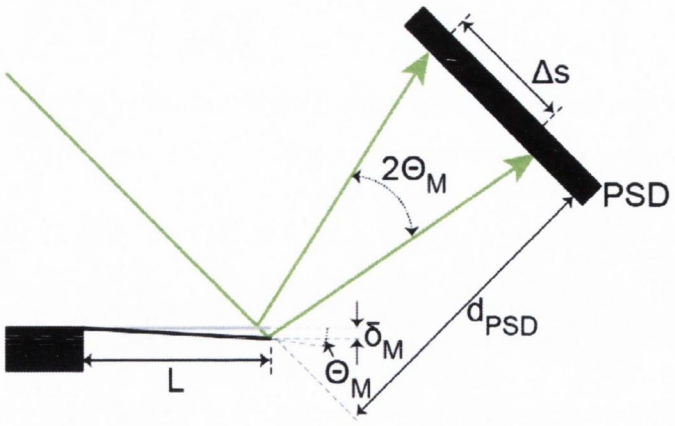

Figure 5: Schematic diagram of the optical beam deflection system used to read-out the deflection, δ_M. of the cantilevers. The laser is focused at the tip of the cantilever and the reflected laser spot is tracked by the position sensitive detector (PSD). Based on the change in position, Δs, on the PSD, the deflection, δ_M, of the cantilever can be calculated (Equation (11)) in relation to the laser path geometry.

The deflection δ and bending angle Θ at the free end of the cantilever due to the momentum M are described by [97]. With the moment of inertia I of the cantilever, the cantilever length L, the cantilever width w, cantilever thickness t and the Young's modulus E:

$$I = \frac{\mathrm{wt}^3}{12} \tag{5}$$

$$\delta_M = \frac{\mathrm{ML}}{EI} \tag{6}$$

$$\Theta_M = \frac{\mathrm{ML}^2}{2EI} \tag{7}$$

By combing equation (4), (5) and (7) and substitution of the Young's modulus E with the ratio between the Young's modulus E and Poisson ratio $E/(1\text{-}v)$ = 181 GPa due to the isotropic surface stress, which is constant within the {100} planes [98], an expression of $\Delta\sigma$ as a function of Θ is obtained:

$$\Delta\sigma = \frac{Et^2}{6L(1-\nu)}\Theta_M \tag{8}$$

The maximal bending angle Θ_M can be described as the relation between the radius R of the curvature and the length L of the cantilever. Hence, the deflection angle Θ_M can be

substituted with $\frac{L}{R}$ and this becomes the original Stoney equation (Equation (3)). However, the bending angle Θ cannot be detected directly by the optical beam deflection method. The PSD can only measure the movement, Δs, of the position of the laser spot as indicated in Figure 5 that is correlated to the bending angle Θ. Therefore, the Stoney equation cannot be applied to relate the position of the laser to the surface stress. In addition, it has been shown, that the Stoney equation does not consider the effect of the clamping of the cantilever to the surface stress induced by the bio-molecular interactions [99]. To circumvent this problem the maximal deflection of the cantilever measured at the tip is recorded. Hence, a relation between the movement of the position of the laser spot on the PSD and the deflection of the cantilever has to be obtained.

The deflection δ as a function of the bending angle Θ is given by combining equation (6) and equation (7):

$$\delta_M = \frac{2\Theta}{L} \tag{9}$$

The angular deflection of the laser beam is twice the bending angle Θ if the bending angle Θ of the cantilever is infinitesimal. Then, the angular deflection of the laser beam can be related to the change in positon of the laser spot on the PSD according to equation (10):

$$2\Theta = \frac{\Delta s}{d_{PSD}} \tag{10}$$

with d_{psd} the distance between the cantilever and the PSD. By combining equation (9) and equation (10) the relation between the change in the spot position on the PSD, Δs, and the deflection δ of the cantilever is given by equation

$$\Delta\delta = \frac{L}{4d_{PSD}}\Delta s = G\Delta s \tag{11}$$

with $G = L/4d_{PSD}$the calibration factor. The calibration factor depends on the geometry of the optical beam path between the cantilever surface and the PSD and the position of the laser on the cantilever defines L. Thus, the calibration factor is unique for each individual measurement setup and has to be accurately callipered for each setup. Additionally, it is possible to determine the calibration factor based on a thermal noise power spectrum from the cantilever and using the equipartition theorem to refer the total potential energy of the

cantilever to the mean square deflection of the cantilever caused by the thermal vibrations [100].

1.3.1.2 Mass Detection: Dynamic Mode

The dynamic operational mode analyses the response of the PSD to an oscillating cantilever read-out by the optical beam deflection method and logs the resonance frequency and the phase of the cantilever over time. An external driving force oscillates the cantilever at one of its resonance frequencies and the change in resonance frequency (shifts or damping) can be related to a change in mass [101, 102] or to the physical properties (viscosity and density) of the surrounding fluid [103, 104].

For the majority of the work outline here, the cantilevers were used as a very fine microbalance, being oscillated by an external driving force (piezocrystal actuator) at one of its resonance frequencies. At room temperature, the cantilever is driven only by the thermal noise k_BT, so that an external driving force has to be applied when measuring in a liquid environment to achieve high enough signal to noise response on the detection system. Current methods to drive cantilevers include photothermal [105, 106], magnetic [107] or piezo crystal [55, 77] actuation. A piezocrystal is a ceramic material that expands or contracts in the presence of a voltage gradient. Consequently, most devices operated in dynamic mode use piezocrystal actuators to drive the cantilever at one of its resonance. In contrast to the static mode, the dynamic mode allows the symmetric functionalisation of the top and bottom surface, as the cantilever resonance frequency shift depends on its additional mass bound to it, and not upon differential surface stress.

The model, on which the data analysis software Peak Tracker written in LabVIEW is described in detail by Braun *et al.* [102]. An outline of this model is presented here.

Taking into account that the cantilevers are rectangular, the eigenfrequencies of a cantilever oscillated *in vacuo* are given by

$$f_{0n} = \frac{\alpha_n^2}{2\pi}\sqrt{\frac{k}{3m_c}} \tag{12}$$

where k, the spring constant, equals $3EI/L^3$, (Young's modulus E, moment of inertia I *and* the length of the cantilever L) m_c is the mass of the cantilever and α_n is the n^{th} positive root

of $1 + \cos\alpha_n \cosh\alpha_n$ and is related to the eigenvalues of the harmonics ($\alpha_1 = 1.875$, $\alpha_2 = 4.694, \ldots, \alpha_n = \pi(n - 0.5)$).

When a cantilever is oscillated in liquid environment, there are several factors which are not present *in vacuo* that have to be considered. A specific mass of liquid (m_l) will also be accelerated with the cantilever, resulting in additional inertial force acting on the cantilever. The specific mass is proportional to the cantilever volume by

$$m_l = pm_d = p\rho_l V_c \tag{13}$$

where m_d is the displaced mass of the fluid, ρ_l is the density of the liquid, $V_C$the volume of the cantilever and p a coefficient equal to 1 for an ideal fluid.

Taking into account the specific mass of liquid the eigenfrequencies of a cantilever are given by

$$f_{0n} = \frac{\alpha_n^2}{2\pi}\sqrt{\frac{k}{3(m_c + m_l)}} \tag{14}$$

If the cantilever is operated in liquid, the resonance frequency refers to the maximum of the amplitude response. If additional mass, Δm, is bound to the surface of the cantilever uniformly then the total mass is given by

$$m_{total} = m_c + m_l + \Delta m \tag{15}$$

Assuming the spring constant, k, does not change then equation (14) can be changed to

$$f'_{0n} = \frac{\alpha_n}{2\pi}\sqrt{\frac{k}{3(m_c + m_l + \Delta m)}} \tag{16}$$

If the additional mass, Δm, is much smaller than the combined mass of cantilever and the co-moved liquid, $m_c + m_l$, then the following approximation can be made:

$$f'_{0n} \approx f_{0n}\left(1 - \frac{1}{2}\frac{\Delta m}{m_c + m_l}\right) \tag{17}$$

resulting in

$$\Delta m = \frac{2(m_c + m_l)\Delta f}{f_{0n}} \tag{18}$$

with $\Delta f = f_{0n} - f'_{0n}$.

The sensitivity, S, of the cantilever is defined as

$$S = \frac{\Delta f}{\Delta m} = \frac{f_{0n}}{2(m_c + m_l)} \tag{19}$$

The sensitivity of a mass sensing cantilever increases with the mode number as indicated by Equation (19), which is valid based on the eigenfrequencies-independent measurement of Δf.

However, the calculated mass uptake by the cantilever is only valid, if the mass is uniformly distributed on the cantilever surface in a thin layer without changing the spring constant [108]. It has been shown, that the position and quantity of adsorbed masses influence the response of the cantilever [109-111].

Operating the cantilever in liquid results in a loss of sensitivity due to the damping effect. To compensate for this loss in sensitivity, the cantilever should be actuated at one or more of its higher resonance modes as predicted by several models [112, 113] and experimentally demonstrated [101, 114]. The quality (Q) factor of a cantilever is given by

$$Q = \frac{2\pi W_s}{W_d} \tag{20}$$

Where W_s is the stored vibrational energy and W_d is the energy lost per cycle of vibration which can include viscous damping due to the surrounding medium, thermoelastic losses and acoustic loses to the support. The Q-factor determines the slope of the curves near resonance in the amplitude spectrum, thus the accuracy of resonance frequency measurements is determined by the Q-factor [53].

The work presented here involves the vibration of cantilevers in a liquid environment, where both the surrounding fluid and the target can affect the properties of the cantilever. There are many known challenges when operating a cantilever sensor in a liquid environment, especially in dynamic mode. In particular the large damping caused by the liquid causes low Q factors and thus lowers the sensitivity. The added mass of the co-moved liquid with the cantilever when it vibrates causes the effective mass of the cantilever to increase, and thus also lowers the sensitivity of the sensor. However, by operating the cantilever at its higher resonance modes some of the sensitivity can be regained. Measuring at higher modes will increase the Q-factor of the cantilever approximately with the mode number [115]:

$$Q_n = \frac{f_n}{f_1} Q_1 \tag{21}$$

Where Q_n is the Q-factor of the resonance mode n and f_n the resonance frequency of mode n.

Furthermore, the signal to noise is better at higher resonance modes due to the drastic reduction of the 1/f noise at higher frequencies. This 1/f noise might be due to the viscoelastic property of the gold coating, which causes structural damping [116]. It might also be caused by 1/f fluctuations of the total laser power of the optical beam deflection method, which may affect the deflection of the cantilever because of the difference in the thermal expansion coefficients of silicon and gold. In addition, operating the cantilever at higher resonance frequencies ensures that any external frequency noise can be excluded due to their low frequencies (e.g. 50/60 Hz electrical noise or vibrations from the adjacent railway tracks).

The sensitivity of a resonating cantilever beam increases as the mode number of the resonance increases. The sensitivity of the cantilever vibrating in air increases linearly with the square of the mode number n [101]. The utilisation of higher resonance mode to increase the sensitivity has been well established [117, 118]. Recent NEMS fabrication technologies have resulted in mass sensing experiments utilising nanomechanical sensors operated in ultra-high vacuum with a resolution of 7 zg (1 zg = 10^{-21} g) [119] and 1.7 yg (1 yg = 10^{-24} g) [120] and operated in ambient condition with a mass resolution of 1 ag [121].

Comparing the resolution of the presented device (in the pg regime) with the literature reveals that the resolution is much lower. Owing to the liquid environment the cantilever is operated in and the quite large dimension of the cantilevers this low resolution has to be anticipated. In order to utilise the cantilevers as biosensors, they should be operated in a physiological liquid environment rather than in ambient condition or in a ultrahigh vacuum. Under those circumstances, the achieved sensitivity for mass and frequency shift detection in liquid is superior.

Throughout this work presented here, the amplitude spectrum has been analysed using a simple harmonic oscillator (SHO) model. The resonance peaks were extracted from the amplitude spectrum and fit using the SHO model [122]:

$$A(f) = A_{bl} + \frac{A_0 f_n^2}{\sqrt{(f^2 - f_n^2)^2 + \frac{f^2 f_n^2}{Q^2}}} \tag{22}$$

where A_{bl} is the amplitude of the baseline, A_0 is the zero frequency amplitude, f is the frequency, and Q the quality factor. The f_n and Q values are extracted from the peaks by a best fit of equation (22) using a Levenberg-Marquardt algorithm.

1.3.2 Read out Method

To read out the cantilever deflections and its resonance frequency, the optical beam deflection technique is used as it provides sub-angstrom resolution [123] and it can be easily implemented [91, 124, 125]. By tracking a laser spot reflected from the cantilever on a position sensitive detector (PSD), the deflection and resonance frequency of the cantilever is measured with a fast response time and excellent linearity [126].

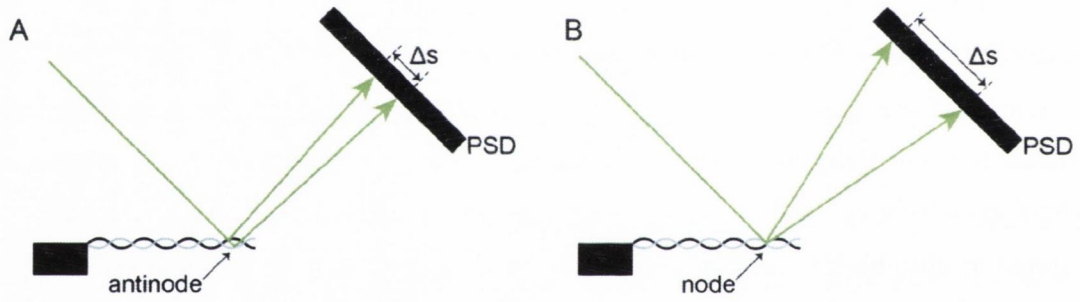

Figure 6: Schematics showing the readout of the dynamic response of the cantilever vibrating at the eighth resonance mode using optical beam deflection. A) The laser is focused near a antinode of the resonating cantilever resulting in a small change (Δs) in position of the laser spot on the PSD. B) By focusing the laser at a node, a larger change (Δs) in position of the laser spot on the PSD is obtained as is correlated to the amplitude of the oscillation.

A vibrating cantilever at its higher resonance mode consists of an alternating pattern of nodes and antinodes as shown in Figure 6. The optical beam deflection method is susceptible to a change in the slope of the oscillating cantilever. Consequently, the laser has to be focused at a node of the resonance mode of the cantilever to achieve the best possible signal.

1.4 Scope

In this thesis the development of a cantilever array based diagnostic device is outlined. The development of a rapid, simple, label-free method for the detection of the cross reactivity of antibodies has been a long-standing goal for researchers. The current biosensor techniques mentioned above either lack the sensitivity and scalability (QCM), bias due to amplification and detection of genetics instead of proteins (PCR) or a label-free measurement procedure (ELISA) compared to the cantilever based technique. Prior to the label-free detection principle cantilever based assays have gained interest for detection of bimolecular interactions in liquid. To the best of the author's knowledge only a limited number of such cantilever array based devices in the literature are capable of reading out both the static and dynamic response of the cantilevers immersed in a physiological environment [55, 127, 128].

The main scope of the thesis is to develop a sensor platform for basic science applications based on a cantilever array that transduces molecular interaction to a measureable signal utilising a label-free technique. The desired required sample volume by the assay is less than 10 µl and several target structures can be monitored in parallel. The design, development and finally the implementation of such an assay in the clinical environment could lead to a situation in which non-invasive samples (e.g. tears or saliva) can be used for antibody monitoring. Owing to the mismatch of the available non-invasive sample volume and required volume by the different assays non-invasive samples cannot be studied at the moment. The implementation of an assay offering the possibility to analyse non-invasive samples would offer the possibility to conduct vaccination outcome monitoring where antibodies induced after immunisation are detected. This monitoring process would allow conducting vaccine trials low priced compared to the current monitoring process involving invasive samples and highly skilled scientists.

The platform contains a measurement chamber suitable for biohazardous samples with the cantilever array inside, an automated sample handling system and an upgraded instrument control software. The developed chamber allows for high quality diagnostic measurements in a physiological environment. The final application in this thesis is the use of the device as a vaccine-screening platform to investigate molecular interactions of malaria vaccine candidates, to check the cross reactivity of various antibodies to individual candidates and

the ability of a cantilever based detection system to compete with the standard ELISA analysis.

Briefly, the cantilever surfaces will be functionalised with a sensing layer containing bio-recognition elements (antibodies, antigens or other specific recognition proteins) that are suitable for the desired target application. Exposure of the cantilever array to a sample in which the analyte under study is present will produce a differential change of the mechanical properties of the cantilever sensors, which can be measured.

Chapter 2 outlines the development of the device. This includes the design, assembly of the device and a detailed discussion of the measurement chamber and instrument control.

Chapter 3 presents the characterisation tests of the device conducted to determine the limits of the device and create a standard operating procedure.

Chapter 4 outlines the general procedure to perform a cantilever assay.

Chapter 5 introduces the application of the traveling knife-edge method for the laser focusing process, that is important in the context of dynamic mode analysis.

Chapter 6 describes work on the use of the cantilever array as a biosensor to investigate the cross reactivity of malaria vaccine candidate UK-39 to three different antibodies.

Chapter 7 provides a conclusion about the device and provides an outlook for future work including changes to the measurement chamber and sensing applications of the device.

1.5 References

[1] WHO 2008 Global Malaria Action Plan. In: *World Health Organization,* p 274
[2] WHO 2011 World Malaria Report 2011. In: *World Health Organization,* p 259
[3] Alonso P L, Brown G, *et al.* 2011 A Research Agenda to Underpin Malaria Eradication *PLoS Med* **8** e1000406
[4] WHO 2013 World Malaria Report 2013. In: *World Health Organization,* p 286
[5] Cowman A F, Berry D and Baum J 2012 The cellular and molecular basis for malaria parasite invasion of the human red blood cell *The Journal of Cell Biology* **198** 961-71
[6] Greenwood B M, Bojang K, *et al.* 2005 Malaria *Lancet* **365** 1487-98
[7] (MVI) P M V I Program for Appropriate Technology in Health Malaria Vaccine Initiative. (World Wide Web
[8] Breman J G, Alilio M S and White N J 2007 Defining and Defeating the Intolerable Burden of Malaria III. Progress and Perspectives *The American Journal of Tropical Medicine and Hygiene* 77 vi-xi

[9] Sadasivaiah S, Tozan Y and Breman J G 2007 Dichlorodiphenyltrichloroethane (DDT) for Indoor Residual Spraying in Africa: How Can It Be Used for Malaria Control? *The American Journal of Tropical Medicine and Hygiene* **77** 249-63
[10] WHO 2011 The use of DDT in malaria vector control. WHO position statement. In: *World Health Organization*: World Health Organization) p 9
[11] WHO 2006 The use of DDT in malaria vector control. WHO position statement. ed W H Organization p 2
[12] Bloland P B 2001 Drug resistance in malaria.
[13] Ashley E A, Dhorda M, *et al.* 2014 Spread of Artemisinin Resistance in Plasmodium falciparum Malaria *New Engl J Med* **371** 411-23
[14] Lakhani S 1992 Early clinical pathologists: Edward Jenner (1749-1823) *J Clin Pathol* **45** 756-8
[15] Plotkin S A 2005 Vaccines: past, present and future *Nat Med*
[16] Raven P, Johnson G, *et al.* 2010 *Biology*: McGraw-Hill Science)
[17] Murphy K 2011 *Janeway's Immunobiology*
[18] Thera M A and Plowe C V 2012 Vaccines for Malaria: How Close Are We? *Annu Rev Med* **63** 345-57
[19] Richie T L and Saul A 2002 Progress and challenges for malaria vaccines *Nature* **415** 694-701
[20] Moorthy V S, Good M F and Hill A V S 2004 Malaria vaccine developments *Lancet* **363** 150-6
[21] Thévenot D R, Toth K, *et al.* 2001 Electrochemical biosensors: recommended definitions and classification *Biosensors Bioelectron* **16** 121-31
[22] Kasemo B 2002 Biological surface science *Surf Sci* **500** 656-77
[23] Vo-Dinh T 2007 *BioMEMS and Biomedical Nanotechnology*, ed M Ferrari, *et al.*: Springer US) pp 1-20
[24] Myszka D G 1999 Improving biosensor analysis *J Mol Recognit* **12** 279-84
[25] Vestergaard M d, Kerman K and Tamiya E 2007 An Overview of Label-free Electrochemical Protein Sensors *Sensors* **7** 3442-58
[26] Nelson B P, Grimsrud T E, *et al.* 2000 Surface Plasmon Resonance Imaging Measurements of DNA and RNA Hybridization Adsorption onto DNA Microarrays *Anal Chem* **73** 1-7
[27] Turner A P F 2013 Biosensors: sense and sensibility *Chem Soc Rev* **42** 3184-96
[28] Perumal V and Hashim U 2014 Advances in biosensors: Principle, architecture and applications *Journal of Applied Biomedicine* **12** 1-15
[29] Chuangchaiya S and Persson K E M 2013 How Should Antibodies against P. falciparum Merozoite Antigens Be Measured? *J Trop Med* **2013** 6
[30] Lequin R M 2005 Enzyme Immunoassay (EIA)/Enzyme-Linked Immunosorbent Assay (ELISA) *Clin Chem* **51** 2415-8
[31] Branson B M 2007 State of the Art for Diagnosis of HIV Infection *Clin Infect Dis* **45** S221-S5
[32] Bolarinwa I F, Orfila C and Morgan M R A 2014 Development and Application of an Enzyme-Linked Immunosorbent Assay (ELISA) for the Quantification of Amygdalin, a Cyanogenic Glycoside, in Food *J Agric Food Chem* **62** 6299-305
[33] Miura K, Orcutt A C, *et al.* 2008 Development and characterization of a standardized ELISA including a reference serum on each plate to detect antibodies induced by experimental malaria vaccines *Vaccine* **26** 193-200
[34] Crowther J R 2009 *The ELISA Guidebook* vol 516 (Humana Press: Springer)
[35] Davies C 2013 *The Immunoassay Handbook (Fourth Edition)*, ed D Wild (Oxford: Elsevier) pp 29-59

[36] Otto A 1968 Excitation of nonradiative surface plasma waves in silver by the method of frustrated total reflection *Z Phys* **216** 398-410
[37] Jung L S, Nelson K E, *et al.* 2000 Binding and Dissociation Kinetics of Wild-Type and Mutant Streptavidins on Mixed Biotin-Containing Alkylthiolate Monolayers *Langmuir* **16** 9421-32
[38] Karlsson R and Fält A 1997 Experimental design for kinetic analysis of protein-protein interactions with surface plasmon resonance biosensors *J Immunol Methods* **200** 121-33
[39] Moon S, Kim D J, *et al.* 2010 Surface-enhanced plasmon resonance detection of nanoparticle-conjugated DNA hybridization *Appl Opt* **49** 484-91
[40] Boozer C, Kim G, *et al.* 2006 Looking towards label-free biomolecular interaction analysis in a high-throughput format: a review of new surface plasmon resonance technologies *Curr Opin Biotechnol* **17** 400-5
[41] Sauerbrey G 1959 Verwendung von Schwingquarzen zur Wägung dünner Schichten und zur Mikrowägung *Z Phys* **155** 206-22
[42] Konash P L and Bastiaans G J 1980 Piezoelectric crystals as detectors in liquid chromatography *Anal Chem* **52** 1929-31
[43] Nomura T and Okuhara M 1982 Frequency shifts of piezoelectric quartz crystals immersed in organic liquids *Anal Chim Acta* **142** 281-4
[44] Speight R E and Cooper M A 2012 A Survey of the 2010 Quartz Crystal Microbalance Literature *J Mol Recognit* **25** 451-73
[45] Bouchet-Spinelli A, Reuillard B, *et al.* 2013 Oligosaccharide biosensor for direct monitoring of enzymatic activities using QCM-D *Biosensors Bioelectron* **49** 290-6
[46] Richert L, Variola F, *et al.* 2010 Adsorption of proteins on nanoporous Ti surfaces *Surf Sci* **604** 1445-51
[47] Chandrasekaran N, Dimartino S and Fee C J 2013 Study of the adsorption of proteins on stainless steel surfaces using QCM-D *Chem Eng Res Des* **91** 1674-83
[48] Höök F and Kasemo B 2007 *Piezoelectric Sensors,* ed A Janshoff and C Steinem: Springer Berlin Heidelberg) pp 425-47
[49] Wegener J, Janshoff A and Steinem C 2001 The quartz crystal microbalance as a novel means to study cell-substrate interactions In situ *Cell Biochem Biophys* **34** 121-51
[50] Chen Q, Tang W, *et al.* 2010 Amplified QCM-D biosensor for protein based on aptamer-functionalized gold nanoparticles *Biosensors Bioelectron* **26** 575-9
[51] Dixon M C 2008 Quartz crystal microbalance with dissipation monitoring: enabling real-time characterization of biological materials and their interactions *J Biomol Tech* **19** 151-8
[52] Sharma M K, Rao V K, *et al.* 2011 A novel piezoelectric immunosensor for the detection of malarial Plasmodium falciparum histidine rich protein-2 antigen *Talanta* **85** 1812-7
[53] Tamayo J, Kosaka P M, *et al.* 2013 Biosensors based on nanomechanical systems *Chem Soc Rev* **42** 1287-311
[54] Mertens J, Rogero C, *et al.* 2008 Label-free detection of DNA hybridization based on hydration-induced tension in nucleic acid films *Nat Nano* **3** 301-7
[55] Jensen J, Maloney N and Hegner M 2013 A multi-mode platform for cantilever arrays operated in liquid *Sensors Actuators B: Chem* **183** 388-94
[56] HuberF, Lang H P, *et al.* 2013 Direct detection of a BRAF mutation in total RNA from melanoma cells using cantilever arrays *Nat Nano* **8** 125-9

[57] Ghatnekar-Nilsson S, Lindahl J, *et al.* 2005 Phospholipid vesicle adsorption measured in situ with resonating cantilevers in a liquid cell *Nanotechnology* **16** 1512

[58] Thundat T, Warmack R J, *et al.* 1994 Thermal and ambient-induced deflections of scanning force microscope cantilevers *Appl Phys Lett* **64** 2894-6

[59] Gimzewski J K, Gerber C, *et al.* 1994 Observation of a chemical reaction using a micromechanical sensor *Chem Phys Lett* **217** 589-94

[60] Thundat T, Wachter E A, *et al.* 1995 Detection of mercury vapor using resonating microcantilevers *Appl Phys Lett* **66** 1695-7

[61] Berger R, Delamarche E, *et al.* 1997 Surface Stress in the Self-Assembly of Alkanethiols on Gold *Science* **276** 2021-4

[62] Godin M, Williams P J, *et al.* 2004 Surface Stress, Kinetics, and Structure of Alkanethiol Self-Assembled Monolayers *Langmuir* **20** 7090-6

[63] Lang H P, Berger R, *et al.* 1998 Sequential position readout from arrays of micromechanical cantilever sensors *Appl Phys Lett* **72** 383-5

[64] Fritz J, Baller M K, *et al.* 2000 Translating Biomolecular Recognition into Nanomechanics *Science* **288** 316-8

[65] McKendry R, Zhang J, *et al.* 2002 Multiple label-free biodetection and quantitative DNA-binding assays on a nanomechanical cantilever array *Proceedings of the National Academy of Sciences* **99** 9783-8

[66] Huber F, Hegner M, *et al.* 2006 Label free analysis of transcription factors using microcantilever arrays *Biosensors Bioelectron* **21** 1599-605

[67] ZhangJ, Lang H P, *et al.* 2006 Rapid and label-free nanomechanical detection of biomarker transcripts in human RNA *Nat Nano* **1** 214-20

[68] Lechuga L M, Tamayo J, *et al.* 2006 A highly sensitive microsystem based on nanomechanical biosensors for genomics applications *Sensors Actuators B: Chem* **118** 2-10

[69] Ramos D, Arroyo-Hernández M, *et al.* 2009 Arrays of Dual Nanomechanical Resonators for Selective Biological Detection *Anal Chem* **81** 2274-9

[70] Yue M, Stachowiak J C, *et al.* 2008 Label-Free Protein Recognition Two-Dimensional Array Using Nanomechanical Sensors *Nano Lett* **8** 520-4

[71] Wu G, Datar R H, *et al.* 2001 Bioassay of prostate-specific antigen (PSA) using microcantilevers *Nat Biotech* **19** 856-60

[72] Backmann N, Zahnd C, *et al.* 2005 A label-free immunosensor array using single-chain antibody fragments *Proc Natl Acad Sci USA* **102** 14587-92

[73] Zhang J, Lang H, *et al.* 2013 Development of Robust and Standardized Cantilever Sensors Based on Biotin/Neutravidin Coupling for Antibody Detection *Sensors* **13** 5273-85

[74] Grogan C, Raiteri R, *et al.* 2002 Characterisation of an antibody coated microcantilever as a potential immuno-based biosensor *Biosensors Bioelectron* **17** 201-7

[75] Knowles T P, Shu W, *et al.* 2008 Label-free detection of amyloid growth with microcantilever sensors *Nanotechnology* **19** 384007

[76] Michael B, Filippo G B, *et al.* 2013 Nanomechanical recognition of prognostic biomarker suPAR with DVD-ROM optical technology *Nanotechnology* **24** 444011

[77] Braun T, Ghatkesar M K, *et al.* 2009 Quantitative time-resolved measurement of membrane protein-ligand interactions using microcantilever array sensors *Nat Nano* **4** 179-85

[78] Binnig G, Quate C F and Gerber C 1986 Atomic force microscope *Phys Rev Lett* **56** 930-3

[79] Anja B, Søren D, *et al.* 2011 Cantilever-like micromechanical sensors *Rep Prog Phys* **74** 036101
[80] Lang H P, Ramseyer J P, *et al.* 2007 An Artificial Nose Based on Microcantilever Array Sensors *Journal of Physics: Conference Series* **61** 663
[81] Battiston F M, Ramseyer J P, *et al.* 2001 A chemical sensor based on a microfabricated cantilever array with simultaneous resonance-frequency and bending readout *Sensors Actuators B: Chem* **77** 122-31
[82] Moulin A M, O'Shea S J, *et al.* 1999 Measuring Surface-Induced Conformational Changes in Proteins *Langmuir* **15** 8776-9
[83] Raiteri R, Nelles G, *et al.* 1999 Sensing of biological substances based on the bending of microfabricated cantilevers
[84] Pinnaduwage L A, Wig A, *et al.* 2004 Detection of trinitrotoluene via deflagration on a microcantilever *J Appl Phys* **95** 5871-5
[85] Senesac L and Thundat T G 2008 Nanosensors for trace explosive detection *Mater Today* **11** 28-36
[86] Calleja M, Nordström M, *et al.* 2005 Highly sensitive polymer-based cantilever-sensors for DNA detection *Ultramicroscopy* **105** 215-22
[87] Nordström M, Keller S, *et al.* 2008 SU-8 Cantilevers for Bio/chemical Sensing; Fabrication, Characterisation and Development of Novel Read-out Methods *Sensors* **8** 1595-612
[88] Zhang Y, Kim H H, *et al.* 2013 Polymeric cantilever sensors functionalized with multiamine supramolecular hydrogel *Sensors Actuators B: Chem* **178** 47-52
[89] Lang H P, Hegner M and Gerber C 2010 *Springer Handbook of Nanotechnology*, ed B Bhushan: Springer Berlin Heidelberg) pp 427-52
[90] Datar R, Kim S, *et al.* 2009 Cantilever Sensors: Nanomechanical Tools for Diagnostics *MRS Bull* **34** 449-54
[91] Putman C A J, De Grooth B G, *et al.* 1992 A detailed analysis of the optical beam deflection technique for use in atomic force microscopy *J Appl Phys* **72** 6-12
[92] Lang H P, Hegner M and Gerber C 2005 Cantilever array sensors *Mater Today* **8** 30-6
[93] Watari M, Galbraith J, *et al.* 2006 Investigating the Molecular Mechanisms of In-Plane Mechanochemistry on Cantilever Arrays *J Am Chem Soc* **129** 601-9
[94] Michel G, Vincent T-C, *et al.* 2010 Cantilever-based sensing: the origin of surface stress and optimization strategies *Nanotechnology* **21** 075501
[95] Stoney G G 1909 The Tension of Metallic Films Deposited by Electrolysis *Proceedings of the Royal Society of London Series A* **82** 172-5
[96] Janssen G C A M, Abdalla M M, *et al.* 2009 Celebrating the 100th anniversary of the Stoney equation for film stress: Developments from polycrystalline steel strips to single crystal silicon wafers *Thin Solid Films* **517** 1858-67
[97] Miyatani T and Fujihira M 1997 Calibration of surface stress measurements with atomic force microscopy *J Appl Phys* **81** 7099-115
[98] Brantley W A 1973 Calculated elastic constants for stress problems associated with semiconductor devices *J Appl Phys* **44** 534-5
[99] Javier T, Jose J R, *et al.* 2012 Quantification of the surface stress in microcantilever biosensors: revisiting Stoney's equation *Nanotechnology* **23** 475702
[100] Mishra R, Grange W and Hegner M 2012 Rapid and Reliable Calibration of Laser Beam Deflection System for Microcantilever-Based Sensor Setups *Journal of Sensors* **2012** 6
[101] Ghatkesar M K, Barwich V, *et al.* 2007 Higher modes of vibration increase mass sensitivity in nanomechanical microcantilevers *Nanotechnology* **18** 445502

[102] Braun T, Barwich V, *et al.* 2005 Micromechanical mass sensors for biomolecular detection in a physiological environment *Physical Review E* **72** 031907
[103] Ghatkesar M K, Rakhmatullina E, *et al.* 2008 Multi-parameter microcantilever sensor for comprehensive characterization of Newtonian fluids *Sensors Actuators B: Chem* **135** 133-8
[104] Bircher B A, Duempelmann L, *et al.* 2013 Real-Time Viscosity and Mass Density Sensors Requiring Microliter Sample Volume Based on Nanomechanical Resonators *Anal Chem* **85** 8676-83
[105] Bircher B A, Duempelmann L, *et al.* 2013 Photothermal excitation of microcantilevers in liquid: effect of the excitation laser position on temperature and vibrational amplitude *Micro & Nano Letters, IET* **8** 770-4
[106] Inaba S, Akaishi K, *et al.* 1993 Analysis of the resonance characteristics of a cantilever vibrated photothermally in a liquid *J Appl Phys* **73** 2654-8
[107] Han W, Lindsay S M and Jing T 1996 A magnetically driven oscillating probe microscope for operation in liquids *Appl Phys Lett* **69** 4111-3
[108] Tamayo J, Ramos D, *et al.* 2006 Effect of the adsorbate stiffness on the resonance response of microcantilever sensors *Appl Phys Lett* **89** -
[109] Ramos D, Tamayo J, *et al.* 2006 Origin of the response of nanomechanical resonators to bacteria adsorption *J Appl Phys* **100** -
[110] Ramos D, Calleja M, *et al.* 2007 Measurement of the Mass and Rigidity of Adsorbates on a Microcantilever Sensor *Sensors* **7** 1834-45
[111] Dohn S, Schmid S, *et al.* 2010 Position and mass determination of multiple particles using cantilever based mass sensors *Appl Phys Lett* **97** -
[112] Elmer F-J and Dreier M 1997 Eigenfrequencies of a rectangular atomic force microscope cantilever in a medium *J Appl Phys* **81** 7709-14
[113] Van Eysden C A and Sader J E 2007 Frequency response of cantilever beams immersed in viscous fluids with applications to the atomic force microscope: Arbitrary mode order *J Appl Phys* **101** -
[114] Ghatkesar M K, Braun T, *et al.* 2008 Resonating modes of vibrating microcantilevers in liquid *Appl Phys Lett* **92** -
[115] Garcia R and Herruzo E T 2012 The emergence of multifrequency force microscopy *Nat Nano* **7** 217-26
[116] Paolino P and Bellon L 2009 Frequency dependence of viscous and viscoelastic dissipation in coated micro-cantilevers from noise measurement *Nanotechnology* **20** 405705
[117] Dohn S, Sandberg R, *et al.* 2005 Enhanced functionality of cantilever based mass sensors using higher modes *Appl Phys Lett* **86** -
[118] Then D, Vidic A and Ziegler C 2006 A highly sensitive self-oscillating cantilever array for the quantitative and qualitative analysis of organic vapor mixtures *Sensors Actuators B: Chem* **117** 1-9
[119] Yang Y T, Callegari C, *et al.* 2006 Zeptogram-Scale Nanomechanical Mass Sensing *Nano Lett* **6** 583-6
[120] ChasteJ, EichlerA, *et al.* 2012 A nanomechanical mass sensor with yoctogram resolution *Nat Nano* **7** 301-4
[121] Li M, Tang H X and Roukes M L 2007 Ultra-sensitive NEMS-based cantilevers for sensing, scanned probe and very high-frequency applications *Nat Nano* **2** 114-20
[122] Jensen J and Hegner M 2012 Predictions of the Compressible Fluid Model and its Comparison to Experimental Measurements of Factors and Flexural Resonance Frequencies for Microcantilevers *Journal of Sensors* **2012** 7

[123] Meyer G and Amer N M 1990 Simultaneous measurement of lateral and normal forces with an optical-beam-deflection atomic force microscope *Appl Phys Lett* **57** 2089-91
[124] Raiteri R, Grattarola M, *et al.* 2001 Micromechanical cantilever-based biosensors *Sensors Actuators B: Chem* **79** 115-26
[125] Ziegler C 2004 Cantilever-based biosensors *Anal Bioanal Chem* **379** 946-59
[126] Mäkynen A 2000 Position-sensitive devices and sensor systems for optical tracking and displacement sensing applications *Academic Dissertation to be presented with the assent of the Faculty of Technology, University of Oulu, Finland*
[127] Ghatkesar M K, Lang H-P, *et al.* 2008 Comprehensive Characterization of Molecular Interactions Based on Nanomechanics *PLoS One* **3** e3610
[128] Bosco F G, Chen C H, *et al.* 2011 High-throughput automated system for statistical biosensing employing microcantilever arrays*23-27 Jan. 2011)* p 877-80

Chapter 2

Instrumentation

This chapter describes the design and development of a device using a cantilever array as biosensors. The cantilevers act as transducers and are operated in static and dynamic mode in a physiological liquid environment. The main components including the measurement chamber, the laser positioning system, the optics, the position sensitive detector, the temperature control and the fluidic system of the device are described in detail. Additionally, the architecture of the instrument control software will be depicted and a brief description of the measurement procedure will be given.

2.1 Introduction

The motivation behind the development of a new measurement chamber for a cantilever based diagnostic device was the following:

- The existing liquid chamber for dynamic mode measurements used a u-shaped glass cover. This cover was difficult to mount, resulting in a leaking liquid chamber due to its construction. Such a configuration is not suitable for biohazardous diagnostic assays. Furthermore, the measurements had to be conducted in a continuous pumping flow mode to avoid drying of the cantilevers and air bubble formation in the liquid chamber.
- The optics of the old devices used a vertical-cavity surface-emitting laser (VCSEL) array, which was mounted on a sliding dovetail mount using a screw to fix the position inside a temperature-controlled box. Focusing and moving the VCSEL spot accurately with micron precision on the cantilever was hampered due to the design. In addition, the VCSELs as used were short-lived and were not commercially available anymore.

- The latest device incorporated a single mode laser diode with an optical rig devised of a 30 mm cage system and 1" optical elements. This setup resulted in a bulky optical fixture and constricted travelling range for the laser in all directions.
- The existing liquid chambers for static mode and dynamic mode measurements required a manually operated external injection loop valve with injection loops volumes ranging from 20 µl to 500 µl.
- The existing devices suffered from a lack of scalability; they are limited to one cantilever array. In addition, the software was not scalable, e.g. no modular structure and outdated software architecture was implemented.

These issues and the application as a diagnostic device for a malaria vaccine cross-reactivity test required a multidisciplinary approach, representing the following technological objectives:

- A leak-proof measurement chamber to conduct biohazardous experiments. The required sample volume of the measurement chamber must be less than 10 µl to generate more data from the same samples.
- Operational mode of the device: capable of measurement of the static and dynamic responses of a cantilever array in a physiological liquid environment. In order to overcome some of the lost sensitivity of the dynamic mode due to working in a liquid environment the actuator in the measurement chamber must be capable to vibrate the cantilever at one or more of its higher resonance modes.
- A three axis positioning system allowing for precise positioning and focusing of the laser on the cantilevers in three axes. This fine positioning and focusing is required to read-out the static mode and the higher resonance mode of vibrations for the dynamic mode with the highest precision.
- A smaller optical rig offering a compact design and less constraint. This allows more flexibility for future improvements of the platform and implementation of additional components within the same temperature controlled setup.
- A sample handling system with minimal required sample volume and a fully automated injection system to minimise the influence of the operator of the device. Hence improving the reliability and reproducibility of the platform.

2.2 Cantilever Array based Diagnostic Device

2.2.1 Overview

An overview of the setup is shown in Figure 7. The setup contains a temperature-regulated box, a chassis and a computer. The box contains a measurement chamber, an optical cage, a laser positioning system, a position sensitive detector and a sample handling system. The chassis is comprised of data acquisition devices and power-supplies. The computer provides a graphical user interface for the instrument control and the data processing algorithm.

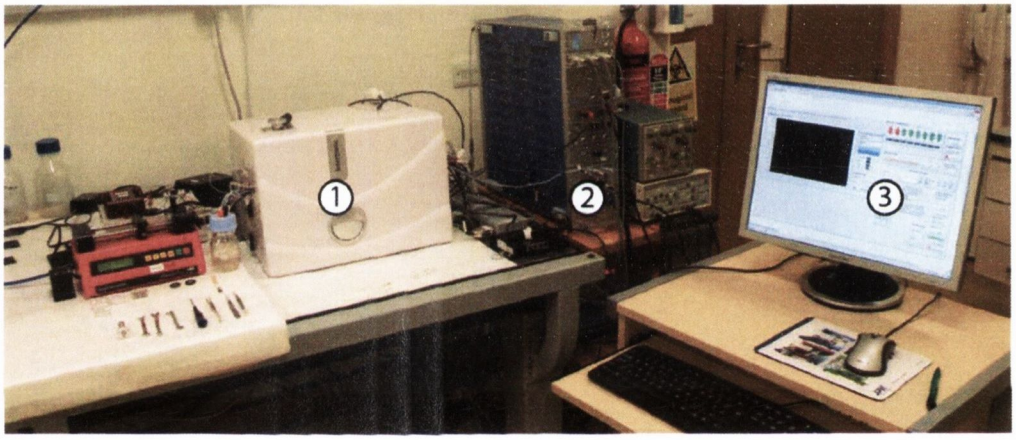

Figure 7: Overview of the cantilever array based diagnostic setup. 1 Temperature-regulated box containing the measurement chamber, the optical cage, the laser positioning system, the position sensitive detector and the sample handling system, 2 Chassis containing data acquisition boards and power-supplies, 3 Computer with the graphical user interface for the instrumentation control and algorithm for the data processing.

2.2.2 Measurement Chamber

The new measurement chamber as shown in Figure 8 is made from poly-ether-ether-ketone (PEEK), which is an opaque, easily machinable semi-crystalline high purity polymer material. PEEK has been chosen because of its excellent wear resistance, which help maintain cantilever pocket and cantilever array clamp reliability, its low moisture absorption, low permeability and low outgassing behaviour. Most important, it is biologically inert and can withstand a wide range of acids, bases, hydrocarbons and organic solvents [1].

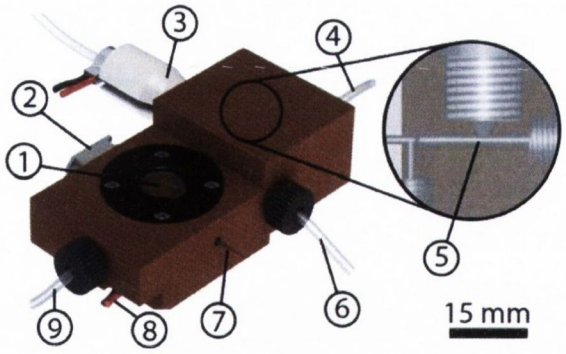

Figure 8: The measurement chamber is comprised of the following parts: 1 Liquid cell with cantilever array inside, 2 Plug for the piezo actuator, 3 Micro-dispensing valve fixed with a manifold mounting nut, 4 Liquid inlet, 5 Outlet nozzle of the micro-dispensing valve, 6 Priming liquid outlet, 7 Thermocouple, 8 Peltier element, 9 Liquid outlet.

The chamber body has two liquid inlets and two outlets. Extruded Teflon tubing (PTFE, ID: .031, OD: .063; Zeus, Orangeburg, USA) is connected at each flat-bottom port (liquid inlet, priming liquid outlet and liquid outlet in Figure 9) using M6 PEEK nuts and flangeless ferrules (Idex Corporation, Illinois, USA). The fourth port houses a micro-dispensing valve (INKX0514300A; The Lee Company, Connecticut, USA) fixed using a manifold mounting nut such that the outlet nozzle is protruding directly into the flow stream as shown in Figure 8. The design of the liquid channel ensures the flow of the liquid is occurring from the side of the cantilever array and only across the cantilevers.

The liquid cell of the measurement chamber that incorporates the cantilever array is depicted in Figure 9. The cantilever array is held within a recessed pocket, which fixes the array at an angle of 18° to the glass cover. The cantilever array is held firmly in place using a PEEK clamp screwed in place using two PEEK screws (PKMP164 ;Solid Spot LLC, Santa Clara, CA, USA). The fixation of the cantilever chip to the support by screws is removing an elastic O-ring element that was used previously in the first generation of the measurement chamber (see Appendix A.2). This further stabilises the sensor read-out and reduces drift after injection of samples. Once the cantilever is fixed in place, a double anti-reflective coated glass cover (Mirogard®; Schott AG, Mainz, Germany) is placed on top of an O-ring seal (d_1 8 mm, d_2 1 mm Viton®; Kubo Tech AG, Effretikon, Switzerland) and retained in place by a black anodised aluminium frame tightened by four screws. The angle of 18 ° (Figure 10 A) of the recessed cantilever array is used in order to avoid the creation of any standing waves and internal reflections (Figure 10 B) from the glass cover and chamber wall, which may cause additional noise. By using the highly transparent glass

cover which offers less than 1% residual reflection, undesirable reflections within the liquid chamber are eliminated.

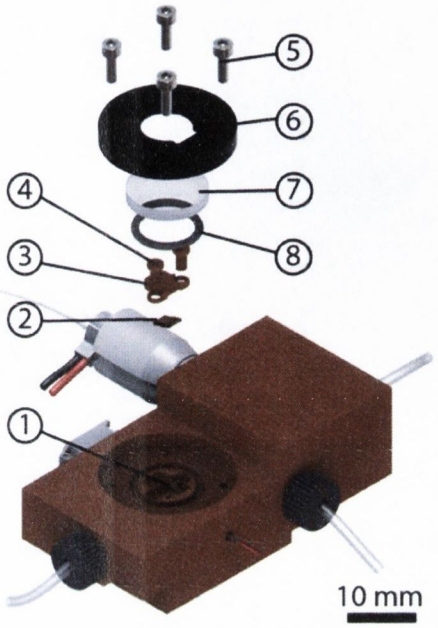

Figure 9: Exploded view of the measurement chamber: 1 Recessed pocket for the cantilever array and liquid cell, 2 Cantilever array, 3 Cantilever array clamp, 4 Two PEEK screws, 5 Screws to tighten the frame, 6 Anodised aluminium frame, 7 Glass cover, 8 O-ring seal.

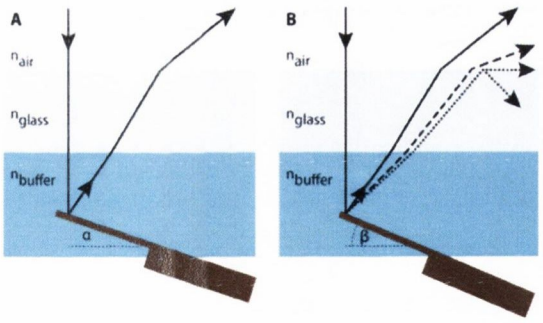

Figure 10: Schematic of the laser path into the chamber, reflected off the cantilever, travelling through the buffer, glass cover, and finally air with refractive indices n_{air} = 1.000277, n_{glass} = 1.52 and n_{buffer} = 1.334, not drawn to scale; The dimensions of the cantilevers are exaggerated for clarity. A) The cantilever array is tilted by angle α of 18° to the glass cover. The solid arrow indicates the reflected laser beam. B) By changing the angle of the cantilever array by 4.5° to an angle β of 22.5° the exit angle of the reflected laser beam changes (dashed reflected laser path) and gets closer to the critical angle ($\beta > 24°$), resulting in total internal reflection (dotted reflected laser path), that has to be avoided.

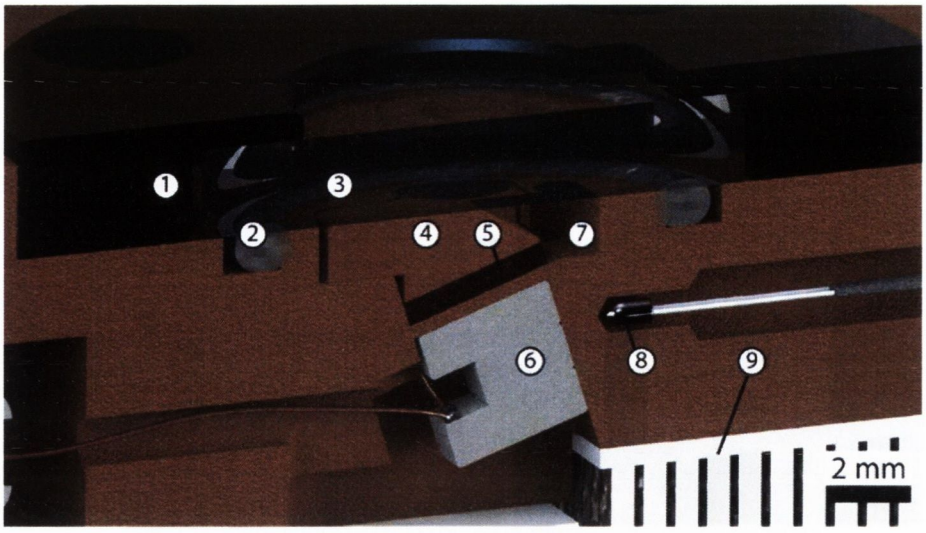

Figure 11: Front section view of the measurement chamber. 1 Black anodised aluminium frame, 2 O-ring seal, 3 Glass cover, 4 PEEK cantilever array clamp, 5 Cantilever array, 6 Piezoelectric stack actuator, 7 Liquid cell, 8 Thermocouple, 9 Peltier element. The gap around the piezoelectric stack is filled up with Loctite® Hysol® 1C [Torr Seal] to provide a rigid environment to direct the energy of the piezoelectric stack towards the cantilever array and further insulation from the liquid.

As shown in Figure 11, the cantilever array body and the piezo actuator are separated by a 200 µm thin membrane. The PEEK clamp fixes the body of the cantilever array tightly and two tiny PEEK screws wedge the clamp into the main body of the measurement chamber. This setup allows coupling of the actuator and the cantilevers without exposing the electric contacts of the piezo actuator to the liquid in the measurement chamber.

To measure the temperature inside the liquid chamber, a precision temperature sensor (SEMI833ET; Hygrosens Instruments GmbH, Löffingen, Germany) is fixed in the PEEK chamber using thermally conductive glue (H70E; Epoxy Technology, Inc. Billerica, MA, USA) in close proximity to the liquid chamber as shown in Figure 11. A peltier element (ET-007-05-15; Global Component Sourcing, Hong Kong, China) is placed below the liquid cell to enable a rapid change of temperature, which can be used during post processing for normalisation of the nanomechanical responses of the cantilevers and ascertain the direction of actual bending from the signals obtained optically.

When the double anti-reflective coated glass cover is built-in, the resultant liquid cell volume is 3.048 µl which is small enough to allow efficient exchange of liquids and minimise the amount of the precious sample required.

For greater experimental flexibility, the chamber can be extended with an injection port manifold. The two point manifold chamber is shown in Figure 12. The design of the chamber allows for up to a four-point manifold, limited by the dimension of the chamber.

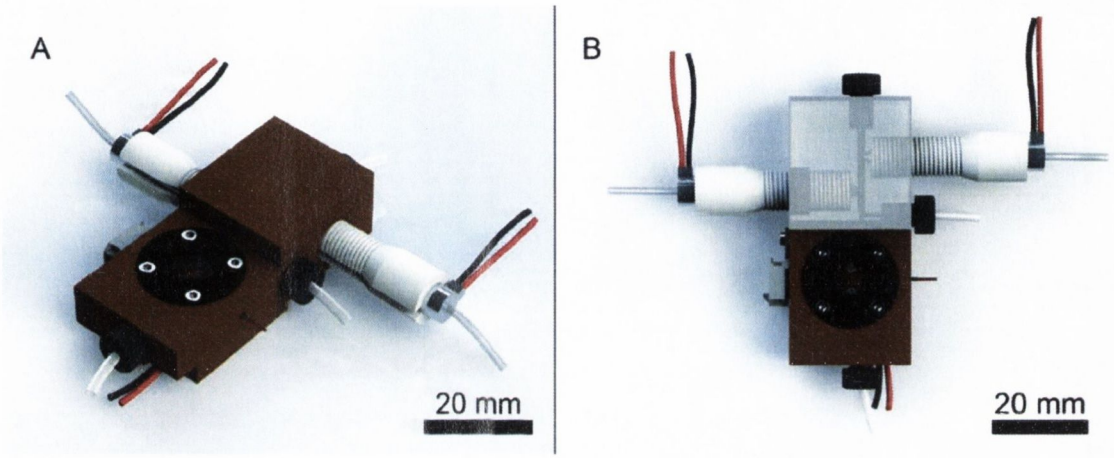

Figure 12: Two point manifold measurement chamber. A) 3d view of the chamber B) Cutaway view of the two point manifold.

2.2.3 Piezo Actuator

Actuating a cantilever in air or liquid is a requirement for dynamic mode mechanical sensing applications [2]. The thermal noise spectrum from the thermal motion does not provide adequate amplitude of motion for higher resonance frequencies in liquid. Current actuating methods in liquid include acoustic [3], magnetic [4] and photothermal [5] excitation. Due to its simplicity and ease of implementation, mechanical excitation, which utilises a piezoelectric stack actuator, is the most often employed actuating method.

For the higher resonance modes of the dynamic mode measurements, a tiny piezocrystal stack actuator has been constructed. The stack is composed of three piezoelectric crystal layers each 1.0 mm thick as shown in Figure 13 A. Two 2x3 mm^2 piezoelectric pieces (Ebl#2 rect nickel, EBL Products INC., East Hartford, USA) and one 2x2 mm^2 piece (Ebl#2 rect nickel, EBL Products INC., East Hartford, USA) are sandwiched together using electrically conductive epoxy resin (EPO-TEK® E4110; Epoxy Technology, Inc. Billerica, USA). The electrical contacts between the layers are achieved by gluing thin copper wires (0.1 mm diameter, 0822942, BLOCK Transformatoren-Elektronik GmbH, Verden, Germany) to the layer with the electrically conductive epoxy resin listed above. The mains connections are made gluing copper wires (0.22 mm diameter, 918811, BLOCK Transformatoren-Elektronik GmbH, Verden, Germany) with the same conductive epoxy

resin to the piezocrystal stack and soldered to the plug (MICRO-FIT 43650-0200, Molex, Shannon, Co. Clare. Ireland). The side gap of the piezocrystal stack is filled up with a soft epoxy resin (EPO-TEK® 301; Epoxy Technology, Inc. Billerica, USA) to retain the electrical connections as visible in Figure 13 B.

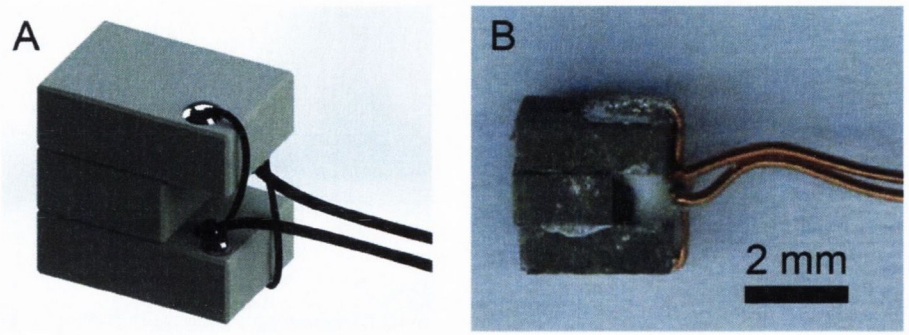

Figure 13: Piezoelectric actuator A) CAD rendered image of the home made piezoelectric actuator stack and its wiring B) The piezo stack prior to gluing in to the measurement chamber underneath the recessed pocket for the cantilever array.

The piezoelectric actuator stack is glued underneath the recessed pocket for the cantilever array body separated by a 200 µm thin PEEK membrane to minimize dissipation and to shield the electric leads using epoxy resin (Loctite® Hysol® 1C [Torr Seal] Agilent Technologies Ireland Ltd, Cork, Ireland). A soft epoxy resin (EPO-TEK® 301; Epoxy Technology, Inc. Billerica, USA) was used to fill the remaining space in the pocket with the piezocrystal actuator stack glued in. On top of the piezo stack a glass ceramic plate with dimension of 15 mm x 10 mm x 2 mm (MACOR, Radionics Ltd., Dublin, Ireland) is glued to seal it from the environment and to provide a rigid backside to direct the energy of the piezoelectric actuator stack towards the cantilever array.

2.2.4 Fluidics

Liquid is introduced to the liquid cell using two different methods as shown in Figure 14. Firstly, a Genie™ Plus Syringe Pump (Kent Scientific Corporation, Connecticut, USA) is used to pump buffer through the measurement chamber. Secondly, a micro dispensing valve is used to introduce the sample of interest to the liquid line and is pressure driven. A compressed air regulator (U33-0.3-M-NFG, Spectron Gas Control Systems GmbH, Frankfurt, Germany) provides the appropriate pressure (e.g. 100 mbar for the experiments) and the desired volume is injected through controlling the opening time of the micro dispensing valve.

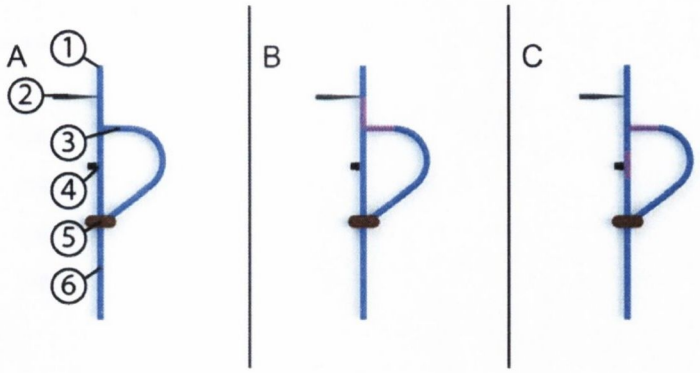

Figure 14: Schematic of the fluidics of the measurement chamber, not drawn to scale. A) The chamber is filled with buffer. 1 Buffer inlet connected to syringe pump, 2 Micro dispensing valve including the sample reservoir, 3 Priming outlet, 4 Liquid cell containing the cantilever array, 5 Three-way valve to control the flow either through the liquid cell or to the priming outlet, 6 Outlet to waste container. The three-way valve controls the direction of the liquid through the measurement chamber either through the liquid cell or by bypassing the liquid cell through the priming outlet. B) The chamber is primed with the purple sample. C) The sample is introduced to the liquid cell by switching the valve 5 and starting the syringe pump connected to the buffer inlet 1.

A three-way manifold mounted miniature rocker isolation solenoid valve (S067A102 12DC; ASCO Valve, Inc. Florham Park, NJ, USA) allows control over whether the liquid flows into the liquid cell of the measurement chamber or whether it bypasses it using the priming outlet. The priming outlet is located between the measurement chamber and the two inlet ports. This outlet allows priming of the micro dispensing valve without introducing sample into the cantilever chamber before it is required.

The sample is loaded manually into the sample reservoir depicted in Figure 15. The outlet of the sample reservoir is linked to the micro dispensing valve by tubing (PTFE, ID: .031, OD: .063; Zeus, Orangeburg, USA). The sample is injected into the measurement chamber by opening the micro dispensing valve for the designated time. The electronic 2-way valve (EV-2-24; Clippard Instrument Laboratory, Inc., Cincinnati, OH, USA) is used to shut off the compressed air line while loading the sample into the sample reservoir.

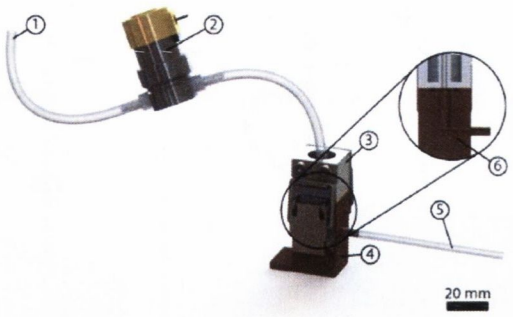

Figure 15: Pressurised sample reservoir used for the sample injection. 1 Compressed air line linked to a compressed air regulator, 2 Electronic 2-way valve to shut off the compressed air line, 3 Detachable sample reservoir lid, 4 Sample reservoir (0-100 µl), 5 Outlet from the sample reservoir connected to the micro-dispensing valve of the measurement chamber, 6 Section view of the sample reservoir.

2.2.5 Method of Detection

To read out the cantilever deflections and its resonance frequency the optical beam deflection technique is used as it provides sub-angstrom resolution [6] and it can be easily implemented [7-9]. A single laser is combined together with a position sensitive detector (PSD) as shown in Figure 16. The PSD is an opto-electronic device that converts an incident light spot into continuous position data with an outstanding resolution. This combination enables a fast response time up to 1.5 MHz and excellent linearity [10].

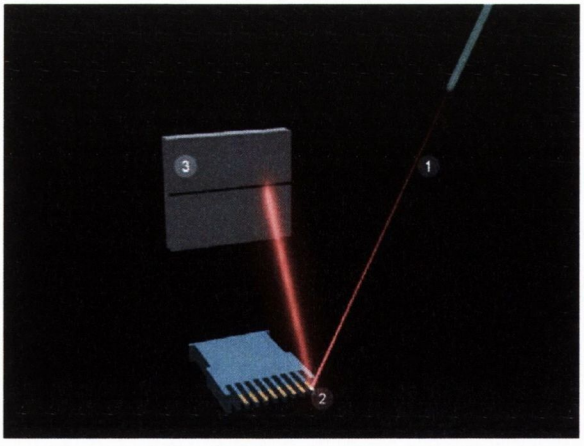

Figure 16: Optical beam deflection read-out technique: The incident single laser (1) is reflected of the cantilever (2) on to the position sensitive detector (3).

By tracking a reflected laser spot from the cantilever on a PSD, the deflection and resonance frequency of the cantilever is measured. The PSD utilised is able to detect a light

spot moving over its surface in one dimension, ideally a straight line, perpendicular to the two electrodes.

2.2.6 Optical Cage

Optical read-out is the most commonly used read out method for cantilever based sensors [6]. Additionally, other optical read out systems are deployed to detect dynamic responses and deflections of micromechanical elements, such as astigmatic detection systems [11], and high-speed scanners [12] with similar resolutions, but they lack the simplicity of an optical beam deflection method based on a single wave length laser. Therefore, this method has been implemented in the device using a 16 mm cage system (SP02 and SR3; Thorlabs Ltd. Cambridgeshire, UK) containing the optical elements to maintain the optic axis. A single wavelength fibre-coupled laser diode (830 nm, 10 mW, C Pin Code, SM Fibre Pigtailed Laser Diode; LPS-830-FC; Thorlabs Ltd. Cambridgeshire, UK) coupled to a collimator package (F280APC-B; Thorlabs Ltd. Cambridgeshire, UK) are linked to the optical cage as shown in Figure 17.

Due to the external laser driver (ITC4001 Benchtop Laser Diode /TEC Controller, 1 A / 96 W; Thorlabs Ltd. Cambridgeshire, UK) and the temperature controlled mount (TCLDM9-TE-Cooled-Mount; Thorlabs Ltd. Cambridgeshire, UK) the laser stabilises within 1% once it has been powered on for 20 minutes, resulting in a free laser power of 10 mW with a line width >200 kHz.

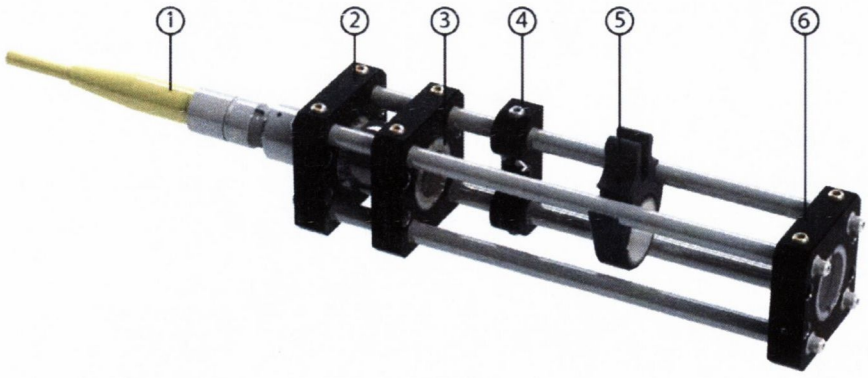

Figure 17: Optical cage system containing the following components: 1 Laser fibre, 2 Cage plate, 3 Cage plate with mounting adapter with a fixed focus collimation package, 4 Cage mounting bracket, 5 Quick-release cage mount with switchable neutral density filter, 6 Cage plate with a 50 mm focal length achromatic doublet.

The collimated laser beam with a diameter of 3.45 mm is focused into a spot of 16 µm diameter on the cantilever using a 50 mm focal length achromatic doublet (AC127-050-B; Thorlabs Ltd. Cambridgeshire, UK) as depicted in Figure 18. To avoid saturation of the position sensitive detector an absorptive neutral density filter with an optical density 1.0 (NE510B; Thorlabs Ltd. Cambridgeshire, UK) mounted in a quick release cage can be inserted into the beam path.

The need for a sophisticated optical system [13] to read-out the dynamic response of the cantilevers if the incident and reflected laser beam share the same path is eliminated, because the laser reflected off the cantilevers is directed onto the position sensitive detectors as shown in Figure 18. The laser enters the measurement chamber from the top through the double anti-reflective coated glass window and is reflected on to the position sensitive detector.

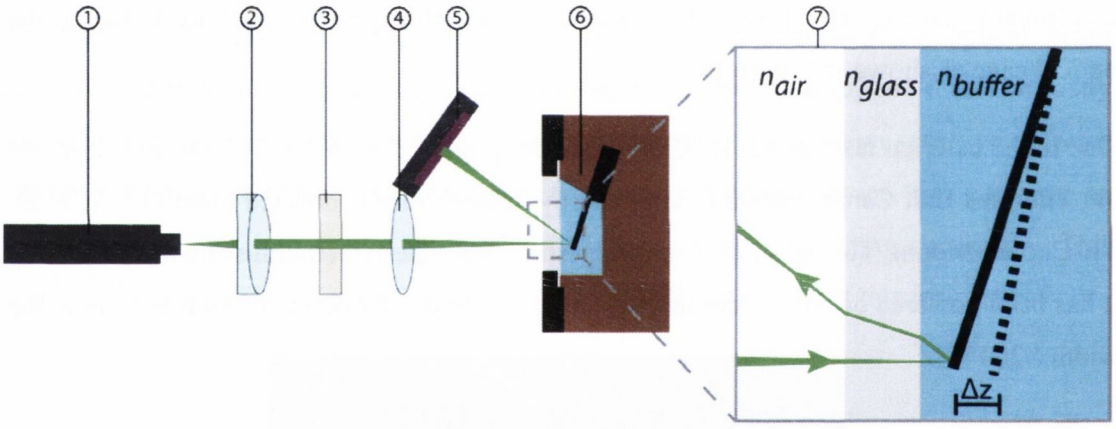

Figure 18: Setup employed to focus the laser on the cantilevers and detect its deflection and dynamic response, not drawn to scale; the dimension of the cantilever is exaggerated for clarity. 1 Single mode fibre-pigtailed 830 nm laser diode, 2 Collimation package, 3 Neutral density filter, 4 Achromatic doublet, 5 Position sensitive detector, 6 Measurement chamber inclosing cantilever array 7 Zoom in of the cantilever in the chamber. Δz is the deflection of the cantilever and n_{air}, n_{glass} and n_{buffer} are refractive indices of the corresponding media.

2.2.7 Positioning System

To read-out the eight cantilevers in an array sequentially, the optical cage has been mounted on a 3 axes positioning system containing two automated micro-translational stages (M-122.2DD and M-110.1DG Precision Micro-Translation Stage; Physik Instrumente Ltd, Bedford, UK) and a linear pico motor actuator (Model 8353; New Focus,

Micro-Controle Spectra-Physics S.A., Évry Cedex, France). The translation stages feature an optical linear encoder with 100 nm and 50 nm, respectively, position resolution and a velocity of 20 mm s^{-1} and 1 mm s^{-1}, respectively. The stages are aligned at right angles to each other as shown in Figure 19 using a lockable xyz micro-translation stage (Gothic Arch 9061-XYZ-M; Newport, CA 92606, USA). The micro-translation stage allows quick initial positioning of the laser spot in the x and y direction using manual travel micrometer heads (Mitutoyo; New Focus, Micro-Controle Spectra-Physics S.A., Évry Cedex, France) with a travel range of 6.35 mm and a resolution of 1 μm.

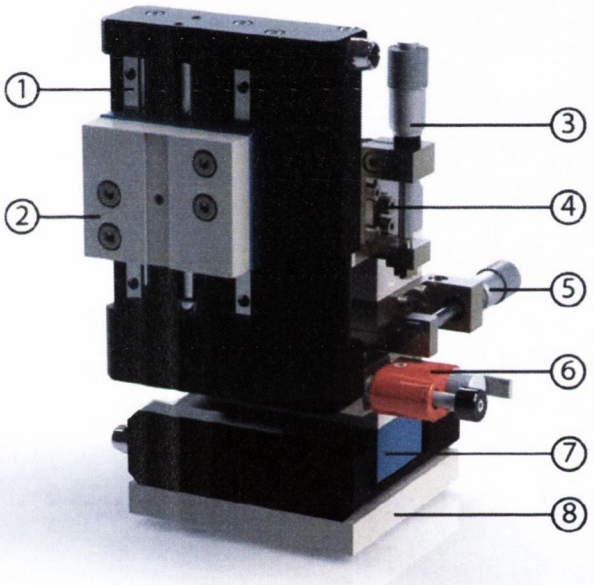

Figure 19: Three axis positioning system for the optical cage: 1 M-122.2DD Micro-translation stage to move the laser from cantilever to cantilever, 2 Holder for the mounting bracket of the optical cage, 3 Manual travel micrometer head for the x direction, 4 XYZ micro-translation stage, 5 Manual travel micrometer head for the y direction, 6 Linear pico motor actuator for the z direction, 7 M-110.1DG Micro-translation stage to move the laser along the cantilevers y-direction, 8 Positioning mounting bracket to the breadboard.

For the z direction, a linear pico motor actuator has been mounted to the z axis of the xyz micro-translation stage. The z-axis actuator offers a resolution better than 30 nm with minimal backlash and a velocity of 0.016 mm/s. Moreover, it holds the position with no power applied resulting in a quick initialisation process. The combination of the linear pico motor actuator together with the micro-translational actuator allows automatic optimal focusing of the laser spot onto the cantilever as described in chapter 4.

2.2.8 Position Sensitive Detector

A one-dimensional position sensitive detector (PSD 1L10-10-A_SU15; SiTek Electro Optics AB, Partille, Sweden) together with an amplification circuit developed in-house is used to record the cantilever response. A position sensitive detector typically consists of a n-type silicon substrate with two resistive layers separated by a p-n junction. On a one-dimensional position sensitive detector, the electrodes are integrated at the opposite ends of the p-type resistive layer as shown in Figure 20.

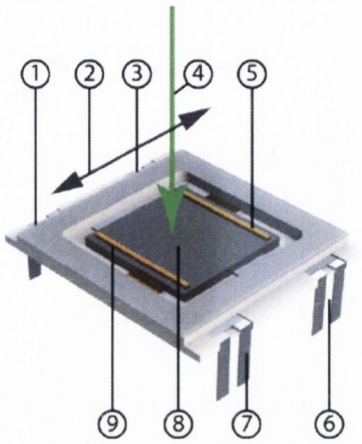

Figure 20: CAD rendered image of a position sensitive detector. 1 Bias input, 2 Moving direction of incident laser beam, 3 Current output Y_2 linked to electrode 2, 4 Incident laser beam, 5 Electrode 2, 6 Bias input, 7 Current output Y_1 linked to electrode 1, 8, Photosensitive surface, 9 Electrode 1

Upon exposure to a spot of incident light a photocurrent is generated which flows from the incident point through the resistive layers to the electrode at the contacts on either side of the sensing area due to the formation of carriers in the depletion region.

The position sensitive detector has four terminals, two bias inputs on the backside and two electrodes outputs on the front side. The photoelectric current generated by the incident laser light flows from the incident point through the resistive layers to the electrode at the contacts on either side of the sensing area due to the formation of carriers in the depletion region. The output current can be seen as an input bias current divided into two output currents, Y_1 and Y_2. The relationship between these two output currents gives the light spot position through the formula [10]

$$Position = \frac{L}{2} \cdot \frac{Y_1 - Y_2}{Y_1 + Y_2} \tag{23}$$

where L = 10 mm is equal to the length of the position sensitive detector area. Equation (23) calculates the laser spot position independent on the intensity of the incident laser spot.

The position sensitive detector together with the amplification electronics board is mounted in a black anodised aluminium housing depicted in Figure 21.

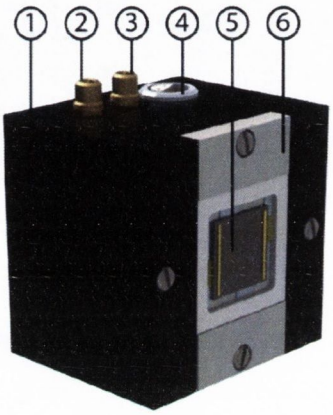

Figure 21: Position sensitive detector mounted in the custom made housing. 1 Black anodised aluminium case consisting of two pieces, 2 Sum signal plug, 3 Differential signal plug, 4 Power plug, 5 Position sensitive detector, 6 Clamp to keep the position sensitive detector in place.

2.2.9 Amplification Electronics

The photoelectric current generated by the incident laser is divided between the two electrodes; the bias voltage is +15 V, resulting in a fast response time due to a smaller barrier layer capacity of the position sensitive detector. The output current Y_1 will increase if the incident laser spot moves closer to the electrode 1 and the output current Y_2 will decrease accordingly. The sum of the two output currents Y1 and Y_2 is constant independently of the position of the incident laser spot.

The currents Y_1 and Y_2 are converted into a negative voltage by the internal transimpedance amplifiers, IC1a and IC1b, respectively, of the first dual operational amplifier (LT1358 CS8 #PBF, Linear Technology, Buckinghamshire SL7 1FD, United Kingdom) as shown in Figure 22. The second dual operational amplifier (LT1358 CS8 #PBF, Linear Technology, Buckinghamshire SL7 1FD, United Kingdom) amplifies the voltage difference between the two inputs (IC2a) and outputs it as the differential signal, corresponding to the location of the laser spot on the position sensitive detector. IC2b of

the second operational amplifier generates the inverted sum of the two input signals and outputs it as a positive sum signal, corresponding to the intensity of the incident laser spot.

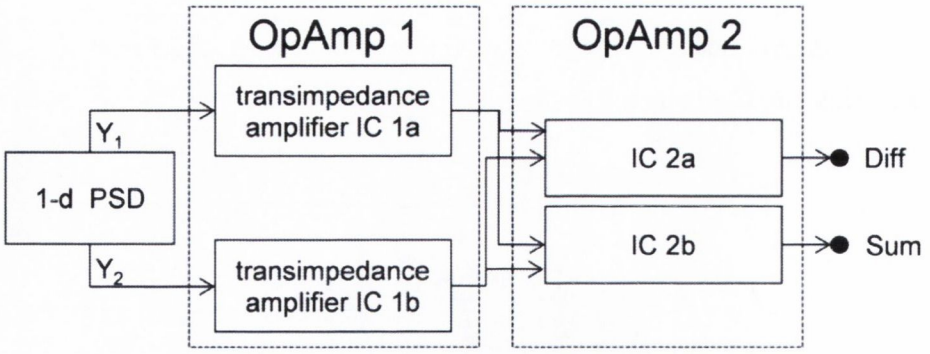

Figure 22: Block schematic of the position sensitive detector amplification electronics. Operational amplifier 1 (OpAmp 1) serves as a current to voltage converter for the two input signals and operational amplifier 2 (OpAmp 2) calculates the sum and differential voltage of the two signals.

2.2.10 Temperature Regulated Box

To ensure a steady temperature, the measurement chamber, samples and peripheral equipment such as optics are all housed within a small refrigeration/heating unit (Intertronic, Interdiscount, Switzerland). The temperature-controlled box has an integrated heating/cooling block in the back. A silent, noise and vibration free fan (ZM-F3 120 mm, Zalman, Seoul, Korea) mounted behind the refrigeration/heating unit distributes the heat into the box and a second fan (XILENCE COO-XPF120; Xilence GmbH, Hildesheim, Germany) is housed inside the box to maintain a uniform temperature within the refrigeration/heating unit. The two fans can be operated at 12V or 5V, respectively, resulting in variable speed and a vibration free operating state at 5V.

The temperature is recorded at three different positions, outside in the room, inside in the box and inside the measurement chamber using precision thermocouples NTC resistors (SEMI833ET; Hygrosens Instruments GmbH, Löffingen, Germany).

2.2.11 Optical Monitoring

To monitor the liquid cell, a USB camera (DigiMicro 2.0 Scale; dnt Drahtlose Nachrichtentechnik Entwicklungs- und Vertriebs GmbH, Dietzenbach, Germany) was disassembled, modified and attached to the optical cage. The camera together with the

software (MicroCapture 20x-200x V2.0; dnt Drahtlose Nachrichtentechnik Entwicklungs- und Vertriebs GmbH, Dietzenbach, Germany) provides real-time information of the measurement chamber inside the closed temperature-controlled box.

2.2.12 Assembled Device

The measurement chamber together with the fluidics components and the optical cage mounted on the three axis positioning system described above are assembled on a breadboard (MB1530M; Thorlabs Ltd. Cambridgeshire, UK) using custom mounting pieces as shown in Figure 23. The distance from the optical cage to the measurement chamber is 50 mm and the distance from the cantilever array to the position sensitive detector 40 mm. The laser beam path is shown in green and was aligned to be levelled horizontally before being focused on the cantilever array.

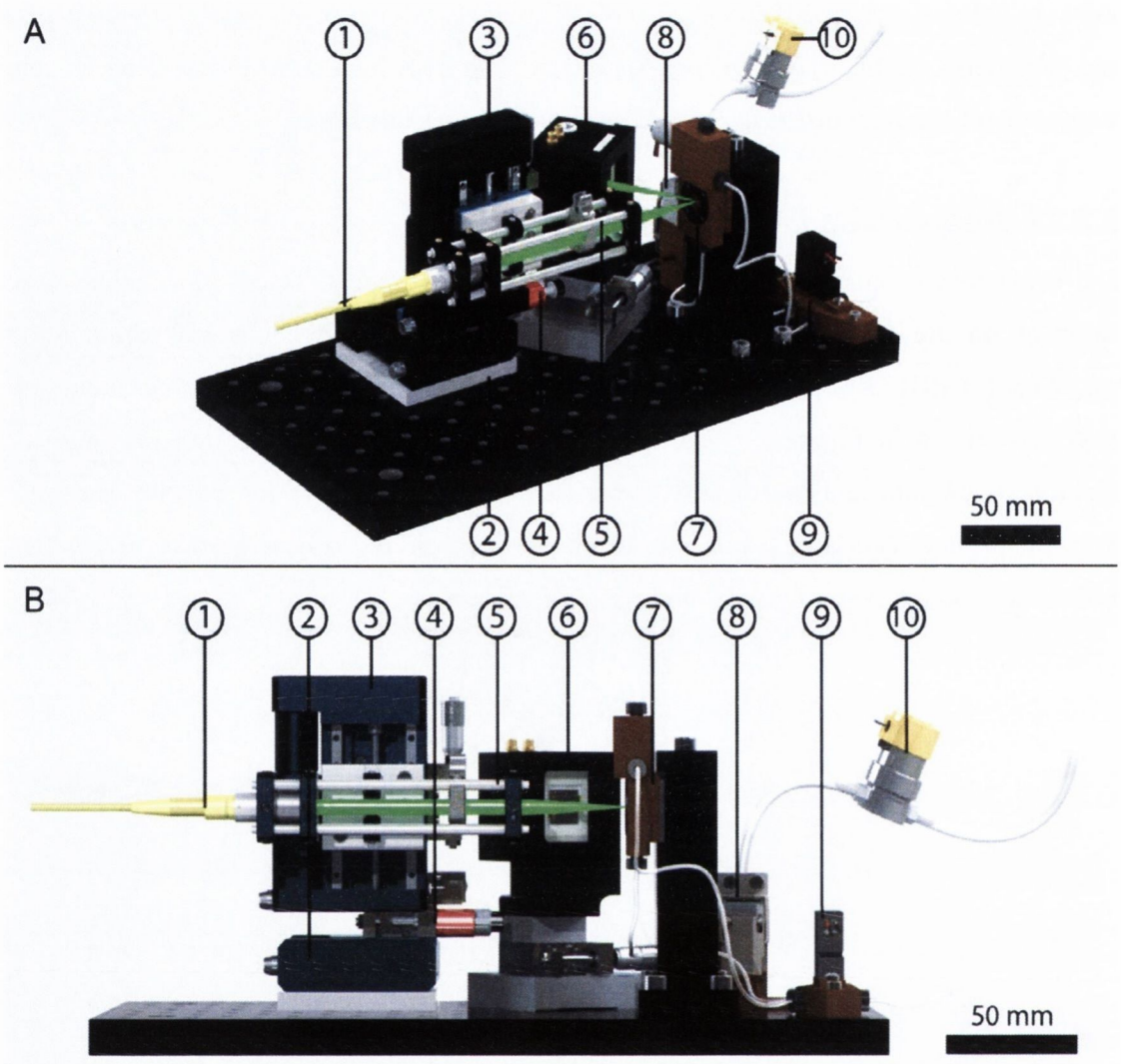

Figure 23: Isometric view A and front view B of the assembled parts mounted on an optical breadboard: 1 Laser fibre, 2 M-110.1DG micro-translation stage to move the laser along the cantilevers (x-direction), 3 M-122.2DD micro-translation stage to move the laser from cantilever to cantilever (y-direction), 4 Linear pico motor actuator for the z direction, 5 Optical rig, 6 Position sensitive detector, 7 Measurement chamber, 8 Sample reservoir, 9 3-Way 2-Position Valves, 10 Electronic 2-way valves.

The breadboard is mounted inside the temperature-regulated box. The box is mounted on an optical table (PG Series; Newport, CA 92606, USA) floating on four pneumatic vibration isolators (I-500 Series; Newport, CA 92606, USA) as shown in Figure 24, eliminating external vibrations. The tabletop of the optical table is grounded to earth, with everything mounted on the table grounded to the tabletop. The micro-translation stages and the linear pico motor actuator are connected to the controllers outside the box fastened to the optical table. A chassis containing the pins to the data acquisition devices (BNC 2110,

National Instruments Corporation Ltd., Newbury, UK and U3-HV, LabJack Corporation, Lakewood, CO, USA) and to the power supplies for the position sensitive detector, Peltier element and the fan inside the box is placed nearby the optical table. Thus, the electrical connections are as short as possible with a minimal amount of couplers to minimise additional electrical noise. The USB data acquisition device (U3-HV, LabJack Corporation, Lakewood, CO, USA) and the power supplies (Switch Mode Power Supplies TML 20103C and TXL 060-24S, Radionics Ltd., Dublin, Ireland) for the fluidics components (2/3 way isolation solenoid valve, micro dispensing valve and electronic 2-way valves) are placed on a shelf above the optical table beside the temperature regulated box. An amplifier (SR560 Low-Noise Preamplifier, Sanford Research Systems, Sunnyvale CA, USA) for the dynamic mode measurement together with the power supply for the temperature regulated box and the peltier element are placed beside the chassis. The computer containing the LabVIEW code to control the device is beside the optical table.

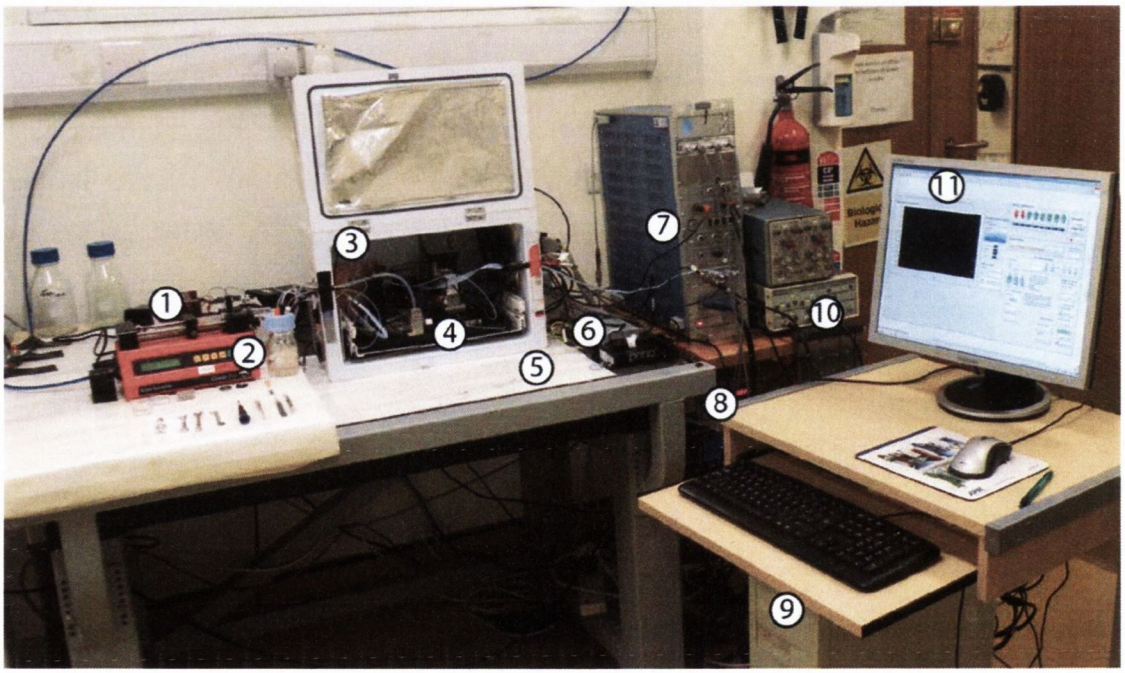

Figure 24: Photograph of the entire setup in the laboratory. 1 USB DAQ device for the fluidics control, 2 Syringe pump, 3 Temperature-regulated box, 4 Breadboard with the mounted components as shown in Figure 23, 5 Optical table floating on pneumatic vibration isolators, 6 Controllers for the positioning system, 7 Chassis containing the DAQ devices and power supplies, 8 Power supply and laser diode controller, 9 Computer with the digitiser board, frequency generator board and the LabVIEW program to control the device, 10 Amplifier, 11 Graphical user interface.

2.3 Programming

2.3.1 Software Architecture

The code to control the device is written in LabVIEW 2013 (National Instruments Corporation Ltd., Newbury, UK). LabVIEW (Laboratory Virtual Instrument Engineering Workbench) is a graphical programming environment developed with intent to ease automating measurements and instrumentations in laboratories [14]. A LabVIEW code is technically a virtual instrument (VI), which can be easily adapted to execute the desired actions (e.g. acquire data). The program interacts with the components of the device and the acquisition and analysis of the data. The design pattern is based on the producer/consumer paradigm, the high-level objects are shown in Figure 25. The architecture consists of parallel loops that are split in two categories: producers and consumer loops. The communication between the two types of loops is achieved by using data queue references. A data queue reference emulates a command and data-messaging pipeline, where the data packets containing commands and data are enqueued by one or more producer loops and dequeued to one consumer loop. The consumer loop then handles the commands and data received from the producer loop. The queue acts a buffer for the generated data, allowing an unlimited commands for asynchronous processing to be sent to the four parallel consumer loops, so that each event case can execute its code quickly and avoid any graphical user interface (GUI) and central processing unit (CPU) lockup.

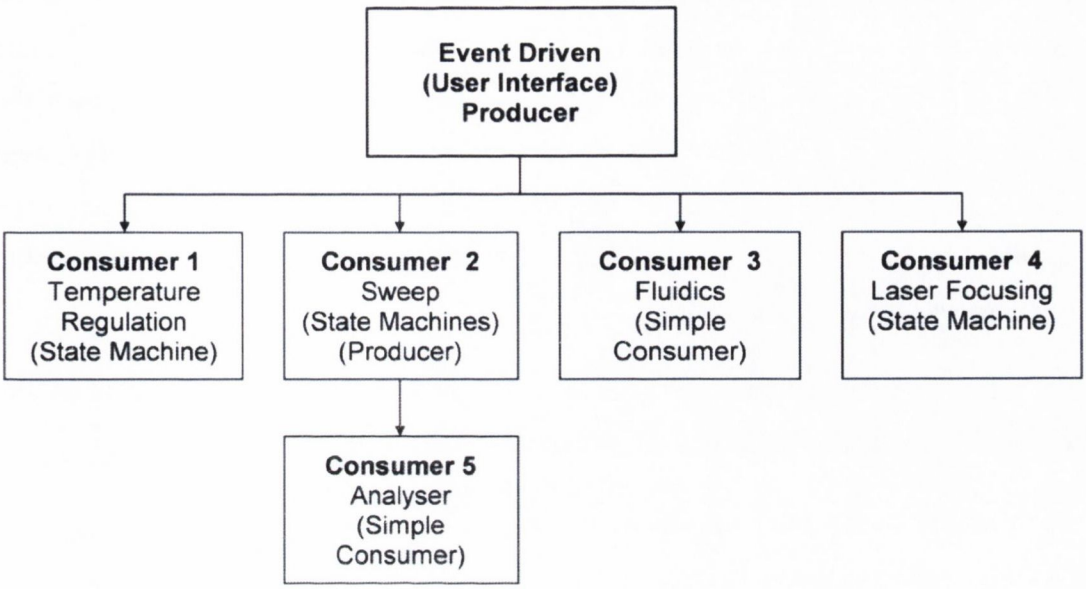

Figure 25: The main architecture of the LabVIEW code. The event driven producer is the main loop connected to the consumer loops by data queue references. The producer adds data packets containing commands and data to the queue references and the consumer loops remove the data packets from the queue and handle the commands and data received from the producer loop. The queues act as buffer for the generated data and handle the data according to the first-in first-out method.

The main loop consists of an event driven producer loop that is sending the data packets via a data reference queue to the corresponding consumer loops. The consumer loops remove the data packets from the queue and handle the commands and data received from the producer loop. The queues act as a buffer for the generated data and handle the data according to the first-in first-out method. This event-based architecture avoids polling GUI objects resulting in an improved efficiency, performance and reliability of the code. Furthermore, the selected architecture is easily scalable and maintainable for future extensions of the device (e.g. adding a second liquid cell) by adding an additional consumer loop or producer loop, respectively.

2.3.2 Producer Loop

2.3.2.1 Event driven Producer Loop

The event-driven design pattern of the producer loop is a popular paradigm for managing user interfaces and consists of an event structure inside a while loop. The event structure responds to different events occurring during the execution of the code. There are two

types of events occurring: Static events and dynamic events. The static events are caused by actions on the user interface, e.g. mouse click by the user or by the system, e.g. value change (signalling) at which the code broadcasts a system event message. In contrary the dynamic events do not occur on the front panel, the event structure reacts to events caused by the algorithm during the execution of the program. The order of the response of the code to the events depends on the order in which the events occurred and depends on the code allocated to the specific events.

Therefore, after the initialisation process of the program, the main loop remains in an idle state and is listening for the occurrence of events such as:

- Switch on temperature control
- Perform a measurement sweep
- Inject a sample
- Align the laser
- Stop program if an error occurs
- Prevent an uncontrolled shut down of the user interface

When an event as specified above occurs, the event structure automatically wakes up and enqueues the appropriate command to the data reference queue. This will trigger the corresponding consumer loop that will then execute the code. The producer loop will then return to its idle state until the next event occurs, therefore releasing CPU resources that can be used by other tasks of the code.

2.3.2.2 Sweep Loop as a Producer Loop

The consumer loop 2 is a consumer loop and at the same time acts as a producer loop for the consumer loop 5. The sweep loop acquires data as a consumer loop as described in chapter 2.3.3.2, this data of the dynamic mode measurement is then sent via the data reference queue to the consumer loop for the analysis. Therefore, the dynamic data is enqueued immediately after acquisition together with the information about the origin of the data. By sending the data to the analyser loop the acquisition is not slowed by the analysis algorithm and the data acquisition code can be executed in a timely manner.

2.3.3 Consumer Loops

2.3.3.1 Temperature Regulation

The consumer loop 1 is responsible for the temperature-regulated box. The architecture used for it is a simple state machine as shown in Figure 26. If the temperature regulation is switched on, it records the temperature inside the box and uses fuzzy logic to control the heating and cooling element of the box and to log the temperature to a text file. If the temperature regulation is switched on by the user, the command is sent by the producer loop via the data reference queue to the consumer triggering the execution of the code. First the temperature is acquired from the thermocouples by a USB data acquisition device (U3-HV; LabJack Corporation, Lakewood, CO, USA). Based on the measured temperature and the set point, a fuzzy logic algorithm determines if the box has to be cooled or heated by the peltier element in the back of the box. If the user set the control to log the temperature to true, the data is written to a text file on the computer. The regulation process iterates until the user stops the temperature regulation process.

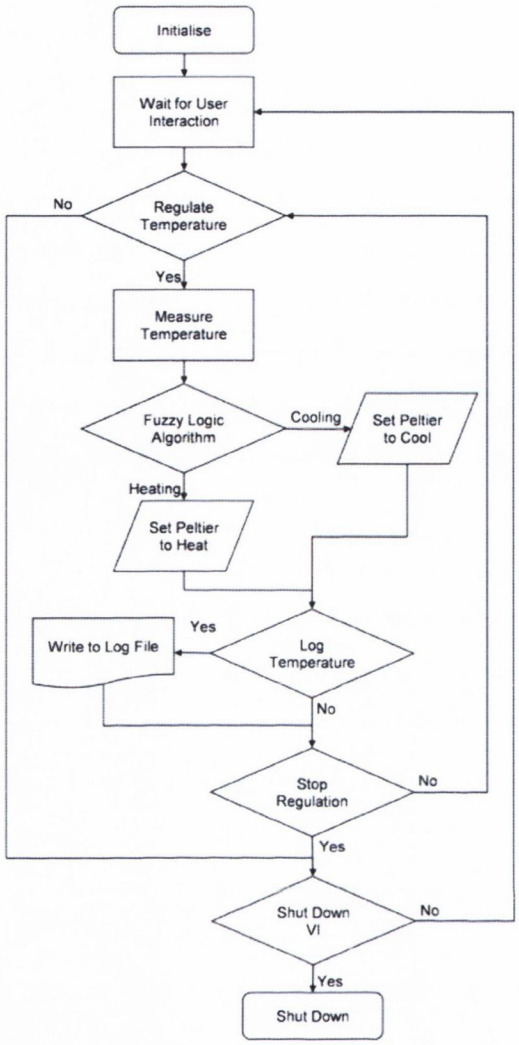

Figure 26: Flowchart of the temperature regulation process (consumer 1). The code executes according to the controls pre-set by the user until the user stops the sweep process.

2.3.3.2 Sweep

The consumer loop 2 is responsible for the read-out of the cantilever array. The architecture used for it is a simple state machine as shown in Figure 27. After initialisation of the program, the user starts the sweep process. This triggers the producer loop to send the start command to the consumer loop. The program executes the modes according to the controls set by the user: either a static mode scan only or dynamic mode scan or both modes sequentially. After each run, the laser spot will be moved to the next active cantilever and the sweep process will continue until the user stops the sweep process.

Dynamic Mode Sweep

Firstly, the laser spot is moved from cantilever to cantilever by the y-axis translational stage and then positioned along the cantilever by the x-axis -translational stage that gives the best response for the selected resonance mode. A frequency generator board (NI PCI 5406; National Instruments Corporation Ltd., Newbury, UK) is used to apply a sinusoidal frequency signal to the piezoelectric stack actuator and a high speed digitiser board (NI PCI 5112; National Instruments Corporation Ltd., Newbury, UK) is used to record the data from the position sensitive detector. The algorithm for the dynamic mode measurement is shown in Figure 28. From the waveform parameters control, a list of frequencies and matching durations are calculated to actuate the cantilevers. The digitiser starts recording a continuous stream of data with a sample rate of 10^7 s^{-1} to the internal buffer of the board, then the sinusoidal actuation signal for the piezo stack actuator is generated by the frequency generator board. The digitiser starts recording the data before the signal is generated by the frequency generator board, therefore the relevant data has to be detected prior to analysis. The relevant data is detected by analysing the waveform from the PSD. The irrelevant data is almost noise free; therefore, by looking for peaks with an amplitude bigger than 0.5 V in the signal the relevant data is detected. Once the relevant data is detected, it is split into chunks corresponding to each separate frequency of the frequency list (e.g. 500 kHz – 900 kHz in 1000 steps) and the amplitude and phase of the response of the cantilever is calculated. Once all data from the buffer is processed and all the frequencies from the frequency list are processed, the data is arranged into arrays of phase data and amplitude data and output to be further processed.

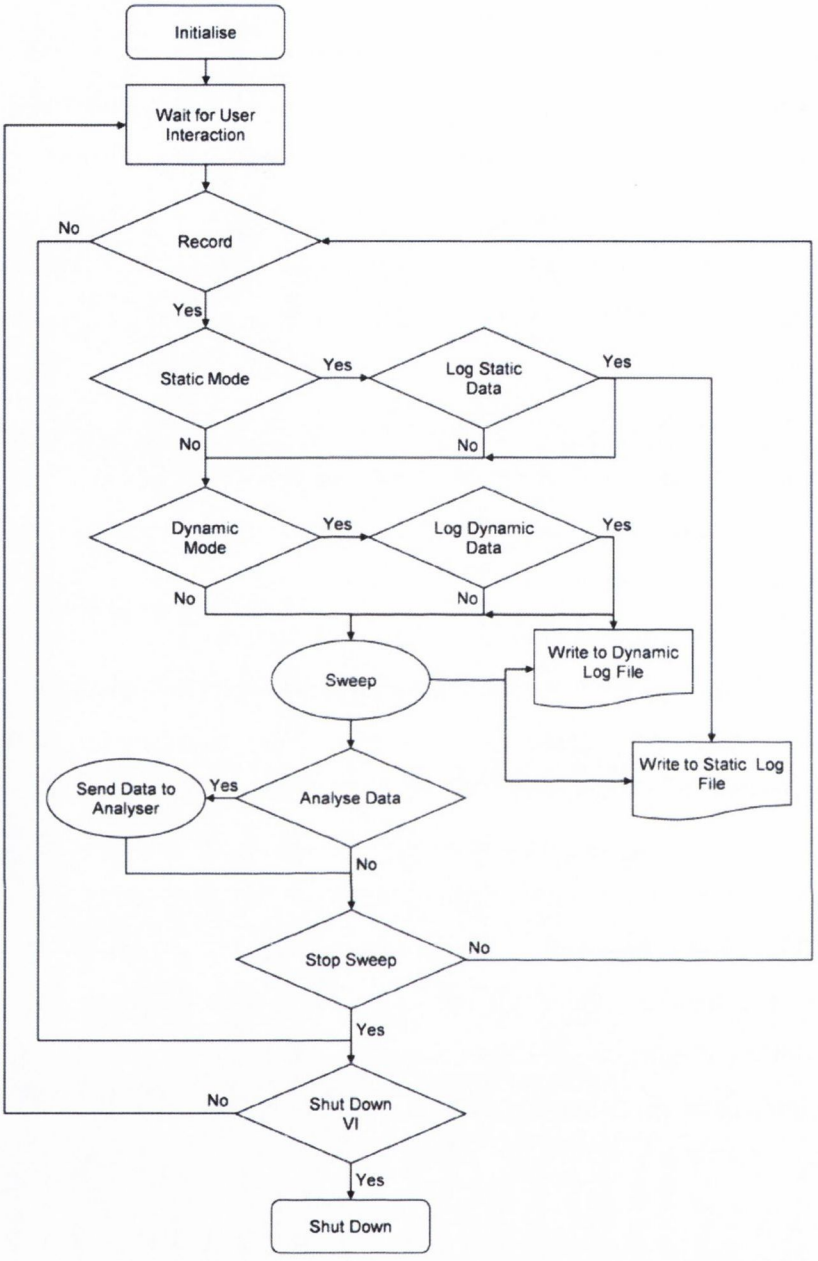

Figure 27: Flowchart of the sweep process (consumer 2 and producer 2). The code executes according to the controls pre-set by the user. The sweep process has to be triggered by the user. Firstly, the mode settings are checked, secondly the logging settings and then the sweep executed. If the data should be analysed immediately, they are sent to the analyser consumer loop by the data queue reference. The sweep process runs until the user stops the sweep process.

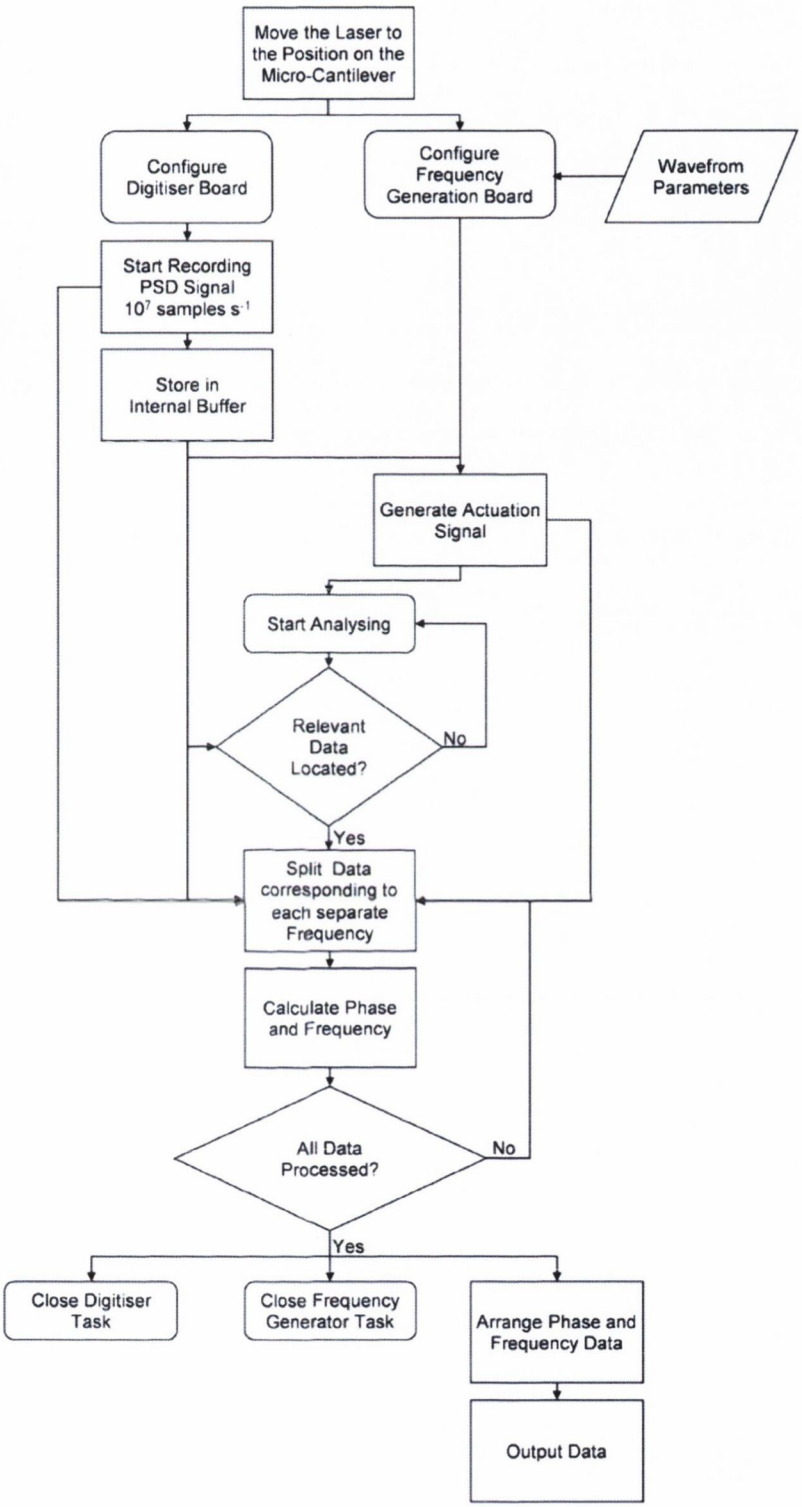

Figure 28: Flowchart displaying the algorithm of the dynamic mode measurement procedure. The laser is moved to the designated location on the cantilever for the dynamic mode measurement. The frequency generator board generates the actuation signal and the signal from the PSD is acquired, processed and output.

Static Mode Measurement

For the static mode measurement, the micro-translation stage moves the laser to the initial position at the tip of the cantilever as shown in Figure 29. The data acquisition board (NI PCI 6221, National Instruments Corporation Ltd., Newbury, UK) is configured to read out 2500 samples from two channels, the sum and differential signal obtained from the amplification circuit from the position sensitive detector with a sample rate of 10 000 s^{-1}. After acquisition of the data, the DAQ task is closed and the data is then DC filtered to remove any vibration effects due to thermal motion of the cantilever. Applying equation (11), the bending of the cantilever can be calculated.

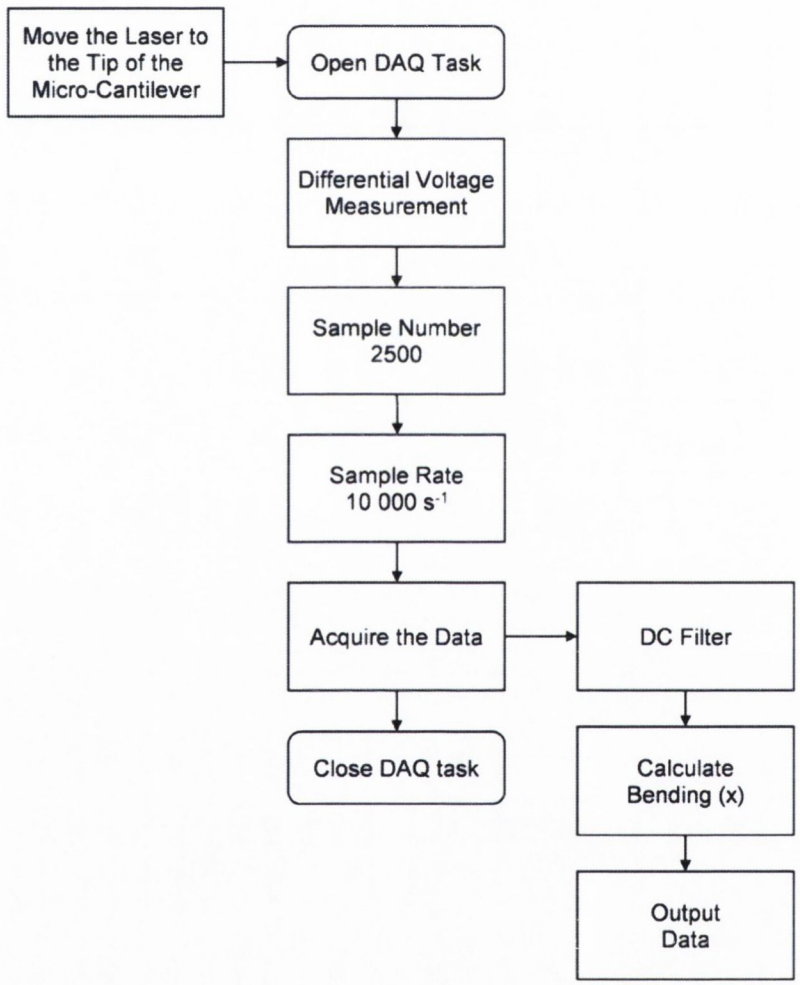

Figure 29: Flowchart displaying the algorithm of the acquisition of the static mode measurement data. First, the laser is moved to the tip of the cantilever, then the connection to the DAQ board is configured and the data acquired followed by filtering the data and finally calculating the bending of the cantilever.

2.3.3.3 Fluidics

The consumer loop communicates with the components of the fluidic setup: the syringe pump, the micro-dispensing valve, the 2-way valve and the 2/3-way solenoid valve as shown in Figure 30. The syringe pump is linked directly to the computer by an RS232 to USB converter and the flow rate and target volume of the syringe pump is set by sending the corresponding command to the pump followed by the run command to start the syringe pump.

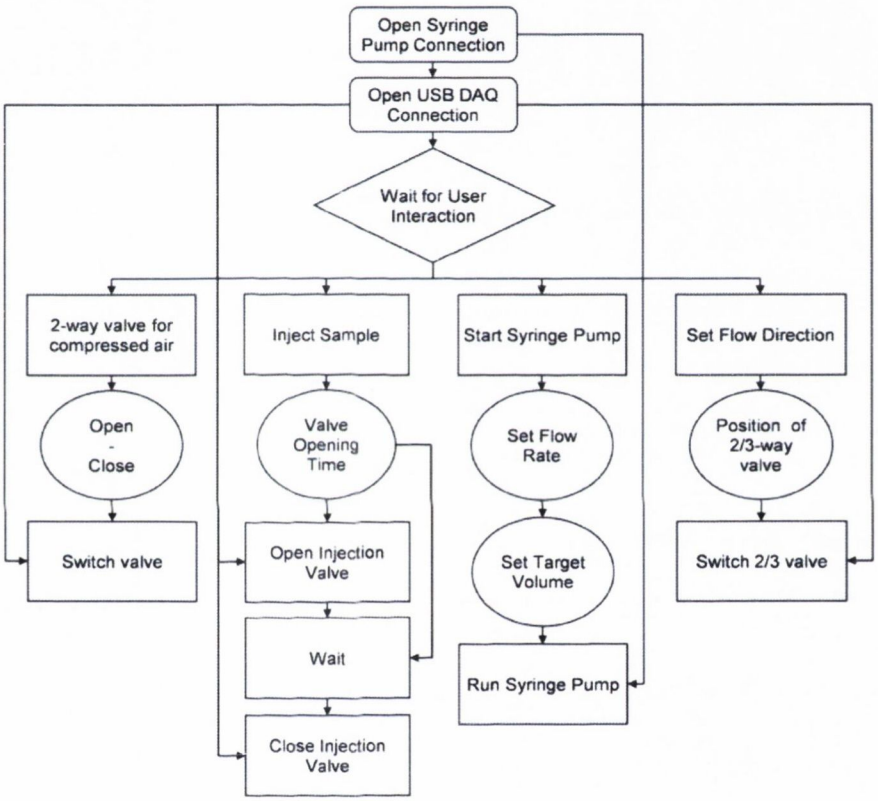

Figure 30: Flowchart of the consumer loop for the fluidics control (consumer 3). The 2-way valve, the injection valve and the 2/3-way valve are switched by 24 V solid-state relays controlled by the USB DAQ device.

The three valves are operated by simple electronics containing a prototyping board (KH102; Radionics Ltd., Dublin, Ireland), three solid state relays (DMO063; Radionics Ltd., Dublin, Ireland) and two power supplies (Switch Mode Power Supplies TML 20103C and TXL 060-24S, Radionics Ltd., Dublin, Ireland) housed in an ABS enclosure (03223000; Radionics Ltd., Dublin, Ireland) controlled by a USB data acquisition device (U3-HV; LabJack Corporation, Lakewood, CO, USA).

2.3.3.4 Laser Focusing

This consumer loop is responsible for the focusing of the laser on the cantilever surface. Therefore, a modification of the well-known travelling knife edge detection method [15-19] has been implemented. Instead of a travelling knife, the laser is the travelling object of the setup. The employment of the travelling knife-edge method is described in more detail in Chapter 4. This allows for a fully automated focusing process of the laser on the cantilever surface by the code shown in Figure 31. The user starts the laser focusing process by sending the start command via the data queue reference to the consumer 4.

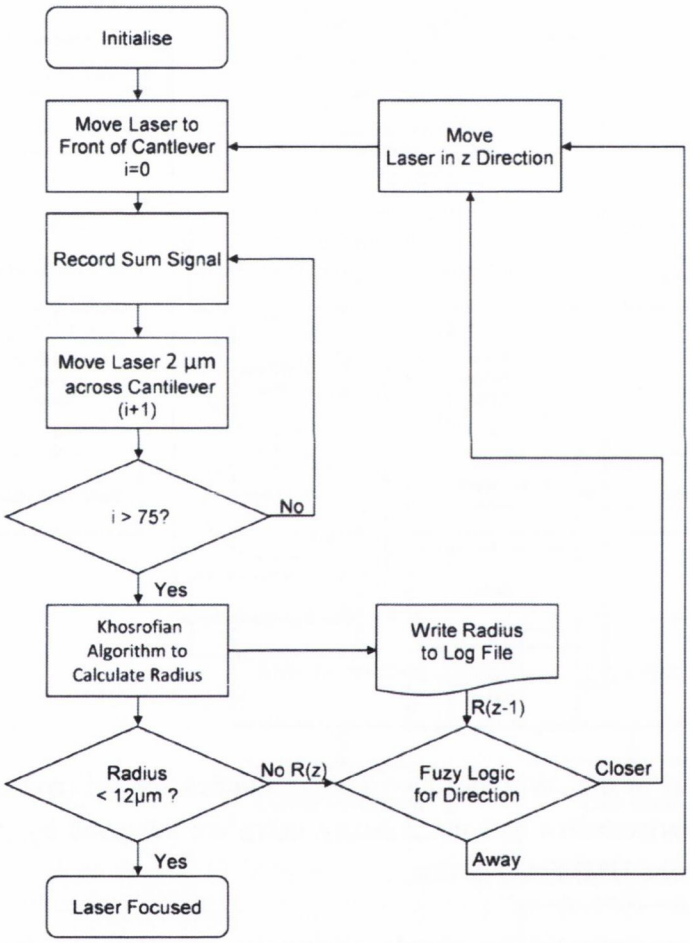

Figure 31: Flowchart for the laser focusing process by the adapted travelling knife edge method (consumer 4). The laser is moved across the cantilever while recording the sum signal of the position sensitive detector. This sum signal corresponds to the intensity of the reflected laser spot on the detector. The revised Khosrofian Algorithm [19] is used to determine the beam radius and the optical cage containing the laser is move closer or away from the measurement chamber until the laser has a radius smaller than 12 µm.

2.3.3.5 Analyser

The consumer 5 loop acts as an analyser for the dynamic mode data. The data is acquired during the sweep process of the consumer loop 2 and then sent by the data queue reference to the consumer 5 for further analysis as shown in Figure 32. The data packet is removed from the queue, the peak locations extracted and the simple harmonic oscillator model is fitted to the experimental data. For each data packet received, the resonance frequency and the amplitude from the simple harmonic oscillator model, are logged to a text file and the model fit is stored in a separate file.

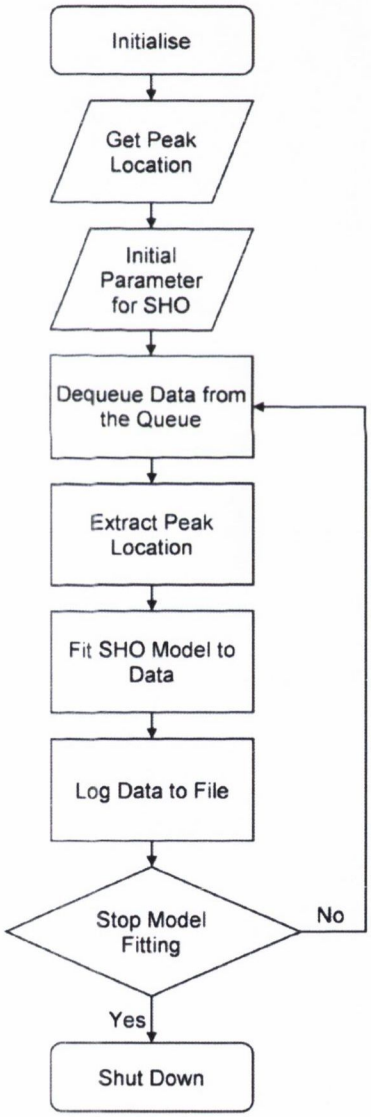

Figure 32: Flowchart of the analyser consumer loop (consumer 5). The simple harmonic oscillator (SHO) model is fitted to the experimental data and the resonance frequency is extracted from the fit.

2.4 Measurement Procedure

The device allows the investigation of both the dynamic and the static response of the cantilevers as shown in Figure 33 (blue and green arrows). The measurement procedure can be split in three main steps:

1. Fine positioning of the laser spot on the cantilever by the positioning system.
2. Detection of the dynamic mode responses of the cantilever and processing of the signal to obtain the resonance frequency change (Δf) with respect to time (t).
3. Acquisition of the summation and differential signal from the position sensitive detector and calculation of the change in deflection (Δz) with respect to time (t).

Owing to the software architecture, the temperature-regulated box is controlled independent of the measurement procedure. The heating/cooling element is modulated according to the output of the Fuzzy Logic of the algorithm to maintain a stable temperature. The flow of the buffer and the injection of the sample by the injection valve is regulated independent of the three main steps by the LabVIEW code and triggered by interactions on the GUI.

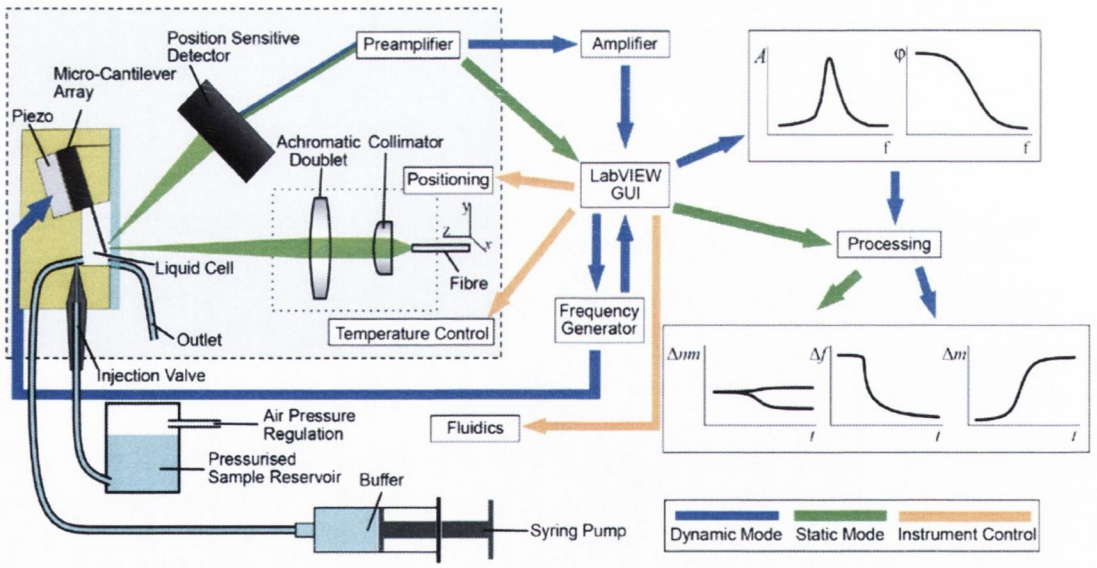

Figure 33: Schematic of the device control and measurement procedure. The response of the cantilevers is investigated by using optical beam deflection method. The measurement procedure, can be divided into three steps. The laser spot is positioned on the cantilever of interest by the micro-translation stages and then the resonance modes and bending, respectively, of the cantilever are obtained sequentially.

2.5 References

[1] Quadrant 2011 Ketron® 1000 PEEK Data Sheet. (World Wide Web

[2] Johnson B N and Mutharasan R 2012 Biosensing using dynamic-mode cantilever sensors: A review *Biosensors Bioelectron* **32** 1-18

[3] Degertekin F L, Hadimioglu B, *et al.* 2001 Actuation and characterization of atomic force microscope cantilevers in fluids by acoustic radiation pressure *Appl Phys Lett* **78** 1628-30

[4] Han W, Lindsay S M and Jing T 1996 A magnetically driven oscillating probe microscope for operation in liquids *Appl Phys Lett* **69** 4111-3

[5] Inaba S, Akaishi K, *et al.* 1993 Analysis of the resonance characteristics of a cantilever vibrated photothermally in a liquid *J Appl Phys* **73** 2654-8

[6] Meyer G and Amer N M 1990 Simultaneous measurement of lateral and normal forces with an optical-beam-deflection atomic force microscope *Appl Phys Lett* **57** 2089-91

[7] Raiteri R, Grattarola M, *et al.* 2001 Micromechanical cantilever-based biosensors *Sensors Actuators B: Chem* **79** 115-26

[8] Putman C A J, De Grooth B G, *et al.* 1992 A detailed analysis of the optical beam deflection technique for use in atomic force microscopy *J Appl Phys* **72** 6-12

[9] Ziegler C 2004 Cantilever-based biosensors *Anal Bioanal Chem* **379** 946-59

[10] Mäkynen A 2000 Position-sensitive devices and sensor systems for optical tracking and displacement sensing applications *Academic Dissertation to be presented with the assent of the Faculty of Technology, University of Oulu, Finland*

[11] Hwu E-T, Hung S-K, *et al.* 2007 Simultaneous detection of translational and angular displacements of micromachined elements *Appl Phys Lett* **91** -

[12] Ando T, Kodera N, *et al.* 2001 A high-speed atomic force microscope for studying biological macromolecules *Proceedings of the National Academy of Sciences* **98** 12468-72

[13] Yamashita H, Kodera N, *et al.* 2007 Tip-sample distance control using photothermal actuation of a small cantilever for high-speed atomic force microscopy *Rev Sci Instrum* **78** -

[14] Josifovska S 2003 The father of labview *IEE Review* **49** 30-3

[15] Khosrofian J M and Garetz B A 1983 Measurement of a Gaussian laser beam diameter through the direct inversion of knife-edge data *Appl Opt* **22** 3406-10

[16] Arnaud J A, Hubbard W M, *et al.* 1971 Technique for Fast Measurement of Gaussian Laser Beam Parameters *Appl Opt* **10** 2775-6

[17] Skinner D R and Whitcher R E 1972 Measurement of the radius of a high-power laser beam near the focus of a lens *Journal of Physics E: Scientific Instruments* **5** 237

[18] Bachmann L, Maria Zezell D and Puig Maldonado E 2003 Determination of Beam Width and Quality for Pulsed Lasers Using the Knife-Edge Method *Instrumentation Science & Technology* **31** 47-52

[19] de Araújo M A, Silva R, *et al.* 2009 Measurement of Gaussian laser beam radius using the knife-edge technique: improvement on data analysis *Appl Opt* **48** 393-6

Chapter 3

Device Characterisation

This chapter outlines the characterisation tests performed to determine the properties, limits and performance of the developed device. This includes the calibration of the temperature-regulated box, debugging the capability of the 3 axes positioning system and the implementation of the piezoelectric actuator into the measurement chamber. The performance of the fluidic systems using the injection port will be shown. Some measurements of the cantilever operated in static and dynamic mode will be highlighted to demonstrate the sensitivity of the device and the importance of *in-situ* references for biologically relevant interpretations.

3.1 Introduction

The newly developed device, especially the measurement chamber and the software, had to be evaluated to ascertain that it satisfied the requirements. The purpose of the system testing was to identify any gaps, errors, software bugs and missing functionality. The overall system test of the device included the performance and the functionality of each component to verify that the device functions exactly as intended.

To test the functionality of the device, the following test cases were defined:

- What is the performance of the piezoelectric actuator?
- What volume does the liquid cell require for a complete exchange of the liquid inside?
- How repeatable is the sample injection system?
- What are the limits of the temperature-regulated box?
- How linear is the response of the position sensitive detector?
- How repeatable and accurate is the translation of the positioning system?

- How fast and accurate is the laser focusing process?
- Are there any bottlenecks in the software architecture?
- What is the execution time spent in different cases?
- Are the cases executed in a timely manner?
- How does the software react when overloaded?
- How does the software respond to various kinds of input?

The entire system is viewed as an assembly of components and the interfaces between the components and the interaction within the components had to be tested. The tests involved calibration, testing and standard operating protocol determination for the device. Based on the results of these tests conducted with the first and second generation of the measurement chamber presented in Appendix A.2, the measurement chamber presented in section 2.2.2 has been developed. The laser focusing process is described in detail in Chapter 4.

3.2 Methods and Results

3.2.1 Temperature Regulated Box

3.2.1.1 Calibration of the Thermocouples

For the temperature-controlled box, the three precision thermocouples sensors were calibrated. A standard refrigerator at 4.4 °C and two laboratory incubators at 31°C and 53 °C, respectively, were used as references with a mercury thermometer as an analogue reference.

The thermocouples follow a linear response to temperature which can be expressed as:

$$T = A \times V + B \tag{24}$$

where T is the temperature in degree Celsius, A the slope of the linear fit, V the measured voltage in volts and B the intercept of the linear fit.

Calibrations were conducted for the three thermocouples responsible to record the temperature of the room, inside the box and in the measurement chamber, then plotted as voltage versus temperature as shown in Figure 34. The values for A and B for each thermocouple were extracted from the linear fit (shown in Figure 34) and integrated into the LabVIEW code for the temperature regulation in order to calculate the correct temperature values based on the acquired voltages.

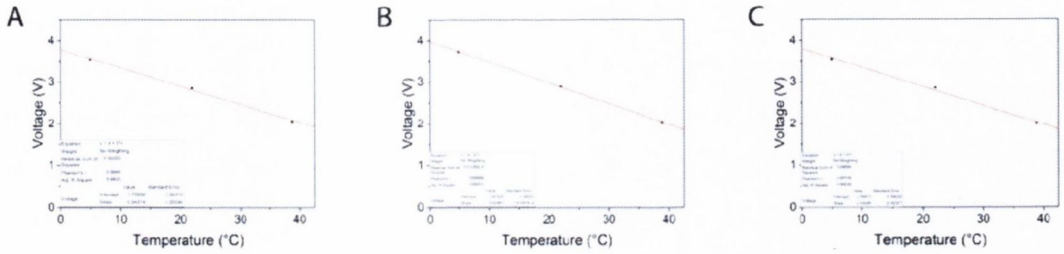

Figure 34: Calibration of the thermocouples used to measure the temperature of the laboratory A, the temperature-controlled box B and inside the measurement chamber C.

Table 1 Thermocouple calibration valuesobtained from equation (24)

Thermocouple	Calibration Value A	Calibration Value B
Room	-0.05308	4.13021
Box	-0.04980	4.03069
Measurement chamber	-0.05365	4.14968

3.2.1.2 Temperature Regulation Capability

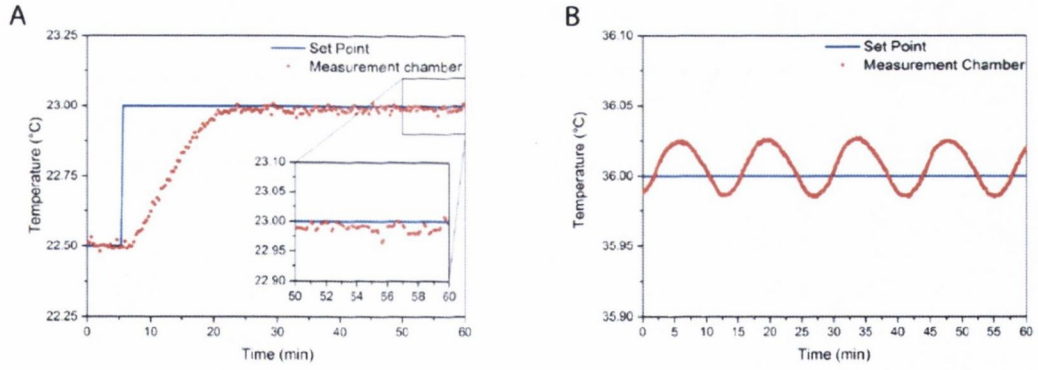

Figure 35: Measured temperature (red dots) inside the measurement chamber and the set-point for the temperature (blue line). A) Increasing the set point by 0.5 °C and the temperature regulation follows within 15 minutes and stabilises with a spread of ± 0.03 °C. B) The temperature-controlled box is not capable of maintaining a stable temperature at 36 °C. The temperature oscillates around the set point of 36 °.

The temperature-regulated box is capable of maintaining the temperature inside the measurement chamber at the set point with a spread of ± 0.03 °C as shown in Figure 35 A. The regulation algorithm is set to acquire the temperature every 4 seconds and regulate the heating/cooling element accordingly. The box is able to reach a stable temperature due to a

set point change within 15 minutes. Due to the Fuzzy Logic algorithm, the time to regulate is independent on the set point increase. The only limitation of the temperature-controlled box is that the heating/cooling element is not powerful enough to cool the box below the room temperature or to maintain a temperature of 36 °C and above as shown in Figure 35 B, even though it is still within the range specified by the manufacturer (10 °C – 40 °C). The temperature inside the measurement chamber starts to oscillate around the set point because the regulation algorithm is not capable of maintaining a stable temperature.

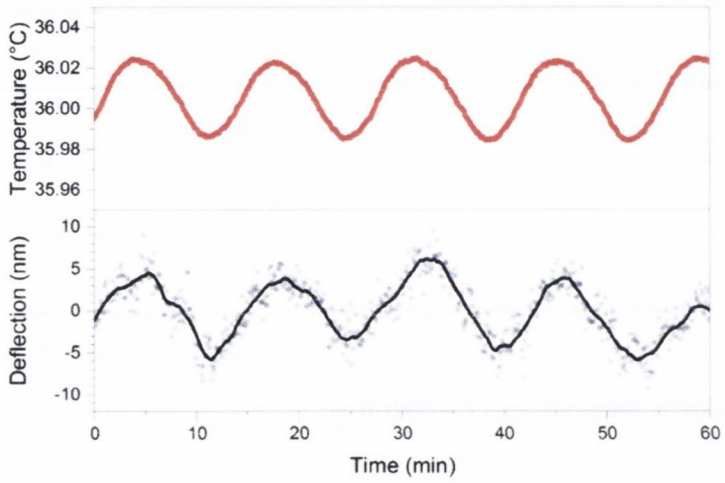

Figure 36: Temperature fluctuations around the set point of 36 °C. The mechanical response of the cantilever to these temperature fluctuations is recorded. The nanomechanical sensor follows the temperature fluctuations with a maximum amplitude of 7.5 nm.

This oscillation of the temperature around the set point is visible in the static mode response of the cantilever as shown in Figure 36. The cantilevers deflection follows the temperature oscillation. The peak to peak oscillation of ± 0.02 °C translates into a mechanical oscillation of ± 7.5 nm with a noise of ± 3 nm within the mechanical signal.

3.2.1.3 Noise

Due to the asymmetric installation of the heating/cooling element inside the temperature-controlled box a fan is used to circulate the air and faster equilibration of the temperature inside the box. To minimise the vibrations induced by the fan inside the temperature-controlled box, the fan can be operated at 12 V or 5 V. At 12 V the fan speed is 1800 rpm with a noise level of approximately 34 dBA. By reducing the operating voltage to 5 V the

speed decreases to 600 rpm with a noise level of approximately 14 dBA according to the manufacturer's instruction. The vibrations inside the temperature-regulated box have been recorded by an accelerometer (SC11 Analysis System; Spicer Consulting Eden Laboratory, Bedfordshire, UK).

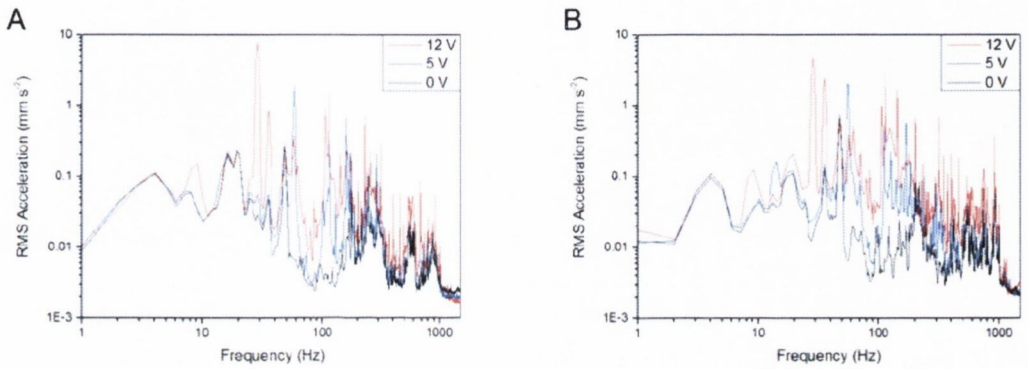

Figure 37: Vibrations inside the temperature-controlled box measured by the accelerometer. The fan operated at 12 V (red), at 5 V (blue) and switched off (0 V black). A) RMS of the acceleration in the x direction. B) RMS of the acceleration in the z direction.

The influence of the fan speed to the noise level inside the box is shown in Figure 37. As shown, setting the fan operating voltage to 5 V results in a low noise setup compared to the 12 V setting. The heating cooling element is still capable of responding to external temperature changes and maintaining a stable temperature inside the box.

The frequency domain investigated is not relevant in dynamic mode measurements. However, for the static mode measurements, the fan induces additional mechanical noise. Due to the liquid environment, the sensor is damped and there is only a small difference observable, nonetheless it is favourable to operate the fan at lowest speed possible.

3.2.2 Position Sensitive Detector

To evaluate the static linearity of the position sensitive detector, the two different output signals of the amplification electronics, the summation and the differential signal, were recorded while moving the laser vertically with respect to the electrodes with a step width of 250 µm. The M-122.2DD miniature translation stage moved the laser across the detector surface and the differential and summation signals were measured using a Tektronix TDS1012 100 MHz 2 Channel Digital Real-Time Oscilloscope (Tektronix, Beaverton, United States).

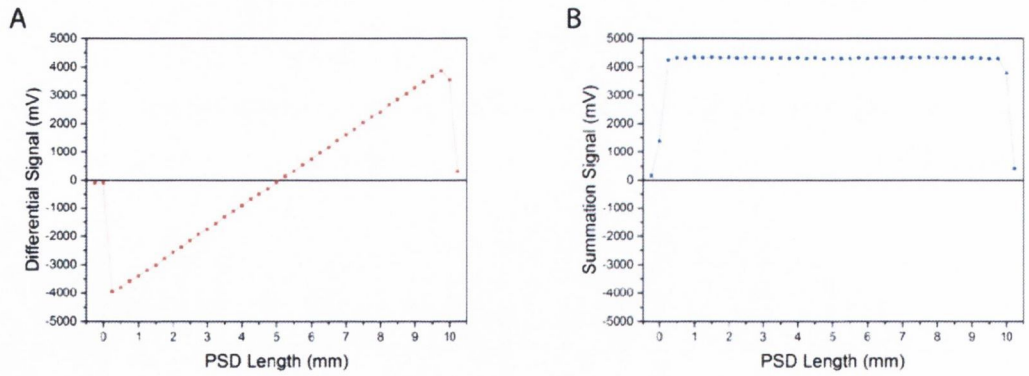

Figure 38: Response of the position sensitive detector to the laser spot moved from one electrode to the other electrode across the active area. The laser is focused directly on to the detector. A) Differential signal and B) Summation signal of the two electrodes.

In addition, the linearity of the position sensitive detector with the reflected laser from the cantilever array was tested. In contrast to the previous measurement setup, where the laser was moved, the position sensitive detector was moved perpendicular to the cantilever array due to constraints of the reflected laser beam path.

To gain the best signal from the position sensitive detector, it is important to have the reflected laser from the cantilever array impinging on the position sensitive detector within the linear area of response; otherwise artefacts can interfere with the measurements. As is depicted in Figure 38, the linear range of the detector spreads across the entire length of 9 mm between the two electrodes.

By switching from the directly focused laser beam to the reflected laser from the cantilever array on to the position sensitive detector, the response is similar as shown in Figure 39. The voltage changes by a factor 10 due to a lower intensity of the incident laser spot on the position sensitive detector. However, the linear response of the detector is independent of the laser power; it depends only on the laser spot size on the detector surface. The size of the laser reflected from the cantilever array on the position sensitive detector is 2.76 mm as calculated in section 4.3.1. As the spot size increases from a theoretical value of 15.32 µm to 2.76 mm, the linear range decreases from 10 mm to approximately 5.5 mm. All subsequent experiments were therefore performed with the reflected laser impinging the PSD within the 5 mm linear range region.

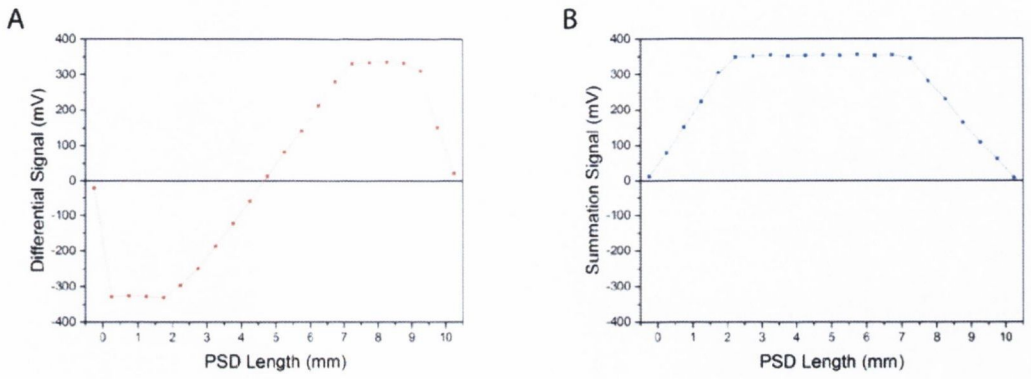

Figure 39: Response of the position sensitive detector to the laser spot moved from one electrode to the other electrode across the active area. The laser is reflected from the cantilever array and the position sensitive detector is translated by a micro-translation stage incrementally by 0.5 mm. A) Differential signal and B) Summation signal of the two electrodes.

3.2.3 Positioning Repeatability

To investigate the capability and reliability of the positioning setup, a gold coated cantilever array was mounted in the measurement chamber without liquid inside and without the glass cover. By mounting the cantilever array in a dry environment, the influence of the liquid environment and the glass cover on the laser position can be expulsed. The position sensitive detector was rotated by 90° to measure the position of the laser spot on the cantilever and not the static response of the cantilever.

The laser position on the cantilever was recorded as the micro-translation stage moved the laser spot by 8 mm for the M122.2DD stage and 2 mm for the M-110.1DG, respectively, from the cantilever towards a virtual location and back to the initial position every 5 seconds. This test procedure has been applied for both micro-translation stages as shown in Figure 40 A and B. The spot position on the cantilever has a spread of ± 2 nm for the M-110.1DG micro translation stage and ± 5 nm for the M-122.2DD micro translation stage with a lower accuracy than the other stage. Within the position spread no change in topographical features are expected due to the laser spot size of 16 µm and the grain size of individual gold grains is in the order of 2-5 n, therefore it is an average over more than 2×10^6 gold grains. The implemented automated micro translation stages allow highly accurate and repeatable positioning of the laser spot in both directions with a fractional spread of the laser spot position.

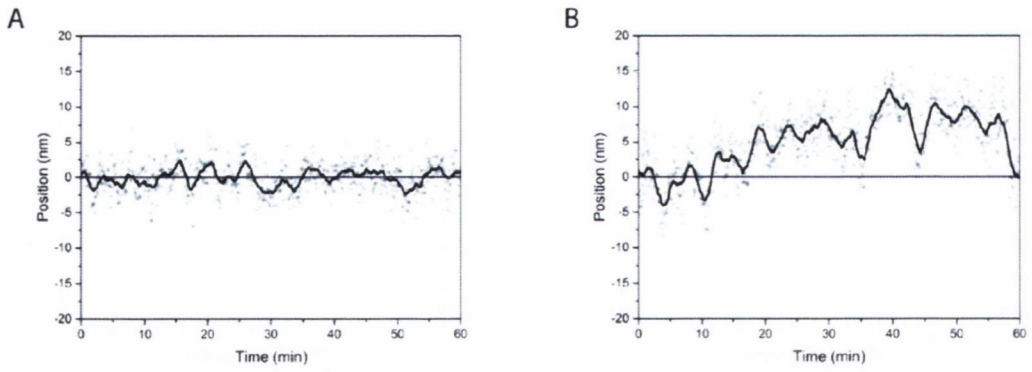

Figure 40: Position of the laser spot on the position sensitive detector vs time. A) The laser was translated in y-direction by the M-110.1DG micro translation stage. The spot position on the detector has a spread of ± 2 nm B) The optical cage was translated in x-direction by the M-122.2DD micro translation stage. This stage offers a lower accuracy and the pot position has a spread of ± 5 nm.

3.2.4 Piezo Actuator

To verify, that the piezocrystal stack actuator is able to transfer sufficient energy to the cantilever array body, the displacement of the actuator was examined by a laser Doppler vibrometer (Polytec Fiber Vibrometer OFV-552, Polytec Ltd., Lambda House, Batford Mill, Harpenden Hertfordshire, AL5 5BZ, UK). This measurement allowed verifying if the membrane was adequately thin and to check if the gluing process of the piezo stack actuator constrained the movement of the actuator.

The piezocrystal stack actuator consist of 3 layers as outlined in section 2.2.3. There were several approaches examined to glue the piezocrystal stack actuator underneath the recessed pocket of the measurement chamber. One approach was to glue the actuator with a high strength resin (Loctite® Hysol® 1C [Torr Seal]), the amplitude of the actuator was excellent (black data Figure 41), however due to the high strength of the resin, over time tiny cracks started to build up at the membrane. This resulted in the risk of shorting the electrical connections to the actuator. Therefore, the electrical connections were insulated from any liquid by filling up the gaps with a soft epoxy resin (EPO-TEK® 301). This additional resin does not constrain the movement of the piezostack actuator (red data Figure 41). A glass ceramic plate is used to insulate the piezoelectric stack from any metal components in the measurement chamber (e.g. Peltier heating element) and to provide a rigid back plate to channel the majority of the energy towards the cantilever body without interfering with the movement of the actuator (blue data Figure 41). As comparison a

piezoelectric stack actuator was glued into a measurement chamber only with the high strength resin, this resulted in a small displacement of the actuator (magenta data Figure 41). Therefore, using the high strength resin to glue the stack into the measurement chamber is not advisable.

It is clear from Figure 41 that the displacement of the piezocrystal stack actuator depends on the glue used to paste it in the measurement chamber underneath the recessed pocket for the cantilever array. Filling up the side gaps of the piezocrystal stack actuator with a soft epoxy resin allowed shielding of the electronics connections from the environment while maintaining a freedom of movement for the actuator.

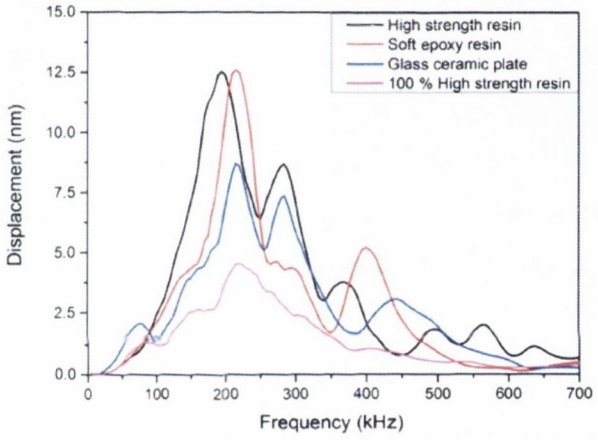

Figure 41: Displacement of the piezocrystal stack actuator glued in the measurement chamber measured by a laser Doppler vibrometer. Black curve corresponds to the displacement of a piezo stack glued on the membrane in the measurement chamber with a high strength resin (Loctite® Hysol® 1C [Torr Seal]). Filling up the side gaps with a soft epoxy resin (EPO-TEK® 301) does not constrain the displacement of the actuator as indicated by the red curve. After sealing the actuator by a glass ceramic plate glued on to it with the high strength resin, the displacement is depleted (blue curve). The displacement of a piezo stack glued in completely with the high strength resin is shown by the magenta curve.

To test if the piezo stack linear actuator creates non-flexural peaks in the resonance spectrum of the response of the cantilevers, the amplitude (e. g. maximal displacement) of the actuator was measured using a laser Doppler vibrometer (Polytec Fiber Vibrometer OFV-552, Polytec Ltd., Lambda House, Batford Mill, Harpenden Hertfordshire, AL5 5BZ, UK). The comparison, shown in Figure 42, of the amplitude of the piezoelectric actuator and the actuated cantilever vs. frequency shows that the piezoelectric actuator does not

create any non-flexural peaks in the amplitude spectrum of the cantilever. Otherwise, the analysis of the amplitude spectrum would be hampered by a convolution of the two response. For example in Figure 42 if the resonance peak at 220 kHz and the maximum amplitude of the piezoelectric stack actuator would convolute, the resonance peak could not be identified as a resonance peak. It has been shown, that the motion in the nanometre regime of the actuator translates into a micrometre motion of the cantilever in air [1].

This actuation method produces a frequency response unaffected by spurious contributions of noise from mechanical coupling through liquids. However, it appears that the peak heights (amplitude) and clarity of the flexural resonance modes of the cantilever are slightly affected by the displacement of the piezoelectric stack actuator. Due to the limited maximum frequency of the laser Doppler vibrometer setup, it was not possible to measure the displacement of the actuator at frequencies higher than 700 kHz. Nevertheless, this contribution of the actuator to the amplitude spectrum is negligible: The low-noise amplifier used allows a high pass and low pass filter to be applied to the output from the PSD prior to the digitiser and provides an excellent boosting of the resonance peaks with respect to the noise levels. Consequently, the peak heights are dependent on the amplification settings of the amplifier.

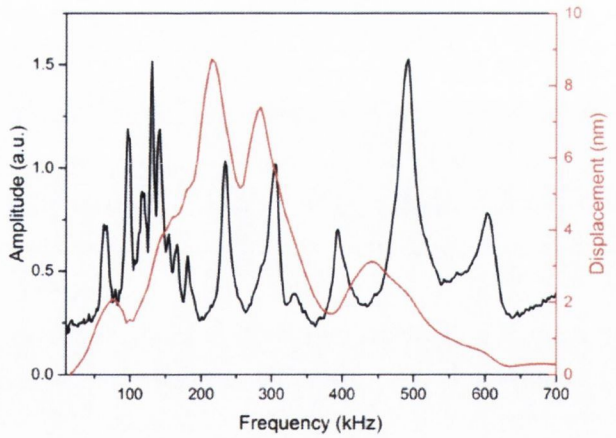

Figure 42: Compromise of the displacement of the piezoelectric stack actuator measured in air (red curve) and the amplitude (black curve) of an actuated cantilever in liquid vs. frequency. The piezoelectric actuator does not create any non-flexural peaks in the amplitude spectrum. The displacement of the actuator was measured using a laser Doppler vibrometer (Polytec Fiber Vibrometer OFV-552, Polytec Ltd., Lambda House, Batford Mill, Harpenden Hertfordshire, AL5 5BZ, UK).

3.2.5 Dynamic Mode: Amplitude and Phase Spectra

Several components from the previous dynamic mode setup have been upgraded resulting in an improved performance of the dynamic mode measurements. The amplifier (Tektronix TM502A; Oplink solutions, Fremont, CA, USA) has been replaced by a high-performance, low-noise preamplifier (SRS SR560; Stanford Research Systems, Inc., Sunnyvale, CA, USA). The preamplifier allows a high pass, low pass or band pass filter to be applied to the output from the position sensitive detector before the digitiser processes the data. As a result the resonance peaks are boosted with respect to the noise levels.

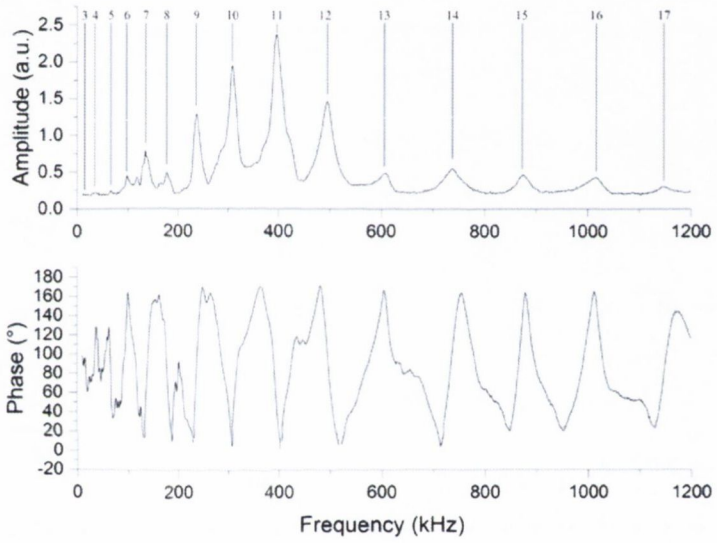

Figure 43: The amplitude and phase spectrum of a 1 µm thick cantilever from 10 kHz to 1200 kHz in nanopure water. The flexural resonance modes from 3 – 17 are indicated by the mode numbers in the amplitude spectrum. The spectrum comprises 1000 data points, each point is the average of 10,000 samples, sampled at a frequency of 10^7 samples s^{-1}.

A frequency spectrum of a gold coated 1 µm thick cantilever (Micro-and Nanofabrication group, IBM Zurich Research Laboratory, Rüschlikon, Switzerland) from an array in liquid is shown in Figure 43. The flexural resonance modes from mode 3 to mode 17 are noticeable. The frequency range spans from 10 kHz to 1.2 MHz and contains 1000 data points. Each data point of the spectrum is the average of 10,000 samples taken at a frequency of 10^7 samples s^{-1}. This frequency resolution is not optimal for real measurements; hence, not all the flexural resonance modes are then monitored. However, the software allows the recording of three independent frequency ranges with each range consisting of 1000 data points. This allows the user to zoom in to the flexural resonance mode of interest and record the spectrum with a higher frequency resolution.

3.2.6 The Importance of a Reference Sensor

To demonstrate the importance of having an *in-situ* reference sensor and the capability of the dynamic mode of the cantilever array in a liquid environment, the temperature inside the measurement chamber was increased incrementally by 0.5 °C as shown in Figure 44. Two frequency ranges (200 kHz – 500 kHz and 500 kHz – 900 kHz) were swept every 30 seconds, upon which dynamic mode measurements and the temperature were recorded. The flexural resonance modes from mode 11 and 12 were tracked in the first frequency range and mode 13 in the second range. The resonance frequency shift observed originates from the change of the properties of the cantilever and the surrounding liquid (most likely by the change in viscosity) with increase in temperature. At an increased temperature, the density and viscosity of the liquid decreases resulting in less co-moved mass by the cantilever, hence the resonance frequency increases.

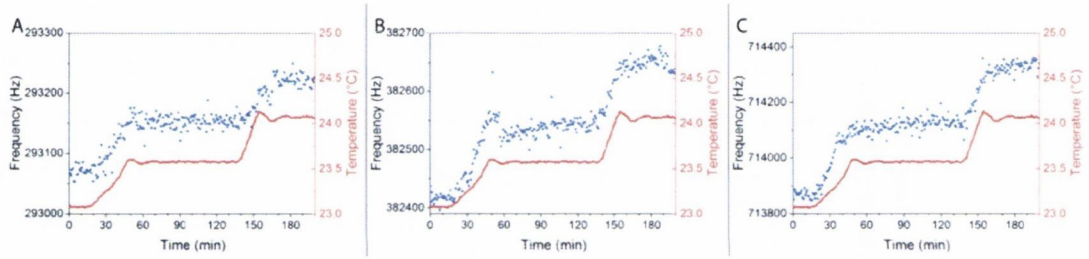

Figure 44: Frequency response of the flexural resonance (A: modes 10, B: mode 11 and C: mode 14) of a cantilever in nanopure water to a temperature increase of 0.5 °C inside the measurement chamber (red line).

By extracting the absolute frequency changes of mode 10, mode 11 and mode 14 for each temperature increase by 0.5 °C, it is clearly observable that the sensitivity increases with the mode number as shown in Figure 45 and described by Ghatkesar *et al.* [2]. The analysis of this temperature increase assumes that the spring constant of the cantilever remains constant during the experiment which might be not true. The spring constant can be changed due to an increase in stress on the cantilever as induced by a temperature increase [3, 4].

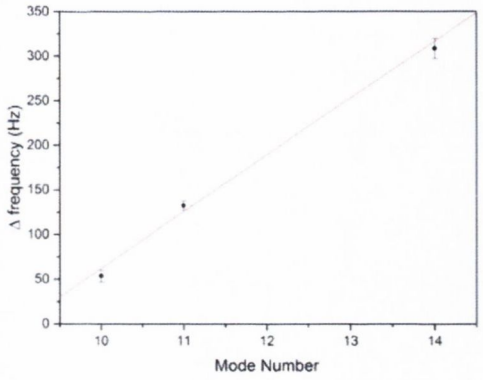

Figure 45: The averaged maximum frequency shift (Δf) of 4 cantilevers vs. mode number. The higher modes are more sensitive to external stimulus (e.g. temperature increase).

To highlight the importance of differential measurements using reference cantilevers, Figure 46 shows a plot of the dynamic signal of two cantilevers responding to a temperature increase and the differential signal between both cantilevers from mode 14 from the measurement shown in Figure 44. The futility of making biologically relevant interpretations using a single cantilever is highlighted when you consider any sample introduced to the cantilever may have a slight variation in temperature/viscosity/refractive index to the buffer fluid. The differential signal shows the elimination of these environmental effects using a reference cantilever considering a homogeneous mixing in the fluid cell and no gradient within the cell. A single cantilever taken on its own would show a significant change in resonance frequency (indicating a viscosity change) of 225 Hz whereas the differential signal is 0 ± 50 Hz.

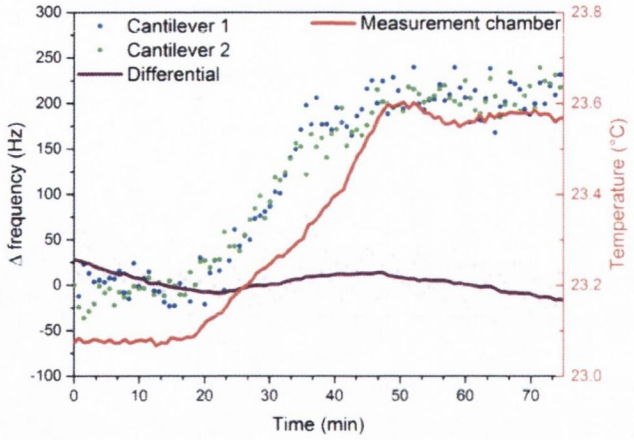

Figure 46: Differential dynamic signal. The plots of cantilevers 1 and 2 (blue and green) show the response of the cantilevers to an increase in temperature. However, the differential signal shows (purple) how environmental effects such as temperature changes (red curve) can be reduced through using cantilevers as a reference sensors.

The need for a reference cantilever not only for the dynamic mode measurements but as well for the static mode was demonstrated by increasing the temperature every 2 hours from 23 °C by 0.5 °C until a temperature of 24.0 °C was reached. The dual mode sweep occurred every 30 seconds, upon which dynamic mode measurements, static mode deflection and temperature were recorded. For the dynamic mode operation, the range for the frequency sweep was set from 200 kHz to 500 kHz within which three resonance mode peaks were contained.

The base-line corrected deflection and raw data of the dynamic mode measurements for an individual cantilever are shown in Figure 47 along with the corresponding temperature recorded through time. Corresponding jumps in the static and frequency signals are clearly visible as the temperature is increased. This highlights the sensitivity of the device to temperature changes in static mode due to the different thermal expansion coefficients of the silicon chip and the gold layer deposited on the upper surface of the cantilevers (Si: 3×10^{-6} K^{-1}, Au: and 14×10^{-6} K^{-1}). In dynamic mode, the shift in resonance frequency is due to the changing properties of the surrounding fluid. The flexural resonance mode 10 was analysed.

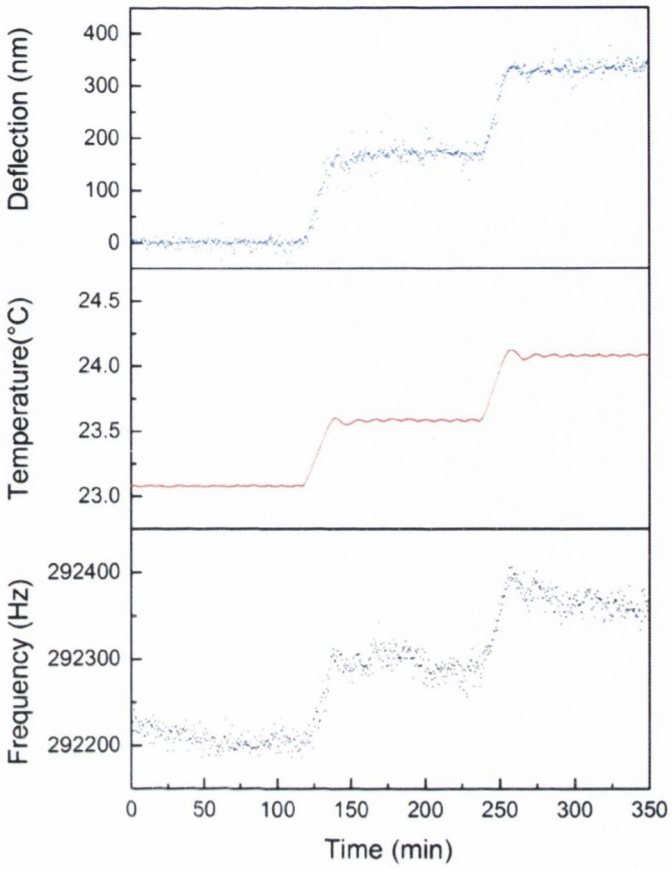

Figure 47: Static (deflection) and dynamic response (resonance frequency of mode 10) of a cantilever to increases in temperature. The dynamic and static response of the cantilever can be seen to closely track any changes in temperature over time. Here, two 0.5 °C increases in temperature result in ~170 nm change in deflection and ~100 Hz change in frequency.

3.2.7 Fluidics Performance

The measurement chamber has been tested to be leak-proof. The thin membrane that was designed is robust enough to prevent shortage towards the electrical elements underneath the cantilever array body and still provide sufficient energy transduction for actuation for the dynamic mode measurements. Based on calculations from the CAD drawing of the new measurement chamber, when the glass cover is fixed in place the volume of the liquid cell is 3.048 µl. To determine the minimal amount of sample required for a measurement, the mixing and exchanging behaviour of the liquid cell was investigated. The liquid cell was filled with nanopure water before sample containing dyed nanopure water was injected and then pushed into the fluid cell. The exchange and mixing manner inside the liquid cell was monitored by a USB camera (DigiMicro 2.0 Scale; dnt Drahtlose Nachrichtentechnik Entwicklungs- und Vertriebs GmbH, Dietzenbach, Germany). The time it takes to flush the

liquid cell completely depends on the flow rate of the liquid. However, the required volume to exchange the sample in the liquid cell is independent of the flow rate. For a flow rate of 10 $\mu l \cdot min^{-1}$ it takes up to 36 seconds to get a homogenous 3D distribution in the liquid, resulting in an approximate sample volume of 6 µl needed. In the experiment performed with a flow rate of 50 $\mu l\ min^{-1}$, which corresponds to the highest flow rate set, it takes less than 8 seconds to exchange the liquid in the liquid cell completely, or less than 6.6 µl of liquid are used to flush the cell.

The influence of the pumping speed of the syringe pump upon the mechanical response of the cantilevers has been investigated. Buffer was flown through the measurement chamber at different rates of flow (0 $\mu l\ min^{-1}$, 1 $\mu l\ min^{-1}$, 5 $\mu l\ min^{-1}$, 10 $\mu l\ min^{-1}$, 25 $\mu l\ min^{-1}$, 50 $\mu l\ min^{-1}$ and 100 $\mu l\ min^{-1}$) and the frequency response of the cantilever array was recorded at mode 10 and 11 as shown in Figure 48.

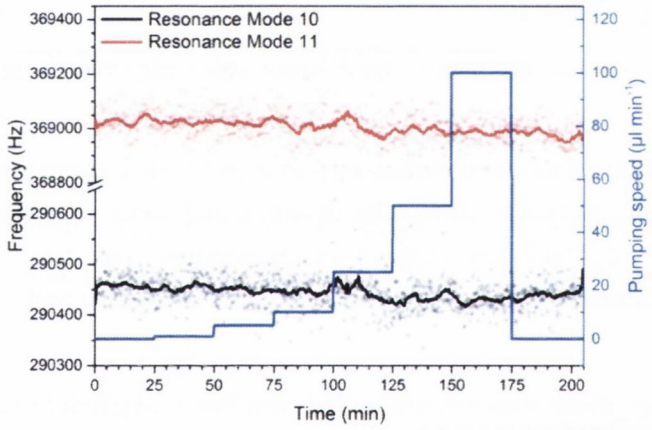

Figure 48: Frequency response of mode 10 (black curve) and mode 11 (red curve) to different pumping speeds (blue curve) of the syringe pump. The pumping speed was varied from 0 $\mu l\ min^{-1}$, 1 $\mu l\ min^{-1}$, 5 $\mu l\ min^{-1}$, 10 $\mu l\ min^{-1}$, 25 $\mu l\ min^{-1}$, 50 $\mu l\ min^{-1}$ and 100 $\mu l\ min^{-1}$ as shown by the blue curve. There is no visible specific response of the cantilever frequency to the different pumping speeds.

The continuous flow of buffer through the liquid cell does not introduce any obvious specific periodic effect to the frequency response and there is no observable frequency shift as the flow rate increases, nor is there any effect in the noise of the system. This makes the dynamic mode, in particular, suitable for use in continuous flow experiments. It was noticed that the frequency response of the cantilevers decreased sometimes slightly at higher pumping speed as shown in Figure 49 if the fluid is introduced from outside the

temperature-controlled box. This decrease is due to a decrease of the temperature inside the liquid cell, i.e. there was not enough time for the liquid to reach the temperature inside the measurement chamber. This temperature fluctuations lead to a change in density and viscosity of the surrounding liquid and a change in the stiffness of the cantilever due to the bimetallic effect [5], hence a change in the resonance frequency. The temperature-controller of the box is not capable of maintaining a stable temperature inside the liquid cell if new liquid is introduced at a high flow rate. The temperature drops by less than $^{1}/_{50}$ of a degree Celsius and this temperature change is visible in the frequency response of the cantilever at the higher resonance modes.

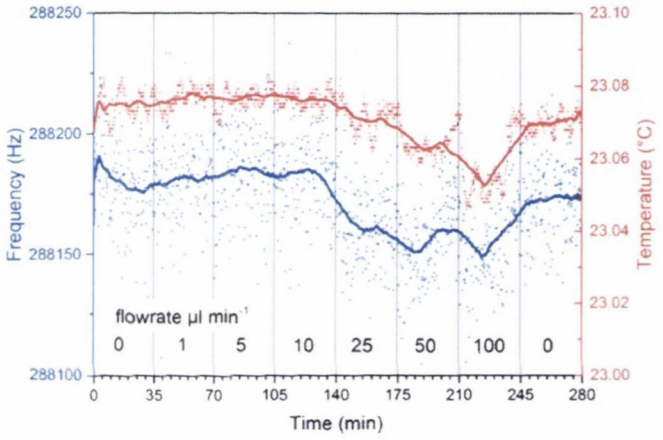

Figure 49: Frequency response of mode 10 to different pumping speed of the liquid through the measurement chamber and to different temperature inside the measurement chamber. The obvious decrease in resonance frequency at flow rates higher than 25 µl min^{-1} is induced by temperature instability inside the liquid cell as shown by the red curve. By stopping the buffer flow, the temperature stabilises again and the frequency recovers.

To investigate the injection behaviour of the injection valve, 100 µl volume of nanopure water was loaded into the sample reservoir and the injection valve was primed. A series of injections at a constant pressure of 100 mbar was performed with increasing valve opening times from 31 ms to 40 ms in 1 ms increments. The sample injection line was secured along a graduated surface and the sample meniscus was monitored after each injection to determine the volume of fluid injected. A digital microscope (Dino-Lite Pro HR AM7000 series; Dino-Lite, The Netherlands) was used to give the required resolution (images shown in Appendix A.4). To determine the volume injected, the pixel location of the meniscus along the graduated scale was determined using image analysis from before and

after injection. This difference in pixels was then converted to length, and hence volume, using the ratio of millimetres to pixels which could be easily calculated. The data (Figure 50 A) clearly shows how the volume injected can be controlled by the opening time by 10 ms. Volumes from 4 µl to 5 µl could be injected by varying the opening time. Should finer control of the injected volumes be required, the reservoir pressure could also be adjusted.

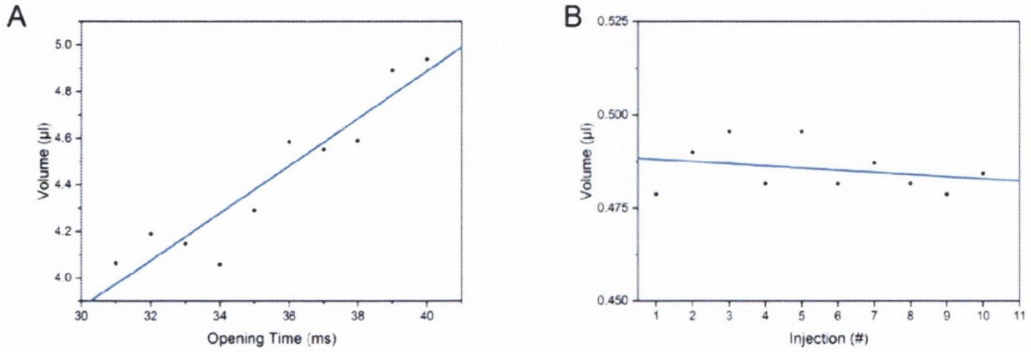

Figure 50: Injection behaviour A) Sample volume against valve opening time at 100 mbar and reservoir volume 100 µl. The plot clearly shows how the volume injected can be controlled by adjusting the opening time of the valve. Volumes from 4 µl to 5 µl could be injected by varying the opening time by 10 ms. B) Reproducibility of the injected volumes. Samples of 500 nl volumes were injected consecutively at 100 mbar. The coefficient of variation (CV) for this series of droplets is 1.3%.

A series of ten 500 nl samples was also injected to study the reproducibility of the injected volumes and was analysed using the same method as above. The data (Figure 52 B) shows slight variations around the trend line, nonetheless, superb reproducibility was demonstrated as the coefficient of variation for this injection series was 1.3%.

To investigate the injected volume in the liquid cell, a cantilever array was mounted in the measurement chamber in nanopure water. The frequency response to different densities and viscosities was recorded. The measurement chamber was primed with a 5% glycerol solution as shown in Figure 14 B. The 5% glycerol solution is then introduced to the liquid cell by switching on the syringe pump for 36 seconds at a flow rate of 10 µl min^{-1}, this is exchanging the volume of the liquid cell completely. The frequency reaches a stable signal within 3 minutes. The liquid cell was rinsed after 25 minutes stable measurements with 30 µl of nanopure water at a flow rate of 10 µl min^{-1}. There is a clearly visible change in frequency at the beginning of each liquid exchange, the red and blue dashed areas in Figure 51. This might originate from the initial rotation of the syringe pump. The frequency

response of mode 10 and mode 11 to this solution exchange is shown in Figure 51. It is clearly visible, that mode 11 is more susceptible to the viscosity and density change than mode 10 as it has been shown previously [6].

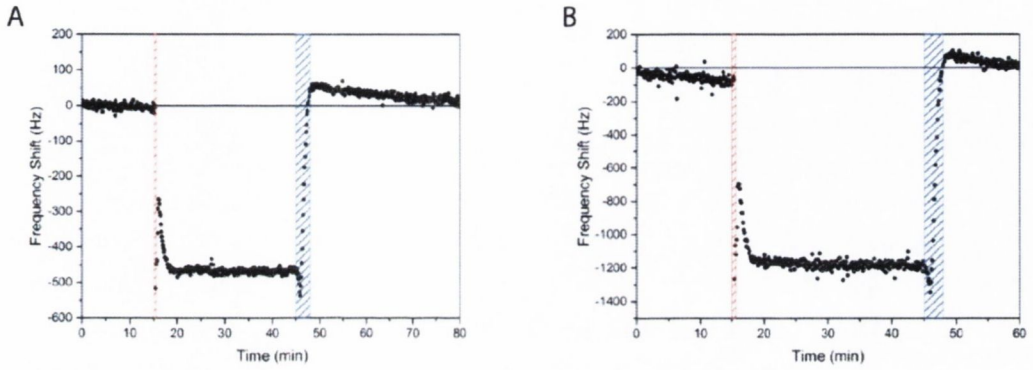

Figure 51: Frequency behaviour of a 1 µm thin cantilever to different densities and viscosities. The cantilever array is immersed in nanopure water in the fluid cell. Two injections are indicated by the dashed areas: red: 9.2 µl of 5% glycerol injection followed by 10 µl min^{-1} for 36 seconds, blue: rinsing the liquid cell with nanopure water 10µl min^{-1} for 180 seconds. A) Mode 10 and B) Mode 11.

Once the maximum frequency shift was determined, the reproducibility was investigated by the following procedure. The measurement chamber was primed with 9.2 µl 5% glycerol and the 5% glycerol was pushed into the liquid cell by the syringe pump for 36 seconds at a flow rate of 10 µl min^{-1}. 5 minutes after the injection, the liquid cell was rinsed with 30 µl of nanopure water and the injection cycle was executed again as shown in Figure 52. The response of the cantilever is for the three injections the same as for the single injection shown in Figure 51, which indicates that the same volume of 5% glycerol has been introduced repeatedly to the liquid cell without diffusion into the nanopure water as adumbrate in Figure 14 B and C. However, the time between the injections is not sufficient long enough to reach a stable signal again as obtain in Figure 51, which was taken into account for subsequent experimental protocols.

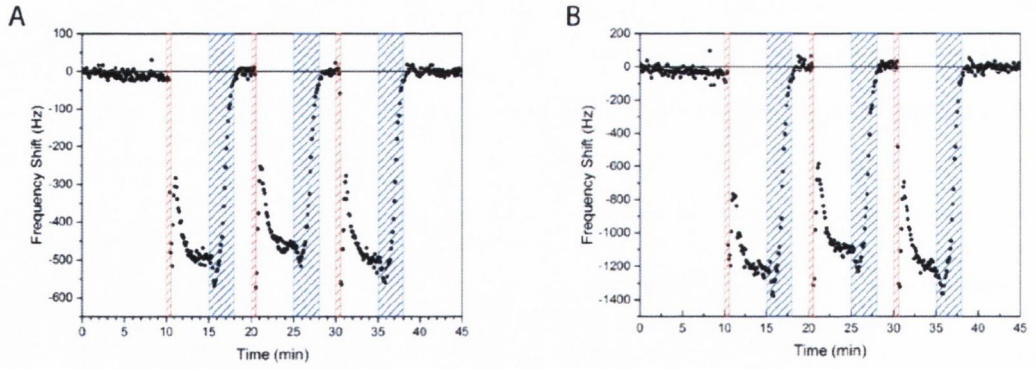

Figure 52: Frequency behaviour for different densities and viscosities. Three consecutive injections are indicated by the red dashed areas: priming with 9.2 µl of 5% glycerol injection followed by pushing it to the liquid cell with a flow rate of 10 µl min^{-1} for 36 seconds. Rinsing of the liquid cell is indicated by the blue: dashed areas: water with a flow rate of 10µl min^{-1} for 180 seconds. A) Mode 10 and B) Mode 11.

3.2.8 Software Performance

LabVIEW Desktop Execution Trace Toolkit (National Instruments Corporation Ltd., Newbury, UK) together with the Profile Performance and Memory tool from LabVIEW 2013 was used to perform a dynamic code analysis. This analysis includes monitoring, detection and profiling of execution time, memory usages, undesired behaviour and memory and reference leaks.

The advantage of the implemented software architecture for the device control is that the producer loop is not polling for data; it is executed only when an event is generated by the graphical user interface. Hence, the execution time is not dominated by the producer loop allocating enough CPU and memory to the consumer loops. This architecture results in a responsiveness of the code to front panel controls within 100 ms without utilising more than 27% of the CPU time in contrast to the old software where the CPU usage was between 90 and 99% during a measurement.

To limit the memory usage the implementation of global variables and local variables in the code has been minimised. Global and local variables cause LabVIEW to generate copies of the data in the memory to process them resulting in an increased memory usage. The use of subVIs allows LabVIEW to reclaim memory from the subVIs when they are not executed, resulting in decreased memory usage. Hence, all major function are performed in subVIs.

Table 2 Execution time and memory usage for the different tasks

Process	Execution Time (ms)	Memory Usage (MB)
Main producer (GUI)	5	30.5
Temperature regulation	63.48	4.4
Static read-out*	4912	24.2
Dynamic read-out*	15223	253.1
Laser alignment step	84.2	125.2
Fluidic control	2-100	0.9
Peak analyser	92.48	1.9

*for 8 cantilevers sequentially

The execution time and maximal memory usage for all processes of the device software are shown in Table 2. The temperature regulation loop runs once every 4 seconds and the execution time is 63 ms with a maximum memory usage of 4.4 MB. One fitting process of the laser focusing process takes 12.6 s (150 steps of 84 ms each); resulting in the focusing of the laser conducted in less than 2 minutes (depending on the number of iterations needed). The fluidic control loop runs once upon being triggered by the producer and the execution time is between 2 ms and 100 ms depending on the settings. The read-out of the dynamic response of all 8 cantilevers takes 15.2 seconds with a sampling rate of 10^7 samples s^{-1} to satisfy Nyquist's theorem and avoid aliasing. The dynamic mode read-out contains the most memory and CPU intensive code, data is pushed onto the local buffer of the digitiser board and copied to the local memory and processed by the CPU at the same time. 10,000 samples are averaged for each point in the resonance spectrum. To read-out the static signal of all the cantilevers, the execution time is 4.9 seconds. Combining the two read-out methods in one measurement results in an execution time of 21.3 seconds for all 8 cantilevers. Analysing four peaks of a resonance spectrum of the cantilever takes on average 92.48 ms. The execution time for the analyser increases significantly if the noise of the resonance spectrum increases. The more noise in the spectrum, the more CPU time required to fit the data to the simple harmonic oscillator model.

3.3 Discussion

The newly developed measurement chamber fulfils the requirements as stated in section 2.1. The measurement chamber is leak proof, suitable for biohazardous substances and features a liquid cell incorporating the cantilever array with a volume of 3 µl. The integrated sample loading system together with the fully automated injection system allows for repeatable and reproduceable injection of nano to microliter dispense sample volume. The automation of the sample handling minimises the influence of the operator on the outcome of the experiments, thus increasing measurement data reliability. Based on the measurements shown in section 3.2.7 it was possible to determine a standard measurement protocol as shown in section 5.5.

The temperature-regulated box housing the measurement chamber offers a virtually vibration free environment. Operating the fans at 12 V significantly decreases the time taken to reach a stable temperature and the temperature can be maintained at a stable level even when the fan speed is reduced. External vibrations are not an issue for the dynamic mode measurements because the recorded frequencies are too high to be affected by any external sources of noise. On the contrary, the external noise is measurable in static mode experiments. Furthermore, *in-situ* reference cantilevers are key, which enables to compensate for any change in index of refraction, temperature, viscosity and density of the liquid inside the measurement chamber.

The implemented positioning system enables a highly accurate and repeatable positioning of the laser spot in both directions on the cantilevers with a minimal spread of the position. The contribution of this spread to the noise level is negligible in the static or dynamic response of the cantilevers. The automated laser focusing together with positioning of the laser spot allows the read-out of each dynamic mode as the laser spot can be precisely positioned at a node of the resonating cantilever. For example, the node-to-node distance for the 11^{th} higher mode is ca. 50 µm. Reading-out at a node facilitates the largest angular deflection of the laser beam as shown in section 1.3.2. The variable positioning on each cantilever of the array offsets for subtle discrepancies among the cantilevers of the array.

For a reliable optical read-out of the mechanical response of the cantilever, the reflected laser has to be set as accurate as possible in the middle of the active area of the position sensitive device, resulting in zero voltage on the differential signal. Thus, a broad linear range of the position sensitive detector is key to avoid any distorted signals. Furthermore, a

neutral density filter has to be in place to avoid saturation of the detector that causes damage to the amplification electronics.

To compensate for temperature fluctuations within the measurement chamber, induced either by a high flow rate or as shown for a temperature set point of 36 °C or by external factors, it is important to have an *in-situ* reference cantilever. By reference subtractions, external influences such as temperature fluctuations can be minimised as shown by Lang *et al.* [7].

The implemented software architecture is easily scalable without the need to update the hierarchy of the code. New functionality can be embedded as additional consumer loops utilising the parallelisation capability of the architecture. Additionally, the code is broken up into well-defined components that run independently. This modularity allows the exchange of code or upgrade of parts of the hardware for future expansion quickly with minimal effort. The independent parts of the code are de-coupled well-enough from each other, that they can be even reused as standalone software (e.g. dynamic mode analyser) or in a future up-scaled project.

3.4 References

[1] Maloney N, Lukacs G, *et al.* 2014 Device for filamentous fungi growth monitoring using the multimodal frequency response of cantilevers *Rev Sci Instrum* **85** -

[2] Ghatkesar M K, Barwich V, *et al.* 2007 Higher modes of vibration increase mass sensitivity in nanomechanical microcantilevers *Nanotechnology* **18** 445502

[3] Lachut M J and Sader J E 2012 Effect of surface stress on the stiffness of thin elastic plates and beams *Physical Review B* **85** 085440

[4] Lachut M J and Sader J E 2007 Effect of Surface Stress on the Stiffness of Cantilever Plates *Phys Rev Lett* **99** 206102

[5] Jianqiang H, Changchun Z, *et al.* 2002 Dependence of the resonance frequency of thermally excited microcantilever resonators on temperature *Sensors and Actuators A: Physical* **101** 37-41

[6] Ghatkesar M K, Rakhmatullina E, *et al.* 2008 Multi-parameter microcantilever sensor for comprehensive characterization of Newtonian fluids *Sensors Actuators B: Chem* **135** 133-8

[7] Lang H P, Berger R, *et al.* 1998 Sequential position readout from arrays of micromechanical cantilever sensors *Appl Phys Lett* **72** 383-5

Chapter 4

Automated Laser Focusing

This chapter describes a fully automated process to focus the laser on the cantilever surface. This focusing process allows to obtain the highest response and resolution possible using the optical beam deflection method. The implemented algorithm is based on the revised travelling knife edge method to determine the laser spot size diameter. By comparing the theoretical value of the laser spot size with the experimental result the laser is focused in an iterative manner using the 3 axes positioning system.

4.1 Introduction

The nanomechanical response of the cantilever is recorded utilising the optical beam deflection method [1, 2], where a laser is reflected off the cantilever surface on to a PSD as described in section 2.2.5. To obtain the highest resolution possible for the deflection measurements, the laser has to be positioned at the apex of the cantilevers where the maximum deflection occurs [3]. To acquire the maximum response for all the flexural modes of vibrations of the cantilever operated in dynamic mode, the laser has to be precisely positioned at a node as described in section 1.3.2 and focused on the cantilever surface. It has been shown that a smaller laser spot on the cantilever results in a maximum signal to noise ratio because of the small region of maximum slope [4]. In addition, the sign of the slope of higher flexural modes varies along the cantilever, therefore focusing the laser on the area at the free end of the cantilever and the next node provides a good compromise between high frequency sensitivity and static mode measurement [5].

For example, the node-to-node distance for the 15^{th} higher flexural mode of a 500 µm long cantilever is ca. 33 µm. Hence the angle sensitive region is approximately 11 µm long. Therefore, the laser spot has to be well focussed and positioned such that it spans a large section of the cantilever over which the slope is of high absolute value [6]. If the laser is

not focused correctly, the fine positioning at a node is not possible, resulting in an amplitude spectrum with a low signal to noise ratio Hence, the laser has to be finely focused on the cantilever and must be moved to its optimum position on the cantilever to obtain maximum detection sensitivity, high response and resolution for both operational modes.

The position of the 3 axes positioning system with the optical cage mounted on it with respect to the cantilevers has to be determined based on an initial focusing of the laser on the cantilever surface. The distance between the cantilever surface and the achromatic doublet is determined by the focal length of the lens. The initial distance between the cantilever and the lens is set by the travel micrometer heads mounted on the xyz micro-translation stage. Based on the laser spot size, the ideal position of the optical cage can be determined.

4.1.1 Laser Spot Size Calculation

The spot size D_{CL} of the laser focused on the cantilever surface can be calculated using the basic optics formula for the beam diameter at the waist of a beam [7].

$$D_{CL} = \left(\frac{4\lambda}{\pi}\right)\left(\frac{f}{D_{COLL}}\right) \tag{25}$$

where D_{CL} is the diameter of the spot on the cantilever, λ the wavelength of the laser, f the focal length of the lens and D_{COLL} the collimated beam diameter as shown in Figure 53.

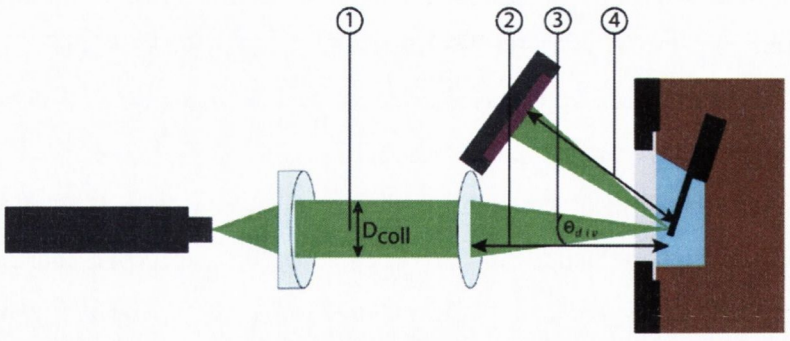

Figure 53 Schematic for the spot size calculation on the cantilever surface, not drawn to scale, laser beam size exaggerated for clarity. 1 Collimated laser beam, 2 Focal length of the bi-convex lens used to focus the laser beam on the cantilever surface, 3 beam divergence, 4 Distance $d_{cl\text{-}psd}$ between the cantilever surface and the position sensitive detector.

The depth of focus (DOF) of the laser spot can be calculated by [7]:

$$\mathrm{DOF} = \left(\frac{8\lambda}{\pi}\right)\left(\frac{f}{D_{COLL}}\right)^2 \tag{26}$$

where DOF is the depth of focus of the focussed laser beam, λ the wavelength of the laser, f the focal length of the lens and D_{COLL} the collimated beam diameter as shown in Figure 53. The depth of focus determines the accuracy expected for the translation stage in the y-direction to align the optical cage with respect to the cantilever surface.

The spot size of the reflected laser beam on the position sensitive detector can be calculated by applying the following equations

$$\Theta_{div} = 2arctan\left(\frac{D_{COLL}}{2f}\right) \tag{27}$$

$$D_{CL} = \frac{4\lambda}{\pi\Theta_{div}} \tag{28}$$

$$D_{PSD} = 2\left(d_{cl-psd}\right)tan\left(\frac{\Theta_{div}}{2}\right) \tag{29}$$

4.1.2 Laser Spot Size Determination

To automate the focusing process on the cantilever surface, the knife-edge method to determine the beam width of a Gaussian laser beam is applied [8]. The knife-edge method can be used in either both axes [9] or only on one axis [10] of a laser beam. The initialisation process focuses the laser on to the cantilever surface, while measuring the beam radius in the vicinity of the beam waist. This quick and inexpensive method gives the most accurate determination of the waist radius by analysing data obtained by the application of the modified traveling knife-edge technique.

The experimental principle is shown in Figure 55. The modification of the traveling knife-edge method includes to translate the laser beam across the knife instead of moving the knife across the laser beam. The laser is translated across the cantilever surface whereas the cantilever acts as a knife-edge and the laser beam is reflected onto the position sensitive detector. The PSD measures the intensity of the reflected light as the sum signal. By moving the laser incrementally across the cantilever surface, less light is reflected and the measured sum signal continuously decreases to zero. This intensity data is analysed and the laser beam radius can be extracted as a function of the position of the laser on the

cantilever according to the Khosrofian and Garetz algorithm [10]. This algorithm has been widely used to determine the radius of a symmetric Gaussian laser beam [9] with intensity I as described by equation (30):

$$I(x) = I_0 exp\left[-2\frac{(x-x_0)^2}{w^2}\right] \tag{30}$$

Where I_0 is the peak intensity at the centre of the laser beam, located at x_0, x is the transverse Cartesian coordinate of any point with respect to an origin conveniently chosen in the middle of the cantilever, and w is the laser beam radius. By integration of *I(x)* the total power P_T is obtained as shown by equation (31).

$$P_T = \int_{-\infty}^{+\infty} dx\, I(x) = \frac{\pi w^2 I_0}{2} \tag{31}$$

The transmitted power P_t is expressed by equation (32):

$$P_t = \int_{x}^{+\infty} dx'\, I(x') \tag{32}$$

By measuring the transmitted power P_t while moving the laser spot incrementally across the cantilever in the x direction as shown in Figure 55, it is possible, by using equation (32), to determine the beam radius. However, equation (32) has no known analytical solution. Khosrofian and Garetz [5] have published an inversion algorithm to calculate the beam radius resulting in a simpler, equivalent mathematical expression to equation (32):

$$P_N(x) = \frac{1}{1 + exp[-(a_0 + a_1 t + a_2 t^2 + a_3 t^3)]} \tag{33}$$

Where

$$a_0 = -6.71389 \times 10^{-3}$$

$$a_1 = -1.55115$$

$$a_2 = -5.13306 \times 10^{-2}$$

$$a_3 = -5.49164 \times 10^{-2}$$

$$t = (2/w_x)(x - x_0)$$

$$P_N(x) = P(x)/P_T = \text{Normalised power}$$

The error of the determined laser beam radius using equation (33) is only 0.05% [9] equal to the experimental errors in best conditions. By using equation (33) and the coefficient a_0, a_1, a_2 and a_3 listed above, the parameters w_x and x can be easily fitted to the experimental data. De Araújo et al [11] have shown recently that the inversion algorithm by Khosrofian and Garetz has to be revisited. The coefficient a_0 and a_2 converge numerically to zero, resulting in new non-null adjusted coefficients a_1 and a_3, resulting in a simplified version of equation (33) which can be expressed in an elementary manner:

$$P_N(x) = \frac{1}{1 + exp[a_1 t + a_3 t^3]} \tag{34}$$

With the coefficient

$$a_1 = -1.597106847$$

$$a_3 = -7.0924013 \times 10^{-2}$$

4.2 Materials & Methods

Manual travel micrometer heads mounted on the x and y micro-translation stages as described in section 2.2.7 are used for the initial positioning of the laser spot on the cantilever array. The laser spot is positioned in the middle at the tip of the first cantilever of the array as shown in Figure 54.

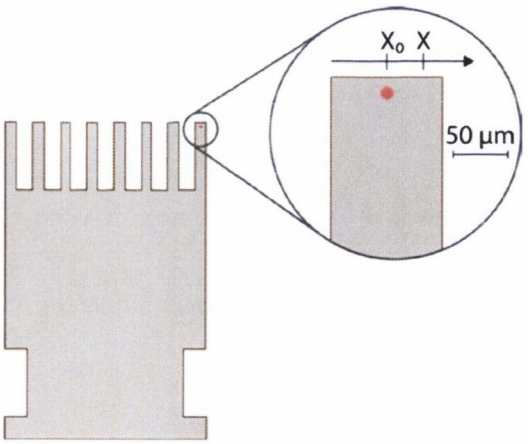

Figure 54 Initial setup for the knife-edge measurement. Inset is showing the laser spot on the cantilever surface, with the dimension exaggerated for clarity. The laser is moved across the cantilever in the x direction, e.g. from X_0 position to X position with a step width of 2 µm.

The position sensitive detector logs the intensity of the reflected laser beam from the cantilever surface and outputs the intensity as the sum signal. After each recording, the micro-translational stage translates the laser beam 2 µm across the cantilever surface as indicated by Figure 54 in the x direction. These two steps are repeated 75 times, resulting in the laser spot missing the cantilever surface completely as shown in Figure 55 and the sum signal of the position sensitive detector decreasing to zero.

After the 75 iterations of the knife-edge measurements are finished, the model from De Araújo [11] is fitted to the experimental data and the radius of the laser beam on the cantilever surface is obtained. Based on the obtained radius, the optical cage is moved closer or further away from the measurement chamber followed by a knife-edge measurement to obtain the radius of the newly focused laser beam. This process is repeated until the radius of the laser beam on the cantilever surface is less than 10 µm. The code for the optical beam alignment is described in more detail in chapter 2.

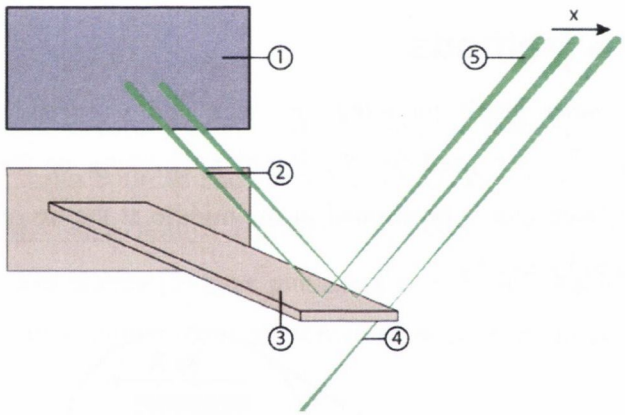

Figure 55 Experimental setup of the laser focusing process, not drawn to scale. 1 Position sensitive detector, 2 Reflected laser beam, 3 Cantilever, 4 Laser beam missing the cantilever, 5 Incident laser beam is moved by the micro-translation incrementally in the x direction indicated by the arrow until it misses the cantilever surface completely. After each incremental translation of the laser beam, the position sensitive detector records the intensity of the reflected laser beam.

4.3 Results

4.3.1 Laser Spot Size Calculation

The laser spot diameter D_{CL} of the laser beam focused on the cantilever surface is calculated using equation (25):

$$D_{CL} = \left(\frac{4\lambda}{\pi}\right)\left(\frac{f}{D_{COLL}}\right)$$

with the following parameters: λ is the wavelength of the laser (830 nm), f isthe focal length of the lens (50 mm) and D_{COLL} is the collimated beam diameter (3.45mm). Using the values mentioned above for the setup, the calculated diameter of the laser spot on the cantilever is 15.32 µm.

Using the values above, the depth of focus can be calculated using equation (26):

$$\text{DOF} = \left(\frac{8\lambda}{\pi}\right)\left(\frac{f}{D_{COLL}}\right)^2$$

The depth of focus is around 443 µm. This indicates the precision required of the positioning system for the optical cage in relation to the cantilever surface.

The size of the laser spot on the position sensitive detector is calculated by equation(27) (29) resulting in a laser spot size on the position sensitive detector of 2.76 mm.

$$D_{PSD} = 2\left(d_{cl-psd}\right)tan\left(\frac{\Theta_{div}}{2}\right)$$

4.3.2 Laser Alignment Using the Knife-Edge Method

By applying the modified knife-edge method as described above, the laser focusing process on the cantilever surface is automated as described in section 2.3.3.4. The manual travel micrometer heads are used for the initial focusing of the laser on the surface. The resulting laser spot size on the cantilever is in the order of 150 to 300 µm (data shown in Appendix A.5). After five iterations of the alignment process, the obtained beam radius on the cantilever surface is 21.9 µm as shown in Figure 56.

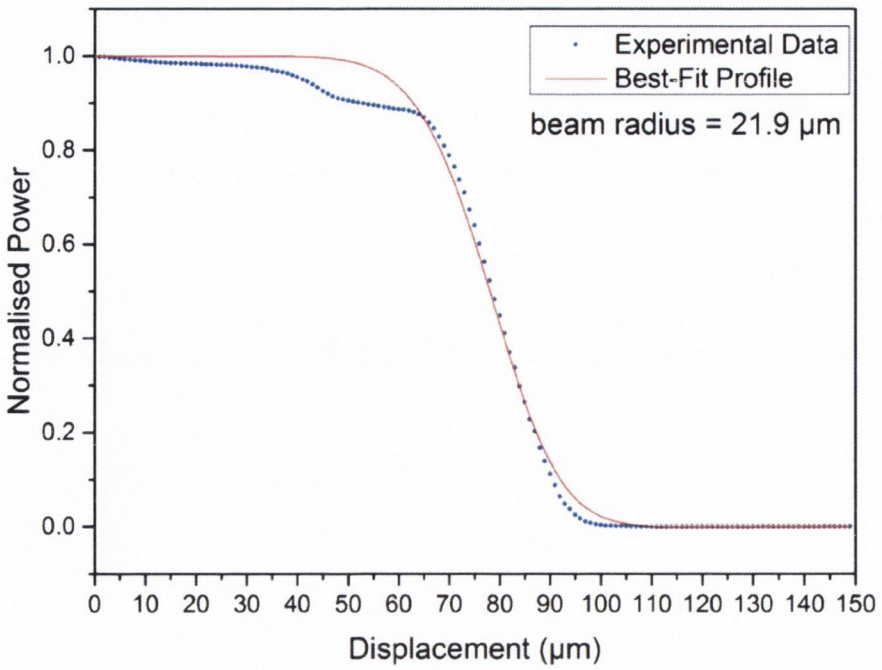

Figure 56: Normalised transmitted power of the laser beam measured as a function of the laser position in the x direction. Blue dots represent the experimental data, red line the best-fit profile. The beam radius value of 21.9 µm on the cantilever surface has been obtained from the best-fit profile.

Followed by one more focusing step, moving the optical cage closer to the measurement chamber, the knife-edge measurement outputs a laser beam radius of 9.6 µm, which is close enough to the theoretical value of 7.66 µm calculated above to stop the laser focussing process.

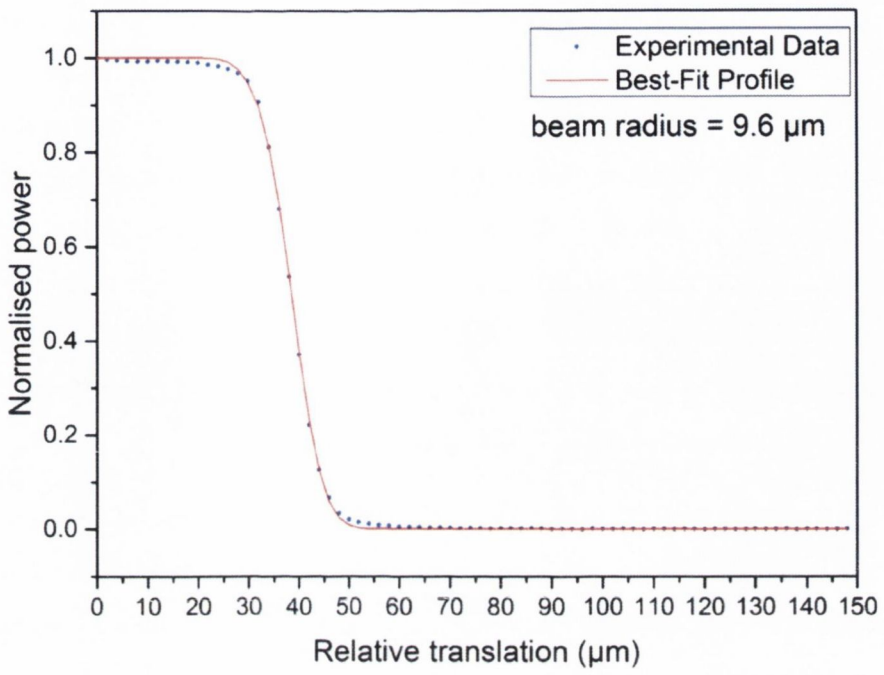

Figure 57: Normalised transmitted power of the laser beam measured as a function of the laser position in the x direction. Blue dots represent the experimental data, red line the best-fit profile. The beam radius value of 9.6 µm on the cantilever surface has been obtained from the best-fit profile.

4.4 Discussion & Conclusion

By applying the simple method of the modified travelling knife-edge method to obtain the laser beam diameter on the cantilever surface, it is possible to automate the initialisation process. There are no significant differences in the radius of the single wavelength laser beam translated between the different cantilevers within one array (data not shown) by the micro-translation stage. Hence, conducting the focusing process on one cantilever surface of the array is sufficient for all eight cantilevers.

Due to the depth of focus of 443 µm, the final beam radius is achieved within a range and final focussing is valid even if the cantilevers are slightly bent. Hence, there is room for cantilevers bending marginally in "up or down direction" without much change in the beam radius.

If the surface of the cantilever has been non-uniformly coated, this focussing process might result in different values for the laser beam diameter: Non-uniform metal deposition on the surface or different bio-functionalisation of the cantilevers can result in changes of the

reflectivity of the surface, hence change in intensity of the reflected laser beam within one cantilever. Big differences in the obtained laser beam radius on the cantilever surface might be an indicator for a misalignment of the measurement chamber in the custom-made holder mounted to the breadboard, a non-horizontal mounted optical cage or a non-orthogonal assembly of the lockable xyz micro-translation stages. Additionally, the differences might arise from the fabrication process of the measurement chamber. Even though a CNC milling machine fabricated the chamber it is possible to end up with a measurement chamber within which the recessed pocket for the cantilever array is misaligned resulting in a inclined cantilever array.

This automated initialisation process for the laser is very helpful for conducting measurements at higher resonance modes. It minimises the influence of the operator of the device to obtain the highest resolution possible and reading out the higher flexural modes of vibrations of the cantilevers.

4.5 References

[1] Meyer G and Amer N M 1990 Simultaneous measurement of lateral and normal forces with an optical-beam-deflection atomic force microscope *Appl Phys Lett* **57** 2089-91

[2] Putman C A J, De Grooth B G, *et al.* 1992 A detailed analysis of the optical beam deflection technique for use in atomic force microscopy *J Appl Phys* **72** 6-12

[3] Javier T, Valerio P, *et al.* 2012 Imaging the surface stress and vibration modes of a microcantilever by laser beam deflection microscopy *Nanotechnology* **23** 315501

[4] Schäffer T E and Hansma P K 1998 Characterization and optimization of the detection sensitivity of an atomic force microscope for small cantilevers *J Appl Phys* **84** 4661-6

[5] Stark R W 2004 Optical lever detection in higher eigenmode dynamic atomic force microscopy *Rev Sci Instrum* **75** 5053-5

[6] Schäffer T E and Fuchs H 2005 Optimized detection of normal vibration modes of atomic force microscope cantilevers with the optical beam deflection method *J Appl Phys* **97** -

[7] Corporation N 2014 Gaussian Beam Optics Tutorial. (World Wide Web

[8] Arnaud J A, Hubbard W M, *et al.* 1971 Technique for Fast Measurement of Gaussian Laser Beam Parameters *Appl Opt* **10** 2775-6

[9] Bachmann L, Maria Zezell D and Puig Maldonado E 2003 Determination of Beam Width and Quality for Pulsed Lasers Using the Knife-Edge Method *Instrumentation Science & Technology* **31** 47-52

[10] Khosrofian J M and Garetz B A 1983 Measurement of a Gaussian laser beam diameter through the direct inversion of knife-edge data *Appl Opt* **22** 3406-10

[11] de Araújo M A, Silva R, *et al.* 2009 Measurement of Gaussian laser beam radius using the knife-edge technique: improvement on data analysis *Appl Opt* **48** 393-6

Chapter 5

Performing Cantilever Assays

The basic preparation steps to convert a cantilever array into a biosensor assay are described in this chapter. Firstly, the different cleaning steps of the silicon array are outlined. Secondly, the metal deposition procedure to obtain a thin gold layer is presented. Finally, the techniques to functionalise the cantilevers individually are discussed.

5.1 Introduction

To convert silicon cantilever arrays into a bio-sensor assay, a bio-recognition layer has to be attached to the cantilever to enable the sensor to act as a specific transducer element. The bio-recognition layer will interact with the analyte of interest and the physicochemical change within or at the bio-recognition layer is converted by the cantilever to a physically gaugeable signal: frequency change and deflection, respectively. These signals are recorded using the optical beam deflection method.

The bio-recognition layer consists of immobilised bio-receptor molecules that are selective for the target analyte molecules. The performance of the cantilever assays depends on the bio-recognition layer and interface between this layer and the cantilever surface. Hence, the reproducibility of the assay is only as good as the reproducibility of the immobilisation of the bio-receptor molecules. Careful formulation of the bio-recognition layer is key for a successful and reliable assay; the adhesion layer between the silicon surface of the cantilever and the bio-recognition layer is an important part of the assay.

The assay preparation follows the same principle for all of the experiments discussed in this thesis. The cantilever array has to be cleaned prior to a 2 nm titanium and 21 nm gold layer deposition. This gold surface acts as an adhesion layer for a self-assembled monolayer [1, 2]. ω-functionalised alkanethiols are used which adsorb spontaneously from

solutions onto the surface of gold. This self-assembled monolayer acts as the link to the bio-recognition layer of the cantilever assay [3, 4].

5.2 Cantilever Cleaning

The surface of the cantilever arrays (IBM Zurich Research Laboratory, Rüschlikon, Switzerland) can contain organic and particulate contaminants remaining from the fabrication process. Prior to metal layer deposition and bio-functionalisation, the silicon surface has to be cleaned, otherwise the topography of the final gold layer can vary greatly (e.g. uneven roughness) with a direct impact on the efficiency of the formation of the self-assembled monolayer [2] and finally reducing the sensing capability of the assay.

5.2.1 Grease and Solvent Removal

A general degreasing procedure is performed to remove the surfactants on the surface of the cantilever arrays. Any remaining grease, adventitious deposits and remaining adhesives from the fabrication process and the packaging are removed. The cantilever arrays are cleaned sequentially in baths of acetone, ethanol and nano pure water, respectively. The protocol for the grease and solvent removal is presented in Appendix B.1.1.

5.2.2 UV Ozone Cleaning

UV cleaning, prior to plasma cleaning and bio-functionalisation, removes any monomolecular layers of chemically bound organics on the surface of the cantilever arrays. Chemisorbed and covalently bound molecules of adventitious organics, desorb from the silicon surface by oxidation activated by the UV radiation. The UV radiation excites the contaminant molecules (e.g. cleaning solvent residues, human skin oil) on the surface of the cantilever array. Atomic oxygen is formed when molecular oxygen is dissociated by the 184.9 nm wavelength and ozone by the 253.7 nm wavelength. The excited contaminant molecules react then with atomic oxygen to form volatile molecules that desorb from the surface.

A gold surface fouls at ambient laboratory conditions; this fouling hampers the bio-functionalisation of the cantilevers. Owing to the high surface energy of the gold surface the organic molecules from the ambient air are adsorbed easily [5]. The adsorption energy of an organic contaminant from air [6] is lower than the activation energy for chemisorption of long alkylthiols $(CH_2)_{10}$ onto the surface of gold [7]. Hence, the

formation of the self-assembled monolayer on the gold surface is impaired by these pre-absorbed molecules from ambient air.

As a result of this fouling process, the gold surface has to be cleaned and activated prior to the bio-functionalisation [8] according to the protocol presented in Appendix B. The protocol for the UV cleaning for the silicon surface prior to plasma cleaning is presented in Appendix B.1.2.

5.2.3 Plasma Cleaning

It is key to have a clean silicon surface prior to the metal deposition. Plasma cleaning removes layers of organic contaminants from the silicon surface of the cantilever arrays that are not removed by the UV cleaning procedure. The organic contaminants are decomposed by an oxidation reaction. The plasma generates UV light, that is able to cleave any organic bonds and this allows drawing out of hydrogen atoms and adds oxygen atoms [9, 10]. The volatile hydrocarbon products are then pumped out of the vacuum chamber [11]. The protocol used for the plasma cleaning of all cantilever arrays is described in Appendix B.1.3.

5.3 Thin Film Deposition

A gold layer is required on the surface of the cantilever so that thiol chemistry can be used to covalently link ω-functional alkylthiol molecules to form functional self-assembled monolayers [12, 13] that represent a chemical surface activated to bind biomolecules subsequently. The gold layer is also favourable for use as a reflection layer for the optical beam deflection read-out technique [14].

An evaporation system (Temescal FC 2000; Temescal, Livermore, USA) is used for the deposition of thin films of titanium and gold on to the cantilever arrays. A 2 nm thin layer of titanium was deposited on the silicon to improve the adhesion of the gold layer [15]. Without breaking the vacuum, a 21 nm layer of gold was deposited on top of the titanium layer. Both metals were evaporated using electron beam evaporation using the parameters from Table 3.

Table 3 The parameters for the Temescal FC 2000 evaporation system.

	Titanium	Gold
Method	E-Beam	E-Beam
Pressure (Torr)	$< 2 \times 10^{-6}$	$< 2 \times 10^{-6}$
Rate (Å/s)	0.2	0.5
Thickness (nm)	2	21

A controlled roughness is of importance for the performance of the sensors, the gold surface had a root mean square roughness of 0.8 nm, with a grain size of 35 nm [16]. It has been shown, that the sensitivity of the cantilevers operated in static mode depends significantly on the topology of the surface [17]. Furthermore, the thin film depositions allow for a mechanical calibration of the cantilever sensor by applying a heat pulse to the cantilever array due to different thermal expansion coefficients of silicon, titanium and gold.

5.4 Bio-Functionalisation

To use the cantilever array as a biosensor, a bio-recognition interface has to be immobilised on the gold coated surface. Owing to the 8 cantilevers within an array, it is possible to have multiple bio-recognition interfaces. This allows the investigation of different biological interactions within one array including an *in-situ* reference bio-recognition interface which improves the reliability of the measurement [18]. This *in-situ* reference cantilever allows the decoupling of signals caused by environmental instabilities, such as non-specific adsorption, external noise, ionic strength and temperature fluctuations.

Self-assembled monolayers (SAM) of thiolates on the gold surface of the cantilever provides one simple route to functionalise the sensor surface by organic molecules. A SAM offers a well-defined and organised surface providing an ideal interface for immobilisation of biomolecules [19]. The formation of the SAM on the cantilevers is obtained usually by two techniques; immersion of cantilevers in liquid filled capillary technique [20, 21] or the micro dispensing techniques [22-24].

5.4.1 Capillary Immersion Technique

The capillary immersion technique uses glass capillary tubes (ID 180 ± 10 µm, OD 240 ± 10 µm, length 75 mm, King Precision Glass Inc., California, USA). Prior to use, the capillaries are cleaned according to the protocol in Appendix B.1.4. The glass capillary tubes are precisely aligned with the 8 cantilevers as shown in Figure 58 A using a custom built capillary functionalisation device. The cantilevers are inserted into the ends of the capillaries as shown in Figure 58 B with the help of manual micro translation stages. At the other end, the capillaries are immersed in an Eppendorf tube which acts as a reservoir containing the thiolated molecules suspended in an appropriate solution to facilitate the immobilization of the probes on to the gold surface. Different molecules can be used resulting in an individual functionalisation for each cantilever as displayed in Figure 58 C and D. The immersion times of the cantilevers differ dependent on the functionalisation being carried out.

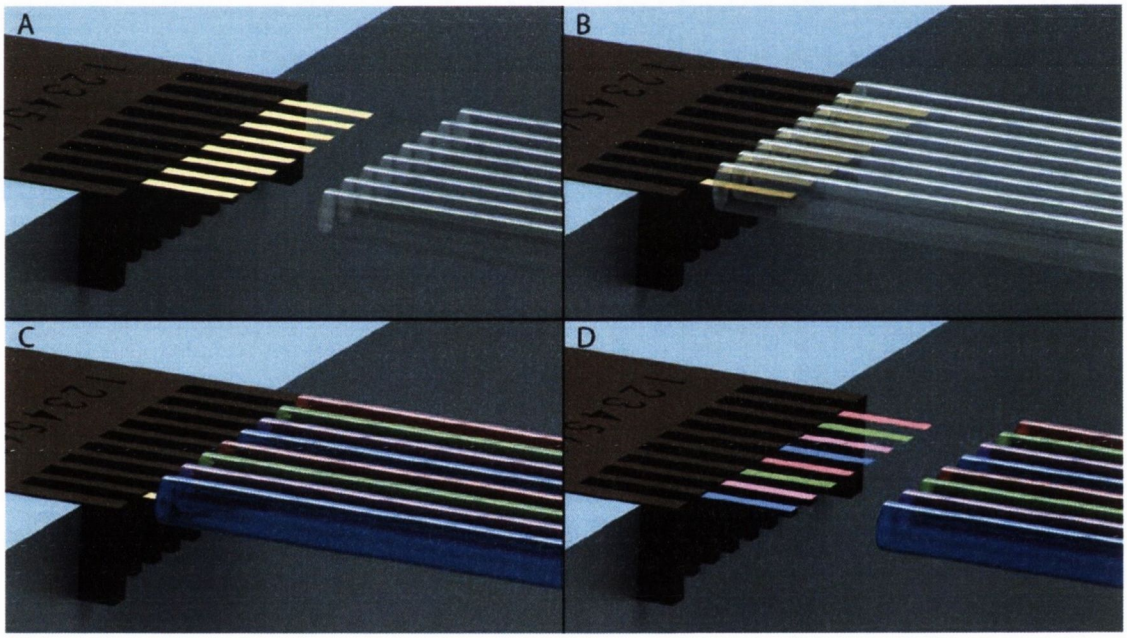

Figure 58: Functionalisation of the cantilevers using the capillary immersion technique. A) The capillaries are aligned to the gold coated cantilevers, the pitch from the centre of each capillary matches that of the cantilevers in the array B) The cantilevers are aligned with the capillaries. Each capillary can be filled from the opposite end with solution containing the molecules C) Immersion of the cantilever in the capillaries filled with the functionalisation solutions. Each capillary has its unique sample reservoir resulting in individual functionalisation of each cantilever D) The individual functionalised cantilever array extracted from the capillaries.

5.4.2 Micro Dispensing: Ink-Jet Printing

Ink-jet printing has been used in the functionalisation of cantilevers with living cells [22], alkanethiols and single-stranded DNA oligomers [21] and membrane proteins [25]. The droplet formation is achieved by a piezoelectric actuator on a micropipette. The actuator generates short waves upon an applied voltage. When the kinetic energy of these short pressure waves is adequate to overcome the surface tension of the micropipette opening, a droplet is formed. The microdispensing system (MD-P-801; Microdrop, Norderstedt, Germany) consists of a piezo-driven pipette (AD-K-501; Microdrop, Norderstedt, Germany) mounted on a three axis micro positioning system. A pipette with a nozzle diameter of 50 µm is used. The volume of the formed droplet depends mostly on the diameter of the nozzle, the release from the nozzle depends on the viscosity of the solvent used and the voltage and pulse length applied to the piezoelectric actuator.

5.5 Measurement Procedure

The process sequences of a cantilever assay are shown in Figure 59. A cantilever array is prepared and functionalised according to the protocol outline above. The sample of interest is loaded into the pressurised sample and the injection valve is primed. Then a functionalised cantilever array is placed in the measurement chamber and clamped down by the clamp. The syringe pump pushes then buffer through the chamber to fill up the liquid cell until the cell is flooded, then the glass cover is placed as a seal and kept in place by the frame. The measurement chamber is then mounted in the custom-made holder inside the temperature-regulated box. After reaching a stable temperature inside the box, the recording of the nanomechanical response of the cantilevers starts. The temperature is regulated according to the output of the Fuzzy Logic algorithm to maintain a stable temperature.

The device outlined can be operated in both dynamic and static mode. When set to dual mode operation, the laser spot cycles through the cantilevers sequentially, taking firstly a dynamic measurement and then a static measurement before moving onto the next cantilever. A LabVIEW program (described in detail in section 2.3) controls the movement of stages, dictates the frequencies sent to the piezoelectric actuator and performs analysis of the signals output from the PSD.

To check the stability of the functionalised cantilevers a buffer injection has to be performed prior to the injection of the sample. A fractional response of the cantilever to the buffer injection is acceptable. However, the response from the reference and probe cantilevers should be the same to exclude any false signals based on the different functionalisation of the cantilevers.

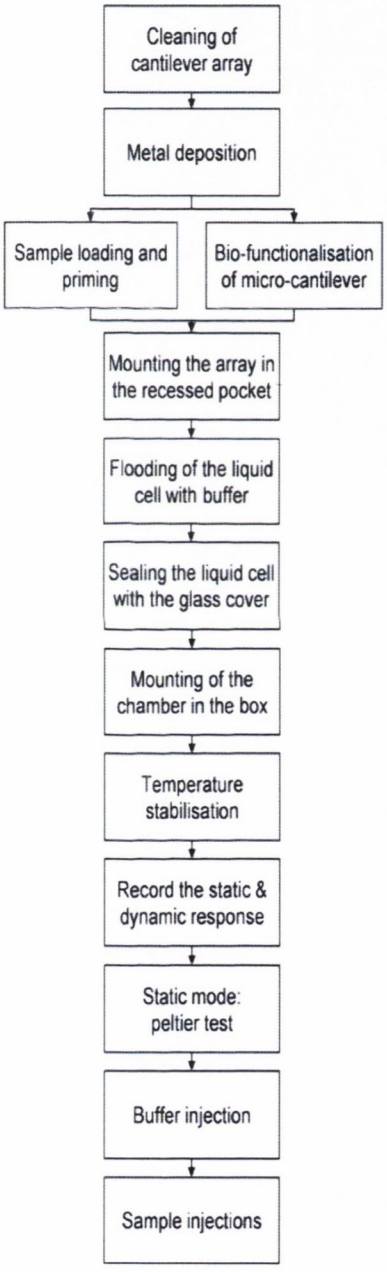

Figure 59: Process sequences of a cantilever assay.

5.6 References

[1] Folkers J P, Laibinis P E and Whitesides G M 1992 Self-assembled monolayers of alkanethiols on gold: comparisons of monolayers containing mixtures of short- and long-chain constituents with methyl and hydroxymethyl terminal groups *Langmuir* **8** 1330-41

[2] Vericat C, Vela M E, *et al.* 2010 Self-assembled monolayers of thiols and dithiols on gold: new challenges for a well-known system *Chem Soc Rev* **39** 1805-34

[3] Ferretti S, Paynter S, *et al.* 2000 Self-assembled monolayers: a versatile tool for the formulation of bio-surfaces *TrAC, Trends Anal Chem* **19** 530-40

[4] Ostuni E, Yan L and Whitesides G M 1999 The interaction of proteins and cells with self-assembled monolayers of alkanethiolates on gold and silver *Colloids Surf B Biointerfaces* **15** 3-30

[5] Smith T 1980 The hydrophilic nature of a clean gold surface *J Colloid Interface Sci* **75** 51-5

[6] Dubois L H and Nuzzo R G 1992 Synthesis, Structure, and Properties of Model Organic Surfaces *Annu Rev Phys Chem* **43** 437-63

[7] Trapnell B M W 1953 The Activities of Evaporated Metal Films in Gas Chemisorption *Proceedings of the Royal Society of London Series A Mathematical and Physical Sciences* **218** 566-77

[8] Ron H, Matlis S and Rubinstein I 1998 Self-Assembled Monolayers on Oxidized Metals. 2. Gold Surface Oxidative Pretreatment, Monolayer Properties, and Depression Formation *Langmuir* **14** 1116-21

[9] Lin Y-S 2003 A surface analysis on oxygen plasma-cleaned gold pattern-plated substrates for wire bondability *Surf Coat Technol* **173** 47-57

[10] Hook D A, Olhausen J A, *et al.* 2010 Evaluation of Oxygen Plasma and UV Ozone Methods for Cleaning of Occluded Areas in MEMS Devices *Microelectromechanical Systems, Journal of* **19** 1292-8

[11] Hess D W and Reinhard K A 2008 *Handbook of Silicon Wafer Cleaning Technology (Second Edition)*, ed K A Reinhardt and W Kern (Norwich, NY: William Andrew Publishing) pp 355-427

[12] Love J C, Estroff L A, *et al.* 2005 Self-Assembled Monolayers of Thiolates on Metals as a Form of Nanotechnology *Chem Rev* **105** 1103-70

[13] Schreiber F 2000 Structure and growth of self-assembling monolayers *Prog Surf Sci* **65** 151-257

[14] Putman C A J, De Grooth B G, *et al.* 1992 A detailed analysis of the optical beam deflection technique for use in atomic force microscopy *J Appl Phys* **72** 6-12

[15] Sexton B A, Feltis B N and Davis T J 2008 Characterisation of gold surface plasmon resonance sensor substrates *Sensors and Actuators A: Physical* **141** 471-5

[16] Mishra R 2012 Selective Gene Fishing in Complex Genomic Environments Using Micro-Cantilevers: Applications in RNAi Therapy. In: *PhD Thesis, Centre for Research on Adaptive Nanostructures and Nanodevices and the School of Physics,* (Ireland: Trinity College Dublin)

[17] Weissmüller J and Duan H 2008 Cantilever Bending with Rough Surfaces *Phys Rev Lett* **101** 146102

[18] Lang H P, Berger R, *et al.* 1998 Sequential position readout from arrays of micromechanical cantilever sensors *Appl Phys Lett* **72** 383-5

[19] Chaki N K and Vijayamohanan K 2002 Self-assembled monolayers as a tunable platform for biosensor applications *Biosensors Bioelectron* **17** 1-12

[20] McKendry R, Zhang J, *et al.* 2002 Multiple label-free biodetection and quantitative DNA-binding assays on a nanomechanical cantilever array *Proceedings of the National Academy of Sciences* **99** 9783-8

[21] A. Bietsch, J. Zhang, *et al.* 2004 Rapid functionalization of cantilever array sensors by inkjet printing *Nanotechnology* **15** 873

[22] G. Lukacs, N. Maloney and Hegner a M 2012 Ink-Jet Printing: Perfect Tool for Cantilever Array Sensor Preparation for Microbial Growth Detection *Journal of Sensors* **2012** 7

[23] Alexander B, Jiayun Z, *et al.* 2004 Rapid functionalization of cantilever array sensors by inkjet printing *Nanotechnology* **15** 873

[24] Bietsch A, Hegner M, *et al.* 2004 Inkjet Deposition of Alkanethiolate Monolayers and DNA Oligonucleotides on Gold: Evaluation of Spot Uniformity by Wet Etching *Langmuir* **20** 5119-22

[25] Braun T, Ghatkesar M K, *et al.* 2009 Quantitative time-resolved measurement of membrane protein-ligand interactions using microcantilever array sensors *Nat Nano* **4** 179-85

Chapter 6

Investigation of the UK-39 Peptide Cross Reactivity

The investigation of the reactivity of the vaccine candidate UK-39 towards three antibodies (SP3, EP3 and EP9) while operating the cantilever array in static and dynamic mode is described in this chapter. The static mode results show an average deflection of 26 ± 8 nm for the SP3, 0 ± 3 nm for the EP3 and 6 ± 3 nm for the EP9 antibodies. These findings were confirmed by the dynamic mode measurements showing the highest reactivity for the SP3 antibodies with a maximum mass uptake of 380 ± 30 pg. The EP3 and EP9 measurements resulted in a maximum mass uptake of 80 ± 40 pg and 160 ± 25 pg, respectively. It is found that the cantilever based label-free assay is capable of distinguishing different reactivities of the UK-39 peptides.

6.1 Introduction

6.1.1 UK-39 Peptide

The Swiss Tropical and Public Health Institute and partners have developed a synthetic peptide closely resembling the natural conformation of the major surface protein of the sporozoite, this peptide is named UK-39 [1]. Immunisation of mice, rabbits and humans with UK-39 delivered by immuno-potentiating influenza virosomes (IRIVs) resulted in high titres of sporozoite cross-reactive antibodies [1, 2]. IRIVs are characterized as spherical vesicles, with a mean diameter of 150 nm composed of influenza surface glycoproteins and a mixture of natural and synthetic phospholipids [3]. These vesicles serve as an antigen carrier system with exogenous antigens to elicit antibody responses

and/or encapsulated antigens in their lumen to elicit T cell responses [4]. Thus, based on the size, structure and composition of the IRIVs, they pose as a vaccine adjuvant (e.g. to improve the immune response) for efficacious vaccination, as was demonstrated for hepatitis A and influenza [5].

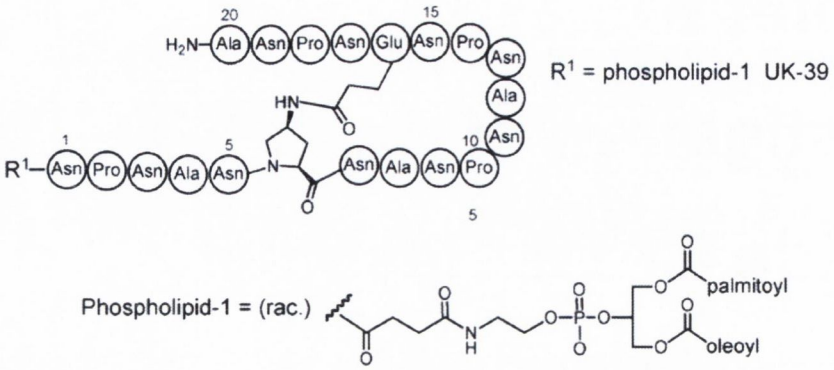

Figure 60: Structure of Peptide UK-39. The UK-39 synthetic peptide is phospholipid phospatidylethanolamine conjugated. Adapted from Okitsu *et al.*, [1].

Measuring of antibody responses in humans against recombinant parasite antigens by enzyme immunoassays has been widely applied in population studies but it is still unclear how antibody levels relate to inhibitory function. Furthermore, such assays typically do not measure antibody affinity (e.g. strength of interaction between a single antigen binding site and a single antigenic determinant) and fine specificity (e.g. the ability of the immune response to interact with individual antigens.), which may be critical for inhibitory activity. At present, functional assays to evaluate inhibitory effects during *P. falciparum* sporozoite invasion require primary human hepatocytes and freshly isolated sporozoites from salivary glands of infected mosquitoes. A major problem of malaria vaccine development is the absence of assays to correlate *in vitro* and *in vivo* protection. The value of current assays can only be estimated until the results are confirmed with clinical efficacy of vaccine candidates [6]. The aim of the cantilever based assay is to measure antibody specificity towards the UK-39 vaccine candidate in a label-free manner. This could lead to a better understanding of the immunology of the parasite and reduce redundancy within vaccine development.

A key parameter for selecting vaccine candidates is the cross reactivity of elicited antibodies with the native target antigen on the cell surface of the parasite. The vaccination triggers the immune response and ideally, the elicited antibodies exhibit a strong reactivity

including a strong affinity and fine specificity towards the target antigen. The UK-39 peptide has structural and antigenic similarity with the native repeat region of the key sporozoite vaccine antigen circum-sporozoite protein (CSP) [1]. This vaccination candidate target is the sporozoites stage of the malaria live cycle (see section 1.1.2). Hence, a successful pre-erythrocyte vaccine would break the live cycle at an early stage in the human host by blocking invasion of malaria sporozoites into the liver cells [7].

UK-39 delivered by influenza virosomes has been investigated in a phase Ib malaria vaccine trial in a population of 50 malaria semi-immune (developed a partially protective immunity) individuals at the Ifakara Health Institute in Bagamoyo, Tanzania [8]. The endpoint titer determined by ELISA (see section 1.2.2) specific for the Apical membrane antigen (AMA, a leading candidate antigen for inclusion in a subunit vaccine, e.g. containing the antigenic parts of the pathogen) [9, 10] and UK-39 peptide was significantly higher compared to the control group.

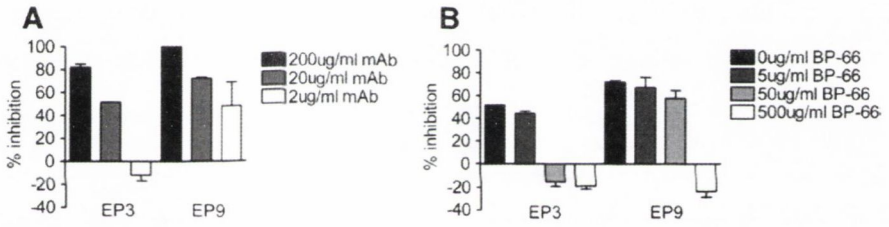

Figure 61: Hepatocyte invasion inhibition by anti-UK-39 monoclonal antibodies EP3 and EP9. A) Shown is the mean percentage of inhibition compared to a PBS control ± SD for duplicates. B) Competition of invasion inhibition by increasing concentrations of PB-66 peptide (a derivative of UK-39). Inhibitory monoclonal antibodies were used at a constant concentration of 20 µg ml^{-1}. (Taken from Okitsu *et al.*, [1]).

The data obtained by ELISA from previous studies indicate that there is a strong cross reactivity between the UK-39 binding antibodies EP3 and EP9 and *P. falciparum* sporozoite specific antibody SP3 [1]. The cross reactivity between the UK-39 synthetic peptide and monoclonal (a single pure type) UK-39 binding antibodies EP3 and EP9 (immunogen UK-39) (Figure 61) and monoclonal SP3 antibodies (immunogen *P. falciparum* sporozoites) was assessed by a cantilever assay operated either in static or dynamic mode.

6.1.2 Cantilever Surface Modification

The cantilever surface has to be rendered into a specific bio-recognition surface for the study of the cross reactivity of the different antibodies with the UK-39 peptide. Therefore, a method to anchor UK-39 synthetic peptides and AMA peptides on the cantilever surface is needed and an immobilisation strategy for the antibodies on the cantilever surface has to be selected. The immobilisation process of the synthetic peptides and antibodies must preserve the biological activity of the molecules. A reproducible and reliable method for the conversion of the gold coated cantilever into a biosensor is the use of self-assembled monolayers (SAMs). Due to the control over the properties of the interface at the molecular scale of SAMs, they are used as models for studying protein interactions, such as cell adhesion studies and protein adsorption [11-13]. SAMs have been utilised to modify the properties of sensor surfaces such as cantilever sensors [14-17], SPR [18, 19] or QCM [20, 21] sensors.

The general structure of a SAM made of alkanethiols is shown in Figure 62. The alkanethiols spontaneously assemble in a single layer on a gold surface until a stable structure of minimum energy is achieved [22]. By selecting specific chemical head-groups, such as hydroxyl groups for hydrophilic surfaces or methyl-terminated groups for hydrophobic surfaces, the surface properties of the SAM can be controlled with subsequent covalent anchoring of desired proteins [23]. This allows for specific interactions with the analyte under study while minimising, ideally, inhibition of non-specific protein adsorption.

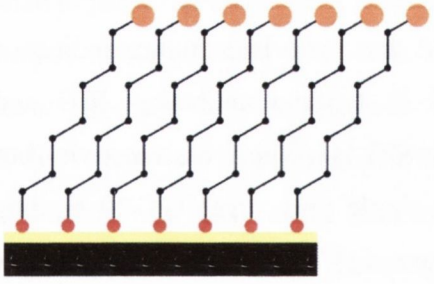

Figure 62 Schematic of an ideal self-assembled monolayer on a gold-coated silicon surface, not drawn to scale. The alkyl chain (black dots) functions as a spacer between the functional terminal head group (amber) and the sulfydryl (R-SH) group (red). The organic interface at the terminal head group determines the surface properties. The interface defined by the alkyl chain has a well-defined thickness depending on the amount of carbon atoms and acts as a physical barrier.

The formation of a SAM occurs by a spontaneous chemical reaction between the sulfydryl group and the gold surface, as the system approaches equilibrium [24]. The alkyl chain length determines the order of the SAMs; short alkyl chains (less than 8 carbons) lack adequate non-covalent interactions (e.g. hydrogen bonds, electrostatic and van der Waals forces) between the alkyl chains to produce well-ordered monolayers. Nonetheless, using very long spacer molecules for a SAM, the monolayer will be less ordered and can affect the sensing performance by decreasing the sensitivity [23, 25].

SAMs are utilised to avoid non-specific adsorption of biomolecules (biofouling) onto surfaces. A common way to induce anti-fouling SAM is to employ molecules with a poly(ethylene glycol) (PEG) as a head-group [26], the well-established protein-repellent properties of PEG renders the SAM surface into an antifouling surface [27-30].

Poly(L-lysine)-graft-poly(ethylene glycol) (PLL-*g*-PEG) is used to protect the silicon surfaces of the cantilevers from biofouling. PLL-*g*-PEG is a graft copolymer consisting of PEG chains grafted onto a PLL polycationic backbone [31]. The copolymers spontaneously adsorb from aqueous solutions onto negatively charged surfaces via electrostatic interactions [32]. The fast and stable immobilisation of the graft on negatively charged surfaces is facilitated by the positive charges of the protonated primary amine groups of the PLL backbone in a neutral aqueous environment. PLL-*g*-PEG has been employed in various applications for modification of biosensor interfaces [33-35].

6.2 Static Mode Study

To study the reactivity of the UK-39 synthetic peptide with the different antibodies, the peptide has to be immobilised on the cantilever surface. The subsequent interaction of the peptide with the antibodies under study will lead to a change in surface stress, hence a deflection of the cantilevers. To exclude external factors, differential read-out of the nanomechanical response of the cantilevers is mandatory. Therefore, reference cantilevers should have a similar surface as the probe cantilever but should not interact with the analyte under study. Hence, a peptide similar to the UK-39 has to be selected as a reference.

AMA synthetic peptides have similar properties to the UK-39 peptides and are therefore selected as reference peptides. The EP3 and EP9 antibodies elicited by the UK-39 peptides are specific for the UK-39 and do not interact with the AMA peptide [36]. Hence, the

cantilevers surfaces will be functionalised with UK-39 peptides as sensing sensors and AMA peptides as reference sensors.

6.2.1 Materials & Methods

6.2.1.1 Materials

Silicon cantilever arrays (IBM Research Laboratory, Rüschlikon, Switzerland) with eight cantilevers per array were used for all measurements. The cantilevers feature a thickness of 1 µm, a length of 500 µm, a width of 100 µm and a spring constant of 0.05 Nm^{-1}. The cantilevers were set on a 250 µm pitch and cantilevers from the same wafer were used for all experiments. All chemicals were purchased from Sigma-Aldrich (Ireland Limited, Arklow, Wicklow, Ireland) unless stated otherwise.

6.2.1.2 Dynamic Light Scattering Measurements

Dynamic light scattering (DLS) is a useful technique to evaluate particle size and size distribution of proteins in solution [37]. The size and distribution of UK-39 peptides and AMA peptides in PBS have been analysed to assess an immobilisation strategy.

DLS determines the velocity distribution of particles moving under the Brownian motion by measuring dynamic fluctuations of intensity of scattered light. The decay time of these fluctuations is inversely proportional to the diffusion coefficient of the particles under study. Applying the Stokes-Einstein formula, Equation (35), the particle size (hydrodynamic radius R_h) can be calculated:

$$R_h = \frac{k_b T}{6\pi\eta D} \tag{35}$$

With k_b the Boltzmann constant, T the temperature, η the dynamic viscosity of the buffer and D the diffusion coefficient obtained by the DLS measurement. The diffusion coefficient D is obtained from the relation between the scattering vector, the wavelength of the laser light, the scattering angle and the time-dependent correlation function of the scattered light the decay time [38].

The size and size distribution of PE conjugated UK-39 and AMA peptides in PBS have been determined using a size analyser (Zetasizer Nano ZS; Malvern Instruments Ltd, Malvern, United Kingdom). Different concentrations shown in Table 4 of peptides in PBS, pH 7.4 at 25 °C have been measured prior to and after filtration (0.22 µm Millex® syringe

filter units; Sigma Aldrich Ireland Limited, Arklow, Wicklow, Ireland) and analysed (Zetasizer Software 7.10; Malvern Instruments Ltd, Malvern, United Kingdom).

Table 4: Concentrations of the UK-39 and AMA peptides in PBS, pH 7.4 for the size analysis

Sample	mg ml^{-1}	mg ml^{-1}	mg ml^{-1}
UK-39	0.1	0.05	0.02
AMA	0.1	0.05	0.02

6.2.1.3 Cantilever Functionalisation

Self-assembled alkanethiols act as hydrophobic SAMs on the gold surface, the hydrophobic surface of the SAM allows for the formation of a phospholipid containing bilayer. The alkanethiols SAM maximises hydrophobic interactions and the PE conjugated UK-39 and AMA peptide vesicles fuse to the SAM, resulting in a stable bilayer on the cantilever surface. This method is well-established to render a gold surface into a biomimetic surface [39-44]. It is believed that the hydrophobic effect is the driving force for the self-assembly on the SAM by reducing the free energy of the alkanethiols water interface by the formation of the bilayer [45]. It has been shown, that cantilevers can be used to detect changes in the bilayer structure by injection of membrane-interactive polypeptides [46].

In addition, the silicon backside of the cantilever has to be protected from fusion of the UK-39 and AMA peptides and prevent protein adsorption in general. The formation of a PLL-*g*-PEG SAM allows the rendering of the silicon surface of the cantilevers into a protein repellent surface due to the PEG head group of the SAM formation molecule.

The cantilever array was cleaned according to the protocols described in Appendices B.1.1, B.1.2 and B.1.3 prior to gold coating as described in section 5.3. The gold layer on the cantilevers was activated according to the protocol in Appendix B.1.5. An alkanethiol SAM formed directly on gold surfaces renders the sensor surface into a hydrophobic surface. Therefore, the complete cantilever array was immersed in a 1 mM ethanolic solution of 1-octadecanethiol in a 200 µl Eppendorf tube for 60 minutes at room temperature. A schematic of the functionalisation steps is shown in Figure 63 A. The

formation of the biorecognition layer on the surface of individual sensors in capillaries is crucial for obtaining a clear and reproducible sensor response. This is the most important step in the cantilever assay technology.

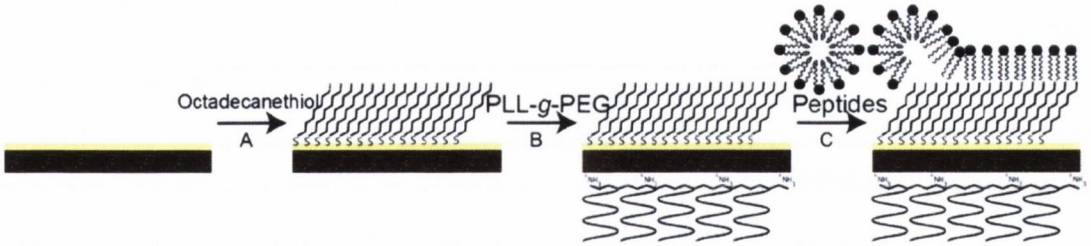

Figure 63: Schematic representation of the functionalisation steps of the gold coated cantilever, not drawn to scale. A) The cantilever array with the cleaned and activated gold surface is immersed completely in a 1 mM ethanolic solution of octadecanethiol to form a hydrophobic SAM. B) By immersion of the entire cantilever array into a PLL-*g*-PEG solution, a SAM on the silicon surface is formed to prevent non-specific adsorption of proteins onto the backside of the cantilevers. C) By adding the solutions containing the peptides (UK-39 and AMA, respectively) to the self-assembled alkanethiols using the capillary method, monolayers of self-assembled phospholipid/alkanethiol bilayer were formed.

After formation of the octadecanethiol SAM, the cantilever array was rinsed with ethanol for 2 minutes, followed by a bath in nanopure water for 2 minutes and finally transferred into HEPES buffer for 5 minutes. To render the backside of the cantilevers into a protein repellent surface, the cantilever array was incubated in a 200 µl Eppendorf tube with 0.25 mg ml^{-1} PLL-*g*-PEG (PLL(20)-*g[3.5]*- PEG(5); SuSoS AG, Dübendorf, Switzerland) in 10 mM HEPES, pH 7.4 for 30 minutes at room temperature (Figure 63 B). This forms a SAM on the silicon oxide surface which has been shown to be highly effective at preventing non-specific adsorption of proteins in an aqueous environment [29, 31]. The cantilever array was rinsed with 10 mM HEPES, pH 7.4 and rinsed again with 10 mM phosphate buffered saline (PBS), pH 7.4.

To form a phospholipid-alkanethiol bilayer on the alkanethiols SAM (Figure 63 C), the cantilever array was mounted on the capillary functionalisation device as described in section 5.4 and the sample reservoir for the different capillaries were filled with the solutions containing the synthetic peptides according to Table 5.

Table 5: Functionalisation of cantilever array

Cantilever	Peptides (0.02 mg ml^{-1} in PBS)
1,3,5,7	AMA
2,4,6,8	UK-39

The cantilevers with the self-assembled alkanethiols monolayer were left in contact with the solution containing UK-39 peptides or AMA peptides in the capillary functionalisation device for 60 minutes. This results in the formation of a phospholipid-alkanethiol bilayer by fusion of the vesicles. After the functionalisation, the cantilever array was mounted immediately in the measurement chamber in PBS.

6.2.1.4 Experimental Protocol

For the bilayer-peptide-antibody experiment, the second generation of the developed measurement chamber was used. The measurement chamber is shown in Appendix A.2.3. This setup incorporates an external analytical injection loop valve (Analytical Injection Loop Valve D UNI; ECOM spol. s r.o. Prague, Czech Republic) together with an external 50 µl stainless steel sample loop (54294000; ECOM S.R.O., Prague, Czech Republic) because of the lack of the injection port of the measurement chamber. The injection loop valve is mounted inside the temperature-regulated box to allow the sample temperature to equilibrate prior to injection. Therefore, prior to the experiment, the measurement chamber, injection loop and all the fluidic components had to be cleaned. The device was flushed with nanopure water while PBS buffer was degassed to avoid the introduction of air bubbles during the experiment. The buffer was then loaded into the syringe and the measurement chamber was flushed at least 3 times. Then the functionalised cantilever array was mounted inside the measurement chamber.

The temperature controlled laser had to be turned on for at least 15 minutes prior to recording the nanomechanical response of the cantilever to maintain an optimum operating current and temperature. As soon as the temperature inside the measurement chamber reached the set-point, the following steps were executed. The static mode was recorded for each cantilever every 15 seconds and the temperature was regulated every 10 seconds.

First, a peltier test (8 seconds with 0.75 V) was performed. The peltier module allows a heat pulse to be applied to the liquid chamber and a subsequent calibration of the mechanical response of the individual cantilevers within the array. After re-establishing a stable temperature, the cantilevers were allowed to equilibrate for 45-60 minutes to acquire a baseline for 30 minutes without a flow of liquid through the measurement chamber.

Secondly, 75 µl of PBS buffer was injected (10 µl min^{-1}) into the measurement chamber to monitor the response of the reference and sample cantilevers to the introduction of fresh buffer in the liquid cell. After the buffer injection, the cantilevers were allowed to equilibrate for 45 to 60 minutes until a stable baseline is reached again. In the meantime, the analytical injection loop valve with the external sample loop (50 µl, 54294000; ECOM S.R.O., Prague, Czech Republic) was primed with the solution containing the antibodies (0.01 mg ml^{-1} in PBS).

Thirdly, the injection loop was switched manually to the injection position and the syringe pushed the buffer together with the sample into the measurement chamber. The total amount of the liquid pushed to the measurement chamber was 75 µl (10 µl min^{-1} for 7.5 min). The raw data was analysed using NOSEtools [47] and subsequently processed using Origin Pro 9.1 (OriginLab Corporation, Northampton, MA, USA).

6.2.2 Results

6.2.2.1 Dynamic Light Scattering Measurements

The structure and size of the PE conjugated peptides in PBS were determined by dynamic light scattering to assess an immobilisation strategy. The size distribution shows that there were two particle size populations for both peptides in solution independent of the concentration as shown in Table 6. The first population features a diameter of around 20 nm and the second a diameter of 300 nm for the UK-39 peptides and 900 nm for the AMA peptides.

Table 6: Average size distribution by intensity after filtration for UK-39 and AMA in PBS

Sample (in PBS)	Average Size (d.nm)	Standard Deviation (d.nm)
UK-39 (0.02 mg ml^{-1})	20.4	4.5
	321.4	110.8
UK-39 (0.05 mg ml^{-1})	22.3	5.2
	350.8	132.2
UK-39 (0.1 mg ml^{-1})	21.7	4.3
	332.2	124.8
AMA (0.02 mg ml^{-1})	21.8	5.6
	984.5	234.2
AMA (0.05 mg ml^{-1})	19.5	4.3
	887.2	254.2
AMA (0.1 mg ml^{-1})	23.1	6.2
	965.7	241.8

To remove the larger population, the peptide solutions were filtered (0.22 µm Millex® syringe filter units; Sigma Aldrich Ireland Limited, Arklow, Wicklow, Ireland) and measured again. However, this filtration did no remove the large population as shown in Figure 64. Hence, the larger population might be an aggregate of the smaller population.

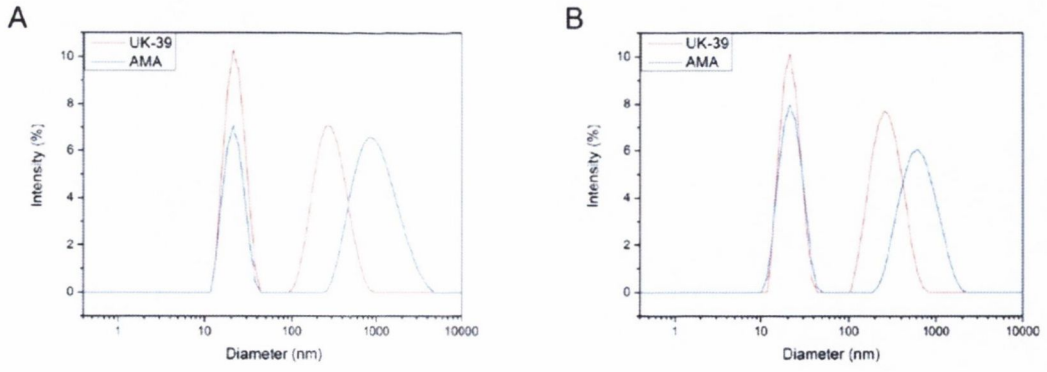

Figure 64: Size distribution by intensity measured by dynamic light scattering. A) UK-39 (0.02 mg ml^{-1}) and AMA (0.02 mg ml^{-1}) distribution prior to filtration. B) UK-39 (0.02 mg ml^{-1}) and AMA (0.02 mg ml^{-1}) size distribution after filtration through a 0.22 µm filter. The larger populations of the peptide is still present after filtration, indicating that the peptides form spontaneously bigger aggregates.

6.2.2.2 Injection of Buffer

To exclude false signals based on the buffer exchange in subsequent sample injections, the response of each functionalised cantilever array towards an injection of PBS buffer only had to be examined. The average response of 4 cantilevers functionalised with UK-39 peptides and 4 cantilevers functionalised with AMA peptides as described in Table 5 is shown in Figure 65 as an example for a properly functionalised cantilever array.

If the buffer injection resulted in random responses of the cantilevers, the subsequent result observed due to antibody samples injection had to be excluded from the data analysis. The obtained signal of the cantilever cannot be linked to the interaction of the antibodies with the bio-recognition layer uniquely; as a result those experiments have to be discarded. The subsequent injection of antibodies was only analysed and considered as a successful experiment, if there was a negligible difference between the reference and probe cantilevers visible after a PBS buffer injection as shown in Figure 65. The large downward bending of the cantilevers is due to a force applied to the top surface of the cantilevers by the flow of the buffer through the measurement chamber (the hatched area in Figure 65).

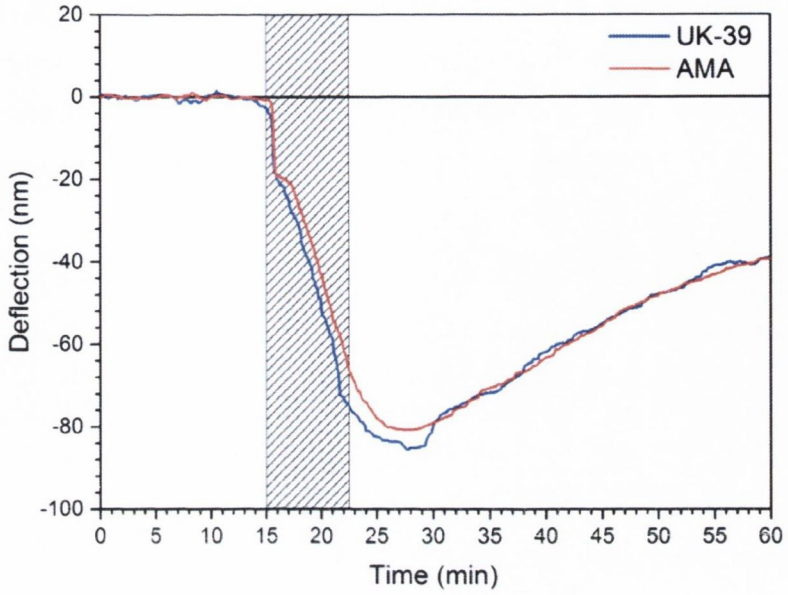

Figure 65: Average response of the cantilevers to the injection of buffer. The hatched area indicates the time of PBS buffer injection (75 µl, 10 µl min^{-1}) into the liquid cell of the measurement chamber to investigate the behaviour of the functionalised cantilevers. Blue data correspond to the average response of the 4 probe cantilevers (UK-39), the red data correspond to the average response of the 4 reference cantilevers (AMA peptides) of the cantilever array. After the injection, there is a negligible difference between the reference and probe cantilevers visible, indicating that there is no non-specific interaction or surface stress evolving between the bio-recognition layers and PBS buffer.

6.2.2.3 Injection of SP3 Antibodies

The heat pulse applied (8 seconds with 0.75 V) to the fluid cell inside the measurement chamber by the peltier element resulted in an increase of the temperature by ca. 1.4 °C, thus resulting in a deflection of the cantilevers. To compensate for the different maximum deflections of the nanomechanical transducer, the signal was normalised to calibrate the response of each cantilever to the mean of the maximum deflection. The calibration factor for each cantilever was used for all subsequent analyses of the bending during the experiment.

Figure 66 shows the averaged, baseline corrected and calibrated data from a cantilever array functionalised with UK-39 and AMA peptides according to Table 5. The hatched area corresponds to the time when the buffer is flowing through the measurement chamber for injection and the grey area corresponds to the period when the target antibody is

present in the fluid cell. There is a large downward bending of the cantilevers observable when the injection of the SP3 antibodies takes place (the hatched area in Figure 66). This bending of the cantilever is due to a force applied to the top surface of the cantilevers by the flow of the liquid through the measurement chamber. However, once the antibodies reached the fluid cell (17.5 minutes) they start to bind immediately to the sensor surface, resulting in a different deflection of the probe cantilevers.

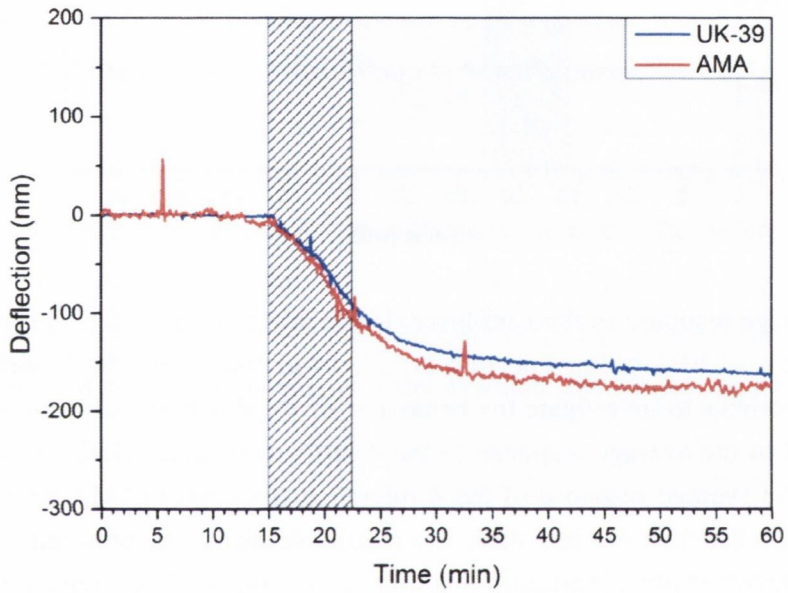

Figure 66: Averaged, baseline corrected and calibrated data of a functionalised cantilever array according to Table 5. The white area corresponds to the time where there was no flow and a stable baseline was acquired. The hatched area indicates the time of the SP3 antibody sample injection (10 µl min^{-1}) into the liquid cell of the measurement chamber and the grey area indicates the presence (no flow) of SP3 antibodies in the liquid cell. Blue data correspond to the average response of the 4 probe cantilevers (UK-39 peptides), the red data correspond to the average response of the 4 reference cantilevers (AMA peptides) of the cantilever array. By subtracting the reference data (AMA) from the probe data (UK-39) the average differential deflection is obtained.

Graph of the average differential deflection of the probe cantilevers vs. time due to the injection of EP3 antibodies

When the average reference response (e.g. AMA functionalised cantilever) is subtracted from the probe response (e.g. UK-39 functionalised cantilever), the average response for each cantilever array is obtained as shown for two arrays in Figure 67 (blue and red data).

The average deflection of the cantilevers after the injection of the SP3 antibodies is 26 ± 8 nm and is shown in black in Figure 67.

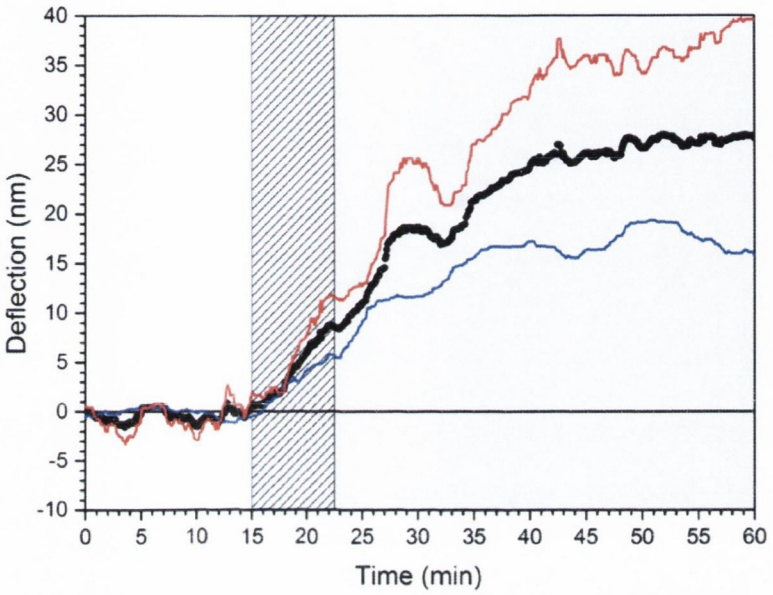

Figure 67: Graph of the average differential deflection of the probe cantilevers vs. time due to the injection of SP3 antibodies. Blue data correspond to the average differential deflection of one array: 4 probe cantilevers (UK-39) vs. 4 reference cantilevers (AMA peptides). The red data set originates from a second array with the same experimental setup, the black data is the average of both cantilever arrays. The hatched area indicates the time of the SP3 antibody sample injection (10 µl min^{-1}) into the liquid cell of the measurement chamber and the grey area indicates the presence (no flow) of SP3 antibodies in the liquid cell. The cantilevers of each array have been functionalised according to Table 5. The differential signal is obtained by subtracting the deflection of the reference cantilever (AMA functionalised) from the probe cantilever (UK-39 functionalised).

6.2.2.4 Injection of EP3 Antibodies

The same procedure as described in section 6.2.2.3 to obtain the calibration factor for each cantilever for the normalisation of the nanomechanical response was performed. The average differential deflection of two cantilever arrays with probe cantilevers functionalised with the UK-39 peptide and the reference cantilevers with AMA peptides due to injection of EP3 antibodies is shown in Figure 68. The differential signal is obtained by subtracting the deflection of the reference cantilevers functionalised with AMA peptide from the probe cantilever functionalised with UK-39 peptides. The red data correspond to the average differential deflection of a first measurement and the blue data correspond to

the average differential deflection of a second experiment. The black data is the average of the two measurements, e.g. 8 cantilevers as probe sensors and 8 cantilevers as reference sensors.

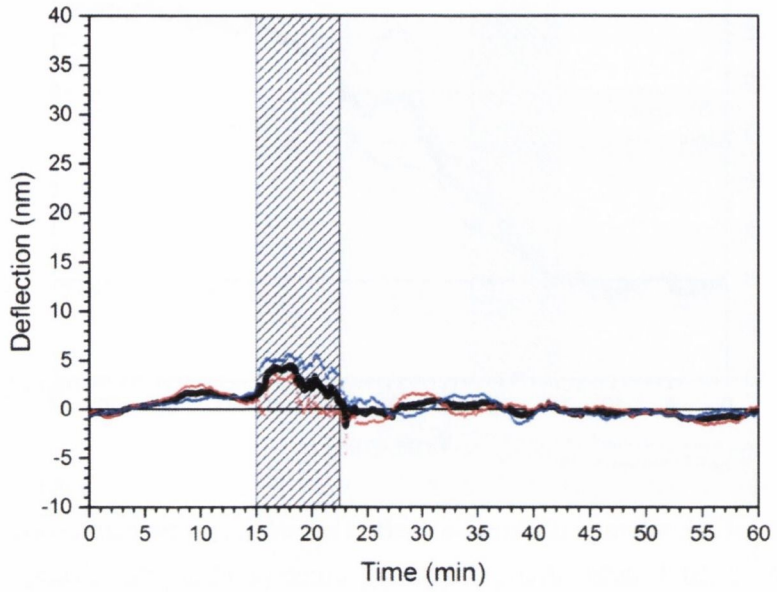

Figure 68: Graph of the average differential deflection of the probe cantilevers vs. time due to the injection of EP3 antibodies. Blue data correspond to the average differential deflection of one array: 4 probe cantilevers (UK-39) vs. 4 reference cantilevers (AMA peptides). The red data set originates from a second array with the same experimental setup, the black data is the average of both cantilever arrays. The hatched area indicates the time of the EP3 antibody sample injection (10 µl min^{-1}) into the liquid cell of the measurement chamber and the grey area indicates the presence (no flow) of EP3 antibodies in the liquid cell. The cantilevers of each array have been functionalised according to the setting from Table 5. The differential signal is obtained by subtracting the deflection of the reference cantilever (AMA functionalised) from the probe cantilever (UK-39 functionalised).

6.2.2.5 Injection of EP9 Antibodies

The same procedure as described in section 6.2.2.3 to obtain the calibration factor for each cantilever for the normalisation of the nanomechanical response was performed. The average differential deflection of the probe cantilever functionalised with the UK-39 peptide due to injection of EP9 antibodies is shown in Figure 69. The differential signal is

obtained by subtracting the deflection of the reference cantilevers functionalised with AMA peptides from the probe cantilevers functionalised with UK-39 peptides. The average deflection of the cantilevers after the injection of the EP9 antibodies is 6 ± 2 nm.

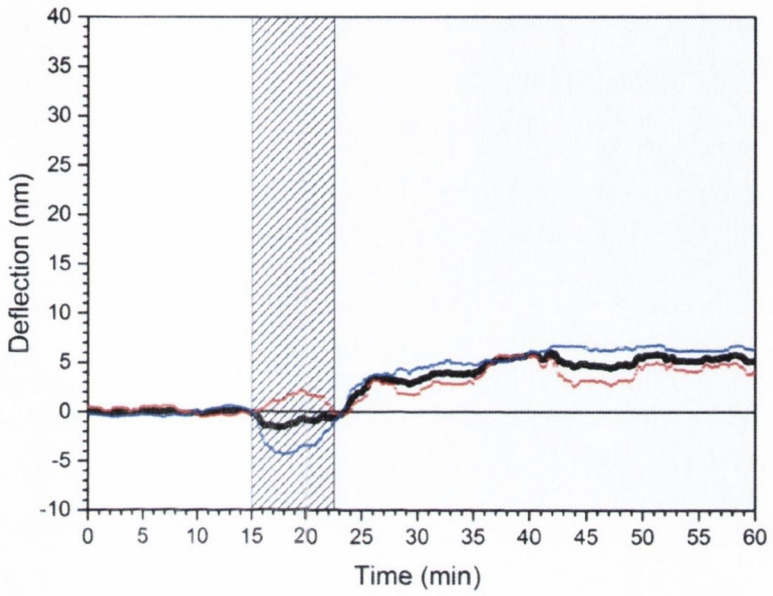

Figure 69: Graph of the average differential deflection of the probe cantilevers vs. time due to the injection of EP9 antibodies. Blue data correspond to the average differential deflection of one array: 4 probe cantilevers (UK-39) vs. 4 reference cantilevers (AMA peptides). The red data set originates from a second array with the same experimental setup, the black data is the average of both cantilever arrays. The hatched area indicates the time of the EP9 antibody sample injection (10 µl min^{-1}) into the liquid cell of the measurement chamber and the grey area indicates the presence of EP9 antibodies in the liquid cell. The cantilevers of each array have been functionalised according to the setting from Table 5. The differential signal is obtained by subtracting the deflection of the reference cantilever (AMA functionalised) from the probe cantilever (UK-39 functionalised).

6.2.3 Discussion

The static mode measurements indicate that the UK-39 peptide has a higher reactivity to the *P. falciparum* sporozoite specific antibody than to the UK-39 binding antibodies EP3 and EP9. The injection of SP3 antibodies leads to an average deflection of the cantilevers of 26 ± 8 nm. In contrast, there is no significant differential deflection of the cantilevers visible in response to the injection of the UK-39 binding antibodies. In the case of the EP3

antibodies an average deflection of 0 ± 3 nm (~10 times smaller than the SP3 antibody deflection) is observed and for the EP9 antibodies a deflection of 6 ± 3 nm (~5 times smaller than the SP3 antibody deflection).

The small or non-existent differential deflection of the cantilevers in response to the injection of the UK-39 binding antibodies could be explained as follows: either there is no reactivity of the EP3 antibodies with the UK-39 peptides or they feature the same reactivity with the UK-39 and AMA peptides resulting in a zero differential deflection. An interaction of the UK-39 peptides with the SP3 antibodies is expected but not stronger than the one of the UK-39 binding antibodies, because the UK-39 peptide closely resembles the natural conformation of the major surface protein of the sporozoite and the immunogen of the SP3 antibodies are the *P. falciparum* sporozoites.

The bending of the cantilevers observable as long as the syringe pump is switched on is based on the flow of the liquid across the cantilevers. This bending is in most injections observable as a random bending of the cantilevers that cannot be completely compensated by the differential analysis but it vanishes when the flow is stopped. Therefore, the data acquired during the time of any injection of liquid through the measurement chamber is excluded from the data analysis.

6.3 Dynamic Mode Study

To study the reactivity of the UK-39 synthetic peptide with the different antibodies utilising the dynamic mode of the device, the antibodies were immobilised on the cantilever surface. The subsequent interaction of the immobilised antibodies with the injected UK-39 synthetic peptide leads to a measurable mass uptake, hence a change in resonance frequency of the cantilever. To exclude external factors, differential read-out of the nanomechanical response of the cantilevers is mandatory.

6.3.1 Materials & Methods

6.3.1.1 Materials

Cantilever arrays as described in section 6.2.1.1 were used for the dynamic mode study. The arrays chosen had thicknesses of 1 µm, with lengths and widths of 500 µm and 100 µm respectively. All chemicals were purchased from Sigma-Aldrich (Ireland Limited, Arklow, Wicklow, Ireland) unless stated otherwise.

6.3.1.2 Cantilever Functionalisation

The cantilever array was cleaned according to the protocols described in Appendix B.1 prior to gold coating as described in section 5.3. The gold layer on the cantilevers was activated according to the protocol in Appendix B.1.5. To immobilise the antibodies on the cantilever surface a N-hydroxysuccinimide (NHS)-terminated SAM was used. The covalent anchoring of proteins containing amino-goups to the SAM is simple, rapid and reproducible [48]. Primary amines on lysine residues and the N-terminus of each polypeptide chain of the antibodies react with the NHS-activated carboxylic acid groups of the SAM and immobilise the antibodies covalently to the cantilever surface randomly due to multiple primary amines of the antibodies.

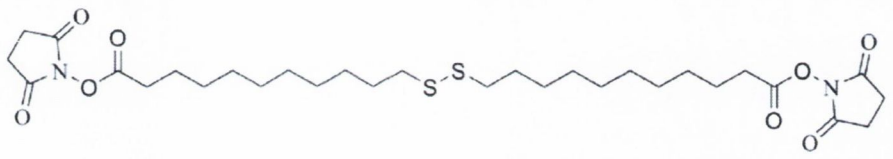

Figure 70: Structural formula of dithiobis(succinimidyl undecanoate) (DSU). The disulphide undergoes S-S bond dissociation and adsorbs on the gold surface as two separate alkanethiol species forming a NHS-SAM [48].

To obtain a NHS-terminated SAM, the gold coated cantilever array was immersed in a 1 mM dithiobis(succinimidyl undecanoate) (DSU) solution (chemical structure shown in Figure 70) (D537-10; Dojindo EU GmbH, Munich, Germany) in dioxane 1,4 in a 0.2 ml Eppendorf tube for 45 minutes at room temperature. The functionalisation steps for the antibody immobilisation are shown in Figure 71.

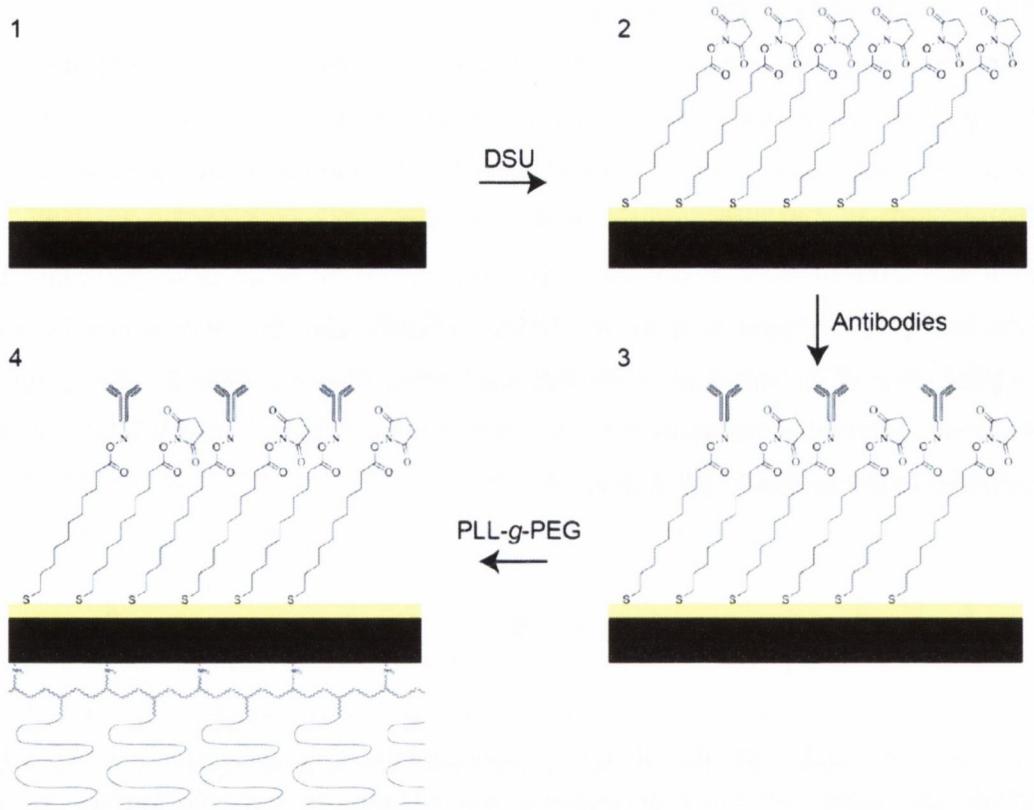

Figure 71: Schematic representation of the functionalisation steps of the gold coated cantilever, not drawn to scale. The cleaned and activated gold surface of the cantilever (1) is immersed in a 1 mM dithiobis(succinimidyl undecanoate) (DSU) in dioxane 1,4 to form a NHS-terminated SAM (2). By adding the antibodies (SP3, EP3 and EP9), the primary amines of the antibodies react with the NHS-activated carboxylic acid groups of the SAM and immobilise the antibodies covalently to the cantilever surface (3). A PLL-*g*-PEG SAM on the silicon surface is formed to prevent non-specific adsorption of proteins onto the backside of the cantilevers (4).

After formation of the DSU SAM, the cantilever array was rinsed with dioxane and then with acetone and dried with nitrogen. The antibody immobilisation was performed immediately afterwards in the capillary functionalisation device for 30 minutes according to the setup shown in Table 7. To render the silicon surface of the cantilevers into a protein repellent surface, the functionalised cantilever array was immersed in a 200 µl Eppendorf tube with 0.25 mg ml^{-1} PLL-*g*-PEG (PLL(20)-*g[3.5]*- PEG(5); SuSoS AG, Dübendorf, Switzerland) in 10 mM HEPES [4-(2-hydroxyethyl)pipera-zine-1-ethanesulfonic acid, adjusted to pH 7.4 with 1M sodium hydroxide solution for 30 minutes at room temperature. This forms a SAM on the silicon oxide surface which has been shown to be highly effective at preventing non-specific adsorption of proteins in an aqueous

environment [29, 31]. The cantilever array was rinsed with 10 mM HEPES, pH 7.4 and rinsed again with 10 mM PBS, pH 7.4 for 2 minutes and finally mounted in the measurement chamber. As reference sensors, cantilevers with a SAM with protein repellent properties were used. A hydroxyl terminated SAM was formed on the gold surface of the reference sensors to passivate the surface against nonspecific binding [49]. The functionalisation setup is shown in Table 7.

Table 7: Functionalisation setup of the cantilever array for the immobilisation of antibodies

Cantilever	Antibody (0.01 mg ml^{-1} in PBS)
1,5	SP3
2,6	EP3
3,7	EP9
4,8	OH-SAM (in ethanol as a reference)

6.3.1.3 Experimental Protocol

For this experiment, the latest generation of the developed measurement chamber incorporating the sample injection port was utilised. Therefore, prior to the experiment, the measurement chamber and all the fluidic components had to be cleaned. The device was flushed with nanopure water while the operating buffer was degassed to avoid the introduction of air bubbles during the experiment. The buffer was then loaded into the syringe and the measurement chamber was flushed at least 3 times with 250 µl buffer. After filtration through a 0.22 µm filter (Millex® syringe filter units; Sigma Aldrich Ireland Limited, Arklow, Wicklow, Ireland) the sample UK-39 peptide in PBS (0.02 mg ml^{-1}) was loaded into the sample reservoir and the measurement chamber was primed. Then the functionalised cantilever array was mounted in the recessed pocket of the liquid cell.

The temperature controlled laser had to be turned on at least for 15 minutes prior to the recording of the nanomechanical response of the cantilever to maintain an optimum operating current and temperature. As soon as the temperature inside the measurement chamber reached the set-point, the following steps were executed. The dynamic mode was

recorded for each cantilever every 30 seconds and the temperature was regulated every 6 seconds.

After reaching a stable temperature within the measurement chamber, the cantilevers were allowed to equilibrate for 45-60 minutes to acquire a baseline for 30 minutes without a flow of liquid through the measurement chamber. Then, the syringe introduced 8 µl of PBS into the measurement chamber to monitor the response of the reference and sample cantilevers to the introduction of fresh buffer in the liquid cell. As shown in section 3.2.7 the injection of more than 6 µl exchanges the total volume of the liquid cell. After the buffer injection, the cantilevers were allowed to equilibrate again for 45 to 60 minutes until a stable baseline is reached.

Finally, 8 µl of the UK-39 peptide in PBS is introduced by the injection port and pushed into the liquid cell by the syringe pump with a flow rate of 10 µl min^{-1} for 36 seconds. The raw data was analysed and processed by the Peak Tracker algorithm of the LabVIEW code as described in section 2.3.

6.3.2 Results

The frequency spectra obtained from the cantilever measurements were processed using the Peak Tracker software described in section 2.3 to obtain the resonance frequency and the shift of the flexural resonance peak. Ultimately, based on the frequency shift, the additional bound mass on the cantilever surface was calculated based on the model presented in section 1.3.1.2. The response from the reference cantilevers functionalised with the hydroxyl terminated SAM was subtracted from the probe cantilevers to account for any non-specific adsorption of protein to the cantilever sensors and to compensate for any drift in the system.

Three resonance modes from each cantilever were recorded between 300 kHz and 650 kHz, corresponding to the 11^{th} (centre frequency of 354.290 kHz) and 12^{th} (443.405 kHz) and 13^{th} (545.010 kHz) flexural resonance modes, with 1000 points per frequency sweep (frequency resolution 350 Hz). An additional experiment was conducted where two resonance modes from each cantilever were recorded between 500 kHz and 750 kHz, corresponding to the 13^{th} (549.599kHz) and $14t^{h}$ (665.783 kHz), flexural resonance modes, with 1000 points per frequency sweep (frequency resolution 250 Hz). The amplitude spectra for the two experiments are given in Appendix A.6.

The differential frequency responses of the 11th and 12th flexural resonance mode from the probe cantilevers functionalised with the different antibodies are shown in Figure 72. The 13th flexural mode had to be excluded from the analysis due to a large weighted mean square error in the fitting process between the best nonlinear fit and Y values. There is a clear decrease in the frequency of the probe cantilevers functionalised with SP3 antibodies upon the injection of the UK-39 peptides. The other two probe cantilevers (EP3 and EP9 antibodies) show a fractional frequency decrease.

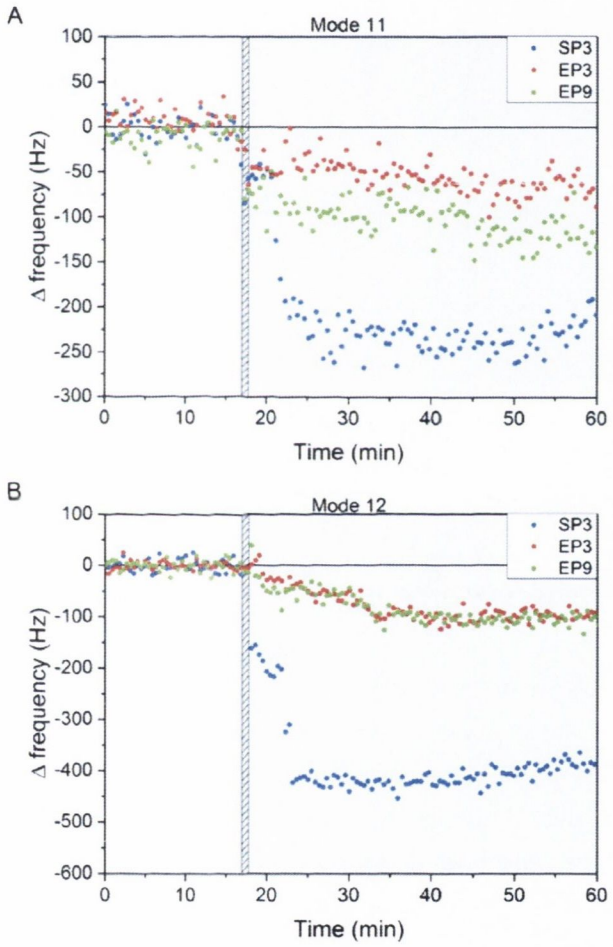

Figure 72: Graph of the baseline corrected and reference subtracted frequency shift of A) 11th flexural resonance mode and B) 12th flexural resonance mode of the different functionalised (SP3, EP3 and EP9 antibodies, respectively) cantilevers vs. time due to the injection of UK-39 peptides in PBS (0.02 mg ml^{-1}). The hatched area indicates the time of the injection (8µl, 10 µl min^{-1}) into the liquid cell of the measurement chamber and the grey area indicates the presence of UK-39 peptides in the liquid cell. By subtracting the reference data (hydroxyl-terminated SAM) from the probe data (SP3, EP3 and EP9 antibodies), any external influence can be excluded.

The average bound mass on the surface of the cantilevers was then extracted from the frequency spectra by processing the frequency data. Figure 73 shows the average mass uptake of the cantilevers based on the frequency response of the 11th and 12th flexural resonance modes. There is an average gain in mass of 285 ± 30 pg for the SP3 functionalised cantilevers, 65 ± 10 pg for the EP3 and 90 ± 15 pg EP9 for the functionalised cantilevers.

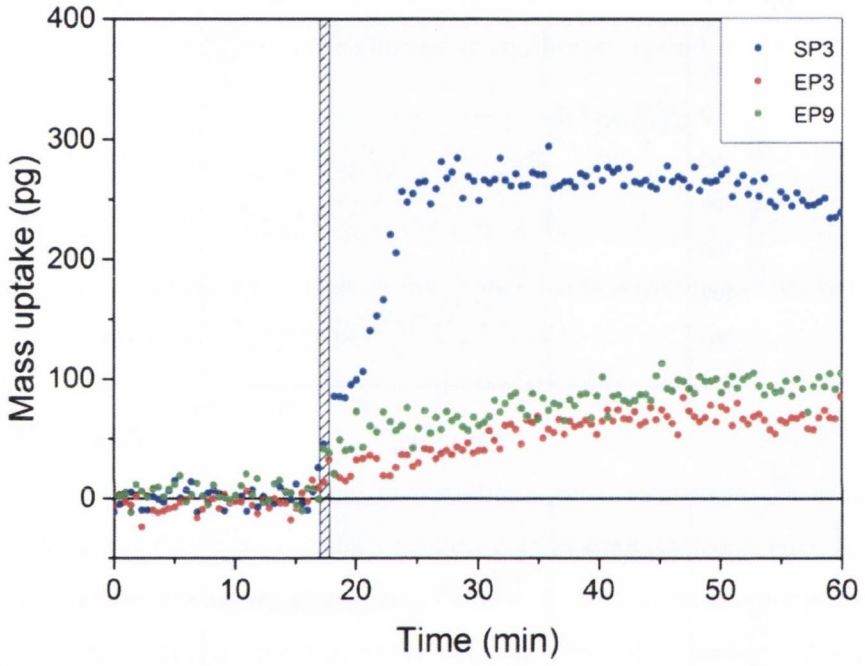

Figure 73: Graph of calculated average mass bound on the different functionalised (SP3, EP3 and EP9 antibodies) cantilevers vs. time due to the injection of UK-39 solution (0.02 mg ml^{-1}) based on the frequency response of the 11th and 12th flexural resonance modes. The left axis shows the bound mass to the cantilever surface. The hatched area indicates the time of the UK-39 peptides in PBS (0.02 mg ml^{-1}) injection (8µl, 10 µl min^{-1}) into the liquid cell and the grey area the presence of the UK-39 in the liquid cell. The frequency shifts (as shown in Figure 72) calculated by the Peak Tracker software are converted into the bound mass on the cantilever. There is an average mass gain of 285 ± 30 pg for the SP3 functionalised cantilevers and 65 ± 15 pg for the EP3 and 90 ± 15 pg EP9 functionalised cantilever observable.

The average differential frequency responses of the 13th and 14th flexural resonance modes from the probe cantilevers functionalised with the different antibodies are shown in Figure 74. There is a clear decrease in the average frequency of the probe cantilevers

functionalised with SP3 antibodies upon the injection of the UK-39 peptides. The EP3 functionalised cantilevers show the smallest change in resonance frequency, while the EP9 functionalised cantilever show a moderate change in resonance frequency.

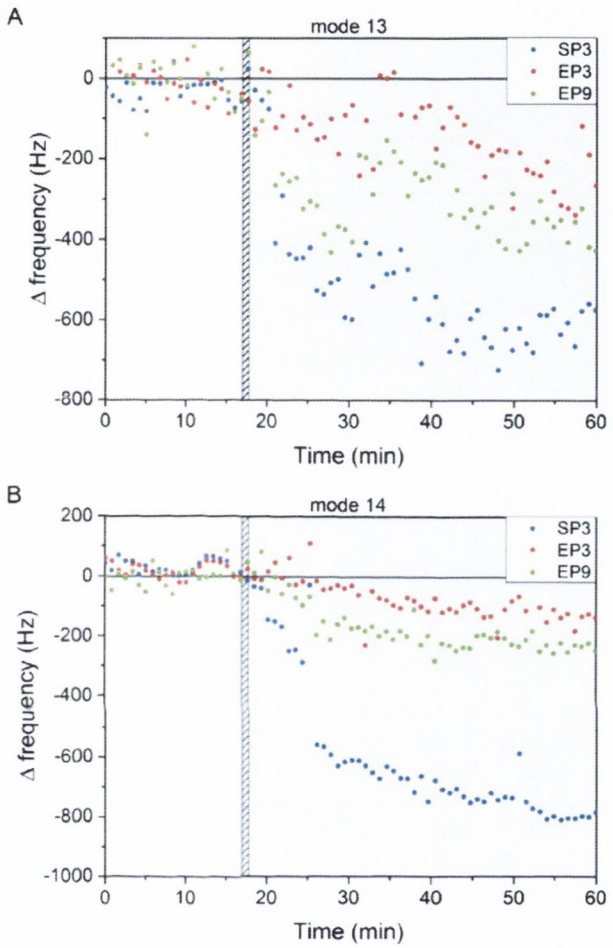

Figure 74: Graph of the baseline corrected and reference subtracted frequency shift of A) 13th flexural resonance mode and B) 14th flexural resonance mode of the different functionalised (SP3, EP3 and EP9 antibodies) cantilever vs. time due to the injection of UK-39 peptides (0.02 mg ml^{-1}). The hatched area indicates the time of the UK-39 peptide injection (8µl, 10 µl min^{-1}) into the liquid cell of the measurement chamber and the grey area indicates the presence of UK-39 peptides in the liquid cell. By subtracting the reference data (hydroxyl-terminated SAM) from the probe data (SP3, EP3 and EP9 antibodies), any external influence can be excluded. The frequency spectra acquired during the experiment was processed by the Peak Tracker software to obtain the resonance frequencies.

The average bound mass on the surface of the cantilevers was then extracted from the frequency spectra by processing the frequency data. Figure 75 shows the average mass

uptake of the cantilevers based on the frequency response of the 13th and 14th flexural resonance modes. There is an average mass uptake of 380 ± 30 pg on the SP3 functionalised cantilevers observable. The EP3 functionalised cantilever featured a mass uptake of 80 ± 40 pg at most and the EP9 functionalised cantilever a maximum mass uptake of 160 ± 25 pg.

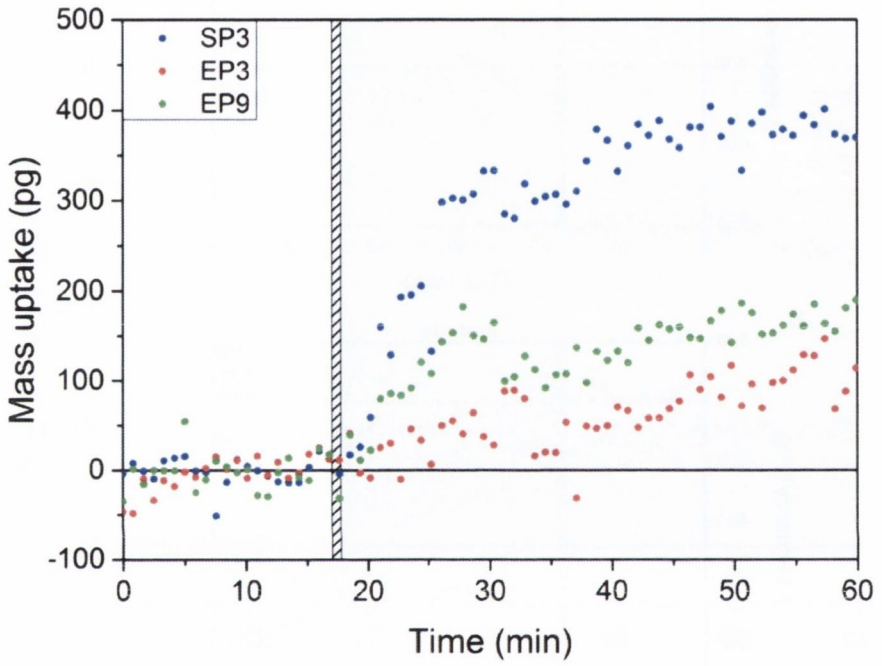

Figure 75: Graph of calculated average mass bound on the different functionalised (SP3, EP3 and EP9 antibodies, respectively) cantilevers vs. time due to the injection of UK-39 solution (0.01 mg ml^{-1}) based on the frequency response of the 13th and 14th flexural resonance modes. The left axis shows the bound mass to the cantilever surface. The hatched area indicates the time of the UK-39 peptide injection (8µl, 10 µl min^{-1}) into the liquid cell of the measurement chamber and the grey area the presence of the UK-39 in the liquid cell. The frequency shifts calculated by the Peak Tracker software are converted into the bound mass on the cantilever. There is an average mass gain of 380 ± 30 pg for the SP3 functionalised cantilevers, 80 ± 40 pg for the EP3 functionalised cantilevers and 160 ± 25 pg for the EP9 functionalised cantilevers.

Normalisation of the frequency shift of the experiments shown in Figure 72 and Figure 74 allows the comparison of the response of the different flexural resonance modes. The normalised frequency shift and the average for the SP3, EP3 and EP9 functionalised cantilevers are shown in Figure 76. It is visible, that the normalised responses of the

cantilevers are in line with each other, indicating that the frequency responses correlate with the mode number.

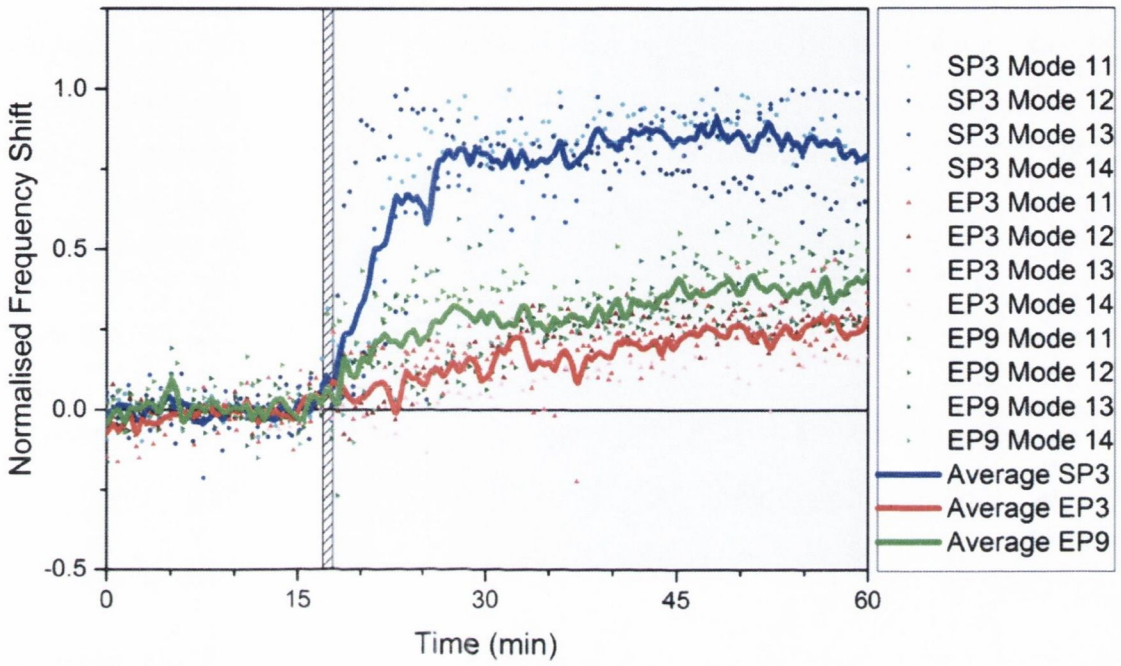

Figure 76: Normalised frequency shift of two cantilever arrays. The hatched area indicates the time of the UK-39 peptide injection (8µl, 10 µl min^{-1}) into the liquid cell of the measurement chamber and the grey area indicates the presence of UK-39 peptides in the liquid cell. The blue data correspond to the SP3, the red to the EP3 and the green to the EP9 functionalised cantilevers. The average shown is the average over the two measurements and different flexural resonance modes.

6.3.3 Discussion

The dynamic mode measurements indicate that the UK-39 peptide has a higher reactivity to the *P. falciparum* sporozoite specific antibody than to the UK-39 binding antibodies EP3 and EP9. The mass uptake is based on the additional buffer within the vesicles, which cannot diffuse around the sensor. The injection of UK-39 peptides leads to a mass uptake on the SP3 functionalised cantilever of up to 380 ± 30 pg. The EP3 functionalised cantilevers show a maximum mass uptake of 80 ± 40 pg and the EP9 functionalised cantilevers of 160 ± 25 pg. The reactivity of the EP3 antibodies to the UK-39 peptide is about a third of the reactivity of the SP3 antibodies and the reactivity of the EP9 antibodies a fifth of the SP3 reactivity. This indicates that fewer vesicles composed of UK-39

peptides have linked with the bio-recognition surface on the EP3 and EP9 functionalised cantilever than on the SP3 functionalised cantilever.

The normalisation of the frequency response of the different flexural resonance modes of the different measurements shows that the measurement is reproducible. The noise level of the higher modes is bigger due to the increase sensitivity of the higher modes and depends as well on the quality of the amplitude spectrum. It is possible that the fitting process cannot be completed, as this was the case for the 13^{th} mode for the first experiment. Thus, a part of a high noise level can be related to the quality of the tracked resonance peaks.

The model used to calculate the mass uptake is based on the assumption that the mass is evenly distributed over the entire surface of the cantilever [50]. The detection of a mass uptake is dependent on the position of the mass on the surface of the cantilever and is well documented in the literature [51-53]. Therefore, it is possible that masses positioned near a node of resonance will not result in a frequency shift and hence, will not be detected.

6.4 Conclusion

These experimental results indicate that it is possible to detect the reactivity of the malaria vaccine candidate UK-39 to different antibodies in a label free manner in a physiological environment. The subtraction of the response of the reference cantilevers from that of the probe cantilevers allows any non-specific binding of the peptides to be subtracted from the measurement so that only the response from the peptides-antibody interactions are examined.

The ability of the UK-39 peptide to react with SP3 antibodies has been shown by the static mode measurement confirmed by the dynamic mode measurement in which the SP3 functionalised cantilevers feature the maximum mass uptake and deflection. On the contrary, the UK-39 peptide shows the lowest reactivity towards the EP3 antibodies, indicated by the inexistent deflection of the cantilevers in the static mode measurements and the lowest mass uptake in the dynamic mode measurements. The EP9 antibodies feature a moderate reactivity towards the UK-39 peptide, a small deflection was observed in the static mode measurements and a medium mass uptake measured in the dynamic mode.

The low reactivity between the UK-39 peptide and the EP3 and EP9 antibodies was not expected because the UK-39 peptide is their immunogen. Hence, it was anticipated that the antibodies feature a strong specificity and reactivity towards the UK-39 peptide. The dynamic and static mode results show that the EP9 antibodies have minimally higher reactivity to the UK-39 peptide than the EP3 antibodies. The nanomechanical responses to the reactivity of the UK-39 peptide to the SP3, EP3 and EP9 based on the static and dynamic mode measurement are summarised in Table 8. The high cross-reactivity of the UK-39 peptide with the SP3 antibodies could be beneficial for the vaccine candidate. It shows that there is an interaction with antibodies elicited by different but similar antigens (e.g. *P. falciparum* sporozoites for the SP3 antibodies).

Table 8: Summary of the reactivity of the UK-39 peptide based on the nanomechanical responses of cantilevers operated in dynamic and static mode.

Antibody	Reactivity
SP3	high
EP3	low
EP9	moderate

The small mass uptake of the EP3 and EP9 functionalised cantilever and the minimal deflection of the cantilevers operated in static mode highlight the need for a proper reference cantilever. The proper functionalisation of the cantilevers is key for reproducible experiments.

In contrast to the findings presented here, the literature shows that SP3, EP3 and EP9 antibodies have a reactivity to the UK-39 peptide [1]. However, the reactivity of the antibodies is classified only into coarse categories: cross-reactive, weakly cross-reactive; and not determined. The three antibodies under investigation are all classified as cross-reactive. The inhibitory activity of EP3 and EP9 antibodies was asses by performing *in vitro* invasion inhibition assays. The EP3 antibodies (200 mg/ml) caused 82% invasion inhibition while the EP9 antibodies (200 mg/ml) caused 100% invasion inhibition [1]. The outcomes of the cantilever assays classify the EP3 antibodies and EP9 antibodies reactivity likewise; EP3 antibodies feature a lower cross-reactivity than the EP9 antibodies.

The cantilever assays allow classifying the cross-reactivity in a qualitative manner. To confirm this initial outcome more measurements are required. The minimal amount of sample required to perform these experiments allows the generation of more data, thus a statistically more robust set of data. The experiment presented here provides a good proof of concept for future use of cantilevers to investigate the reactivity of vaccine candidates to different antibodies.

6.5 References

[1] Okitsu S L, Kienzl U, *et al.* 2007 Structure-Activity-Based Design of a Synthetic Malaria Peptide Eliciting Sporozoite Inhibitory Antibodies in a Virosomal Formulation *Chem Biol* **14** 577-87

[2] Genton B, Pluschke G, *et al.* 2007 A Randomized Placebo-Controlled Phase Ia Malaria Vaccine Trial of Two Virosome-Formulated Synthetic Peptides in Healthy Adult Volunteers *PLoS One* **2** e1018

[3] Westerfeld N and Zurbriggen R 2005 Peptides delivered by immunostimulating reconstituted influenza virosomes *J Pept Sci* **11** 707-12

[4] Rinaldo Z 2003 Immunostimulating reconstituted influenza virosomes *Vaccine* **21** 921-4

[5] Zurbriggen R, Novak-Hofer I, *et al.* 2000 IRIV-adjuvanted hepatitis A vaccine: in vivo absorption and biophysical characterization *Prog Lipid Res* **39** 3-18

[6] Moorthy V S and Dubovsky F 2005 *Molecular Approaches to Malaria*: American Society of Microbiology)

[7] Moorthy V S, Good M F and Hill A V S 2004 Malaria vaccine developments *Lancet* **363** 150-6

[8] Cech P G, Aebi T, *et al.* 2011 Virosome-Formulated *Plasmodium falciparum* AMA-1 & CSP Derived Peptides as Malaria Vaccine: Randomized Phase 1b Trial in Semi-Immune Adults & Children *PLoS One* **6** e22273

[9] Mueller M S, Renard A, *et al.* 2003 Induction of Parasite Growth-Inhibitory Antibodies by a Virosomal Formulation of a Peptidomimetic of Loop I from Domain III of Plasmodium falciparum Apical Membrane Antigen 1 *Infect Immun* **71** 4749-58

[10] Biswas S, Spencer A J, *et al.* 2012 Recombinant Viral-Vectored Vaccines Expressing Plasmodium chabaudi AS Apical Membrane Antigen 1: Mechanisms of Vaccine-Induced Blood-Stage Protection *The Journal of Immunology* **188** 5041-53

[11] Faucheux N, Schweiss R, *et al.* 2004 Self-assembled monolayers with different terminating groups as model substrates for cell adhesion studies *Biomaterials* **25** 2721-30

[12] Ekblad T and Liedberg B 2010 Protein adsorption and surface patterning *Current Opinion in Colloid & Interface Science* **15** 499-509

[13] Arima Y and Iwata H 2007 Effect of wettability and surface functional groups on protein adsorption and cell adhesion using well-defined mixed self-assembled monolayers *Biomaterials* **28** 3074-82

[14] Fritz J 2008 Cantilever biosensors *Analyst* **133** 855-63

[15] Rastegar A J, Vosgueritchian M, *et al.* 2013 Nanomechanical Actuation of a Silicon Cantilever Using an Azo Dye, Self-Assembled Monolayer *Langmuir* **29** 7118-24

[16] Gorelkin P V, Mukhin D S, *et al.* 2010 New self-assembled monolayer coated cantilever for histidine-tag protein immobilization *Mendeleev Commun* **20** 329-31
[17] Ndieyira J W, Watari M, *et al.* 2008 Nanomechanical detection of antibiotic-mucopeptide binding in a model for superbug drug resistance *Nat Nano* **3** 691-6
[18] Mrksich M, Sigal G B and Whitesides G M 1995 Surface Plasmon Resonance Permits in Situ Measurement of Protein Adsorption on Self-Assembled Monolayers of Alkanethiolates on Gold *Langmuir* **11** 4383-5
[19] Mark S S, Sandhyarani N, *et al.* 2004 Dendrimer-Functionalized Self-Assembled Monolayers as a Surface Plasmon Resonance Sensor Surface *Langmuir* **20** 6808-17
[20] Park I-S, Kim D-K, *et al.* 2004 Development of a direct-binding chloramphenicol sensor based on thiol or sulfide mediated self-assembled antibody monolayers *Biosensors Bioelectron* **19** 667-74
[21] Sharma M K, Rao V K, *et al.* 2011 A novel piezoelectric immunosensor for the detection of malarial Plasmodium falciparum histidine rich protein-2 antigen *Talanta* **85** 1812-7
[22] Gracias D H, Tien J, *et al.* 2000 Forming Electrical Networks in Three Dimensions by Self-Assembly *Science* **289** 1170-2
[23] Schreiber F 2000 Structure and growth of self-assembling monolayers *Prog Surf Sci* **65** 151-257
[24] Hakkinen H 2012 The gold-sulfur interface at the nanoscale *Nat Chem* **4** 443-55
[25] White R J, Phares N, *et al.* 2008 Optimization of Electrochemical Aptamer-Based Sensors via Optimization of Probe Packing Density and Surface Chemistry *Langmuir* **24** 10513-8
[26] Deng L, Mrksich M and Whitesides G M 1996 Self-Assembled Monolayers of Alkanethiolates Presenting Tri(propylene sulfoxide) Groups Resist the Adsorption of Protein *J Am Chem Soc* **118** 5136-7
[27] Malmsten M 1998 Formation of Adsorbed Protein Layers *J Colloid Interface Sci* **207** 186-99
[28] Malmsten M, Emoto K and Van Alstine J M 1998 Effect of Chain Density on Inhibition of Protein Adsorption by Poly(ethylene glycol) Based Coatings *J Colloid Interface Sci* **202** 507-17
[29] Heuberger M, Drobek T and Spencer N D 2005 Interaction Forces and Morphology of a Protein-Resistant Poly(ethylene glycol) Layer *Biophys J* **88** 495-504
[30] Michel R, Pasche S, *et al.* 2005 Influence of PEG Architecture on Protein Adsorption and Conformation *Langmuir* **21** 12327-32
[31] Kenausis G L, Vörös J, *et al.* 2000 Poly(l-lysine)-g-Poly(ethylene glycol) Layers on Metal Oxide Surfaces: Attachment Mechanism and Effects of Polymer Architecture on Resistance to Protein Adsorption† *The Journal of Physical Chemistry B* **104** 3298-309
[32] Ruiz-Taylor L A, Martin T L, *et al.* 2001 Monolayers of derivatized poly(l-lysine)-grafted poly(ethylene glycol) on metal oxides as a class of biomolecular interfaces *Proc Natl Acad Sci USA* **98** 6
[33] Ma H, Hyun J, *et al.* 2004 "Non-Fouling" Oligo(ethylene glycol)- Functionalized Polymer Brushes Synthesized by Surface-Initiated Atom Transfer Radical Polymerization *Adv Mater* **16** 338-41
[34] Marie R, Beech J P, *et al.* 2006 Use of PLL-g-PEG in Micro-Fluidic Devices for Localizing Selective and Specific Protein Binding *Langmuir* **22** 10103-8
[35] Marie R, Dahlin A B, *et al.* 2007 Generic surface modification strategy for sensing applications based on Au/SiO2 nanostructures *Biointerphases* **2** 49-55

[36] Okitsu S L, Mueller M S, *et al.* 2008 Preclinical profiling of the immunogenicity of a two-component subunit malaria vaccine candidate based on virosome technology *Human Vaccines* **4** 106-14
[37] Powers K W, Brown S C, *et al.* 2006 Research Strategies for Safety Evaluation of Nanomaterials. Part VI. Characterization of Nanoscale Particles for Toxicological Evaluation *Toxicol Sci* **90** 296-303
[38] Zakharov P and Scheffold F 2009 *Light Scattering Reviews 4,* ed A Kokhanovsky: Springer Berlin Heidelberg) pp 433-67
[39] Plant A L 1993 Self-assembled phospholipid/alkanethiol biomimetic bilayers on gold *Langmuir* **9** 2764-7
[40] Plant A L 1999 Supported Hybrid Bilayer Membranes as Rugged Cell Membrane Mimics *Langmuir* **15** 5128-35
[41] Rusmini F, Zhong Z and Feijen J 2007 Protein Immobilization Strategies for Protein Biochips *Biomacromolecules* **8** 1775-89
[42] Glasmästar K, Larsson C, *et al.* 2002 Protein Adsorption on Supported Phospholipid Bilayers *J Colloid Interface Sci* **246** 40-7
[43] Tero R, Watanabe H and Urisu T 2006 Supported phospholipid bilayer formation on hydrophilicity-controlled silicon dioxide surfaces *PCCP* **8** 3885-94
[44] Love J C, Estroff L A, *et al.* 2005 Self-Assembled Monolayers of Thiolates on Metals as a Form of Nanotechnology *Chem Rev* **105** 1103-70
[45] Meuse C W, Niaura G, *et al.* 1998 Assessing the Molecular Structure of Alkanethiol Monolayers in Hybrid Bilayer Membranes with Vibrational Spectroscopies *Langmuir* **14** 1604-11
[46] Pera I and Fritz J 2006 Sensing Lipid Bilayer Formation and Expansion with a Microfabricated Cantilever Array *Langmuir* **23** 1543-7
[47] Braun T, Ghatkesar M K, *et al.* 2007 Digital processing of multi-mode nano-mechanical cantilever data *Journal of Physics: Conference Series* **61** 341
[48] Wagner P, Hegner M, *et al.* 1996 Covalent immobilization of native biomolecules onto Au(111) via N-hydroxysuccinimide ester functionalized self-assembled monolayers for scanning probe microscopy *Biophys J* **70** 2052-66
[49] Sigal G B, Mrksich M and Whitesides G M 1998 Effect of Surface Wettability on the Adsorption of Proteins and Detergents *J Am Chem Soc* **120** 3464-73
[50] Braun T, Barwich V, *et al.* 2005 Micromechanical mass sensors for biomolecular detection in a physiological environment *Physical Review E* **72** 031907
[51] Maloney N, Lukacs G, *et al.* 2014 Device for filamentous fungi growth monitoring using the multimodal frequency response of cantilevers *Rev Sci Instrum* **85** -
[52] Dohn S, Schmid S, *et al.* 2010 Position and mass determination of multiple particles using cantilever based mass sensors *Appl Phys Lett* **97** -
[53] Dohn S, Sandberg R, *et al.* 2005 Enhanced functionality of cantilever based mass sensors using higher modes *Appl Phys Lett* **86** -

Chapter 7

Conclusions and Outlook

7.1 Conclusion

A diagnostic device utilising cantilever arrays to distinguish malaria antibodies was designed, developed, optimised, automated and successfully applied to real biological samples. The fast, accurate and automated read-out of the static and dynamic response of the cantilever sensors immersed in the physiological environment of the analyte under study was achieved by the optical beam deflection method by a laser mounted on automated micro-translation stages. In the static mode of operation, the noise level of the deflection for a 500 µm long and 1 µm thick cantilever is in the order of ± 2 nm. For mass sensing using cantilevers with the same dimensions, the device allows the read-out up to the 17^{th} flexural resonance mode with excellent signal to noise levels. The implementation of a third micro-translation stage allows for automated fine focusing of the laser on the cantilevers, thus resulting in clean frequency spectra.

The incorporated injection port in the measurement chamber enables the local injection of sub microliter volumes of sample with excellent repeatability. The volume of the liquid cell of the measurement chamber is 3 µl. For a single measurement only 6 µl of sample is required to guarantee that the liquid in the liquid cell is exchanged completely. Reducing the sample volume required enables the ability to generate a larger set of data from the same total sample volume and hence the conservation of precious material. A completely automated laser focusing method was integrated thereby reducing user interaction for the initialisation process.

The new instrument control and data analysis software was written in LabVIEW. The chosen software architecture offers scalable, readable, and maintainable code modules.

This allows the implementation of additional hardware or software code to the existing device in a timely manner without the need to change the whole software.

The fully automation of the device together with the user-friendly operation procedure enable reducing errors due to user interaction. Resulting in the greatest resolution possible from experiment to experiment and increasing experiment-to-experiment repeatability.

The comparison of the two modes of operation shows, that the static mode is more susceptible towards fluidics injection, the deflection measurement in a differential manner as shown is mandatory. This is why the dynamic mode is the favourable mode for the current setup. The dynamic mode is more robust by assuming a constant viscosity of the solutions; it showed a direct response in a reproducible manner. The scaling of the dynamic response with the direct parallel measurements of the different resonance modes provides a better control than the static mode. Nonetheless, the static mode features a great potential for a cantilever based biosensor and should not be excluded in future developed platforms.

Using this device the affinity of different antibodies to the malaria vaccine candidate UK-39 has been demonstrated operating in static and dynamic mode. The antibody functionalised cantilevers are capable of binding vesicles featuring antigens on their surface. The mass uptake measured by the dynamic mode is based on the additional buffer within the vesicles which cannot diffuse around the sensor.

The newly developed device was used to investigate cross-reactivity of the UK-39 malaria vaccine candidate to three different antibodies: the UK-39 binding antibodies EP3 and EP9 and the *P. falciparum* sporozoite specific antibody SP3. It was shown operating the cantilevers in dynamic mode that the SP3 antibodies had a higher affinity for the UK-39 peptides than the EP3 and EP9 antibodies. The affinity of the EP3 antibody is about a fifth of the SP3 affinity and the EP9 antibody affinity is about a third. The SP3 antibodies functionalised cantilevers had a maximum mass uptake of 380 $\pm$ 30 pg, while the EP3 and EP9 experiments resulted in a maximum mass uptake of 80 $\pm$ 40 pg and 160 $\pm$ 25 pg, respectively.

The finding, that the SP3 antibodies and UK-39 peptide feature the highest affinity were confirmed by the static mode study, where the SP3 antibody injection lead to the greatest deflection of the cantilevers of 26 $\pm$ 8 nm. The EP3 antibodies injection resulted in an

about 20 times smaller deflection of 0 ± 3 nm and the EP9 antibodies injection in a roughly 5 times smaller deflection of 6 ± 3 nm than the SP3 measurement. The investigation of the cross-reactivity by the cantilever assay shows, in a qualitative manner, that the SP3 antibodies have the highest affinity to the UK-39 peptides.

Measuring the binding of antibodies in dynamic mode to the sensor surface is scarcely achievable with the mass resolution of the current setup due to the small molecular mass of antibodies. The futility of making biologically relevant measurements using a single cantilever has been highlighted considering any sample introduced to the cantilever may have a slight variation in temperature/viscosity/refractive index to the buffer fluid. The differential signal shows the need for a reference cantilever to eliminate these environmental effects. To sum up, the device matches major requirements of protein assay techniques, such as miniaturised format, low consumption of analyte and real time measurements.

The implementation of the presented device in the form of a point-of-care device will be a challenging task. Firstly, the cantilever sensor functionalisation requires a skilled and trained operator and is labour intensive, hence costly procedure. Secondly, the shelf life of the functionalised cantilevers has to be examined and the ideal storage condition to be determined. Thirdly, the applied read-out method, the optical beam deflection method is the major drawback method of the device. Albeit it excellent resolution the read-out technique lacks the simplicity of a point-of-care technology with nanomechanical sensors with integrated read-out technology. As a final point, the required temperature stability and electrical equipment pose a challenge to a point-of-care setup if it will be deployed in field trials in developing countries. Therefore, the presented work here proves that nanomechanical sensors are applicable as biosensors in a research lab environment and make a start towards a point-of-care implementation.

7.2 Outlook

7.2.1 Experimental

For a more conclusive assessment of the affinity of the different antibodies to the UK-39 peptide, more experiments are required which will be carried out in the near future. The generated data will allow a more detailed statistical analysis and reinforce the preliminary

findings of the affinity of the EP3, EP9 and SP3 antibodies to the UK-39. The experimental work presented in Chapter 6 is the foundation for an assay to detect specific vesicular particles. The assay can be used to detect cross reactivity of different vesicle based vaccines to determine the ideal target candidate.

To verify the interpretation of the sensor response, it is recommended to implement a second analysis method into the measurement procedure. A method which allows verifying the presence of the analyte under study on the sensor surface could be the introduction of a secondary antibody that identifies a free region of the captured analyte. This second antibody could exhibit fluorescent labels or it could be tethered to a gold nanoparticle that acts as a mass and plasmonic label. The binding of the second antibody could then be detected by the cantilever as additional mass on the cantilever sensor and the fluorescence label could be detected by fluorescence microscopy or the captured nanoparticles would serve as optical cavity that might boost the plasmonic signal of the nanoparticles.

Proper functionalisation of the cantilevers is key for a successful assay. A site-specific immobilisation of the antibodies or antigens, respectively on the sensor surface could improve the sensitivity and selectivity of the assay. This would require an implementation of automated cantilever functionalisation technologies within the measurement chamber.

For the static mode study, it would be beneficial to have a more controlled surface functionalisation The DLS measurements indicated that there are two size populations and filtration did not remove the larger population. Therefore, vesicles made of phosphatidylethanolamine (PE) with a more defined size distribution containing different amount of UK-39 peptides would allow a more controlled functionalisation using alkane-thiol/phospholipid bilayers. The peptide density could be altered on the sensor surface.

For the UK-39 measurement, it would be advantageous to have access to UK-39 peptides that are not PE conjugated. This would allow the immobilisation of the UK-39 peptide directly to the sensor surface, hence in a more controlled way and with a higher receptor density. This might result in a better resolution of the static mode.

Another approach to immobilise UK-39 peptides on the sensor surface could be via ω-functionalised SAM. With UK-39 peptides covalently coupled to the SAM, it might be possible to investigate the influence of the receptor density on the sensor surface by static and dynamic mode. Unfortunately, the company producing the UK-39 peptides shut down

the production of the UK-39 peptides, therefore only PE conjugated UK-39 peptides are available for further experiments.

Changing the functionalisation protocol to a direct immobilisation of the antigen/antibody on the bare silicon cantilever could result in more consistent results due to the omission of the metal deposition step. However, this would imply the loss of the reflective gold surface for the optical beam deflection read-out resulting in a lower intensity of the reflected laser beam.

Further applications of the device could include the investigation of liposome formulation. Liposome formulations (phospholipid-based vesicles) are used as drug delivery systems to potentiate the therapeutic efficacy while reducing toxicities of conventional medicines [1]. By using liposomes with specific binding sites to deliver them to explicit locations [2], cantilevers could be used to determine the binding affinity of the liposomes to the different binding sites.

7.2.2 Instrumentation

The presented cantilever based device lays the foundation for cantilever based assays. It offers a robust platform with a decent noise level and a fast performance. However, if the assays want to be competitive with the current bio-sensing technologies, there are amendments to the device required. The new measurement chamber provides clean amplitude and phase spectra with a good liquid exchange behaviour of the fluid cell. A redesign of the measurement chamber to a platform incorporating multiple recessed pockets for cantilever arrays would allow for better statistics or the detection of several analytes in parallel. The off-line functionalisation of the cantilever to obtain a bio-recognition interface by the capillary technique or micro dispensing technique is a major drawback of the device. The functionalisation step is labour intensive and involves manual handling of the cantilever array by the operator.

To overcome this drawback a functionalisation channel for the measurement chamber for each individual cantilever array would simplify the functionalisation process and increase the reliability of the assay. The functionalisation steps could be done *in-situ* and monitored by the static mode (e.g. building up of surface stress due to the formation of a SAM). However, this on-line functionalisation is only possible if there are at least two cantilever arrays present in the measurement chamber, otherwise the *in-situ* reference subtraction is

not possible and external factors influencing the measurement cannot be excluded. Utilising a setup with two or more arrays requires that the arrays are mechanically comparable.

It would be worth studying the influence of the angle of the recessed pocket for the cantilever array on the signal to noise ratio of the signals obtained. A worthwhile study would be to reduce the angle from 18 degrees to a value between 12 and 18 degrees, it would be possible to investigate the influence of the chamber geometry onto the performance. However, this would be a time consuming process, to machine the different chambers first and to glue the piezo-crystal stack actuators and the implementation of a mirror to point the reflected laser onto the PSD would be necessary.

The fluidics components (injection valve and priming system) could be detached from the measurement chamber as a separate manifold. This would allow for greater design flexibility for the machining process of the chamber and allow for future expansion with an unlimited number of injection ports. Another amendment could include a switchable valve (e.g. 2/3 way valve for 2 buffers or 2/4 way for 3 buffers, respectively) with multiple inlets connected to different buffer reservoirs. This would allow for injection of large volumes (in the millilitre regime) of different types of buffers into the liquid cell.

To read-out more than one cantilever array in the measurement chamber the travel range of the micro-translation stage of the optical cage has to be increased and the same applies for the active area of the position sensitive detector. To keep the existing position sensitive detector and to increase the flexibility of the system, it is recommended to change the operational principle. The position sensitive detector and the optical cage including the laser should be at a fixed position and the new designed measurement chamber should be mounted on two micro-translation stages, which would translate the chamber in x and y direction. This setup would allow scaling up the number of arrays in the measurement chamber limited only by the travel range of the micro-translation stages. The components required for such a setup have been purchased recently.

The employed temperature-regulated box allows the maintenance of the temperature inside at a constant level, however, the temperature within the box is not completely homogeneous. A larger box incorporating a base made of a stainless steel plate heat exchanger linked to a flow cycle thermostat could resolve this problem, resulting as well in a faster stabilisation of the temperature inside the box. Additionally, the size of the box

would allow mounting of the sample reservoirs and syringe pumps within the box allowing the buffers and samples to reach and maintain the thermodynamic equilibrium faster. Thus, introducing the liquid into the measurement chamber with the same temperature as the buffer would not result in temperature induced signals. A device comprising a simple heat exchanger similar to the described one above exists in the lab and could be advanced and applied to future developed instruments.

To simplify the device, it is desirable to utilise in the future piezoresistive cantilevers or resonators, this would allow removing all optical elements, including the position sensitive detector and positioning system resulting in a further miniaturisation of the fluid cell with a smaller sample volume required. However, operating piezoresistive or piezoelectric cantilevers in a physiological environment is challenging. The Joule heating of piezoresistive sensing elements may influence the interaction with the analyte, the sensitivity of the sensors have to be at least in the same range as the current cantilevers and the piezoresistors have to be passivated to facilitate measurements in a liquid environment.

To increase the sensitivity of the device operated in dynamic mode, higher Q factors of the cantilevers are essential. The implementation of parametric actuation of the cantilevers in the current platform could increase the Q factor [3], which has to be tested and compared with the current setup. Decreasing the size of the cantilevers would result in a higher Q factor [4], conversely the functionalisation process and the read-out with the current platform would be a challenge.

To increase the performance of the device, the implementation of field programmable gate arrays (FGPA) hardware for the instrument control is recommended. FPGAs designs employ integrated circuit containing a matrix of configurable logic gates, RAM blocks and very fast I/O and bidirectional data buses designed to be programmed to the required applications [5]. The benefits of the FPGAs would include faster I/O response times, enormous computing power compared with standard digital signal processors which would allow real time analysis of the acquired data and easily scalable and upgradeable to fulfil new functionality requirements [6].

Additionally, the code for the instrument control could be refactored with the LabVIEW real-time module, which would deliver much more precise and predictable timing characteristics. The real-time operating system (RTOS) would prioritise time-critical code (e.g. cantilever actuation and read-out) and less-important tasks (e.g. temperature control

or logging to disk) would obtain a lower priority [7]. This would allow high priority tasks to use as much computing power as they need without slowing down the system. However, a RTOS based instrument control software will not have a better performance than the other systems, the actual performance will still be dependent on the CPU speed, software and memory architecture.

7.3 References

[1] Fan Y and Zhang Q 2013 Development of liposomal formulations: From concept to clinical investigations *Asian Journal of Pharmaceutical Sciences* **8** 81-7

[2] Allen T M and Cullis P R 2013 Liposomal drug delivery systems: From concept to clinical applications *Adv Drug Del Rev* **65** 36-48

[3] Prakash G, Raman A, *et al.* 2012 Parametric noise squeezing and parametric resonance of microcantilevers in air and liquid environments *Rev Sci Instrum* **83** -

[4] Arlett J L, Myers E B and Roukes M L 2011 Comparative advantages of mechanical biosensors *Nat Nano* **6** 203-15

[5] Instruments N 2012 FPGA Fundamentals. National Instruments)

[6] Instruments N 2014 The NI LabVIEW High-Performance FPGA Developer's Guide. (World Wide Web: National Instruments)

[7] Instruments N 2013 Getting Started with the LabVIEW Real-Time Module. (World Wide Web

Appendices

Appendix A

Supplementary Information

A.1 PSD Amplification Electronics

In Table 9 the electronic components for the amplification electronics for the position sensitive detector are listed. The cut-off frequency, fc (Hz) is defined as shown in equation (36).

$$f_c = \frac{1}{2\pi RC} \tag{36}$$

With resistance R = 5.6 k Ω and capacitance C= 10 pF the resulting cut-off frequency f_c is 2.84 MHz. The rise time of the PSD (2L10-SU7) is 0.4 µs, therefore the fastest signal to be detected is 2.5 MHz.

Table 9: Electronic components for the position sensitive detector amplification electronics

Description	Model	Manufacturer
Dual operational amplifier	LT1358 CS8 #PBF	Linear Technology
SMD Metal Film Resistor 3K3 Ω	ERA6APB332V	Panasonic
SMD Ceramic Capacitor 10 pF	223886115109	Phycomp
SMD Ceramic Capacitor 100 nF	C0805C104K4RACTU	Kemet
SMD Metal Film Resistor 5K6 Ω	ERA6APB562V	Panasonic

A.1.1 Schematic of the Amplification Electronics

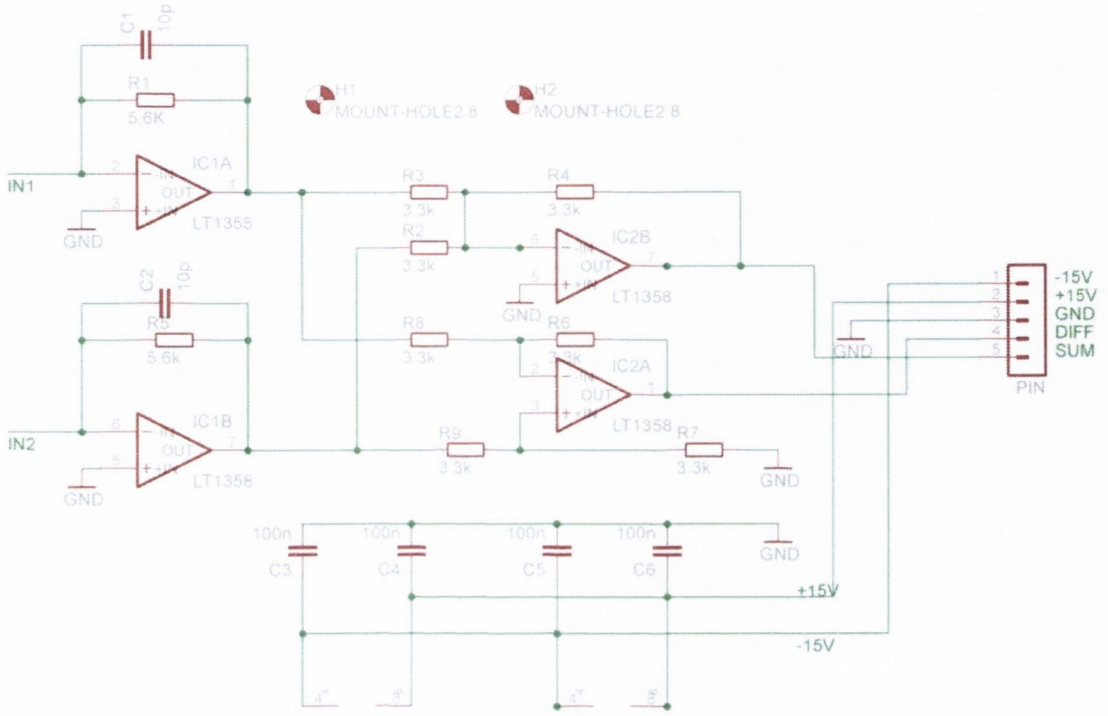

Figure 77: Schematic of the position sensitive detector amplification electronics

A.1.2 Printed Circuit Board of the Amplification Electronics

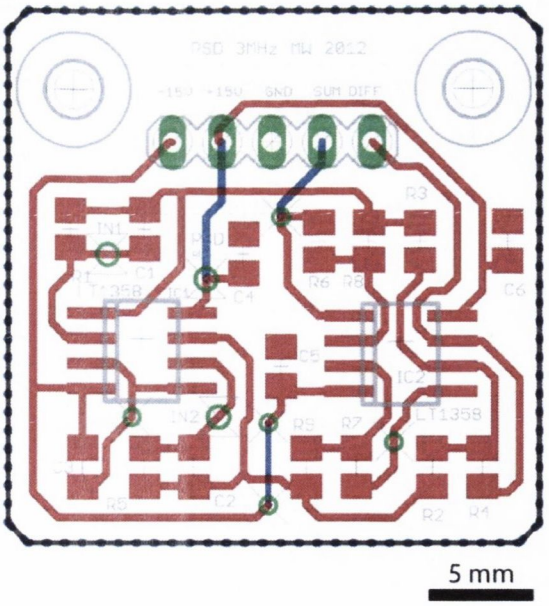

Figure 78: The layout of the printed circuit board for the position sensitive detector amplification electronics.

A.2 Chamber Development

A.2.1 Laser Path Calculations

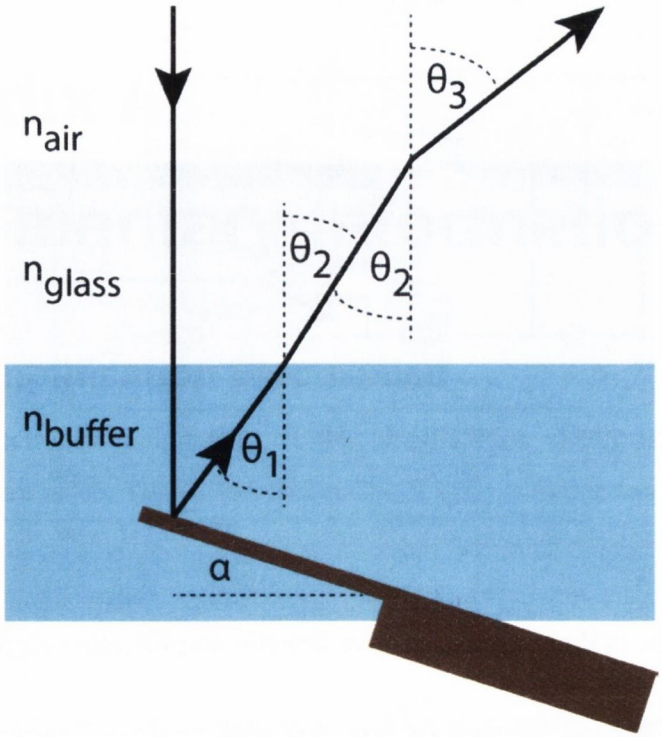

Figure 79: Laser beam path inside the liquid cell, not drawn to scale. The laser path is indicated by the black arrows and the refractive indices n_{air} = 1.000277, n_{glass} = 1.52 and n_{buffer} = 1.334 and α = 18 °, the angle the cantilever array is tilted relative to the chamber surface. The angles of incidence and refraction are indicated by θ_1, θ_2 and θ_3.

The laser beam path in the liquid cell of the measurement chamber is shown in Figure 79 with the refractive indices n_{air} = 1.000277, n_{glass} = 1.52 and n_{buffer} = 1.334 and the angle α = 18 ° at which the cantilever array is tilted relative to the measurement chamber surface. The refractive index for the glass cover is estimated because the manufacturer did not disclose the specifications of the double anti-reflective coated glass.

To calculate the theoretical beam path Snell's Law is applied to the two interface changes. The incident laser beam is not refracted at the two interface changes because of the incident angle of 90 °:

$$\frac{\sin(\theta)}{\sin(\theta_2)} = \frac{n_{buffer}}{n_{glass}} \tag{37}$$

$$\frac{\sin(\theta_2)}{\sin(\theta_3)} = \frac{n_{glass}}{n_{air}} \tag{38}$$

Θ_1 = the angle of incidence at the buffer – glass interface

Θ_2 = the angle of refraction at the buffer – glass interface and angle of incidence at the glass – air interface

Θ_3 = the angle of refraction at the glass – air interface

A.2.2 First Generation

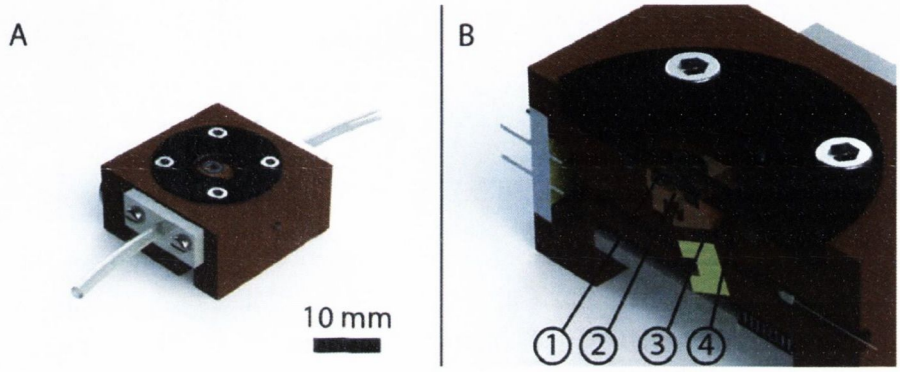

Figure 80: Initial developed measurement chamber A) 3d view B) Cutaway view of the chamber: 1 O-ring to hold the clamp in position, 2 clamp, 3 Cantilever array, 4 liquid cell with a volume of 11.9 µl. The recessed pocket for the cantilever array is at an angle of 22.5 ° with respect to the glass cover surface. The angle of 22.5° was too close to the total internal reflection, the angle has been changed for the subsequent chambers.

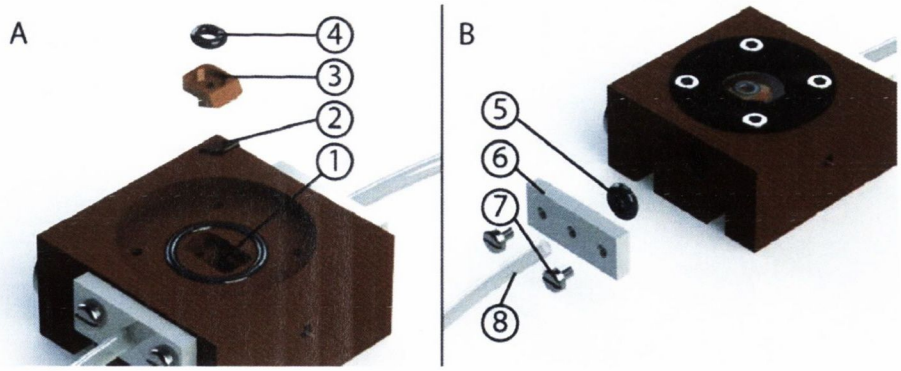

Figure 81: Details of the first generation of the measurement chamber A) 1 Recessed pocket for the cantilever array and the liquid cell with a volume of 14 µl, 2 Cantilever array, 3 Clamp to hold the cantilever array in position, 4 O-ring to press the clamp down by the glass cover. B) Fluidic connections: 5 O-ring as a seal, 6 Bracket to press the O-ring down, 7 Screws to tighten the bracket to the chamber, 8 PEEK tubing with an outer diameter of 1.6 mm.

A.2.3 Second Generation

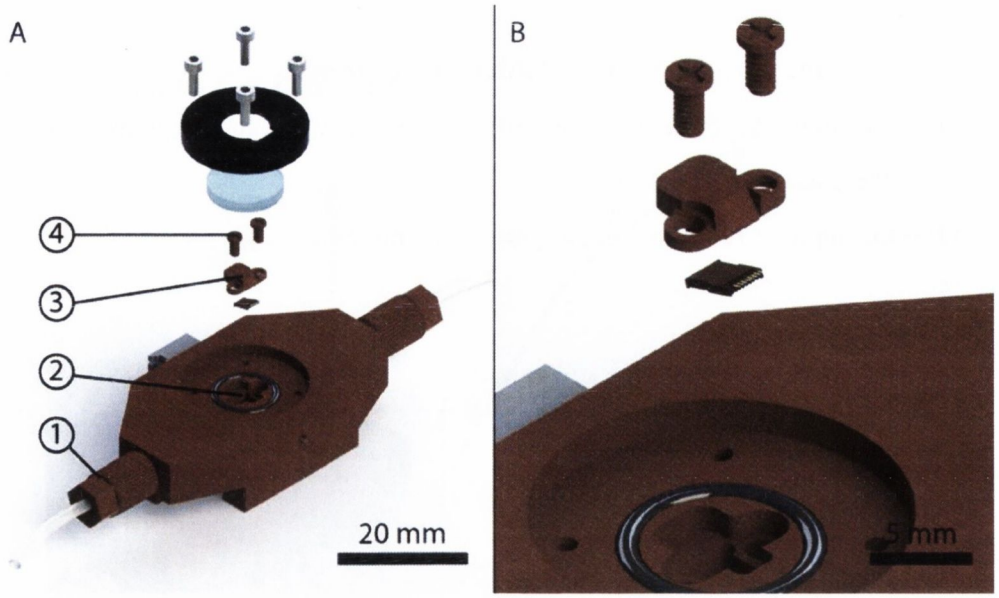

Figure 82: Second generation of the measurement chamber. The benefit of this chamber over the previous was the reduction in volume of the liquid cell, the introduction of fingertight fittings to allow robust connections and the introduction of a screwed fixation to clamp the cantilever array chip to remove the elastic O-ring. A) 1 PEEK 10-32 fingertight fittings replaced the O-ring seals, 2 The recessed pocket for the cantilever array has been modified to an angle of 18° with respect to the glass cover and the volume of the liquid cell was reduced to 8 µl, 3 New cantilever array clamp, 4 PEEK screws to tighten the clamp. B) Close up of the cantilever array clamping system. The clamp with two M 1.6 PEEK screws replacing the o-ring to press down the clamp.

A.2.4 Drawings of the Measurement Chambers: Third Generation

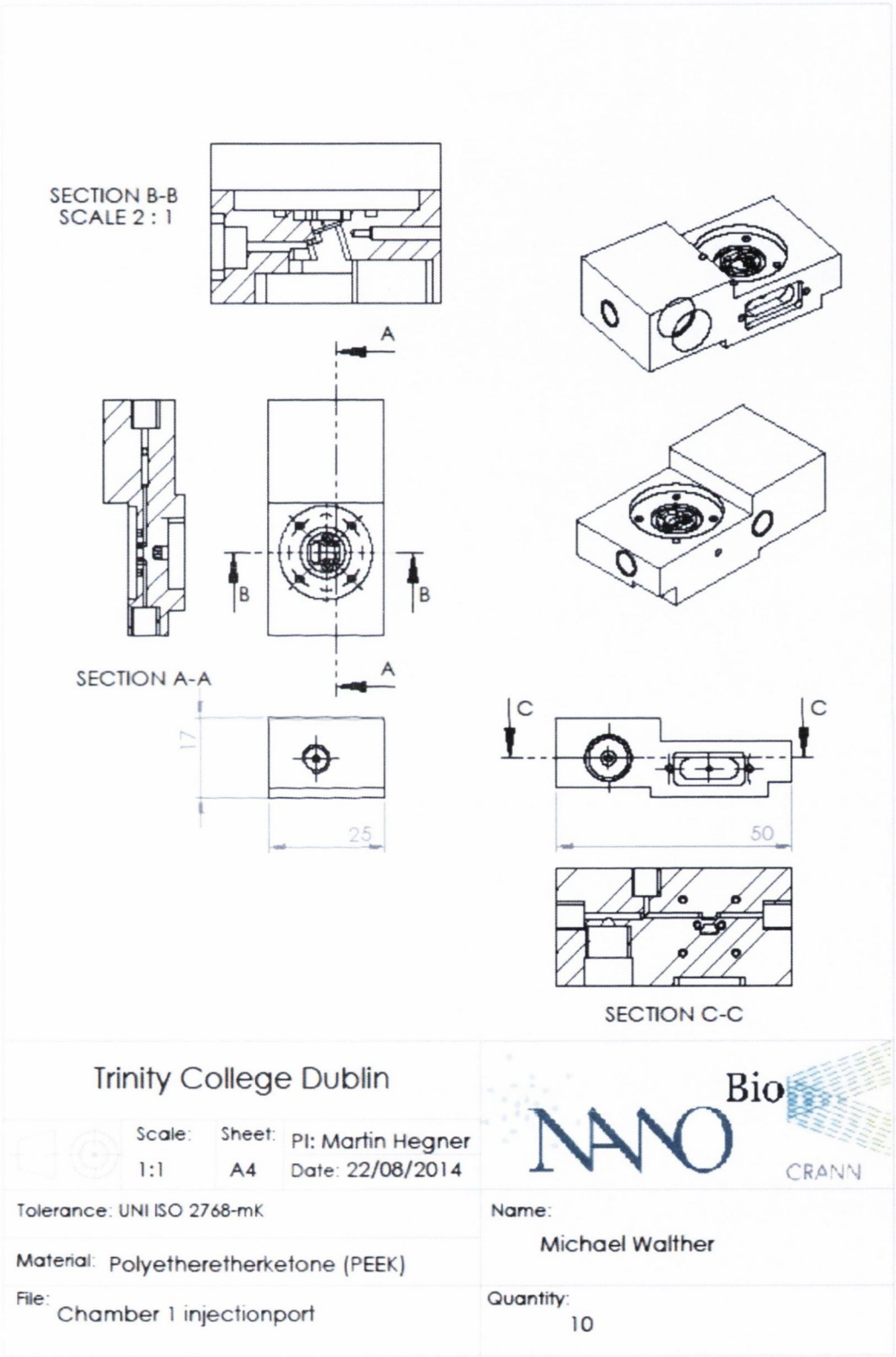

Figure 83: Drawing of the measurement chamber with one injection port. See section 2.2.2 for more information.

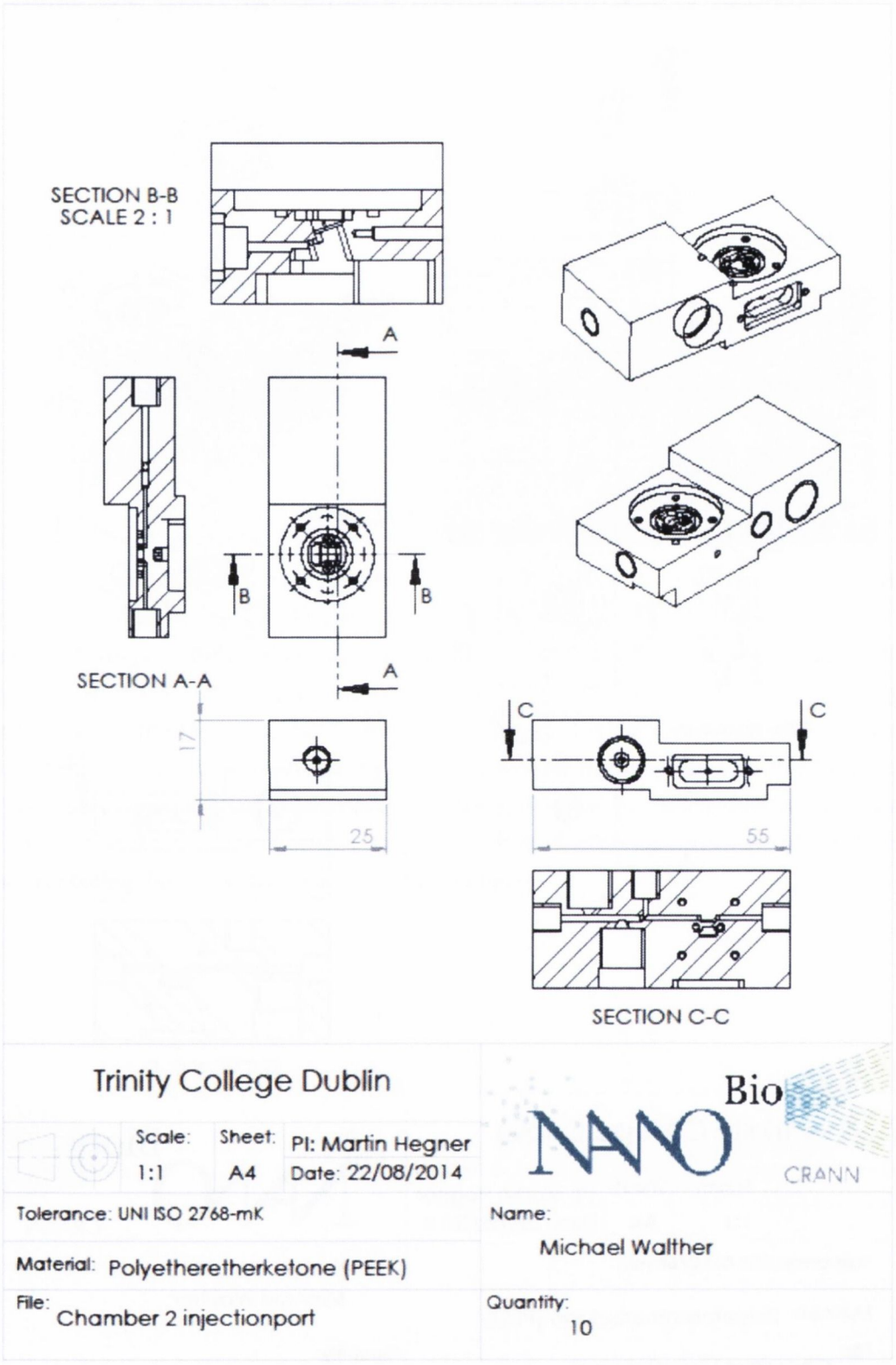

Figure 84: Drawing of the measurement chamber with two injection ports (fourth generation).

A.2.5 Drawing of the Cantilever Array Clamp

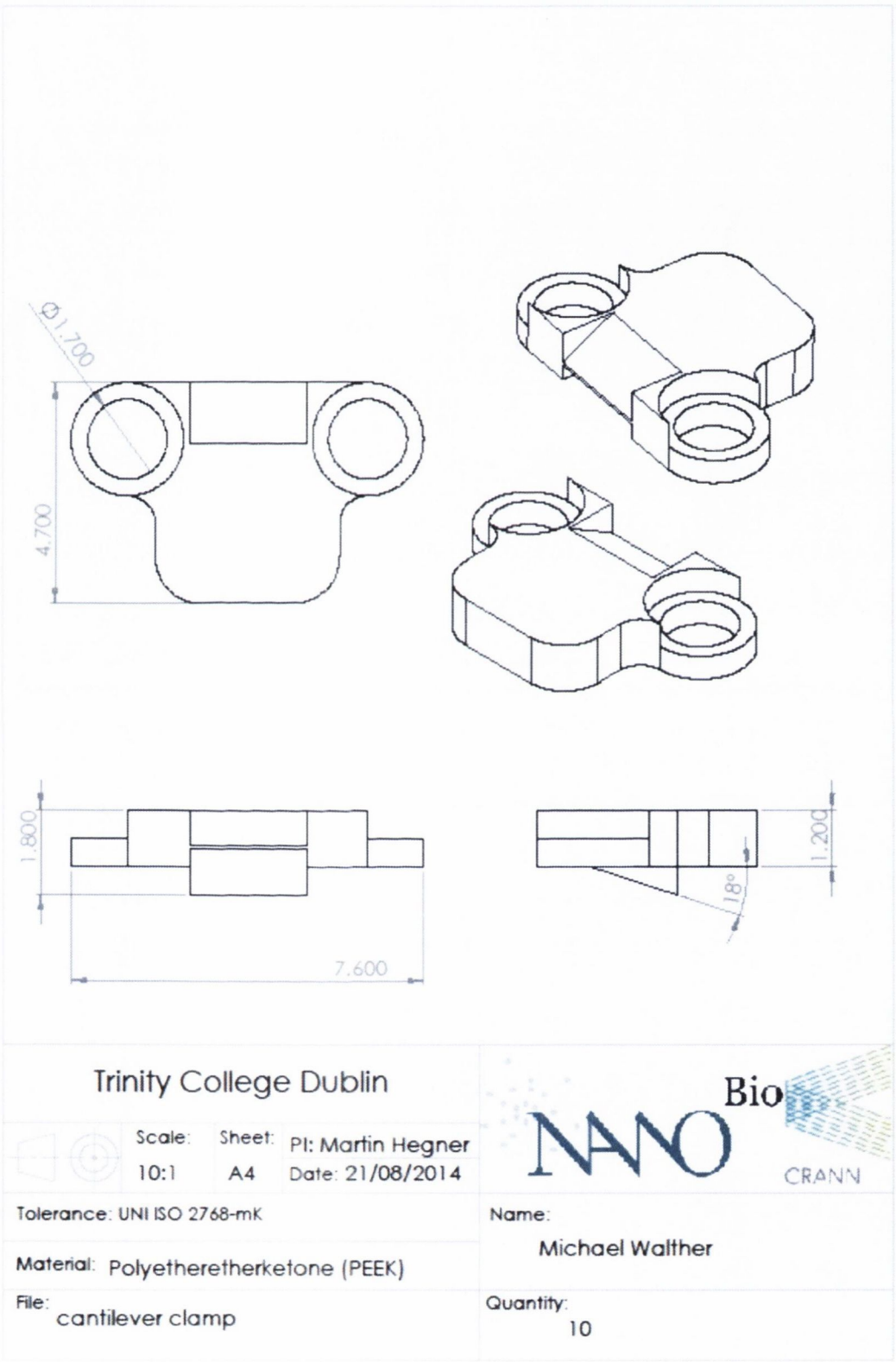

Figure 85: Drawing of the cantilever array clamp.

A.3 LabVIEW code

A.3.1 Temperature Control

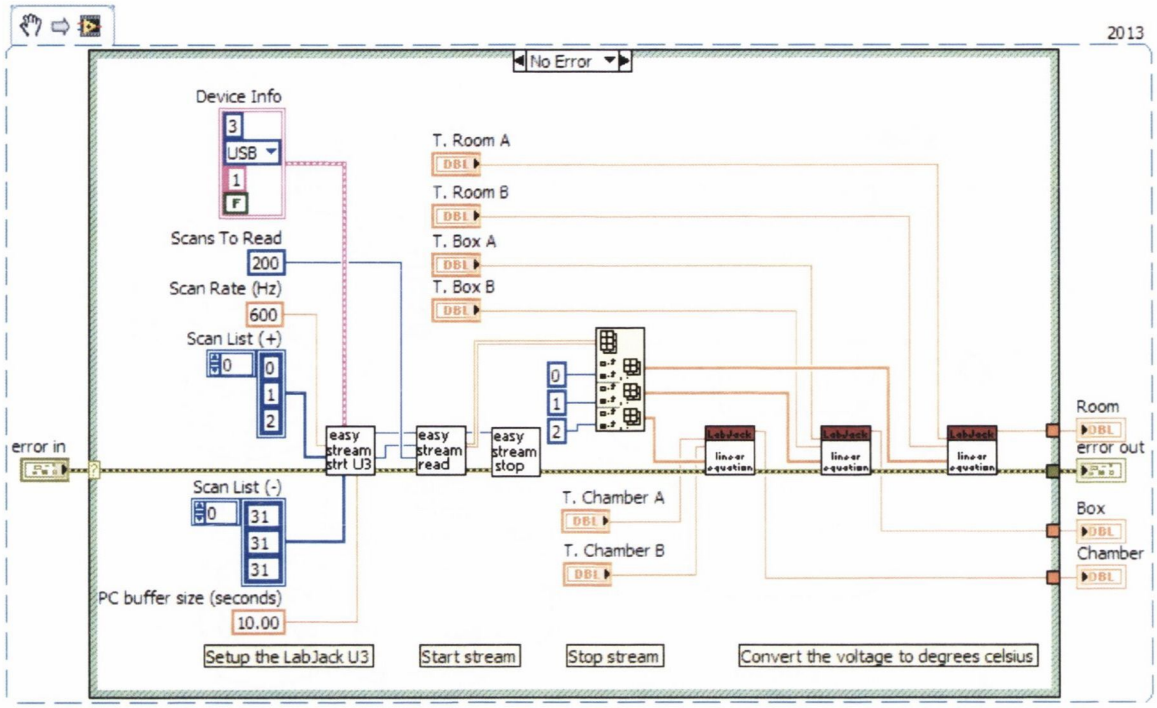

Figure 86: LabVIEW snippet of the block diagram to acquire the temperature of the box, room and measurement chamber.

A.3.2 Sweep Process

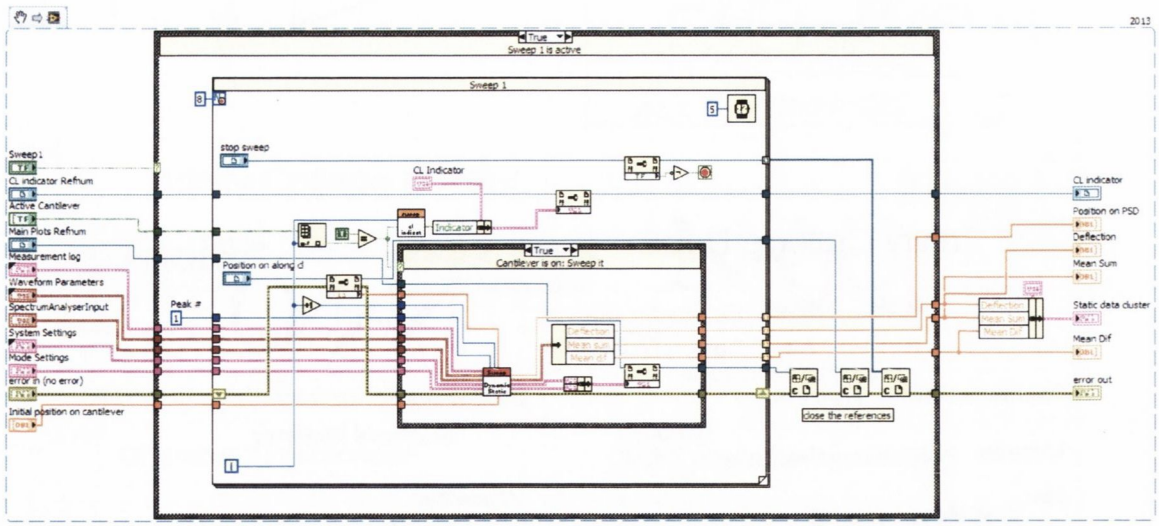

Figure 87: LabVIEW snippet of the block diagram for the sweep process.

A.3.3 Static Mode Measurement

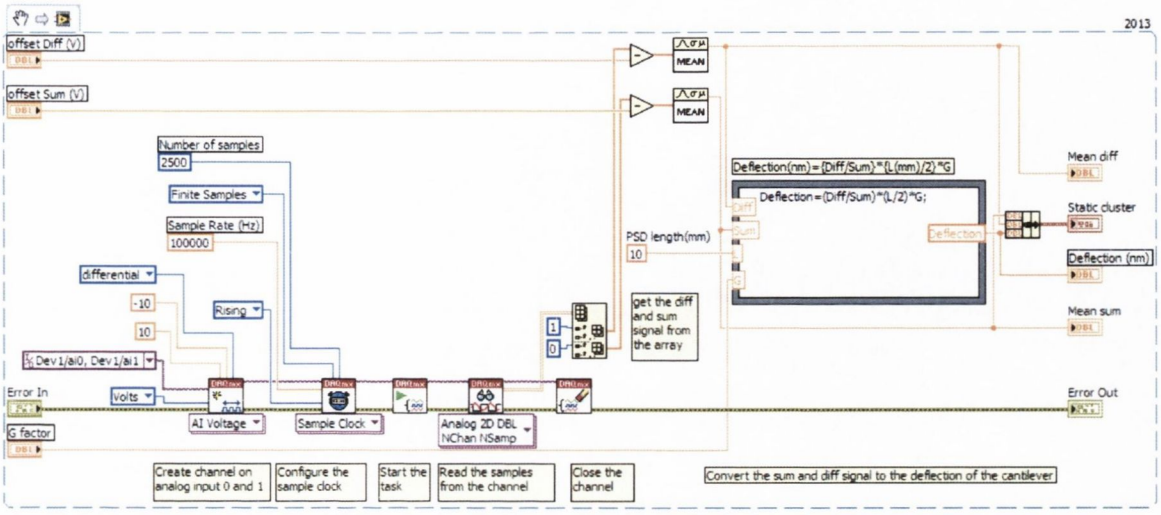

Figure 88: LabVIEW snippet of the block diagram for the static mode measurement, acquiring the summation and differential signal from the position sensitive detector and processing it to get the deflection of the cantilever.

A.3.4 Dynamic Mode Measurement

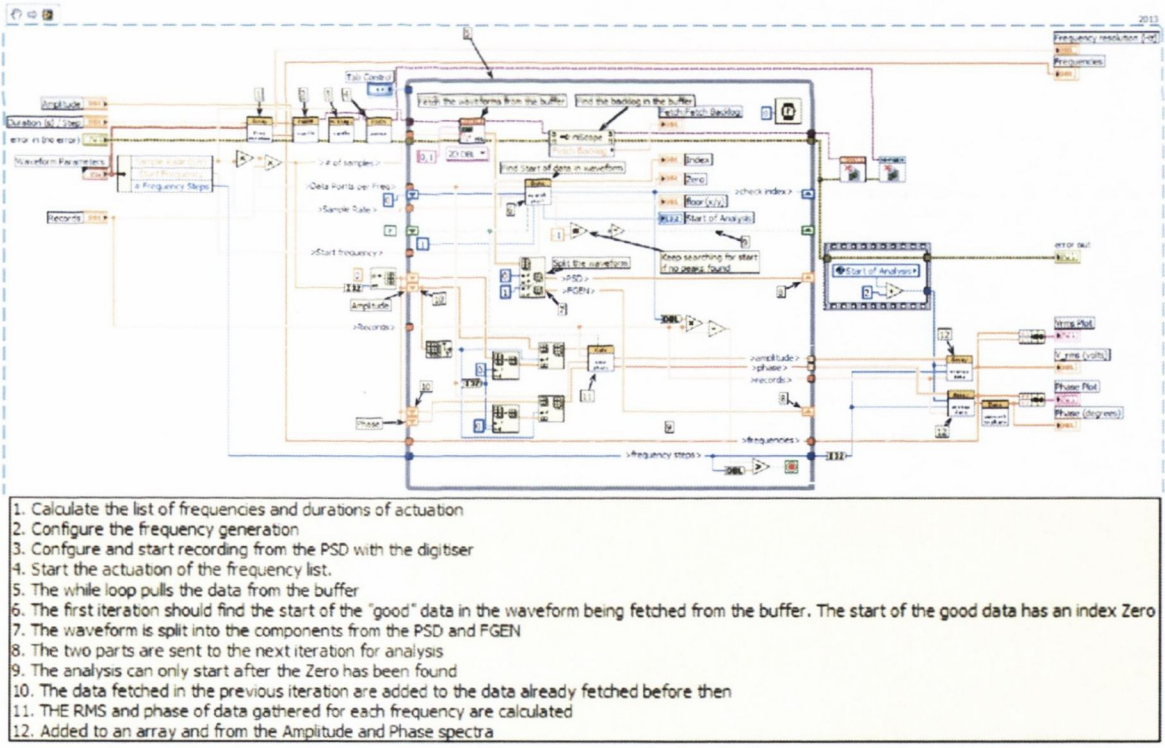

Figure 89: LabVIEW snippet of the block diagram for the dynamic mode measurement

A.3.5 Knife-Edge Measurement

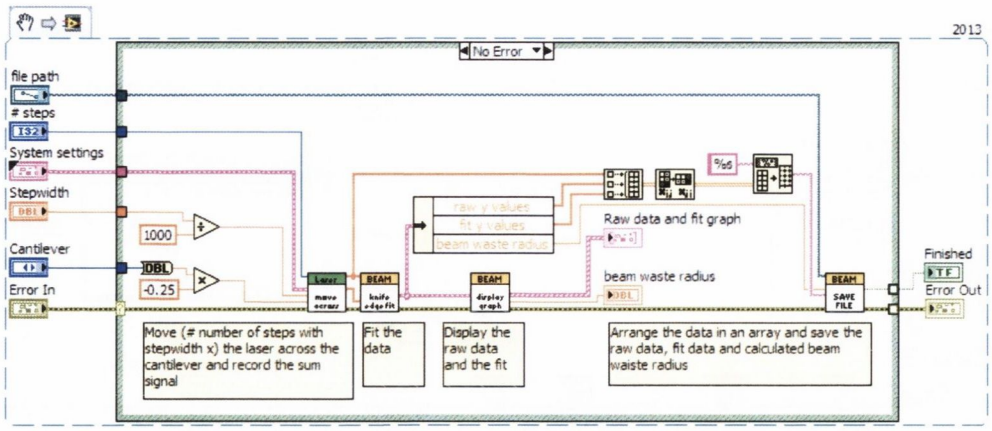

Figure 90: LabVIEW snippet of the block diagram for the knife-edge measurement.

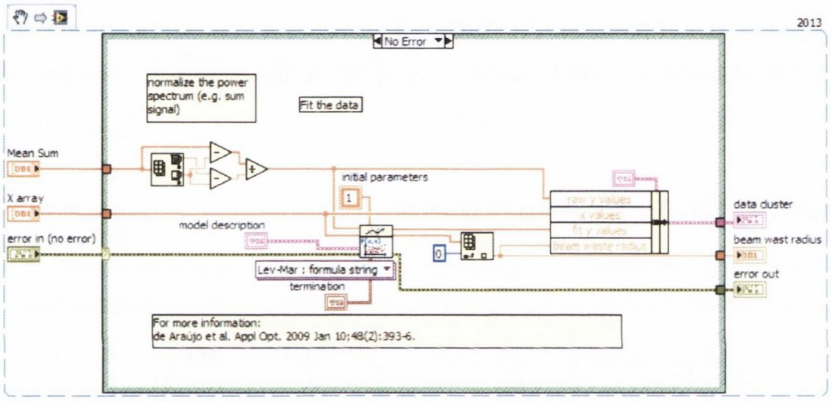

Figure 91: LabVIEW snippet of the block diagram for the fitting process during the knife-edge measurement.

A.3.6 Peak Analyser

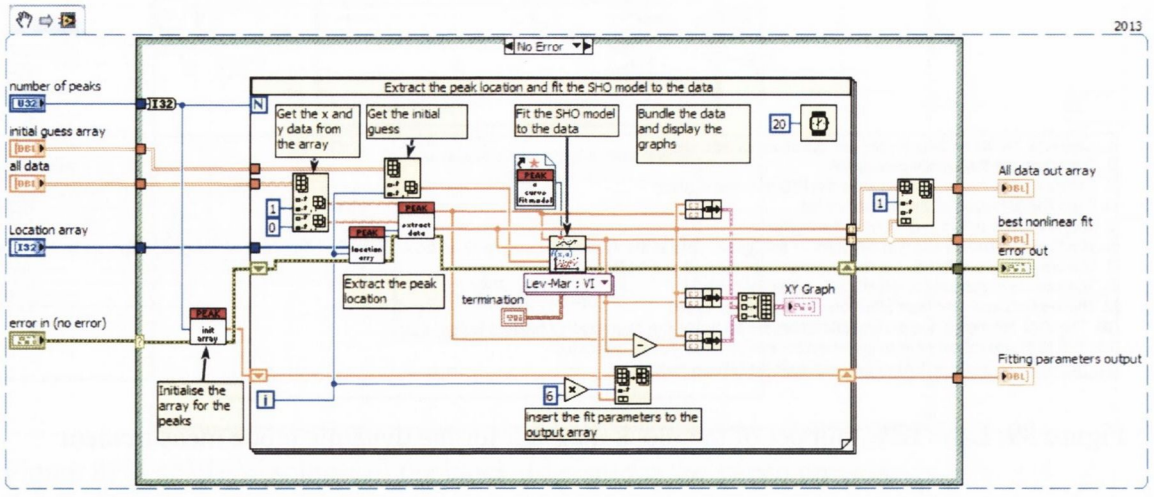

Figure 92: LabVIEW snippet of the block diagram for the peak analysing process.

A.4 Volume of Injected Samples

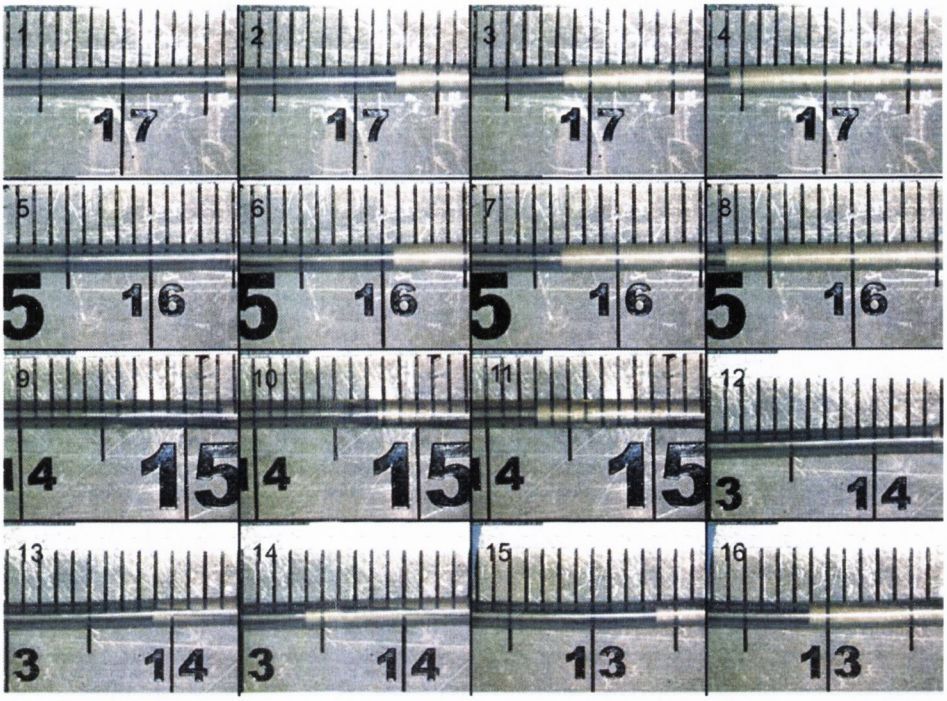

Figure 93: Volume depending on opening time of the injection valve. A series of injections at a constant pressure of 100 mbar were performed with increasing valve opening times from 31 ms to 40 ms in 1 ms increments. The sample meniscus was monitored after each injection to determine the volume of fluid injected (dark colour = liquid, transparent = air). A digital microscope (Dino-Lite Pro HR AM7000 series; Dino-Lite, The Netherlands) was used to give the required resolution.

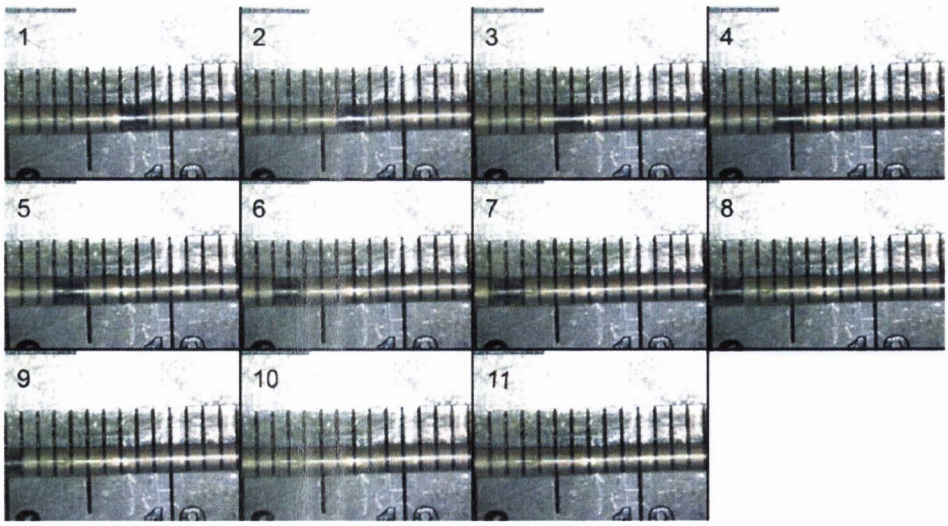

Figure 94: A series of ten 500 nl samples were injected to investigate the reproducibility of the injected volumes. The sample meniscus was monitored after each injection to determine the volume of fluid injected. A digital microscope (Dino-Lite Pro HR AM7000 series; Dino-Lite, The Netherlands) was used to give the required resolution.

A.5 Additional Knife-Edge Measurements Data

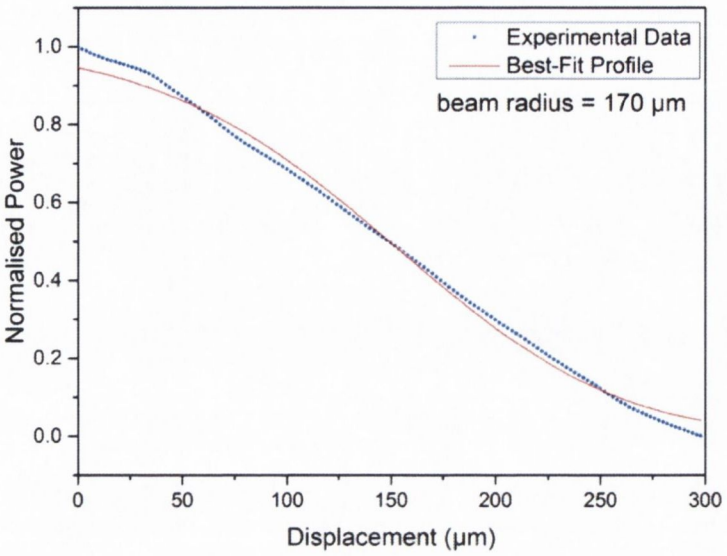

Figure 95: Initial measurement of the radius of the laser beam spot on the cantilever surface after manual focusing resulting in a beam radius of 170 µm.

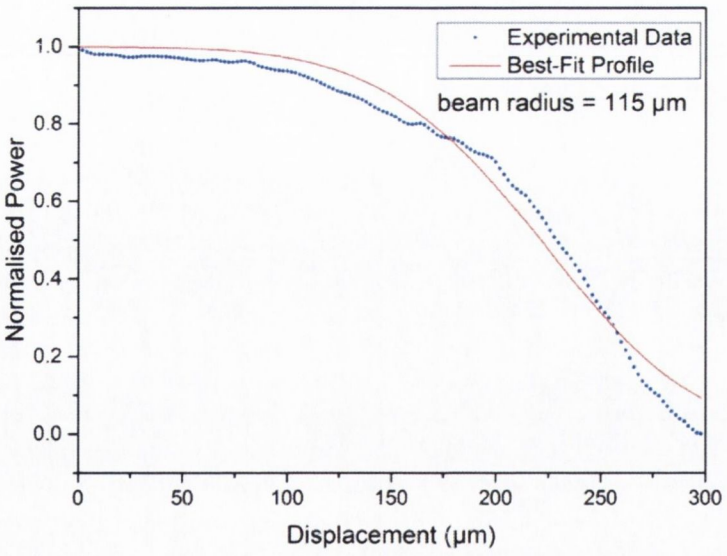

Figure 96: First iteration of the knife-edge measurement. After moving the optical cage closer to the cantilever surface a beam radius of 115 µm is obtained.

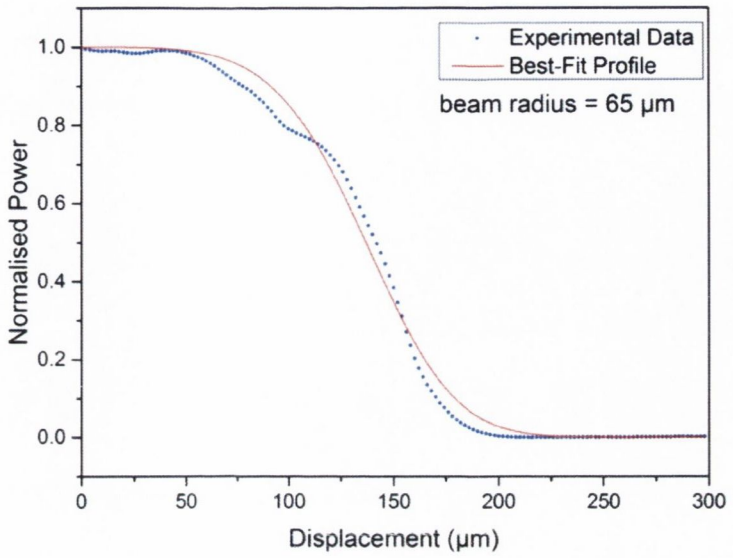

Figure 97: Second iteration of the knife-edge measurement. After moving the optical cage closer to the cantilever surface, a beam radius of 65 µm is obtained.

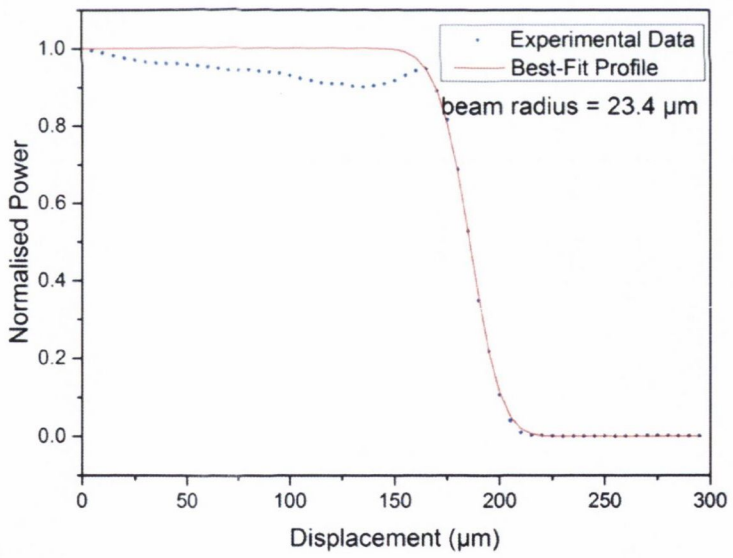

Figure 98: Third iteration of the knife-edge measurement. After moving the optical cage closer to the cantilever surface, a beam radius of 23.4 µm is obtained.

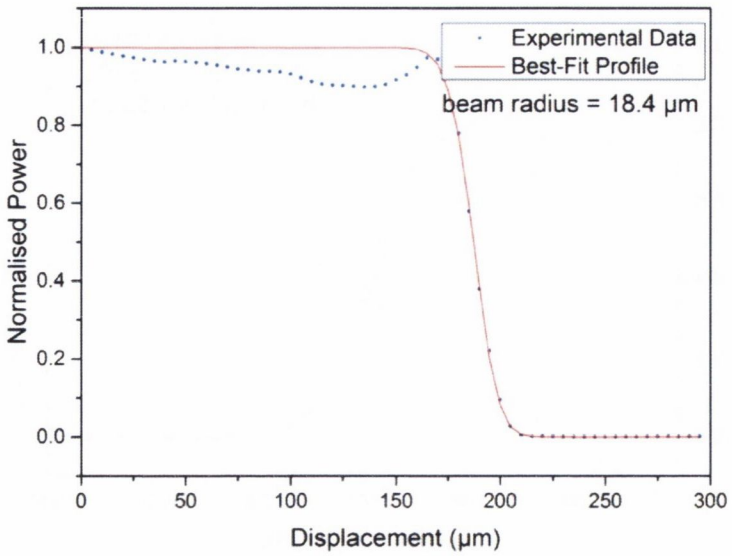

Figure 99: Fourth iteration of the knife-edge measurement. After moving the optical cage closer to the cantilever surface, a beam radius of 18.4 µm is obtained. The laser focusing process is completed when the radius reaches a value below 10 µm (as shown in section 4.3.2).

A.6 UK-39 Vesicle Injection Amplitude Spectra

Supplementary graphs showing the individual raw amplitude spectra for the different functionalised cantilevers for the UK-39 vesicle measurements described in section 6.2.2.

A.6.1 SP3 Antibody Functionalised Cantilever

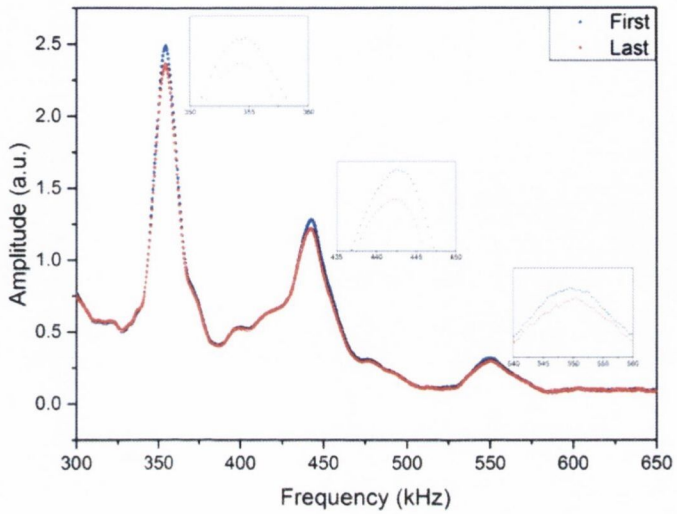

Figure 100: Raw amplitude spectrum for the 11th, 12th and 13th flexural mode for the SP3 antibody functionalised cantilever before (blue) and after (red) UK-39 vesicle injection. The blue spectra correspond to the first and the red spectra to the last recording of the resonance frequency. The three insets show the small change in resonance frequency for each flexural mode.

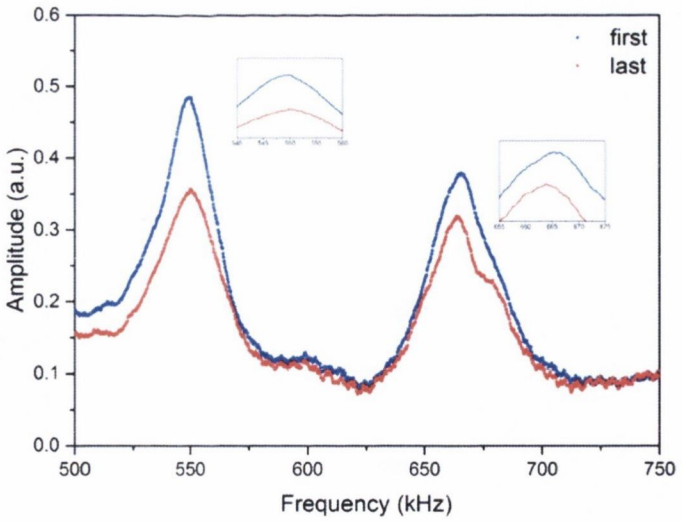

Figure 101: Raw amplitude spectrum for the 13th and 14th flexural mode for the SP3 antibody functionalised cantilever before (blue) and after (red) UK-39 vesicle injection. The blue spectra correspond to the first and the red spectra to the last recording of the resonance frequency. The three insets show the small change in resonance frequency for each flexural mode.

A.6.2 EP3 Antibody Functionalised Cantilever

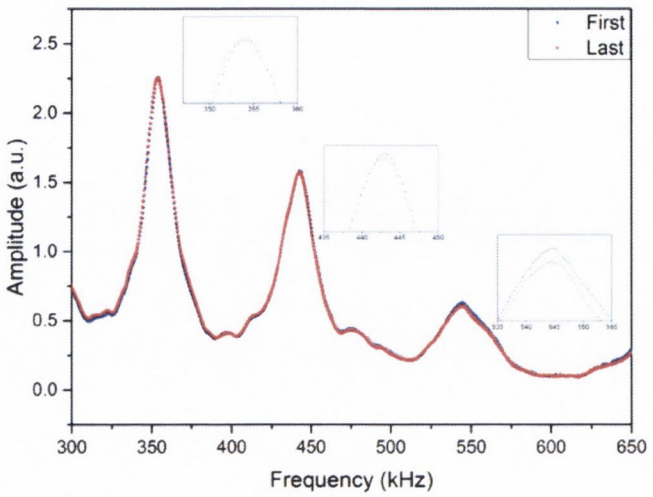

Figure 102: Raw amplitude spectrum for the 11th, 12th and 13th flexural mode for the EP3 antibody functionalised cantilever before (blue) and after (red) UK-39 vesicle injection. The blue spectra correspond to the first and the red spectra to the last recording of the resonance frequency. The three insets show the small change in resonance frequency for each flexural mode.

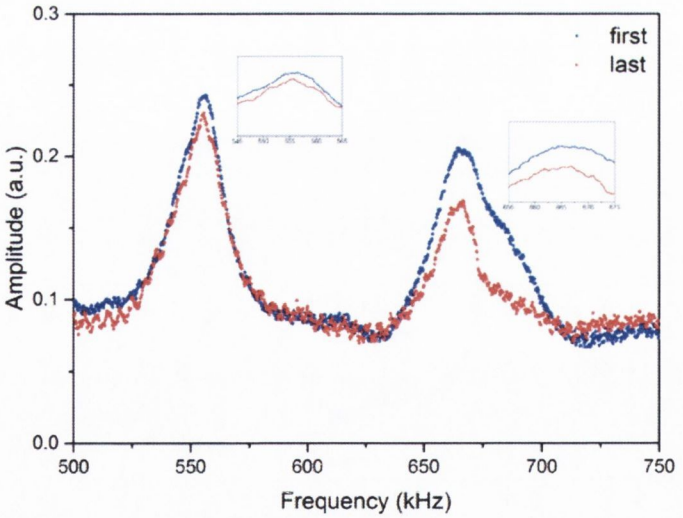

Figure 103: Amplitude spectrum for the 13th and 14th flexural mode for the EP3 antibody functionalised cantilever before (blue) and after (red) UK-39 vesicle injection. The blue spectra correspond to the first and the red spectra to the last recording of the resonance frequency. The three insets show the small change in resonance frequency for each flexural mode.

A.6.3 EP9 Antibody Functionalised Cantilever

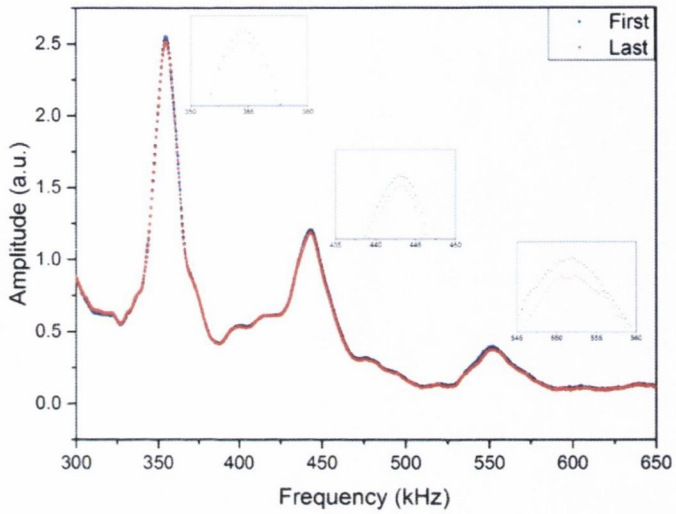

Figure 104: Raw amplitude spectrum for the 11th, 12th and 13th flexural mode for the EP9 antibody functionalised cantilever before (blue) and after (red) UK-39 vesicle injection. The blue spectra correspond to the first and the read spectra to the last recording of the resonance frequency. The three insets show the small change in resonance frequency for each flexural mode.

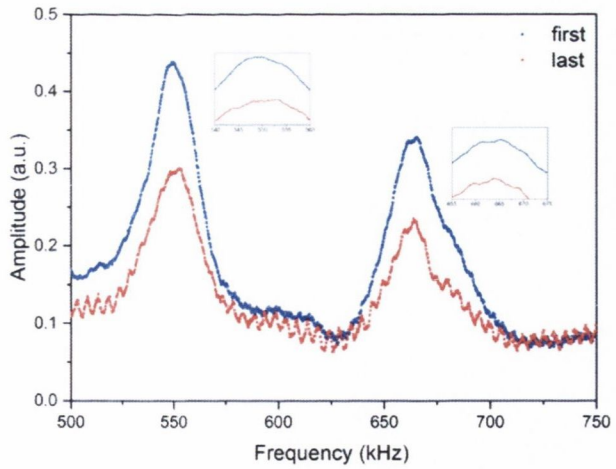

Figure 105: Raw amplitude spectrum for the 13th and 14th flexural mode for the EP9 antibody functionalised cantilever before (blue) and after (red) UK-39 vesicle injection. The blue spectra correspond to the first and the read spectra to the last recording of the resonance frequency. The three insets show the small change in resonance frequency for each flexural mode.

Appendix B

Protocols

B.1 Surface Cleaning Procedures

B.1.1 Standard Wash for Grease and Solvent Removal

This general degreasing procedure is performed in sequence and without much delay between each step. This procedure is useful in removing grease, adventitious organic deposits and remaining adhesives from the wafer container.

Materials

All chemicals were purchased from Sigma-Aldrich (Ireland Limited, Arklow, Wicklow, Ireland) unless stated otherwise.

- Acetone (C_3H_5O), HPLC Grade
- Ethanol (C_2H_6O), HPLC Grade
- Nanopure water
- Filter paper
- Small beakers

Method

1. Immerse in Acetone for at least 10 minutes
2. Dry on filter paper
3. Immerse in Ethanol for at least 5 minutes
4. Dry on filter paper
5. Immerse in Nanopure water for 1 minute
6. Dry on filter paper
7. Immerse in Acetone for at least 5 minutes

8. Dry on filter paper

B.1.2 UV Cleaning of Cantilevers

This procedure removes monomolecular layers of chemically bound organics on the silicon surface of the cantilever arrays. Chemisorbed and covalently bound self-assembled monolayers of adventitious organics, alkane thiols, and silane layers may be removed using this procedure. It is designed to clean the cantilever surface prior to plasma cleaning. This method removes organics that are not removed by procedure B.1.1.

Materials

All chemicals were purchased from Sigma-Aldrich (Ireland Limited, Arklow, Wicklow, Ireland) unless stated otherwise.

- Boekel UV Clean Model 135500 (low energy 0.5 Amp; UVC excitation at 184.9 nm in combination with 253.7 nm)
- Acetone (C_3H_5O), HPLC Grade
- Ethanol (C_2H_6O), HPLC Grade
- Filter paper
- Small beakers

Method

1. Clean the cantilever arrays according to procedure B.1.1
2. Dry on filter paper
3. Place the cantilever array in the Boekel UV-Ozone cleaner, clean the array for 5 minutes
4. Immerse in HPLC grade Acetone for at least 30 minutes
5. Dry on filter paper
6. Store the UV cleaned arrays in HPLC grade Ethanol

B.1.3 Plasma Cleaning of Cantilever Arrays

This protocol is designed to clean the cantilever surface prior to metal deposition. Plasma cleaning removes organic contaminants from the surface of the cantilever arrays that are not removed by procedure B.1.2. The titanium and gold deposition should be performed immediately after the plasma cleaning.

Materials

All chemicals were purchased from Sigma-Aldrich (Ireland Limited, Arklow, Wicklow, Ireland) unless stated otherwise.

- Diener PICO Barrel Asher (Diener Electronic GmbH & Co. KG, Nagolder Str. 61, D-72224 Ebhausen, Germany)
- Acetone (C_3H_5O), HPLC Grade
- Ethanol (C_2H_6O), HPLC Grade
- Filter paper

Method

1. Clean the bare silicon cantilever array according to procedure B.1.2
2. Dry the cantilever arrays on a filter paper
3. Place the cantilever arrays in the customised holder and place it in the plasma chamber
4. Flush the plasma chamber with oxygen (O_2) at least 5 times with a higher pressure to exchange all gas in the chamber completely
5. Reduce the O_2 pressure for the plasma cleaning procedure to 0.3 mbar, 160W, 40kHz
6. Clean it for 3 minutes
7. Immerse the cleaned cantilever arrays in HPLC grade Ethanol
8. Proceed immediately with the titanium gold deposition in the Temescal.

B.1.4 Plasma Cleaning of Glass Capillaries

This protocol is designed to clean the glass capillaries prior to use in the functionalisation device. Plasma cleaning ensures clean and debris-free capillaries which are also rendered highly hydrophilic and hence facilitate easier liquid siphoning from the reservoir.

The plasma cleaning is performed in a Diener PICO Barrel Asher (Diener Electronic GmbH & Co. KG, Nagolder Str. 61, D-72224 Ebhausen, Germany).

Materials

All chemicals were purchased from Sigma-Aldrich (Ireland Limited, Arklow, Wicklow, Ireland) unless stated otherwise.

- Diener PICO Barrel Asher (Diener Electronic GmbH & Co. KG, Nagolder Str. 61, D-72224 Ebhausen, Germany)
- Hotplate

- Ethanol (C_2H_6O), HPLC Grade
- Filter paper

Method

1. Clean the glass capillaries with ethanol
2. Dry the glass capillaries on a filter paper on the hot plate at 120 °C.
3. Place the glass capillaries in the custom made holder and place it in the plasma chamber
4. Flush the plasma chamber with oxygen (O_2) at least 5 times with a higher pressure to exchange all gas in the chamber completely
5. Reduce the O2 pressure for the plasma cleaning procedure to 0.3 mbar, 160W, 40kHz
6. Clean it for 7 minutes
7. Immerse the cleaned cantilever arrays in HPLC grade Ethanol
8. Prior to use, dry the glass capillaries on a filter paper on the hot plate at 120 °C.

B.1.5 UV Activation of the Gold coated Cantilevers

This procedure removes monomolecular layers of chemically bound organics on the gold layer of the cantilever arrays. It is designed to activate the gold surface prior to the functionalisation process.

Materials

All chemicals were purchased from Sigma-Aldrich (Ireland Limited, Arklow, Wicklow, Ireland) unless stated otherwise.

- Boekel UV Clean Model 135500 (low energy 0.5 Amp; UVC excitation at 184.9 nm in combination with 253.7 nm)
- Ethanol (C_2H_6O), HPLC Grade
- Gold coated cantilever array
- Small beakers

Method

1. Rinse the cantilever arrays in ethanol
2. Dry on filter paper
3. Place the cantilever array in the Boekel UV-Ozone cleaner, clean the array for 60 minutes
4. Immerse the cantilever array in the ethanol for 5 minutes

5. Dry on filter paper
6. Proceed immediately with the functionalisation procedure

B.2 Functionalisation Procedures

B.2.1 Alkylthiol SAM

This protocol is designed to functionalise the gold surface of the cantilever with a self-assembled monolayer of alkylthiols (-CH_3 terminated). The alkylthiols SAM renders the gold surface into a hydrophobic monolayer.

Materials

All chemicals were purchased from Sigma-Aldrich (Ireland Limited, Arklow, Wicklow, Ireland) unless stated otherwise.

- 1-Octadecanethiol
- Ethanol (C_2H_6O), HPLC Grade
- Nanopure water, 18 MΩ
- 200 µl Eppendorf tube
- Capillaries
- Clean gold-coated cantilever array

Method

1. Prepare a 1mM 1-Octadecanethiol in ethanol solution.
2. Two methods of functionalisation of the cantilevers:
    a. All 8 cantilevers: Immerse the gold coated cantilever array in the alkylthiol solution in a 200 µl Eppendorf tube for 60 minutes.
    b. Selective functionalisation of the cantilevers: Immerse the gold-coated cantilevers in the alkylthiol solution using the capillary functionalisation technique as described in section 5.4.1 for 60 minutes. Refill the capillary reservoir every 15 minutes to compensate for evaporation of the alkylthiol solution in the capillaries.
3. Rinse the cantilever array thoroughly with ethanol.
4. Rinse the cantilever array with nanopure water.

B.2.2 Hydroxyalkanethiol SAM

This protocol is designed to functionalise the gold surface of the cantilever with a SAM of hydroxyalkanethiol (-OH terminated). The hydroxyalkanethiol SAM renders the gold surface into a hydrophilic monolayer that acts as a blocking agent to prevent non-specific binding of analytes on the gold surface of the cantilever.

Materials

- 11-Hydroxy-1-undecanethiol
- Ethanol (C_2H_6O), HPLC Grade
- Nanopure water, 18 MΩ
- 200 µl Eppendorf tube
- Cleaned capillaries
- Clean gold-coated cantilever array

Method

1. Prepare a 1mM 11-Hydroxy-1-undecanethiol in ethanol solution.
2. Two methods of functionalisation of the cantilevers:
    a. All 8 cantilevers: Immerse the gold coated cantilever array in the hydroxyalkanethiol solution in a 200 µl Eppendorf tube for 60 minutes.
    b. Selective functionalisation of the cantilevers: Immerse the gold-coated cantilevers in the hydroxyalkanethiol solution using the capillary functionalisation technique as described in section 5.4.1 for 60 minutes. Refill the capillary reservoir every 15 minutes to compensate for evaporation of the hydroxyalkanethiol solution in the capillaries.
3. Rinse the cantilever array thoroughly with ethanol.
4. Rinse the cantilever array with nanopure water.

B.2.3 Dithiobis(succinimidyl undecanoate) SAM

This protocol is designed to functionalise the gold surface of the cantilever with a self-assembled monolayer of Dithiobis(succinimidyl undecanoate) (DSU) (-succinimidyl ester terminated). The DSU SAM on the gold surface offers amine-reactive sites on the surface that are used for the immobilisation of protein with α-amine groups.

Materials

- Dithiobis(succinimidyl undecanoate) (DSU), (D537-10; NBS Biologicals Ltd, Huntingdon, United Kingdom)
- 1,4-dioxane
- Acetone $(CH_3)_2CO$ HPLC grade
- 200 µl Eppendorf tube
- Capillaries
- Clean gold-coated cantilever array

Method

1. Prepare a 1mM DSU in 1.4 dioxane or acetone solution
2. Two methods of functionalisation of the cantilevers:
    a. All 8 cantilevers: Immerse the gold coated cantilever array in the DSU solution in a 200 µl Eppendorf tube for 45 minutes
    b. Selective functionalisation of the cantilevers: Immerse the gold-coated cantilevers in the DSU solution using the capillary functionalisation technique as described in section 5.4.1 for 45 minutes.
3. Rinse the cantilever array with 1.4 dioxane.
4. Rinse the cantilever array thoroughly with acetone. Do not use water or methanol to avoid transesterification.
5. Proceed immediately with the protein immobilisation

B.2.4 Protein Immobilisation Procedure

This protocol is designed to couple proteins to the DSU SAM by the reactions of the α-amine of the protein with NHS-activated carboxylic acid groups of the SAM.

Materials

- Protein solutions (amine free buffers are mandatory) at a concentration of 1µg/ml
- Phosphate buffered saline (PBS) buffer
- Capillaries
- DSU functionalised cantilever array

Method

1. Prepare a 1µg/ml protein solution in PBS.
2. Selective functionalisation of the cantilevers: Immerse the gold-coated cantilevers in the protein solutions using the capillary functionalisation technique as described in

section 5.4.1 for 30 minutes. The capillaries are aligned with the cantilevers. Then the capillaries are filled and the array is pushed into the filled capillaries.

3. Rinse the cantilever array, now carrying the covalently immobilised proteins, with PBS buffer solution.

B.3 Silicon Surface Functionalisation Procedure

B.3.1 PLL-g-PEG Silicon Functionalisation

This protocol is designed to render the silicon oxide surface of the cantilevers into a protein repellent surface. The Poly(L-lysine)-graft-poly(ethylene glycol) (PLL-*g*-PEG) is a graft copolymer consisting of PEG chains grafted onto a PLL polycationic backbone that prevents non-specific adsorption of biomolecules onto the oxide surface of the cantilevers.

Materials

- PLL(20)-*g*[3.5]- PEG(2) (SuSoS AG, Dübendorf, Switzerland)
- 10 mM Hepes buffer (pH 7.4)
- Capillaries
- 200 µl Eppendorf tube
- Cantilever array

Method

1. Prepare a 0.25 µg/ml PLL(20)-*g*[3.5]- PEG(2) solution in HEPES
2. Incubate the cantilever array in the Eppendorf tube or the individual cantilevers using the capillary method for 30 minutes.
3. Rinse the cantilever array with Hepes buffer.
4. Proceed immediately with the cantilever assay.

Appendix C
List of Publications, Presentations and Patents

Publications

- Michael Walther, Paul Fleming and Martin Hegner. An optimized measurement chamber for cantilever array measurements in liquid incorporating an automated sample handling system. Submitted *EPJ Techniques and Instrumentation*

Presentations

- 11th International Workshop on Nanomechanical Sensing. Madrid (Spain), May 2014
- 10th International Workshop on Nanomechanical Sensing. Stanford (USA), May 2013
- Idea2Product global competition, Sao Paulo (Brazil), November 2013
- Idea2Product local competition, Trinity College Dublin, (Ireland), September 2013
- International Summer School on Entrepreneurship & Technology Venturing, University of Twente, Enschede (The Netherlands), July 2012

Poster

- 11th International Workshop on Nanomechanical Sensing. Madrid (Spain), May 2014
- Idea2Product global competition, Sao Paulo (Brazil), November 2013
- Researcher Night, Dublin (Ireland), September 2013

- 10th International Workshop on Nanomechanical Sensing, Stanford (USA), May 2013
- PhD Summer School: Micro and Nanotechnology for Label-free Sensing, DTU Copenhagen (Denmark), August 2012
- International Summer School on Entrepreneurship & Technology Venturing, University of Twente, Enschede (The Netherlands), July 2012
- 8th International Workshop on Nanomechanical Sensing, Dublin (Ireland), May 2011

Patents

- PCT/EP2013/073258 A microfluidic device incorporating a nanomechanical sensor (Patent pending)

List of Figures

List of Tables

Glossary

Achromatic doublet

A lens designed to limit chromatic and spherical aberration. It is normally comprised of two separate lenses, one concave and one convex, each with different dispersions.

Adjuvant

A nonspecific stimulator of the immune response to improve the immune response.

Affinity

Strength of interaction between a single antigen binding site and a single antigenitc determinant.

Analyte

Any substance or constituent being subjected to analysis, or which a lab conducts testing.

Antibody

An immunoglobulin produced by plasma cells, which has a specific amino acid sequence and specifically binds to the antigen (e.g., foreign protein) that induced its synthesis; antibodies may also bind to closely related antigens.

Antigen

Any of various substances that causes a specific immune response.

Antigenitc determinant

A structural component of an antigen molecule responsible for its specific interaction with antibody molecules elicited by the same or related antigen.

Assay

A quantitative or qualitative procedure for detecting the presence, estimating the concentration, and/or determining the biological activity of a molecule (e.g. an antibody or antigen). Assays are based on measurable parameters that allow differentiation between sample and control.

Block Diagram

Contains the source code (Control Terminals, Wires, and Structures and various other nodes) of any LabVIEW program, and determines the execution of the program.

Blood plasma

The fluid portion of the blood in which the particulate components are suspended.

Circum-sporozoite protein

A protein involved in sporozoite recognition of host cells in malaria.

Cross-reaction

An interaction between an antibody and an antigen closely related to the antigen that specifically stimulated synthesis of the antibody.

Cross-reactivity

The degree to which an antibody participates in cross-reactions.

Enzyme

A protein that acts as a catalyst during chemical reactions, while remaining apparently unchanged itself by the process.

Erythrocytes

Red blood cells, the main component in the circulating blood.

Exogenous antigens

Antigens originating outside of a cell, tissue, etc.

Fine specificity

The ability of the immune response to interact with individual antigens.

Front Panel

Provides the user interface (containing Controls and Indicators) to the LabVIEW program.

Gametocytes

The sexual form of certain sporozoa, such as malarial plasmodia, found in the erythrocytes.

Glycoproteins

A large group of conjugated proteins covalently linked to one or more carbohydrate groups.

Immunisation

A procedure (e.g. vaccination) for creating resistance to a pathogen (e.g. produce immunity).

Immunity

The state of an individual's existing resistance to a pathogen, whether conferred by a previous infection or via vaccination.

Immunogen

See antigen.

Immunoglobulin

Large glycoproteins that function as antibodies in the immune response by binding the specific antigens.

In vitro

In an artificial environment outside a living organism.

In vivo

Within a living organism.

Inhibitory effects

Tending to stop or slow a process.

Labelling

Linking analytes (e.g. antibodies) under study with some kind of detectable label. Labels are typically chemically linked or conjugated to the desired analyte.

Lyophilisation

The material is frozen and then the pressure is dropped to sublimate the remaining frozen water in the material (freeze-drying).

Monoclonal antibody

An antibody produced by a clone or genetically homogeneous population of hybrid cells.

NOSEtools

A data analysis package for the handling of cantilever array data written by T. Braun implemented in the IGOR Pro environment.

Oligonucleotide (oligo)

A short nucleic acid polymer with fifty or fewer bases.

Pathogen

An agent, e.g. bacterium or virus, that causes disease.

Peptides

A molecule composed of two or more amino acids joined by a peptide bond, which combine to make proteins.

Plasma cells

Type of white blood cell that produces antibodies.

Plasmodium falciparum

A protozoan that causes falciparum malaria.

Polyclonal antibody

Antibody that is derived from different clones of plasma cells but reacts with different antigenic determinant of a particular antigen.

Protein

A complex molecule composed of a sequence of amino acids linked in a genetically controlled linear sequence into one or more peptide chains. Proteins are present in every living cell and form an essential constituent of cells.

Protozoan

A unicellular organism including free-living forms, such as amoeba and parasites.

Serum

Blood plasma with the blood clotting proteins removed.

Thiol

An organic compound that contains a carbon bonded sulfhydrl (SH) group. Thiols form a strong bond with noble metals and can be used to form a SAM. The sulphurgold bond is semi covalent with a strength of 45 kcal/mol.

Titer

The dilution of a serum containing a specific antibody at which the solution retains the minimum level of activity needed to neutralise or precipitate an antigen.

Vaccine

Antigenic material in the form of weakened, killed, or modified pathogens, introduced to the body to induce immunity against a particular pathogen.

Vector

A carrier, especially the animal (usually an arthropod) that transfers an infective agent

from one host to another. Examples are the Anopheles mosquito that carries the malaria parasite *Plasmodium* between humans.

Virtual Instrument (VI)

The basic building block of programs written in LabVIEW. It is similar to a function or subroutine in other programming languages. It includes the Front Panel and the Block Diagram.